

University of Southampton Research Repository ePrints Soton

Copyright © and Moral Rights for this thesis are retained by the author and/or other copyright owners. A copy can be downloaded for personal non-commercial research or study, without prior permission or charge. This thesis cannot be reproduced or quoted extensively from without first obtaining permission in writing from the copyright holder/s. The content must not be changed in any way or sold commercially in any format or medium without the formal permission of the copyright holders.

When referring to this work, full bibliographic details including the author, title, awarding institution and date of the thesis must be given e.g.

AUTHOR (year of submission) "Full thesis title", University of Southampton, name of the University School or Department, PhD Thesis, pagination

UNIVERSITY OF SOUTHAMPTON

FACULTY OF ENGINEERING, SCIENCE & MATHEMATICS

School of Engineering Sciences

MODELLING OF MICROELECTRONIC PROCESSES AND MATERIALS

by

TOBIAS BALLA

Thesis for the degree of Doctor of Engineering Sciences

April 2011

UNIVERSITY OF SOUTHAMPTON

ABSTRACT

FACULTY OF ENGINEERING, SCIENCE & MATHEMATICS

SCHOOL OF ENGINEERING SCIENCES

Doctor of Engineering Sciences

MODELLING OF MICROELECTRONIC PROCESSES AND MATERIALS

by Tobias Balla

Organic electronics promises the creation of electronic components on flexible materials at low temperatures, by fast techniques and more environmentally friendly processes. The research followed two directions. The first part focused on the manufacturing technique nanoimprint lithography (NIL). A comprehensive review was undertaken and process capabilities were compared for trends. It was seen that small feature sizes ($< 50\text{ nm}$) have not been replicated over areas greater than 4 mm^2 , while aspect ratios greater than 10 have not been achieved. A questionnaire addressing market opportunities suggested NIL is likely to compete for the production of devices that currently use electron beam lithography and laser writing processes that are seeking to change their business strategy from a differentiation base to a cost reduction. NIL must also prove to customers that it is an economical investment. However, improvements in stamp creation, analysis techniques and overlay alignment need to be addressed for a larger share of the microfabrication market. It was apparent that physical limits exist to which imprints can be produced and an analytical model could predict these. A model was created to describe the de-embossing step and to explore how the various material properties and process variables interact. It showed a very strong dependence on the achievable aspect ratio on the pattern area ratio and the interfacial shear stress; that de-embossing using fluorinated coatings and current standard polymers is unlikely to fail for post radii on the order of 100 nm due to adhesion and that large area ratios and aspect ratios are more easily achieved by maintaining the polymer/stamp Young's moduli ratio (R_E) in the range 0.003 to 5.

The second part of the research looked at the formation of crescent singularities in thin sheet materials, which affects the production of polymer electronic based devices produced by the sponsoring company. The author compared an analytical model by Cerda and Mahadevan for the formation of developable cones (d-cones) to a finite element (FE) model and showed that explicit elements could mimic the formation of a d-cone. Different elements were analysed for their suitability and the Belytschko-Lin-Tsay (BT) element was

chosen based on its speed, robustness and similarity to the analytical results. An adapted three-point bend test set-up was conceived that would enable specific attributes to be independently varied, to understand their effect on d-cone formation in thin sheets. Digital image correlation (DIC) was used to calculate the displacements and strains. The same set-up was modelled using an FE model with the chosen BT element. The DIC results showed a variation in strain with plunger displacement before the visual appearance of a developable cone and that it occurred between 0.1 and 0.4 % *in-plane* strain. The FE data showed a similar trend to the DIC results, showing a change in strain once a d-cone began to form. Improvements and suggestions were then made advising how to make the DIC and FE models more accurate.

CONTENTS

FIGURESIX

TABLES XIII

DECLARATION OF AUTHORSHIP **XV**

ACKNOWLEDGEMENTS **XVII**

NOMENCLATURE **XIX**

CHAPTER 1: INTRODUCTION **1**

1.1 RESEARCH DIRECTION 2

1.1.1 INDUSTRIAL INVOLVEMENT 3

CHAPTER 2: NANOIMPRINT LITHOGRAPHY **7**

2.1 STAMP 9

2.2 FIELD SIZE AND WAFER 9

2.3 RESIST AND APPLICATION 10

2.4 ALIGNMENT PROCEDURE 10

2.5 PRESSURE APPLICATION 11

2.6 NIL PROCESS CAPABILITIES 11

2.7 RELIEF HEIGHT VERSUS INITIAL RESIST THICKNESS 12

2.8 RESIDUAL LAYER VERSUS INITIAL RESIST THICKNESS 13

2.9 RELIEF HEIGHT VERSUS LINE WIDTH 15

2.10 FEATURE SIZE VERSUS IMPRINT AREA 16

2.11 RELIEF HEIGHT VERSUS IMPRINT AREA 16

2.12 TOLERANCE VERSUS FEATURE WIDTH 17

2.13 DISCUSSION 18

2.14 CONCLUSIONS 20

CHAPTER 3: QUALITATIVE RESEARCH **21**

3.1 PHOTONICS INDUSTRY PERSPECTIVE 21

3.2 MICROFLUIDIC INDUSTRY PERSPECTIVE 21

3.3 MEMORY STORAGE INDUSTRY PERSPECTIVE 22

3.4 MICROELECTRONICS INDUSTRY PERSPECTIVE 22

3.5 MICRO ELECTROMECHANICAL SYSTEMS INDUSTRY PERSPECTIVE 22

3.6 CURRENT RESEARCH APPLICATIONS 22

3.7 POTENTIAL NEAR FUTURE APPLICATIONS 25

3.8 CONCLUSIONS 26

3.9 RESEARCH DIRECTION 27

CHAPTER 4: NANOIMPRINT LITHOGRAPHY MODELLING	29
4.1	MODELLING LITERATURE REVIEW 30
4.1.1	IMPRINTING 30
4.1.2	DE-EMBOSSING 31
4.1.3	ANTI-STICKING LAYERS 33
4.2	DE-EMBOSSING MODEL FORMULATION 35
4.2.1	DE-EMBOSSING OF A POLYMER POST 35
4.2.2	COMPOSITE MODELLING COMPARISON 37
4.2.3	ASSUMPTIONS 37
4.2.4	RESIDUAL LAYER STRESS DISTRIBUTION 39
4.2.5	MATLAB SCRIPT VALIDATION 40
4.2.6	STAMP TOP STRESS DISTRIBUTION 42
4.3	ANALYTICAL MODELLING 43
4.3.1	ENERGY BALANCE EQUATIONS 43
4.3.2	CONSTANT DISPLACEMENT EQUATIONS 45
4.3.3	SCRIPT PROCEDURE 46
4.3.4	ATTRIBUTE VALUES 48
4.4	RESULTS 49
4.5	DISCUSSION 52
4.6	CONCLUSIONS 54
CHAPTER 5: CREASING THIN SHEETS	59
5.1	POLYMER VISION 59
5.1.1	MARKET POTENTIAL 60
5.1.2	DEVICE ISSUES 60
5.1.3	RESEARCH AIMS 60
5.2	BACKGROUND RESEARCH 61
5.3	LITERATURE REVIEW 63
5.3.1	THEOREMA EGREGIUM 63
5.3.2	DEFORMATION OF THIN SHEETS 64
5.3.3	ENERGY FOCUSING 65
5.3.4	DEVELOPABLE CONES 66
5.4	D-CONE FINITE ELEMENT ANALYSIS 69

5.4.1	NUMERICAL SOFTWARE	69
5.4.2	CYLINDRICAL RIM D-CONE	70
5.4.3	ANSYS OPTIONS	71
5.4.4	LS-DYNA OPTIONS	73
5.4.5	SOLVING ELEMENTS	73
5.4.6	OPENING ANGLE MEASUREMENT METHOD	76
5.5	D-CONE RESULTS	77
5.6	D-CONE ELEMENT DISCUSSION	81
5.6.1	ELEMENT CHOICE	81
CHAPTER 6: DEVELOPABLE CONE FORMATION		83
6.1	PHYSICAL EXPERIMENTAL COMPARISON	84
6.1.1	DIGITAL IMAGE CORRELATION SET-UP	85
6.1.2	DIC ERROR MEASUREMENT	86
6.1.3	DIC SPECKLE PATTERN	87
6.1.4	EXPERIMENTAL SET-UP	88
6.1.5	DIGITAL IMAGE CORRELATION ANALYSIS	88
6.2	FINITE ELEMENT ANALYSIS	89
6.2.1	THREE POINT BEND SIMULATION	89
6.2.2	FE VERACITY	92
6.3	EXPERIMENTAL RESULTS AND DISCUSSION	94
6.3.1	DIC AND FE DIRECT AND SHEAR STRAIN VALUES	95
6.3.2	DIC AND FEA SHEET DISPLACEMENT	99
6.3.3	DATA REPRESENTATION	99
6.3.4	MESH DEPENDENCY	100
6.3.5	PEN SHEETS 25 μM THICK	101
6.3.6	PEN SHEETS 50 μM THICK	103
6.3.7	PEN SHEETS 125 μM THICK	104
6.3.8	CONSTANT THICKNESS DISCUSSION	105
6.3.9	20 MM BETWEEN FIXED EDGE AND PRONGS	106
6.3.10	30 MM BETWEEN FIXED EDGE AND PRONGS	107
6.3.11	40 MM BETWEEN FIXED EDGE AND PRONGS	108

6.3.12	50 MM BETWEEN FIXED EDGE AND PRONGS	109
6.3.13	CONSTANT OFFSET DISCUSSION	109
6.4	CONCLUSIONS	110
CHAPTER 7: OVERALL CONCLUSIONS AND FUTURE WORK		113
7.1	FUTURE WORK	114
7.1.1	DIC DATA CAPTURE IMPROVEMENT	115
7.1.2	FE DATA DISCUSSION	118
REFERENCES		119
APPENDIX A: PUBLICATIONS		129
	UNDER REVIEW	129
APPENDIX B: COMPANY QUESTIONNAIRE		131
APPENDIX C: PATENT		133
APPENDIX D: LOVE'S RESULTS COMPARISON		135
APPENDIX E: STRAIN ENERGY DERIVATION		137
APPENDIX F: MATLAB CODE		147
	SHEAR STRESS CALCULATION	147
	EQUATIONS 4.13 AND 4.14 SCRIPT	149
	RESIDUAL LAYER SCRIPT	151
APPENDIX G: ANSYS FE CODE		153
	CIRCULAR RIM MODEL	153
	THREE-POINT BEND MODEL	161
APPENDIX H: IRIDIS SUBMISSION SCRIPT		169
APPENDIX I: JIG DESIGN DRAWINGS		171
APPENDIX J: DVD MATERIAL		183

FIGURES

Figure 1.1: OE-A roadmap for organic and printed electronic applications [2].	2
Figure 2.1: Process flows for: (a) T-NIL and (b) UV-NIL.	8
Figure 2.2: Relief height and resist thickness comparison of TNIL and UVNIL imprinting.	12
Figure 2.3: Schematic illustration of how high relief patterns increase the distance for the polymer to flow, making filling difficult from minimal resist.	13
Figure 2.4: Graph displaying NIL's capability to displace the resist to achieve smaller residual layers, relevant for creating resist masks.	14
Figure 2.5: Graph indicating aspect ratios achieved by NIL at various feature sizes.	15
Figure 2.6: Graph showing feature size versus field size.	16
Figure 2.7: Graph depicting little correlation of the relief heights achieved using NIL over various field sizes.	17
Figure 2.8: Standard deviation and line edge roughness values for NIL imprinted feature sizes.	18
Figure 4.1: Schematic of an example of a chemical process to produce a silane coating on a silicon oxide surface [111].	33
Figure 4.2: Free body diagrams detailing the forces during de-embossing of a polymer post.	36
Figure 4.3: (a) Fully bonded state, equal strain at each cross-section; (b) Interfacial critical strain energy release rate overcome but not the side-wall friction; (c) Strain energy release rate and the side-wall friction is overcome enabling de-embossing.	37
Figure 4.4: Illustration of a cylindrical punch on a semi-infinite half-space under an applied stress. The stress distribution in the residual layer is assumed to be similar.	40
Figure 4.5: a) Two logarithmic distributions emanating out from the punch edge used for the r -values are used calculate the stress in the semi-infinite half-space at different locations; b) Normalized stress distribution σ_z calculated for a semi-infinite half-space that is used to approximate the residual area.	42
Figure 4.6: Illustration of an axisymmetrical cylinder punch on a semi-infinite half-space under an applied stress. The stress distribution in the stamp top is assumed to be similar.	42

Figure 4.7: Graphic description of the superposition principle, explaining how the stress distribution in the stamp top is calculated.	43
Figure 4.8: De-embossing process tree used in Matlab script.	46
Figure 4.9: Crack extension (x) at constant deflection, results in a decrease in the elastic strain energy/increase in surface energy.	47
Figure 4.10: De-embossing limits for shear stress (τ) compared to varying aspect ratios (AR) and area fractions (f).	49
Figure 4.11: De-embossing limits for critical strain energy release rate (G_{IC}) compared to aspect ratio (AR) and area fraction (f).	50
Figure 4.12: De-embossing limits for area fraction (f) as a function of polymer yield strength (σ_{yp}) and stamp/polymer modulus ratio (R_E).	51
Figure 4.13: De-embossing limits for Aspect ratio, AR , as a function of polymer strength (σ_{yp}), and modulus ratio (R_E).	52
Figure 4.14: De-embossing limits for the strain energy release rate (G_{IC}) compared to the aspect ratio (AR) and area ratio (f), with a polymer yield stress (σ_{yp}) of 10 MPa.	53
Figure 5.1: ‘Radius’ by Polymer Vision, using a display made on a rollable plastic film, enabling the screen size to be larger than the device body.	59
Figure 5.2: Five times magnification of a crease tip in patterned PEN viewed through three filters.	61
Figure 5.3: Twenty times magnification of the fifth Au line in Figure 5.2. Fibrous edge of the fractured line can be clearly seen, imaged through three filters.	62
Figure 5.4: Fifty times magnification of the fifth Au line in Figure 5.2; a) Fracture along the top edge in focus; b) Partial fracture along the trough in focus; c) Fracture along the bottom edge in focus.	62
Figure 5.5: A hyperboloid’s surface has a negative Gaussian curvature, a cylinder’s surface has zero Gaussian curvature and a sphere’s surface has a positive Gaussian curvature.	64
Figure 5.6: D-cone from above, pinching paper between thumb and two fingers.	67
Figure 5.7: D-cone from below, pinching paper between thumb and two fingers.	67
Figure 5.8: Static sequence showing the formation of a developable cone.	68

Figure 5.9: Free mesh of sheet employed in ANSYS with mesh refinement in contact regions.....	72
Figure 5.10: Interface pressures show sheet contact with rim providing d-cone location and size.	76
Figure 5.11: Chord measured on the rim at contact points with d-cone.	77
Figure 5.12: D-cone forming for various central displacements, from left to right.	77
Figure 5.13: Comparison of solving times in LS-DYNA for different element theories used.	78
Figure 5.14: Mahadevan and Cerda's published S-curve of numerical values of the contact arc length (\mathcal{r}_c) and its projection (θ_c) as a function of the vertical displacement ε [134].	79
Figure 5.15: Element theory comparison for the creation of a developable cone.	80
Figure 6.1: Variables for the three-point bending set-up, consisting of a thin sheet clamped on one side.	83
Figure 6.2: (a) Test set-up (b) Instron set-up (c) Jig used for physical d-cone experiment.	85
Figure 6.3: DIC camera set-up, with cameras equidistant to the sample and at angles of about 30°	86
Figure 6.4: Alicona TM image analysis of paint speckles on PEN sheet.	87
Figure 6.5: D-cone formation in a sheet with one fixed edge produced by a three-point bend analysis.	90
Figure 6.6: Choosing elements with the greatest ε_y at $\mathcal{z} = 10$ mm, for $b = 125$ μm and $\mathcal{x}_6 = 20$ mm.	91
Figure 6.7: Graph indicating the ε_y strain of the elements about the point of the terminus.	92
Figure 6.8: The effect of hourglassing on an explicit dynamic analysis [161].	93
Figure 6.9: Hourglassing energy as a percentage of internal energy for all FE models.	93
Figure 6.10: Variation in ε_x , ε_y , ε_{xy} and ε_{VM} , for an b of 125 μm and an \mathcal{x}_6 of 20 mm.	95
Figure 6.11: FE ε_x analysis at a \mathcal{z}_p of 5 mm, depicting regions of tension and compression in close proximity.	96
Figure 6.12: DIC interval photos of a d-cone formation for a PEN sheet with an b of 125 μm and an \mathcal{x}_6 of 20 mm.	98

Figure 6.13 DIC and FE x, y and z displacement for an h of 125 μm and x_6 of 20 mm.....	99
Figure 6.14: Mesh dependency comparison for varying thicknesses and an x_6 of 30 mm.	100
Figure 6.15: DIC and FE ε_y and z displacement information for 25 μm sheets.....	101
Figure 6.16: Distorted ridge formation for $x_6 = 25 \mu\text{m}$ and $h = 30 \text{ mm}$ sheet at $z_p = 7 \text{ mm}$, highlighted in red. Sheet 'snaps' to ideal d-cone shape afterwards, initiating from the line of glare at top of image.	102
Figure 6.17: FE ε_y snapshots for x_6 of 30 mm, showing the crescent singularity moving towards the terminus.	103
Figure 6.18: DIC and FE ε_y and z displacement information for 50 μm sheets.....	104
Figure 6.19: DIC and FE ε_y and z displacement information for 125 μm PEN sheets.....	105
Figure 6.20: DIC and FE ε_y and z displacement information for x_6 of 20 mm.....	106
Figure 6.21: DIC and FE ε_y and z displacement information for x_6 for 30 mm.	107
Figure 6.22: DIC and FE ε_y and z displacement information for x_6 of 40 mm.....	108
Figure 6.23: DIC and FE ε_y and z displacement information for x_6 of 50 mm.....	109
Figure 7.1: DIC image through a) right camera; b) left camera, displaying hazy regions and glare.	116
Figure 7.2: DIC correlated strain data. Data loss can be seen due to glare and regions of low contrast.....	117
Figure 7.3: Fracture possibly caused by crescent singularity movement, Polymer Vision 2008.....	118

TABLES

Table 2.1: Nanoimprint Lithography terms.	8
Table 3.1: Qualitative information gathered from questions put to people using microfabrication techniques.	24
Table 4.1: Surface treatments used and their published values for work of adhesion.	34
Table 4.2: Standard material and geometrical values used when constant.	48
Table 5.1: Attribute values used for the creation of the ANSYS model.....	71
Table 5.2: New values used for LS-DYNA control cards for model set-up.	73
Table 5.3: LS-DYNA card alterations to implement various shell theories.	74
Table 6.1: Variables used for d-cone analysis on a clamped sheet.....	84
Table a: Dimensionless variables and stresses calculated by Love.	135
Table b: Dimensionless variables and stresses calculated by Matlab.....	136

DECLARATION OF AUTHORSHIP

I, Tobias Balla

declare that the thesis entitled

MODELLING OF MICROELECTRONIC PROCESSES AND MATERIALS

and the work presented in the thesis are both my own, and have been generated by me as the result of my own original research. I confirm that:

this work was done wholly or mainly while in candidature for a research degree at this University;

1. where any part of this thesis has previously been submitted for a degree or any other qualification at this University or any other institution, this has been clearly stated;
2. where I have consulted the published work of others, this is always clearly attributed;
3. where I have quoted from the work of others, the source is always given. With the exception of such quotations, this thesis is entirely my own work;
4. I have acknowledged all main sources of help;
5. where the thesis is based on work done by myself jointly with others, I have made clear exactly what was done by others and what I have contributed myself;
6. parts of this work have been published prior to submission and a list of journal publications is given in Appendix A.

Signed:.....

12th April 2011

Date:.....

ACKNOWLEDGEMENTS

The completion of this thesis is testament to the patience and help of many people, whom I will always be indebted to. My biggest thanks are to Mark Spearing for his continual support, advice, guidance, ideas and grins of happiness that kept my mood buoyant. His contribution to the EngD and to me as a person has been of *Herculean* proportions and I will be forever grateful. Thank you! I would also like to thank Andrew Monk, Nick van Aerle and Ralf Lichtenberger who have been extremely helpful from bringing this EngD into being, throughout its course and then to completion; their advice and feedback has been extremely beneficial on many occasions. Philippa Reed's input has also been extremely appreciated, thank you for making my EngD happen!

The support of my fellow students in the Engineering Materials Research Group at the University of Southampton has been hugely beneficial, helping me to achieve my goals through their help and tolerance of my questions, moans, procrastinations and tea breaks. I am especially grateful to Stewart, Nik, Andrew, Pete, Thomas, Thilo, Anna, Polly, Prasanna and Mark, I would also like to thank the bio-engineering materials group, especially Alex, Olly, Becky, Mark, Pramod, Catherine, Pete, Hatice and Michael.

The secretarial and technical staff in the school have been amazing and helped me more than they know. Thank you to Gwyneth, Sue, Alessia, Sonya, Dawn, Chris, Erik, Dave and Bob. Michelle Tuttle at the University of Birmingham has also been of enormous assistance and my gratitude goes to her.

I would like to thank the Engineering and Physical Sciences Research Council, Innos and Polymer Vision for their financial support in making this Doctorate possible. My gratitude goes out to all the staff at Innos and Polymer Vision who helped, especially Hayley at Innos who organised so much, thank you.

Thank you to all the souls who helped at a distance. Ivan Wolton and David Baker from the high performance computing centre, I thank you for your help with Iridis. Thank you to Peter Ashburn, Darren Bagnall, Michael Kraft and Hywel Morgan in the Nano research group. Ralf Lichtenberger of Limess; my thanks go to you for helping me through the world of digital image correlation. Thank you to the LSTC and ANSYS support teams for their help with the software packages I used, in particular Morten Jensen and Samy Thippadu, whose advice stopped numerous computers from crashing.

To my family members, thank you Dad for all the help proof reading my thesis. How much you helped you have no idea. Danny, Billie, diolch am helpwch fi hefyd! To the rest of my

friends and family, thank you for all your encouragement and support helping me over the hurdles and through the hoops I encountered on the way.

My final and everlasting thanks are for Joy, min älskling, who showed me how to become a Dr. by leading the way. Her love, support and company made this worthwhile. Du är min livs stora kärlek, tack för hjälper mig!

Finally:

To laugh is to risk appearing the fool,

To weep is to risk appearing sentimental,

To reach out for another is to risk exposing your true self,

To place your ideas, your dreams before the crowd is to risk their loss,

To love is to risk not being loved in return,

To live is to risk dying,

To hope is to risk despair.

To try is to risk failure but the risk must be taken, because the greatest hazard in life is to risk nothing.

The person who risks nothing, does nothing, is nothing.

He may avoid suffering, but he simply cannot learn, feel, change, grow, love, live.

Chained by his certitude's, he is a slave.

He has forfeited freedom,

Only a person who risks is free.

—

Unknown

NOMENCLATURE

a	pre de-embossing state
AFM	atomic force microscopy
AR	aspect ratio
A_{r-m}	resist-mould interface area
A_{r-s}	resist-substrate interface area
ASL	anti-sticking layer
ASTS	automatic surface to surface
A_T	total unit cell area
Au	gold
b	partial de-embossing state
BPM	bit pattern media
BT	Belytschko-Lin-Tsay
BTW	BT element with Belytschko-Wong-Chaing warping stiffness
BTWP	BTW element with full projection
BWC	Belytschko-Wong-Chaing element
c	(Part 1) full de-embossing state, (Part 2) speed of sound
CBA _s	cantilever beam arrays
CCD	charge coupled device
CFD	computational fluid dynamics
CMOS	complementary metal oxide semiconductor
CPU	central processing unit
d-cone	developable cone
DCB	double cantilever beam
DDMS	dimethyldichlorosilane
DIC	digital image correlation
DLC	diamond like carbon
DOF	degrees of freedom
DTR	discrete track recording
EBL	electron beam lithography
E_c	composite Young's modulus
E_h	hourglass energy
E_i	internal energy
EngD	Doctorate of Engineering
E_p	polymer Young's modulus
E_s	stamp Young's modulus
EUV	extreme ultra-violet
f	area fraction
F	Force due to adhesion
FDTS	perfluorodecyltrichlorosilane
FE	finite element
FIB	focussed ion beam
FIS	fully integrated shell element (FIS)
FISH	FIS element with hourglass mode type 8 initiated
Fots	perfluorooctyltrichlorosilane
FvK	Föppl and von Karman
G_{ic}	critical interfacial strain energy release rate
GUI	graphical user interface
b	(Part 1) polymer thickness (Part 2) sheet thickness

h_0	initial thickness of spin coated polymer layer
HEL	hot embossing lithography
hg	hourglass coefficient
ICs	integrated circuits
k	curvilinear co-ordinate distance
LER	line edge roughness
L_s	characteristic length
LSTC	Livermore Software Technology Corporation
MEMs	micro electromechanical systems
mk	mass scaling
MOSFETs	metal-oxide semiconductor field effect transistors
NIL	nanoimprint lithography
ν_{pen}	PEN's Poisson's ratio
ν_{stl}	steel's Poisson's ratio
OE-A	Organic Electronic Association
OLEDs	organic light emitting diodes
OTFTs	organic thin film transistors
OTS	octadecyltrichlorosilane
P	applied load
p	pressure
PEN	polyethylene naphthalate
PIL	photo imprint lithography
PMMA	Polymethylmethacrylate
PMR	perpendicular magnetic recording
PNIL	photo nanoimprint lithography
PS	Polystyrene
PTFE	polytetrafluoroethylene
r	(Part1) post radius, (Part 2) rim radius
R	(Part1) unit cell radius, (Part 2) sheet radius
r_1	inner punch radius
r_o	outer punch radius
r_2	rim contact inner radius
r_3	rim contact outer radius
R_E	polymer/stamp Young's moduli ratio
RFID	radio frequency identification
ρ_{pen}	PEN's density
ρ_{stl}	steel's density
RIE	reactive ion etch
RTNIL	room temperature nanoimprint lithography
SAW	surface acoustic wave
s_c	contact arc length
s_{eff}	effective pattern size
SEM	scanning electron microscopy
SFIL	step and flash imprint lithography
SMEs	small/medium enterprises
SRAM	static random access memory
t	imprint time
T	process temperature
TFS	trichlorosilane
TFTs	thin film transistors
T_g	glass transition temperature

TIL	thermal imprint lithography
TNIL	thermal nanoimprint lithography
$tval$	time
U	strain energy
UVNIL	ultra-violet nanoimprint lithography
UVSIL	ultra-violet soft imprint lithography
vel	velocity
V_{sl}	frictional energy
w	PEN sheet width
x	crack extension
x_1	x -plane offset between plungers above and below sheet
x_2	y -plane offset between plungers above and below sheet
x_3	plunger diameter
x_4	offset between plungers above sheet
x_5	offset between free edge and hemisphere centres above sheet
x_6	offset between the fixed and hemisphere centres above sheet
\tilde{x}	length measurements
\tilde{x}'	slip length
\tilde{z}_p	plunger displacement
γ_m	mould surface free energies per area
γ_r	resist surface free energies per area
γ_{r-m}	resist-mould free energies of adhesion per unit area
γ_{r-s}	resist-substrate free energies of adhesion per unit area
γ_s	substrate surface free energies per area
δ	displacement
ΔG	lowest total free energy of the surface
δ_p	polymer displacement
δ_{rl}	residual layer displacement
δ_{st}	stamp displacement
δ_T	total displacement
Δt_e	time-step
ε	vertical displacement
ε_{VM}	Von Mises strain
ε_x	x strain
ε_y	y strain
ε_z	z strain
ε_{zy}	xy strain
η	polymer viscosity
θ	curvilinear co-ordinate angle
θ_c	contact arc length projection
μCP	micro contact printing
σ_0	applied stress at the 0 surface/boundary
σ_i	first order standard deviation
σ_p	polymer post stress
σ_{p1c}	polymer post stress at boundary 1 in state c
σ_s	stamp stress
σ_{yp}	polymer yield stress
σ_{ys}	stamp yield stress

τ shear stress

CHAPTER 1: INTRODUCTION

Polymer electronics is the field in which plastics assume an electrical and/or electronic function. Also referred to as *organic* electronics because the polymer chains and small molecules are carbon based; as with living molecules, polymer electronics has presented new markets for the electronic industry that it aims to revolutionise. The discovery of conductive polymers was made in 1977 by Heeger, MacDiarmid and Shirakawa [1], who were later awarded the Nobel Prize for chemistry in 2000 for their work. Before then, it was assumed polymers only had insulating properties. From the time of the discovery, it has taken many years for the knowledge to bear fruit in the form of devices. However, it was not in vain. In 2005/2006 the first organic electronics products came to market [2]: passive ID cards, mass printed on paper. Other products soon followed: flexible lithium polymer batteries soon followed for smart cards and mobile consumer products, printed antennae used in radio frequency identification (RFID) tags and large-area organic pressure sensors for retail logistic applications. There are many more markets for polymer electronics and with each new technology, new processing means will need to be researched and devised. Electronic components such as integrated semiconductor structures, light emitting diodes, displays, photovoltaics and sensors are but a few possibilities for products using organic electronics.

Microelectronics using inorganic materials, such as metals and silicon, has had an exponential growth in the twentieth century. A similar pattern is expected for organic electronics in the twenty-first century. Where inorganic electronics use hard, stiff, brittle materials, processed using high temperature techniques and large amounts of energy, organic materials promise the creation of electronic components on flexible materials at low temperatures [3], using less hazardous chemicals, by fast, economic printing techniques and more environmentally friendly processes. Research is now being undertaken to bring these products and processes to fruition. Figure 1.1 illustrates a roadmap created by the Organic Electronic Association (OE-A) for printed and organic electronic applications.

There are a number of challenges still preventing the use of many organic electronic devices. These include:

1. device lifetime;
2. electrical performance;
3. manufacturability;
4. resolution and registration of patterning techniques;

5. substrate flexibility;
6. yield values/cost per device.

To enable these technologies, material, process and design issues for specific devices must be overcome.

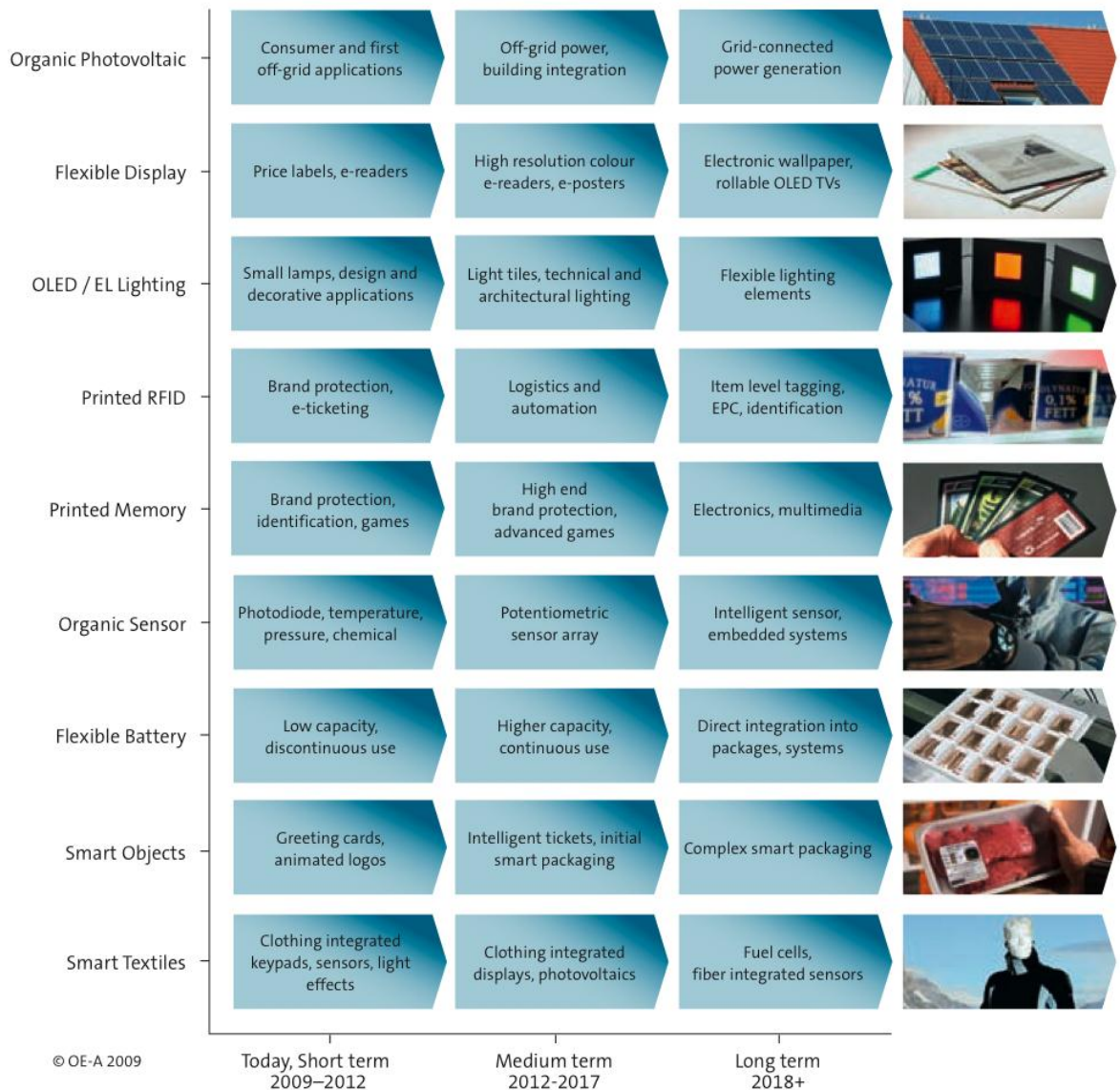


Figure 1.1: OE-A roadmap for organic and printed electronic applications [2].

1.1 RESEARCH DIRECTION

To some extent the principal challenges in organic electronics are inter-related, with many processes, materials and properties affecting one another. However, the work undertaken and published here in looked specifically at issues in the manufacturing of polymer electronics. The research direction was in support of commercial plans for the sponsoring companies. Two separate topics have been addressed. The first part comprises chapters that focused on a manufacturing technique used in microfabrication called nanoimprint

lithography (NIL), which affects the device lifetime, electrical performance, resolution and registration of patterning techniques and yield values. The chapters in the second part document research into crescent singularities that can form when manufacturing polymer electronics on thin sheets, which can ultimately cause device failure.

1.1.1 Industrial involvement

The Engineering Doctorate (EngD) was a four-year doctoral research programme involving a significant taught component. Over 75 % of a research engineer's time over the period was spent working on research interests of the sponsoring company. The EngD at the University of Southampton combined the intellectual challenge of a PhD with taught courses from the Southampton MBA Programme and commercial experience gained through conducting research in collaboration with the industrial sponsor.

The research presented in Part 1 was in partnership with Innos Ltd, a research and development company for innovations in nanoscale technology. They provided commercial and academic institutions with access to processing capabilities, enabling micro and nanofabrication. They developed processes to increase reliability and yields, prototyping new technologies and devices.

Research in Part 2 focused on engineering issues for Polymer Vision. They aim to be a key company in the field of mobile devices by introducing rollable displays, enabling large screens in a pocket-size device. Their research interests look to develop their rollable polymer electronics capabilities for use in multiple generations of mobile devices.

In 2008 Polymer Vision acquired Innos Ltd, who at the time were instructed to develop the rollable display's manufacturing process from an in-house process to a batch production operation. Initially work set out to continue on from research completed in Chapter 1. However it was decided that greater benefits would be achieved for the company by having the research look into another form of material processing, which would benefit the company in the shorter term.

Part 1

CHAPTER 2: NANOIMPRINT LITHOGRAPHY

Innos had an array of toolsets available for innovating process paths and device creation. One of these was an EVG 520 Aligner Bonder. At the time, Innos had no knowledge base on using the machine for imprint lithography. Being a relatively new technique with the potential for use as an alternative to optical lithography, it was felt that it would be beneficial to undertake an analysis on the technique, its current capabilities and to determine whether it was worth the company investing time and finances into innovating the process further.

Chou, Krauss and Renstrom [4] introduced this nanoimprint lithography (NIL) in 1995. They showed its ability to produce nanostructure features and how it could be used for an etch mask as in a lithography process, which is how the name came about. They suggested using NIL to manufacture nanostructures and produce integrated circuits (ICs). Since its introduction, many aspects of the technique have been improved including resist modification [5-8], defect reduction [9, 10], increasing the patterning resolution [11, 12], overcoming stiction problems [12-14], alignment issues [15, 16], distortion and overlay performance [17, 18], modelling and improving polymer flow [19-24]. This has resulted in many toolsets produced by various companies, performing the same function, yet with different toolset designs and processes.

Two current forms of NIL exist commercially: Thermal NIL (TNIL) [25], which uses a thermoplastic or thermo-setting resist, and Ultra-Violet NIL (UVNIL) [5], which uses an ultra violet curing polymer resist; their process flows are shown in Figure 2.1. TNIL was invented first, using polymers of larger molecular weights. When heated above their glass transition temperature, the polymer becomes viscous and under high pressure can be made to flow. UVNIL was invented later as a low-pressure technique, using polymers of lower viscosity i.e. a liquid, to form to the stamp. Various institutions and universities have created their own NIL tools, while commercial toolsets are available from EV Group, Jenoptik Mikrotechnik, Meisyo Kiko, Molecular Imprints, NanoLithoSolution, Nanonex, Obducat, Süss Microtec and others. A third form that has been tested for its feasibility is Ultrasonic NIL [26]. The published research shows that using ultrasonic vibrations as a heat input can mould the polymer in seconds increasing throughput, but causes cavity formations due to non-uniform temperature distribution in the polymer.

Some confusion remains due to a wide range of names that are used for essentially the same technique. Table 2.1 lists some common names and how the differing techniques will be referred to for the remainder of this thesis.

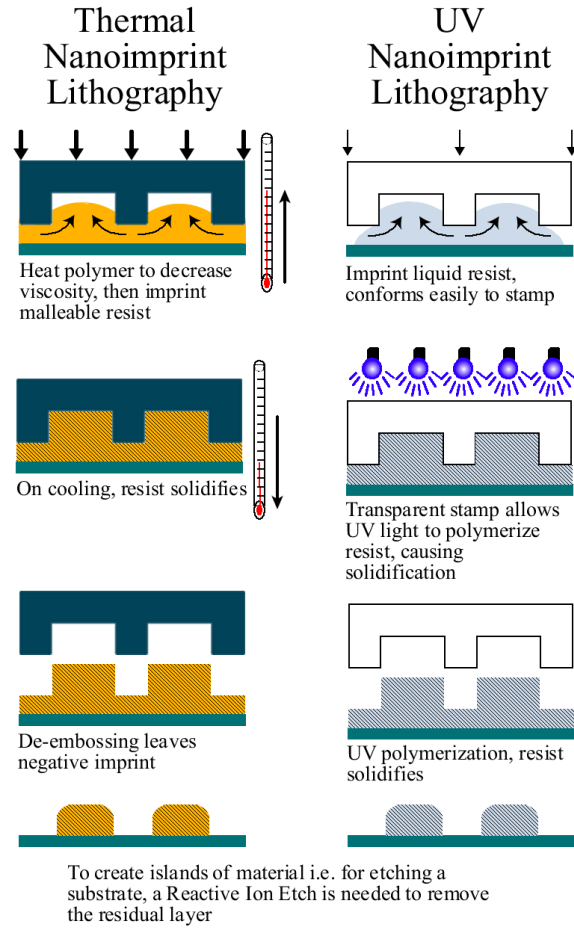


Figure 2.1: Process flows for: (a) T-NIL and (b) UV-NIL.

Table 2.1: Nanoimprint Lithography terms.

Umbrella term	Nanoimprint Lithography (NIL)	
Polymer type	<i>Thermo-setting & thermoplastic polymer</i>	<i>Photo-curing polymer</i>
Name used in literature and for remainder of article	Thermal Nanoimprint Lithography (TNIL) [27]	Ultra-Violet Nanoimprint Lithography (UVNIL) [28]
Other names used in literature	Nanoimprint Lithography (NIL) [29]	Photo Nanoimprint Lithography (PNIL) [11]
	Hot Embossing Lithography (HEL) [30]	Photo Imprint Lithography (PIL) [31]
	Thermal Imprint Lithography (TIL) [22]	Step and Flash Imprint Lithography (SFIL) [5]
	Room Temperature Nanoimprint Lithography (RTNIL) [7]	Ultra-Violet Soft Imprint Lithography (UVSIL) [32]

Each toolset varies in its capabilities based on the design and imprint method used. These features ultimately control the process attributes: pressure distribution, initial resist layer

thickness, imprint uniformity, throughput, alignment and resolution. The following sections emphasize the different features available and their affect on process attributes.

2.1 STAMP

The UVNIL process generally uses a transparent stamp, which can be hard or soft. TNIL in most cases uses a stamp made of a hard material, which retains its shape well when imprinting at high pressures e.g. 5 MPa. Hard stamps are better wearing and easier to handle in an automated separation process. Soft stamps can conform to non-flat wafers, but there is a trade-off between stamp deformation to obtain a uniform imprint and the loss of the pattern profile and resolution [33]. The material chosen also affects the stamp lifespan [34]. Harder materials provide better wear characteristics, while soft stamps have a limited lifespan but can simplify and speed up stamp creation.

The stamp pattern affects the imprint process [35]: a repeating structure over the entire stamp e.g. a grating, may be patterned easily due to a uniform pressure distribution and resist application, while patterning small and large features in close proximity is difficult, as it causes a varying imprint pressure and a non-uniform residual resist.

The tolerances of the stamp ultimately control those of the patterned structure. Defects in the stamp are seen on the patterned resist, including details such as rough line edges from electron beam lithography (EBL) [36]. The stamp features dictate the lowest tolerance that can be achieved.

2.2 FIELD SIZE AND WAFER

Toolsets can be distinguished by whether a full wafer or stepper approach is implemented. Imprinting by step and repeat – similar to a stepper in an optical lithography process – produces a better conformity with the resist, overcoming the waviness of the wafer, while a smaller stamp is also cheaper to make [33]. The alternative is to emboss the entire wafer in one step. This enables large structures covering the entire wafer surface without stitching problems: lining up smaller imprints to create a larger imprint. Whole wafer imprinting increases device throughput and can produce larger patterns, but the substrates exhibit non-flat surfaces; warp values for a 200 mm (8 ") wafer can reach 10 μm [36], creating conformity issues between the stamp and wafer. An increased substrate thickness can help pattern transfer [37], preventing wafer bowing.

Whether a stepper or whole wafer tool is used, toolsets differ in the maximum size of wafer able to be patterned. They range from 50 to 300 mm (2-12 ") [27, 38]. An increased degree of parallelism between the mould and wafer surface is achieved using a smaller wafer,

resulting in a higher uniformity over the imprinted structure [39], whereas larger wafers increase throughput and are preferred for mass production.

2.3 RESIST AND APPLICATION

The resist layer flows and deforms to the stamp pattern on imprinting. The lower the resist viscosity, the less pressure is needed to enable the material to fill the stamp. TNIL heats a thermoplastic or thermo-setting polymer above its glass transition temperature (T_g), reducing its viscosity and enabling it to deform on imprinting [25]. UVNIL uses a UV sensitive polymer that cures when exposed to UV-light.

Resists are applied by spin-coating [8] or by a droplet dispensing process [5, 40, 41]. Spin-on resists can be applied in advance. They are able to cover an entire substrate quickly, thereby increasing the toolset throughput and providing a better uniformity over the wafer surface, which is beneficial for repeating patterned structures. Varying pattern densities are difficult to imprint however with uniform resists and they can cause a varying residual layer [5, 42, 43]. Droplet dispensing allows the user to position locally varying amounts of resist, which can be optimised to the pattern density of the imprinted unit cell, resulting in a more uniform residual layer. However, liquid resists have to be applied just before imprinting and varying the droplet density across the stamp reduces throughput. Liquid resists can also cause an unwanted bead edge around the stamp perimeter [44].

The majority of thermo-resists have higher viscosities and require higher pressures for patterning, compared to UV-resists, which are lower viscosity liquids prior to imprinting and need less pressure to conform to the stamp. UV and thermal curing resists have been developed that are initially a viscous resin that can be spun-on. A small increase in pressure and/or temperature reduces their viscosities turning them into a liquid, enabling low pressure imprinting, which provides better alignment capabilities and precision [27].

Thermo-resists suffer poor dimensional control due to thermal contraction when they cool and solidify below their T_g . UV-curing polymers suffer less shrinkage, some by 2.5 % by volume when polymerisation occurs [45], or by 2.3 % at the base of features [46]. They also set quicker than thermoplastics and thermosetting resists and are less affected by heat transfer rates, increasing processing speed [44].

2.4 ALIGNMENT PROCEDURE

Alignment can be achieved by various means including superposition of optical images using backside alignment, and optical imaging through the material by frontside alignment. Superimposing the stamp and wafer images has produced 100 nm alignment accuracy and

overlay accuracy of 250 nm [47]. Typically this method is used in TNIL applications where a non-transparent stamp is needed for its material properties to mould viscous resists. Alignment occurs prior to imprinting without any *in-situ* adjustment; on contact, any horizontal movement from forces exerted by the polymer cannot be corrected.

Optical alignment through the stamp can be used with transparent stamps, typically in UVNIL applications, as it is a prerequisite for the polymerisation step. With the resist still in a liquid phase, the stamp can make in-plane movements without encountering strong restraining forces and can therefore be aligned and altered prior to polymerisation [17], enabling higher alignment accuracies of as little as 50 nm.

2.5 PRESSURE APPLICATION

Imprinting pressure can be applied by electromechanical or pneumatic mechanisms [48]. Electromechanical actuators allow asymmetric load control distributions, orientation control before contact and the modification of the suspension stiffness. Other mechanical systems employed include a ball and screw system with a flexure stage for self-levelling [47]. However, mechanical loading can induce non-uniform pressure distributions, whereas pneumatic systems create an even pressure across the stamp, enabling a more uniform imprint that is advantageous for achieving uniform residual layers across the stamp [27, 39].

2.6 NIL PROCESS CAPABILITIES

With the various toolsets available with differing characteristics, a wide range of results have been achieved with varying materials. However, there has not been a study into how the attributes affect one another and what results have been achieved: they need to be evaluated in context with the other attributes and process capabilities, which have been achieved in the same experiment, to enable comparison between the different toolsets and set-ups. To this end, the literature review gathered results from NIL articles regarding their imprint tests, to quantify NIL process capabilities. In particular, the process type, line width, relief height, initial resist thickness, residual layer, imprint area and tolerances were recorded as these attributes reflect the ability of NIL to transfer relief accurately and uniformly across a wafer. This information is displayed in graph form, for ease of comparison and to reveal any visible trends.

The study is intended to help to ascertain the current uses of NIL, what devices are being made and where the commercial potential will be with advancing capabilities. Of the articles reviewed, none were able to provide values for all the attributes recorded; few mentioned tolerances and many articles were ambiguous. In cases where the information

was not stated, informed estimates were made from published images and other sources. If this was not possible the information was not included in this study.

2.7 RELIEF HEIGHT VERSUS INITIAL RESIST THICKNESS

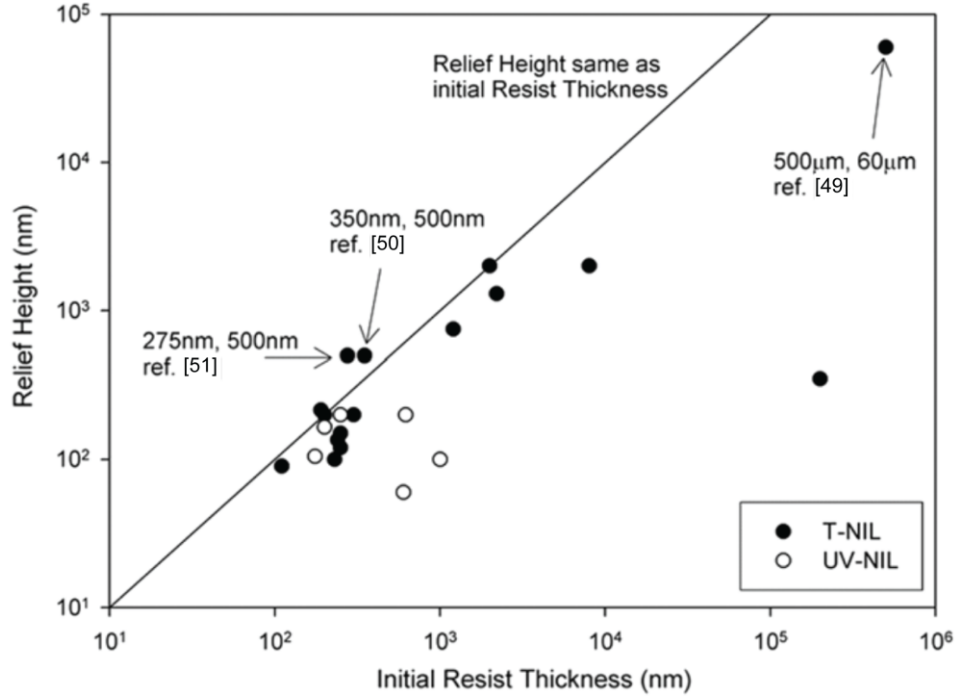


Figure 2.2: Relief height and resist thickness comparison of TNIL and UVNIL imprinting.

Figure 2.2 plots the relief heights against the initial resist thicknesses of the reported imprints and a line representing equal relief height and initial resist thickness. The tallest structures produced were by TNIL. Few experiments produced relief heights greater than the initial resist thickness. The majority of structures had heights of less than a few microns with the exception of the work to produce an electrostatic comb drive with 60 μ m deep features using TNIL [49]. At these length scales, TNIL is relatively simple to perform, while achieving good results.

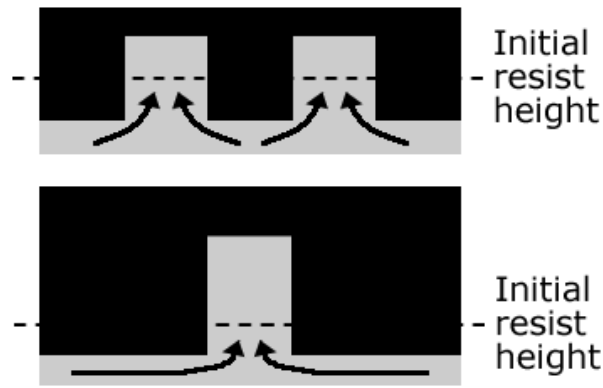


Figure 2.3: Schematic illustration of how high relief patterns increase the distance for the polymer to flow, making filling difficult from minimal resist.

When using NIL as a lithography technique, the residual layer thickness and the relief structure height above the residual layer are important. When creating devices directly from NIL, the residual layer depth variable may be less important. By knowing the pattern density, the amount of initial resist needed to fill the features can be estimated. The imprint relies on the resist to flow and/or shear. For sparse pattern densities, this becomes difficult and requires longer imprint times, higher imprinting pressures and lower viscosity resists. Figure 2.3 illustrates the problem. Imprinting sparse patterns or regions with a greater height than the rest of the stamp, the polymer must travel further to fill these regions and create the tall features from a minimal initial resist thickness. Two studies [50, 51] are highlighted that produced results showing greater relief heights than the initial resist thicknesses. Both experiments used high pressures, temperatures and long imprinting periods (Ref 50: 5 MPa, 150°C; Ref 51: 5 min and 10 MPa, 161°C and 3 min). None of the UVNIL experiments reviewed produced relief heights greater than the initial resist thickness. Higher relief structures need a thicker resist and take longer to imprint. This has implications for the resist application, the height of the patterned structures achievable and the pattern densities.

2.8 RESIDUAL LAYER VERSUS INITIAL RESIST THICKNESS

When using NIL to create a resist mask, the residual layer must be removed, prior to etching of the pattern in the substrate. Residual layer removal is usually achieved by reactive ion etch (RIE). This removal step affects the whole wafer, enlarging feature sizes and thereby reducing accuracy. Reducing the residual layer in the NIL process is important as it limits the effect RIE has on the resist mask, thereby improving tolerance control. From the data collected, few results are available for UVNIL because the initial resist thickness is often unknown when dispensed as droplets.

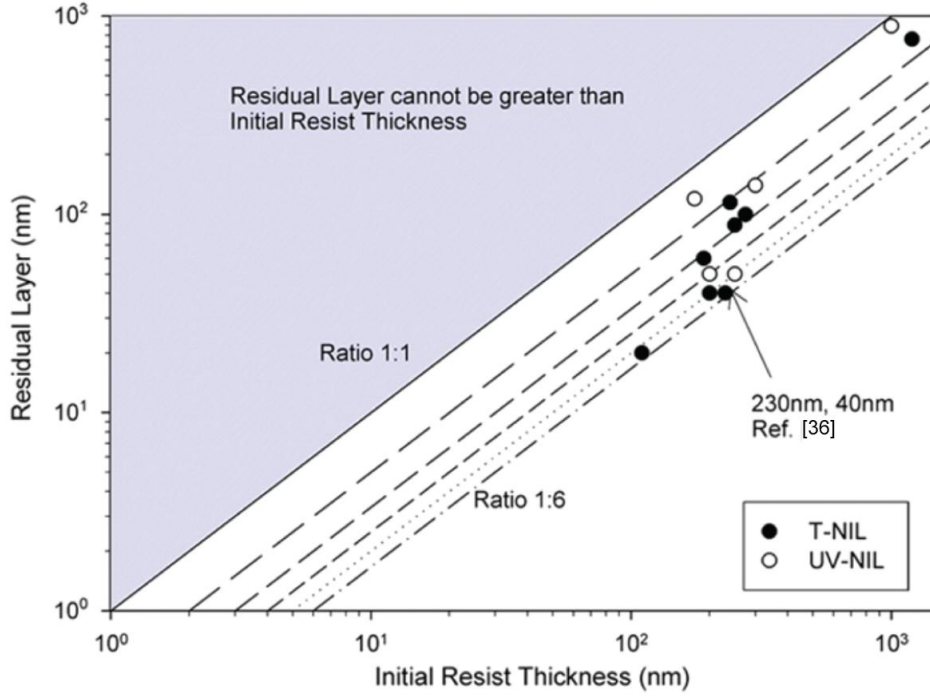


Figure 2.4: Graph displaying NIL's capability to displace the resist to achieve smaller residual layers, relevant for creating resist masks.

The available data is plotted in Figure 2.4. The ratio lines increment from 1:1 to 1:6 and highlight the depth of the residual layer in comparison to the initial height of the resist. A ratio of 1:1 would result if no imprint was made; a ratio of 1:6 suggests the imprinting step has made good use of the resist, wasting less by leaving a thinner residual layer.

The data shows little dependency of the residual layer on the initial resist thickness; with varying residual layers for similar initial resist thicknesses. This is because many other process attributes affect the residual layer; an expression for the polymer squeeze flow height below the stamp relief during imprinting found by Bogdanski *et al.* [52] is:

$$\frac{1}{h^2(t, T)} = \frac{1}{h_0^2} + \frac{2p(t)t}{\eta(T)s_{\text{eff}}^2(t)}, \quad 2.1$$

where h is the polymer thickness, t is the imprint time, T is the process temperature, h_0 is the initial thickness of spin coated polymer layer, η is the polymer viscosity, p is the pressure and s_{eff} is the effective pattern size. The equation is based on the phenomenon of squeezed flow and taking into account the stamp geometry. It exemplifies the various attributes affecting the residual height, with increased imprint time and temperature having the largest effect on reducing residual layer thicknesses. The highlighted result in Figure 2.4 was achieved by Gourgon *et al.* [36] for an array of holes imprinted by TNIL, which had a long imprint time and a high temperature during embossing (5 min, 130°C).

2.9 RELIEF HEIGHT VERSUS LINE WIDTH

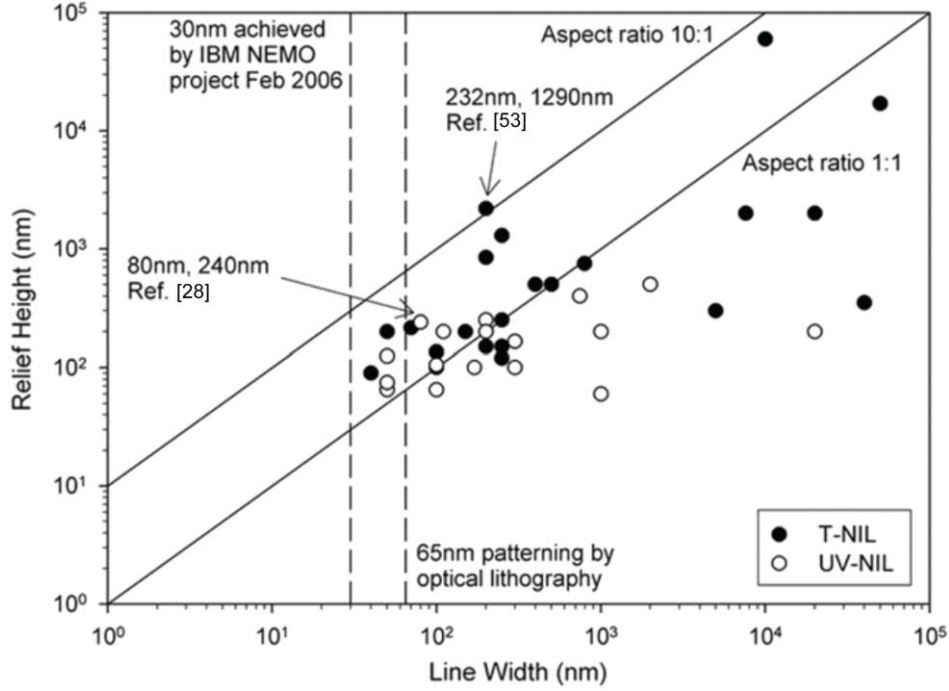


Figure 2.5: Graph indicating aspect ratios achieved by NIL at various feature sizes.

Aspect ratios (AR) reported for post and line features created by imprinting in the literature are shown in Figure 2.5, the majority of results have been produced with AR values close to unity. In general, the aspect ratios achieved using UVNIL are less than those obtained from TNIL; the maximum value found in the literature reviewed for a UVNIL process was 3 [28], compared to 11 for a TNIL process [53]. High aspect ratios by NIL are useful in microfluidic, optoelectronic and photonic applications because the patterned polymer can be used as the device without any additional processing. Compared to etching a substrate to produce relief, the process is quicker and cheaper. The high aspect ratios in [28] and [53] were achieved using fluorine-based additives to reduce the mould surface free energy, thereby reducing the force required for de-embossing.

Physical limitations also impose a limit on the aspect ratios created from smaller line widths, as the total surface free energy is proportional to the surface area, a squared length dimension, while the total elastic strain energy is proportional to the volume, a cubed length dimension. For a given aspect ratio at smaller length scales, the higher surface area to volume ratio implies that there is less strain energy available to overcome the adhesion between stamp and polymer, thereby preventing the de-embossing of smaller features.

2.10 FEATURE SIZE VERSUS IMPRINT AREA

Figure 2.6 is highly relevant, providing an insight into the challenges facing NIL.

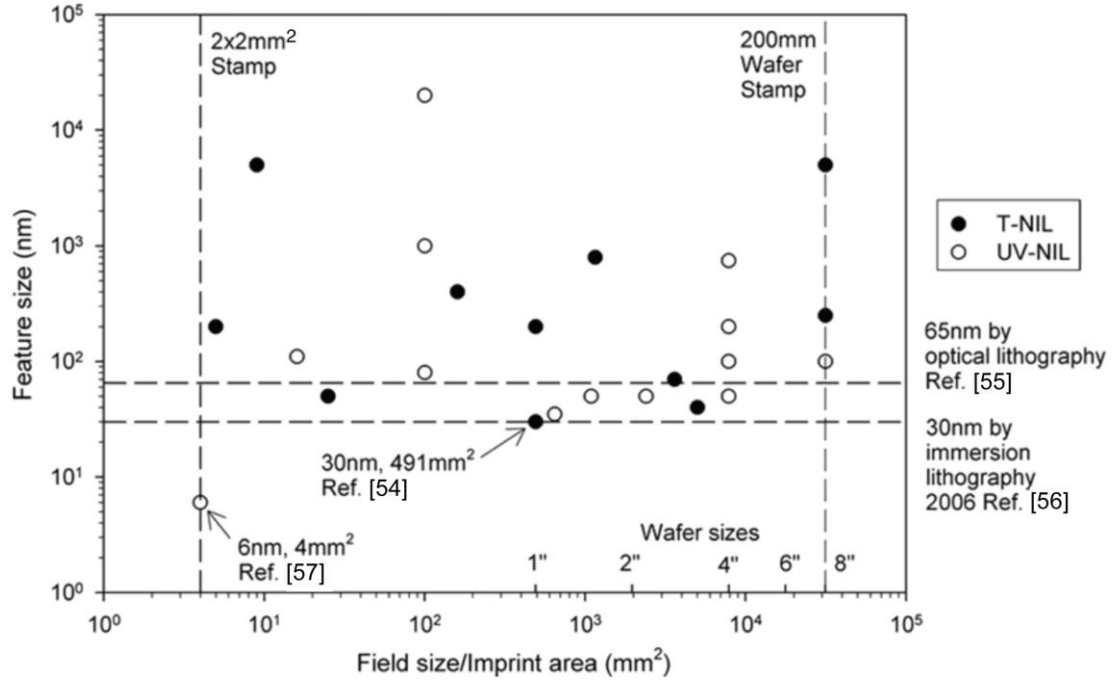


Figure 2.6: Graph showing feature size versus field size.

The imprint area is defined as the area of the stamp causing an impression. Although some results have been performed on larger stamps, they may be marked on the graph with a smaller field size as a large proportion of the stamp is not used. The ideal capabilities for NIL would be to create very small structures patterned by large imprint areas, enabling high throughput. Currently large area stamps can routinely achieve width dimensions below 100 nm and in some cases as small as 30 nm [54], which are comparable to cutting-edge optical lithography [55] and immersion lithography capabilities [56]. Better resolution imprinting below 30 nm has been achieved using UVNIL [57], producing line widths of 6 nm, but with a field size of only 4 mm².

2.11 RELIEF HEIGHT VERSUS IMPRINT AREA

For devices to be created directly by NIL, it is important that the dimensions are not dependent on the wafer size, especially when ramping up for mass production. The comparison shown in Figure 2.7 examines whether the wafer size affects the feature heights created and therefore the capabilities for device production.

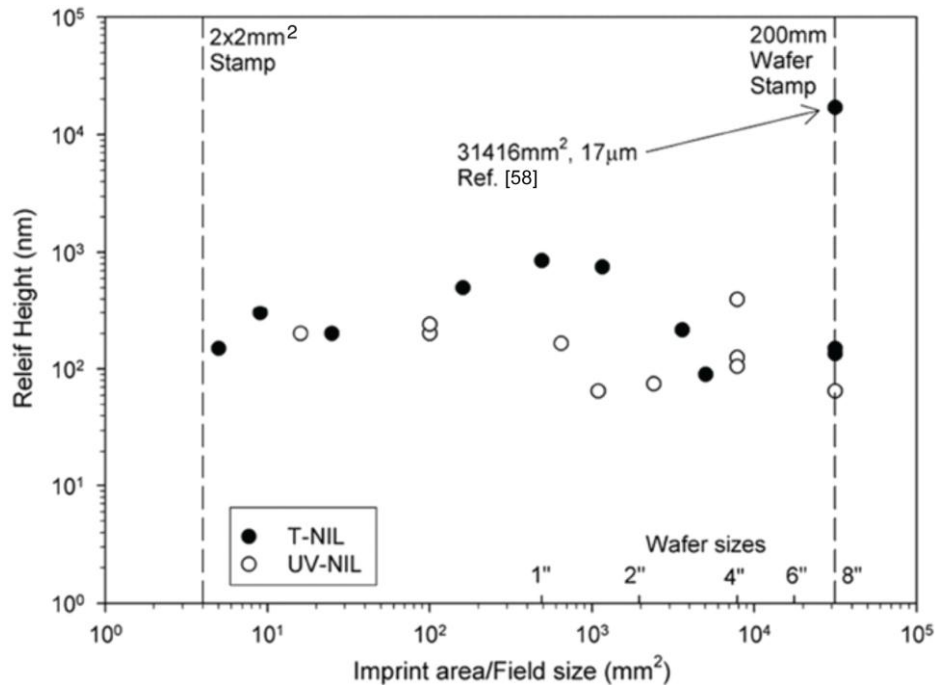


Figure 2.7: Graph depicting little correlation of the relief heights achieved using NIL over various field sizes.

The results show relief height, in the range 50-1000 nm to be independent of the field size used. A TNIL imprint on a large stamp produced relief heights of 17 μm , for line widths ranging from 5 to 50 μm [58]. Although this is an example of an imprinting experiment at the microscale instead of the nanoscale, the results indicate that tall structures can be made using larger imprint areas in NIL, with no dependency on imprint area.

2.12 TOLERANCE VERSUS FEATURE WIDTH

Important in all engineering processes is the precision and accuracy achievable for any production technique. Figure 2.8 shows the tolerances for the feature widths created by NIL processes. The points are grouped by whether this information refers solely to the line edge roughness (LER) values or to other values quoted, such as the standard deviation or the upper and lower values for the feature dimensions. The tightest or smallest tolerance that can be achieved is the LER, which cannot be better than that of the stamp imprint, generally made by EBL. After this value, error is introduced from the imprinting, curing and de-embossing processes, as well as the techniques used to image or measure the results achieved, such as scanning electron microscopy (SEM) and atomic force microscopy (AFM).

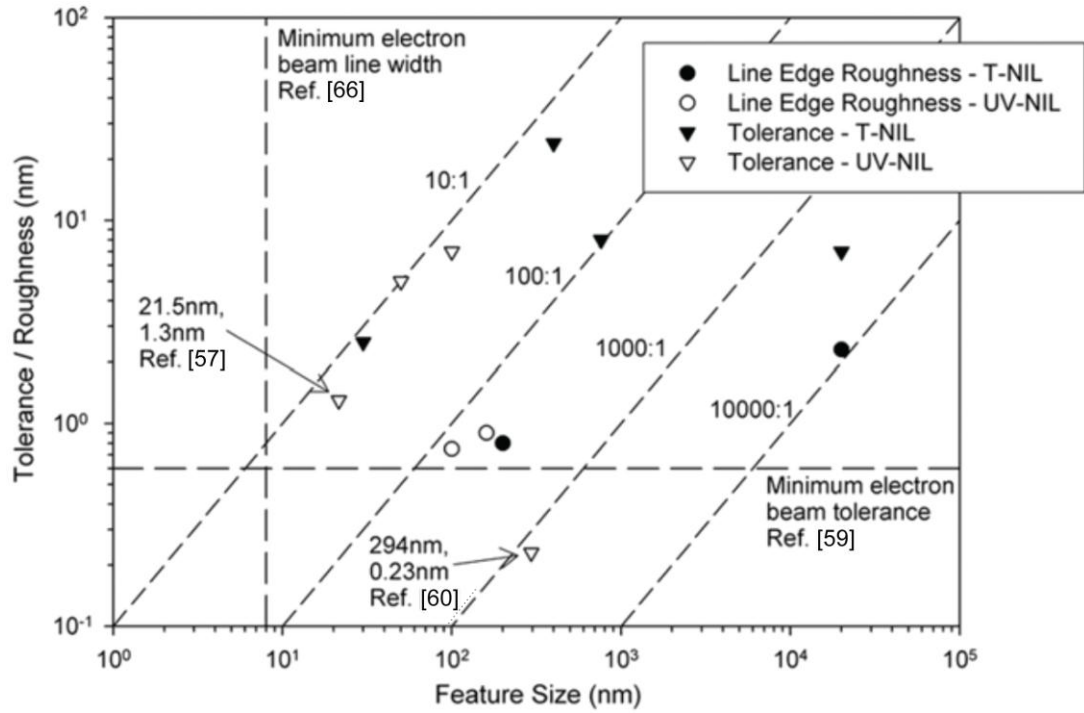


Figure 2.8: Standard deviation and line edge roughness values for NIL imprinted feature sizes.

Despite its importance, few articles reported tolerance values. Some gave standard deviation and accuracy values, which have been approximated as tolerances for this comparison, while others have been found by statistical analysis of line variations, or by the judgement of the authors from images published in the papers. Even for the values stated in the articles, it is unknown how many measurements were used and consequently the accuracy of the reported values. All but one of the values plotted are above those found for a fine-tuned EBL system [59]. The result in question, reported by Hiroshima *et al.* [60] seems very small, which may be explained by the fact it is the standard deviation of the linewidths. It was found by calibration techniques using the line pitch and is the standard deviation of absolute values of the differences in the mean linewidths. The authors chose this calibration technique after suggesting large differences in line widths were presumably caused by insufficient linearity correction by the AFM software. Another notable tolerance value plotted comes from reference [57]; the value quoted was for a first order standard deviation (σ_1) variation of the line pattern created. These tolerances were achieved using Polystyrene (PS) as a negative EBL etch resist, transferring the pattern into silicon dioxide by RIE, and then using this to imprint Polymethylmethacrylate (PMMA).

2.13 DISCUSSION

NIL has the ability to pattern structures at high resolutions, better than by optical lithography, using processes such as EBL or focussed ion beam (FIB) to make the stamp,

with the ability to replicate tiered and 3-D structures without a post-lithography etch. The toolsets are expected to be much cheaper to purchase than those of extreme ultra-violet (EUV) and X-ray lithography, which offer similar resolutions and throughput but have yet to overcome design hurdles such as high power light sources and low optics lifetime [61]. Additionally, process costs for NIL toolsets are projected to be lower than for EUV [62], especially for low device volumes [63].

The semiconductor and microelectronics industry does not consider NIL sufficiently mature for large-scale commercial application. Many devices need multi-layers and require high overlay accuracy. NIL currently is unable to control the alignment to the precision it can pattern, due to shrinkage of the polymer when curing and the limitation of the alignment equipment. Imprinting on pre-patterned substrates may prove difficult as NIL needs to apply enough resist to cover the underlying structure, creating a varying resist depth and final residual layer.

The toolset features affect the process capabilities; higher accuracy overlay alignment is achievable using UVNIL and uniformity over the entire wafer is easier to obtain using spin-on resists. Small stamps pattern to high resolutions, while large stamps increase throughput and enable larger devices. Relief heights greater than the initial resist thickness are hard to achieve and will affect the pattern design and processing route. Reducing the residual layer height is important when using NIL as an etch mask, as this is dependent on the pattern and relief of the imprint. High aspect ratios of 5 or greater with feature widths of below 250 nm have been formed using TNIL, which introduces the capability to imprint a wider variety of devices. Line widths of 100 nm or less have been patterned with large field sizes, over 200 mm wafers in a single imprint. Line widths of 6 nm have even been imprinted – dimensions that EBL is capable of patterning – however this was achieved only over an area of 4 mm². This is smaller than the projection area used in high volume optical lithography and would not be a feasible field size for high volume production. The greater the field size, the more devices that can be produced in a single imprint. NIL must be able to achieve the same resolutions, if not smaller, than optical lithography, with better tolerances and on a larger imprint areas to increase throughput to compete for patterning etch masks and creating other devices.

Despite the ‘promise’ of NIL for patterning sub-25 nm, few articles published since 2003 have demonstrated the ability to achieve these dimensions and only one provided sufficient information to be documented in this study. Tolerance values have been quoted as an order of magnitude less than the feature sizes, though few results are available. This is

partially due to the inability to measure these dimensions with precision due to the physical limitations of SEM and AFM techniques and because the articles reviewed detailed other measurements relating directly to the field of research.

2.14 CONCLUSIONS

It can be seen from these results that some process attributes show correlations. The results are from a range of experiments conducted with different toolsets, materials, personnel and conditions from articles since 2003. The most important results found from this research are:

1. small (<50 nm) feature sizes have yet to be proven on large imprint areas (>4 mm²);
2. aspect ratios (depth to width) of 11 are the largest to have been produced;
3. few relief heights have been made greater than the initial resist thickness used;
4. tolerances of less than a tenth of the imprint feature size have been reported.

CHAPTER 3: QUALITATIVE RESEARCH

The comparison of the process capabilities suggests a range of devices that could be produced using NIL. Academics, scientists, engineers, inventors, managing directors and business people in the microfabrication industry were contacted to verify the quantitative data presented here, to determine the market opportunities for NIL. A questionnaire was formulated referring to the design and creation of their devices, what the limiting factors were, the processes they wanted improved and their opinion of NIL for fabricating their devices. Twenty-one people from various sectors of the microfabrication industry answered, some were contacted again, answering more questions regarding their devices. Other people, including tool manufactures within the industry sectors were also contacted and asked specific questions regarding their field and NIL as a commercial microfabrication process. The answers to the questionnaire and the information collected have been ordered in Table 3.1, the questionnaire used can be seen in Appendix B.

3.1 PHOTONICS INDUSTRY PERSPECTIVE

Many showed interest for the use of NIL to create devices. Reasons included offering reduced costs, increased performance and reduced process steps. At nanometre scales, recurrent relief structures such as arrays and gratings demonstrate quantum effects and can be used for various applications, while NIL also has the potential to enable simultaneous photonic device and complementary metal oxide semiconductor (CMOS) fabrication, reducing costs, size and increasing the device capabilities.

3.2 MICROFLUIDIC INDUSTRY PERSPECTIVE

Microfluidic companies have shown interest for using NIL in production, for similar reasons as for photonics applications and because it avoids using chemicals for producing devices that will carry sensitive materials; imprinting into polymer is a physical process, avoiding contamination issues. However, few devices have been commercialised, with most technologies currently in proof of principle or product development stages. The current high costs of microfluidic components to make the devices and those of associated equipment, the lack of suppliers, commercial infrastructure, industrial standards and maturity of competing technologies are seen as the main barriers for commercial success, with the most promising markets being drug discovery and diagnostics [64].

3.3 MEMORY STORAGE INDUSTRY PERSPECTIVE

In general, memory storage companies believed little commercial opportunity was available in the immediate future for using NIL for patterned media, as it competes with perpendicular magnetic recording (PMR) technologies, which uses optical lithography. Toshiba, Seagate and Hitachi all have PMR drives for sale [65]. Toshiba are researching hard drives based around patterned media having recently purchased an NIL tool [66], while Fujitsu [67], Hitachi [68], Western Digital [69], Seagate [70] and TDK [71] are also researching patterned magnetic media.

3.4 MICROELECTRONICS INDUSTRY PERSPECTIVE

The microelectronic companies believed NIL is not sufficiently mature, that the technique was not appropriate for their devices being made and that the overlay accuracy was not good enough. Though they were not prepared to rule out the technique, they were happy to remain with the optical lithography patterning processes being used and monitor the success of NIL by others. This has been highlighted by the investment made into EUV lithography by companies such as Intel and ASML [62, 72].

3.5 MICRO ELECTROMECHANICAL SYSTEMS INDUSTRY PERSPECTIVE

Companies producing micro electromechanical systems (MEMs) believed that more work was needed in improving etches rather than the pattern transfer. Very few companies had considered NIL, preferring to use the tools already available. One party believed the industry was extremely conservative, sticking to the tools and techniques used previously, while remaining with the same toolsets to keep costs low.

3.6 CURRENT RESEARCH APPLICATIONS

Many devices have been tested using NIL in their fabrication procedure. These can be grouped into the following application fields:

1. photonics;
2. microelectronics;
3. MEMs;
4. microfluidics;
5. patterned media.

Devices already produced using NIL as proof of principle include diffractive optical structures [73], Bragg gratings [74], waveguides [75], waveplates [44], polarisers [76], photonic crystals [77], surface acoustic wave (SAW) devices [78], organic light emitting diodes (OLEDs) [79], organic thin film transistors (OTFTs) [80], metal-oxide

semiconductor field effect transistors (MOSFETs) [39, 81], capacitance comb drives [49], cantilever arrays [82], DNA sequencing [83], micro and nanofluidic channels [84], patterned magnetic media [85], cross-bar circuit switches [86] and static random access memory (SRAM) [57].

Table 3.1: Qualitative information gathered from questions put to people using microfabrication techniques.

Microfabrication fields	Interest	Reasons to use NIL	Uninterested responses
Photonics	Varied: <ul style="list-style-type: none"> • Interest for use in current applications • Interest seen for other applications • Not considering the technology 	<ul style="list-style-type: none"> • Potential to reduce production costs • Better device performance • Reduce overall process steps; minimize errors and defects • Patterning optics and electronics simultaneously 	<ul style="list-style-type: none"> • Making do with the tools available • Dimensions of devices are too big for NIL
Microelectronics	Mild: <ul style="list-style-type: none"> • Prepared to follow other markets if NIL satisfies their pre-requisites 	<ul style="list-style-type: none"> • Fewer process steps • Achieve smaller dimensions • Compatible with current process chains 	<ul style="list-style-type: none"> • NIL not sufficiently mature • Happy to remain with current patterning techniques and monitor NIL advancement • Products to be made with standard foundry equipment • NIL not appropriate for devices being made • Overlay accuracy not good enough
MEMs	Little: <ul style="list-style-type: none"> • Some interest for production of low volume, high cost devices e.g. military applications 	<ul style="list-style-type: none"> • Fewer process steps • Achieve smaller dimensions • 3D forming 	<ul style="list-style-type: none"> • Work needed to improve etches • Prefer to use tools already available • NIL would not offer cost reduction
Microfluidics	Varied: <ul style="list-style-type: none"> • If products came to market, NIL would be likely fabrication route • No need for nanometre resolutions 	<ul style="list-style-type: none"> • Smaller dimensions • Ability to produce identical devices quicker than by current processes • Form devices without etches; they interfere with the chemical and biological reactions • High volumes, low cost 	<ul style="list-style-type: none"> • Other processes more beneficial; 3D injection moulding
Patterned Media	High: <ul style="list-style-type: none"> • Interest from memory storage companies looking to be the first to achieve 1 TB/inch² [67-71, 87] 	<ul style="list-style-type: none"> • Imprint posts to form magnetic ‘islands’ • Few process steps • Quicker and higher resolutions than by optical lithography 	<ul style="list-style-type: none"> • Patterned magnetic media will not be used until 12.5 nm posts and half-pitches are made precisely, accurately and cheaply [88]

3.7 POTENTIAL NEAR FUTURE APPLICATIONS

The NIL process will only be used if a company or sector sees an economic advantage. This will take one of the following forms:

- a) producing the same device at lower cost;
- b) producing a device unable to be made due to physical limitations of current production tools;
- c) producing a new device or one that is similar to a current device, that benefits from better characteristics acquired through NIL fabrication.

Companies mass producing devices will be hesitant to change technologies until there are no other options available. The cost of decommissioning toolsets currently used and the associated loss of manufacturing time are incentives to remain with current process chains, making point **a** an unlikely reason for change. The small/medium enterprises (SMEs), which outsource production and produce batch quantities of their devices, may use NIL to benefit from lower set-up and process costs. However, NIL will need to prove it can meet all their requirements.

Point **b** is a strong push factor for NIL use, although few sectors have reached the physical limitations of their existing tools so the opportunity for NIL is limited. The semiconductor industry is one, which is seeking to pattern high resolutions at high volumes, but many of the companies have publicly made a commitment to research EUV lithography, with development costs for EUV estimated to be in excess of £4 Bn [62]. NIL toolset manufacturers hope to enter this market as a ‘disruptive’ technology, with huge economic gains if successful. However, ASML, a lithography toolmaker, in 2006 shipped Alpha Demo EUV tools, highlighting the continued progress and resistance to NIL [72].

Point **c** is a likely reason for companies to use NIL, enabling them to produce better products. This fits well with the notion that SMEs are likely to try new techniques to gain advantages over competitors. Other factors in favour of using NIL are that start-ups and SMEs producing microfabricated devices generally outsource their fabrication to foundries and require batch production quantities, and are more amenable to new technologies.

Probable NIL markets to compete in are those that currently make devices with EBL and laser writing processes. NIL is able to replicate the features sizes, but is faster at batch or mass production, and cheaper. These techniques are able to change the imprint pattern quickly –

only needing a different input file – enabling faster product alterations. However, for devices of a set process sequence, NIL will be quicker and cheaper.

Devices formed by periodic structures of posts, holes, lines or trenches are most likely to use NIL initially, as these patterns have shown to be easily reproducible, because they do not have large varying feature sizes, creating a uniform wafer pressure and uniform residual layer when imprinting [89, 90]. Micro-lenses may also be an item for NIL to fabricate. Many electronic devices use small lenses, such as digital cameras and mobile phones, whose life spans are less than 10 years. Lenses can be made from polymers that can sustain their integrity for this time period and at lower production costs than by other fabrication methods or materials, such as glass.

3.8 CONCLUSIONS

NIL toolsets differ in their process abilities. In general they either use a small field size and a stepper to create high resolutions, or a large field size for wafer imprinting, increasing throughput. The results indicate that:

1. the initial resist thickness affects the final relief height due to the physical process;
2. NIL is able to achieve aspect ratios greater than 10;
3. NIL has been proven to pattern repetitive sub 50 nm feature sizes using a field size of 1 ” in diameter;
4. the relief height of the structures created is independent of the field size used to imprint.

NIL is able to pattern relief structures quickly and at high resolutions. The toolsets are significantly cheaper than the latest optical steppers, selling for as little as \$100,000 compared with \$18 million for the latest 193 nm optical machines [66], and \$65 million for EUV tools [72]. NIL is likely to compete for the production of devices that currently use EBL and laser writing processes that are seeking to change their business strategy from a differentiation base to a cost reduction. NIL is already being used to manufacture commercial products: a U.S. corporation makes optical components for a Samsung consumer electronics product [91], Heptagon uses an NIL tool to produce microlenses [73] and NanoOpto offers an infra-red filter used in digital cameras and waveplates for CD and DVD drives [92].

NIL has to overcome technical and market barriers for greater acceptance as a microfabrication tool. Better stamp creation is required, which can produce the resolutions needed at high tolerances, while improved analysis techniques of the imprinted wafers would enable better defect and tolerance checking, especially for the creation of smaller feature sizes. The ‘taboo’ in the microfabrication industry of no contact with the wafer needs to be

overcome, while technical issues in patterning and alignment need to be resolved such as forming small and large features in close proximity, imprinting uniformly over entire wafer surfaces, while achieving high pattern resolution and enabling multi-level alignment to similar resolutions as the feature sizes. NIL needs to show it is an economical investment, its biggest push-factor. For each potential market, an analysis is needed as to whether NIL increases the capability, efficiency or output of a device, or reduces the cost of producing devices.

3.9 RESEARCH DIRECTION

The comparison work undertaken in Chapter 2 has been published in the 'Journal of Physics D: Applied Physics' [93]. The work led to two separate research directions, both of use to Innos. From the research, it became apparent that NIL was a quick, affordable patterning method not dissimilar to that used to create CDs and DVDs. It was realised by the author and colleagues at the sponsoring company that if NIL was used with materials that could be added quickly, a process chain can be created for producing microfabricated devices with the potential to be cheaper and quicker than by any other method. This process path has been patented by the author and the sponsoring company and can be viewed in Appendix C [94].

The second research direction from the literature review is modelling of the de-embossing step. The research highlighted dependencies found between process variables. However, little research has looked at how these affect stamp de-embossing. Although many have researched the embossing part of the process, the de-embossing step of the technique has had less attention, with little understanding on how different attributes of a system and the different variables affect what can be achieved. Without successful removal of the stamp from the polymer, the imprint process would not be effective. The empirical data analysis led to the conclusion that there are most likely physical limits to which imprints can de-embossed, which could be predicted in an analytical model. Such a model would be a valuable tool for stamp design, enabling designers to realise what patterns and reliefs are feasible physically, without the cost and time expense of trial and error. Such a model could predict some of the regions on empirical data maps that are infeasible and/or have not been attempted for certain variables. An analytical model would also be a powerful tool, enabling trends to be viewed between process variables, helping to understand how they affect one another, expelling the notion of NIL as a 'dark art', creating de-embossing limits and guides.

CHAPTER 4: NANOIMPRINT LITHOGRAPHY

MODELLING

NIL essentially can be thought of as a three-step patterning process. Initially it embosses a liquid/low viscosity resist with a stamp made of a stiffer material. The polymer deforms by viscous flow and conforms to the negative image of the stamp's pattern. The material is then polymerised, turning it into a solid. This is dependent on the variables that affect the speed and quality of polymerisation such as the time, heat and/or UV irradiation, depending on whether it is TNIL or UVNIL. The third step is the de-embossing of the solidified resist.

All the process steps are critical, but regardless of how well the polymer forms to the mould during the embossing step or the polymerisation of the material, without successful removal of the stamp, the technique fails to imprint. The embossing and polymerisation steps can be greatly enhanced by extending their time periods, changing the resist type, increasing pressure, temperature and/or UV irradiation. However, to make the technique faster for increased throughput, the majority of improvement in these process steps involves formulating new resists to have the beneficial properties, whereas the de-embossing step is dependent on the stamp geometry and the material combination of the resist and stamp. As both parts are solid, the process step is controlled by solid mechanics instead of fluid mechanics or thermodynamics.

Much of the current process knowledge has been gained empirically through trial and error. In the previous chapter, published data on NIL was collected and used to quantify the effects of the process attributes on de-embossing, showing well-defined limits for process metrics such as: aspect ratio, line width and imprint area fractions achieved. To extend these limits and increase the capabilities of the technique, a greater understanding is needed. The majority of work to date has modelled the embossing step, providing equations and guidelines for polymer flow to enable better stamp filling. Research is still continuing in this field looking to improve the modelling capabilities. For de-embossing, a German-Canadian research initiative has begun work on analysing friction coefficients in TNIL for simulation software [95], using a contact algorithm based on a modified Coulomb friction law.

Of the limited research conducted to date, little has been done on the de-embossing process and none has attempted to model the procedure in an analytical form, which would help with process optimisation and/or reduce the amount of finite element analysis (FEA), design and testing undertaken. An analytical model would help aid development by offering information relatively quickly regarding the dependencies and effects of different variables, to enable better

design and use of materials. The following sections present a review of the attempts to model the NIL process (4.1), the development of an analytical based model for the de-embossing step (4.2 and 4.3) and its results (4.4), followed by a discussion (4.5) and conclusion of the work (4.6).

4.1 MODELLING LITERATURE REVIEW

Fundamentally, the modelling processes of the imprinting and de-embossing stages can be explained using fluid mechanics and solid mechanics respectively. Imprinting occurs when a viscous resist under pressure conforms to a stamp. De-embossing occurs when the resist and stamp are both solid materials and are separated.

4.1.1 Imprinting

To imprint, a stamp constructed of a stiff material (relative to the polymer used) is forced into a resist in a viscous state. As the stamp presses into the polymer, the polymer flows to conform to the stamp, creating a negative imprint. The flow is predominantly affected by the polymer's viscosity, which itself is dependent on the temperature. Many types of polymers have been tested: the TNIL resists have in general a high viscosity, which need a stiffer stamp, while UVNIL resists behave more as a liquid, needing a lower pressure for imprinting.

Research has been undertaken to model the imprint step for various process parameters, which depend on the length and time scales to predict stamp filling. Heyderman *et al.* [96] witnessed two different fill mechanisms on imprinting: simple flow from the borders and mounds forming at the centre; they produced a simple 2D squeeze flow theory to calculate the time to displace a given height of polymer with a stamp of a certain width. Scheer and Schulz [97] reported on different filling effects in TNIL. Some of their results could be interpreted by using hydrodynamic theory, while others were dependent on the length scales within the stamps. Hiroshima [98] analysed the imprinting step starting with Stefan's equation, a theoretical treatment of a Newtonian liquid being squeezed between two discs. Bogdanski *et al.* [52] opted to use a modified version that allows for the different length scales found in the imprinting, their expression for the polymer thickness below the stamp base during imprinting is given in Equation 2.1. From flow property measurements, Leveder *et al.* [99] created a rheological model to calculate the viscosity of thin films to enable better simulations, as they suggested the values differ from the bulk values for the materials.

Papers published by Colburn *et al.* [31] and Bonnecaze and Reddy [22] considered resists in a liquid phase prior to polymerisation; their models simulate the flow using Lubrication theory, which allows simplification of the Navier-Stokes equations of motion for the case in which

one dimension is significantly smaller than the others. However, Bonnecaze and Reddy discovered that modifications were needed as the equations presented the fluid flow only in two dimensions, neglecting capillary forces, which they realised play an important factor in governing fluid movement.

Cross *et al.* [100-102] looked at the mechanics of nanoimprint forming. They monitored static and dynamic mechanical characteristics during imprinting and found the elastic strains present during the forming process considerably alter the characteristics of the imprinting step, while the residual stresses within the polymer needed sufficient time for stress relaxation to occur for good pattern transfer.

Lei, Li and Yam [103] used a contact-stress analysis approach to describe the embossing phase for TNIL. However, their research considered macroscopic scales. Although their analysis predicted wall profiles with good accuracy, it is unlikely to be applicable at smaller dimensions, with shear stresses having a greater effect in creating inelastic deformation [102].

Numerical analysis has been undertaken on the imprinting step. Jeong *et al.* [104] studied the effects of capillary forces and the width of stamp grooves on the embossing stage using computational fluid dynamics (CFD). Rowland *et al.* [23] used CFD analysis to analyse the effect of cavity size and film thickness on polymer flow, to create NIL design rules. They showed that three parameters predict the polymer deformation mode: cavity width to polymer thickness ratio, polymer supply ratio and capillary number. Mendels [105] used a sub-modelling approach to form boundary conditions on the stamp, the repeating 'units', comprising of relief and channel details within the features for a single half-channel geometry. CFD results highlighted the effects of non-Newtonian viscosity and surface tension of the polymer at the channel entrance and flow front. The model was also used in a large-scale assembly of sub-elements to simulate a full cross section of the stamp at the millimetre scale. The work raised a number of issues regarding the final mesoscopic structure of the polymer, as macroscopic length scales became increasingly important.

Real time experimental characterisation techniques are now being applied using light scattering to study pressure, temperature and resist deformation to help process optimisation of the embossing phase [106].

4.1.2 De-embossing

Once the polymer has solidified, the stamp needs to be removed from the resist. For small feature sizes, this becomes problematic, with the surface free energies and contact friction

between the sidewalls preventing the stamp from de-embossing, which can cause fracture and deformation of the imprint features.

A simple model was presented by Jung *et al.* [107] that described the problem of stamp detachment according to the standard Griffith energy balance of elastic fracture mechanics. They suggested that there are two final states: either the resist detaches from the mould or the resist adheres to the mould and detaches from the substrate. This is controlled by the state with the lowest total free energy of the surfaces and interfaces (ΔG). For the resist to detach from the mould and adhere to the substrate

$$\Delta G_{\text{resist detaches from mould}} < \Delta G_{\text{resist adheres to mould}}, \quad 4.1$$

which can be written in terms of the independent surface energies and interface areas as

$$A_{r-m}(\gamma_r + \gamma_m - \gamma_{r-m}) < A_{r-s}(\gamma_r + \gamma_s - \gamma_{r-s}), \quad 4.2$$

where A_{r-m} , A_{r-s} are the resist-mould and resist-substrate interface areas respectively, γ_r , γ_s , γ_m are the resist, substrate and mould surface free energies per area respectively and γ_{r-m} , γ_{r-s} are the resist-mould and resist-substrate free energies of adhesion per unit area, respectively.

Equation 4.2 takes into account the total surface area and the interface forces. However, it is too simplistic to model (adequately) the de-embossing stage, as the work does not allow for how individual attributes effect the overall process, such as those indicated by the review in section 2. For instance, there is no reference to the shear stress encountered on the sidewalls of posts or trenches due to friction or the strain energy stored in the polymer and stamp.

Attempts have been made to model the de-embossing step using finite element (FE) models. Worgull and Hecke [108] realised that the tools used to simulate the moulding process at the macroscopic level, such as for injection moulding, were unable to be adapted for nanoimprinting techniques because of the intermediate state between imprinting and moulding. They split the process modelling in two, using Moldflow MPI software to simulate imprinting and ANSYS software for the de-embossing step. They simulated the thermal behaviour of the mould and the friction between the mould and resist for TNIL, assuming viscoelastic properties for the polymer, to optimise the process and improve the mould layout. Their simulations suggest ways to reduce the shrinkage of the polymer, which in turn reduces the contact stress and the de-embossing force [109].

Yuhua, Gang, Yin and Yangchao [110] also used FEA to model the thermal shrinkage in the polymer and the stresses caused in TNIL. They recommended an additional structure, surrounding the patterning field, on the stamp to minimise thermal stress. Using an atomic force microscope (AFM), frictional coefficients were found for a nickel and PTFE coated

stamps imprinting a PMMA polymer. Adhesion and friction during the de-embossing step were then modelled using FEA. The work showed that the lower surface energy associated with PTFE reduced the shear forces on the microstructures.

The de-moulding step has been modelled using FEA for TNIL and UVNIL in Song's thesis [111]. He produced a 2D FEA model for the de-moulding step, which was compared to experimental work. The viscoelastic models gave results suggesting that there are two local stress maximums, causing failure either to occur at the beginning or end of de-embossing and that (as intuition suggests) detachment of the stamp is more difficult for greater aspect ratios. A third chapter reported experimental work on the de-embossing of TNIL. He showed that there was an optimal de-embossing temperature for the chosen material set.

4.1.3 Anti-sticking layers

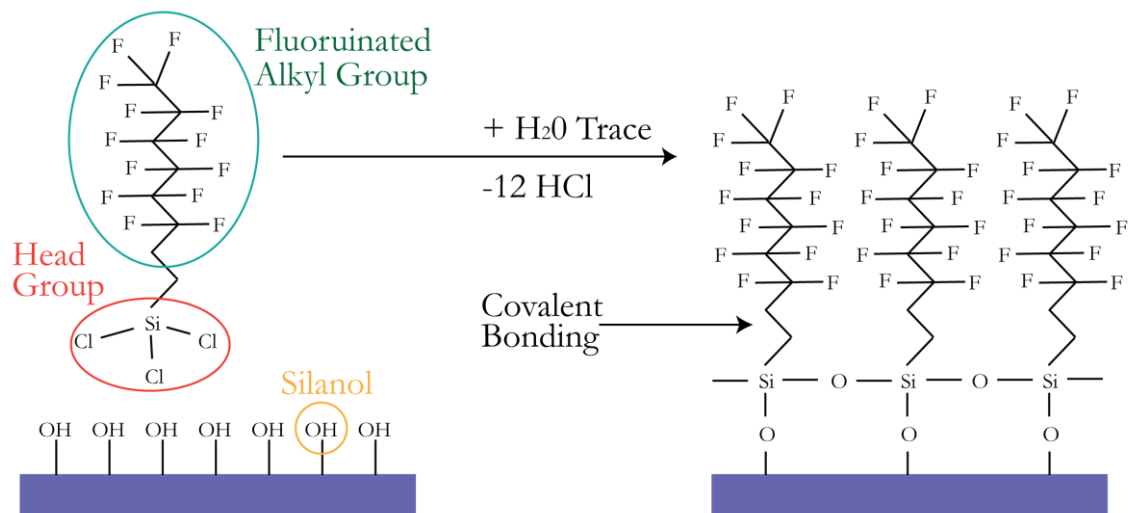


Figure 4.1: Schematic of an example of a chemical process to produce a silane coating on a silicon oxide surface [111].

The majority of work to avoid feature deformation has been to coat the stamp with an anti-sticking layer (ASL), generally a fluorinated silane-based material, which reduces the attractive forces. An example is given by Song [111]. He used a fluorinated silane molecule, whose head group consists of three chlorosilanes and a fluorinated long carbon chain, as in Figure 4.1. When deposited, the chlorinated silane groups form bonds with the hydroxylated silicon surface. Cross-linking between silane groups in neighbouring molecules occurs creating a high-density layer. The reaction leaves a fluorinated tail group, rendering the surface hydrophobic and with a lower surface energy.

There are many different treatments for producing ASLs. These have been grouped and are shown in Table 4.1. Comparing the values obtained, it is seen that Maboudian and Carraro

[112] report the lowest work of adhesion for OTS, DDMS and 1-octadecene. These values were calculated using micron sized cantilever beam arrays (CBAs) [113]. Upon actuation of the beams of various lengths, only those shorter than a characteristic length will have sufficient stiffness to free themselves completely from the substrate after the removal of an actuation force. From this, the work of adhesion is calculated, balancing the elastic energy stored in the beam and the substrate. The authors noted that detachment length is affected by a multitude of factors, including surface roughness, strain gradients in the structural film and relative humidity, which may explain why these values are extremely low [114]. Research by Jang *et al.* [115] shows differing surface energy values for Fots and DDMS, reporting values of 0.49 Jm^{-2} and 0.77 Jm^{-2} respectively, using a four point bend test but at a larger macro scale.

Table 4.1: Surface treatments used and their published values for work of adhesion.

Surface treatments*	Water contact angle (°)	Work of adhesion (Jm^{-2})	Method to calculate work of adhesion	Ref.
FDTS	107	Not reported	N/A	[111]
FDTS	115	12×10^{-6}	Cantilever beam arrays	[112]
OTS	110	5×10^{-6}	Cantilever beam arrays	[112]
DDMS	103	45×10^{-6}	Cantilever beam arrays	[112]
1-Octadecene	104	9×10^{-6}	Cantilever beam arrays	[112]
Fots	95	$22.6 \times 10^{-3}^1$	Estimated from contact angle	[116]
Optool	111.9	$12.6 \times 10^{-3}^1$	Estimated from contact angle	[116]
Aquaphobe CF	Not reported	2.77	Double cantilever beam (DCB)	[117]
Cytonix FSD 4500	Not reported	0.249	Averaged value, using DCBs	[118]
DLC	Not reported	0.17	Averaged value, using DCBs	[118]
DDMS	Not reported	0.77	Four point bend	[115]
Fots	115	0.49	Four point bend	[115]

*FDTS is perfluorodecyltrichlorosilane, OTS is octadecyltrichlorosilane, DDMS is dimethyldichlorosilane, Fots is perfluorooctyltrichlorosilane and DLC is diamond like carbon.

The works compared here show a large variation in values reported for the work of adhesion/fracture energy, which may be due to the different ways the values have been

¹ This value differs by a magnitude of 6 with that given in Table 1 of Tallal's article; a misprint unit of nN/m was published. The author acknowledges it should be mN/m.

calculated. All show however that using ASLs are beneficial and reduce the forces needed for separation at micro and nano scales.

4.2 DE-EMBOSSING MODEL FORMULATION

The literature review has made it clear that there is a lack of analysis and simulation tools for de-embossing, which hinders the advancement of the process. The following sections present the conception and derivation of a semi-analytical model for the de-embossing process. A process tree helps to explain the feedback loops implemented within the numerical model that enable the variable limits to be found. In the results section, graphs have been created for given parameter sets indicating the limits for successful de-embossing. These are reviewed in the discussion, with conclusions following on.

4.2.1 De-embossing of a polymer post

After imprinting, air can become trapped at the top of the features, most notably above posts. On polymerisation, the polymer pattern is likely to shrink, pulling away from the sidewalls and roof of the stamp. The shrinkage of the polymer may help de-embossing, making the removal of the stamp easier as there will be a reduction in the attractive surface and friction forces on the sidewalls. Figure 4.2 shows the free body diagrams (FBDs) of the de-embossing process of an axisymmetrical polymer post when the stamp is withdrawn by an infinitesimal displacement δ . If it is assumed the polymer is softer than the rigid stamp, the polymer, which is now solid, has a Poisson's ratio between 0.3 and 0.5, depending on the type used. Its volume cannot change greatly and so δ of the post between 1 and 2 must be accommodated by the formation of a 'gap' between the stamp and polymer, seen at the base of the post in the FBD in **b**. Peeling then begins at this edge of the stamp and will proceed horizontally along the interface between the stamp and polymer base and vertically between the sidewalls.

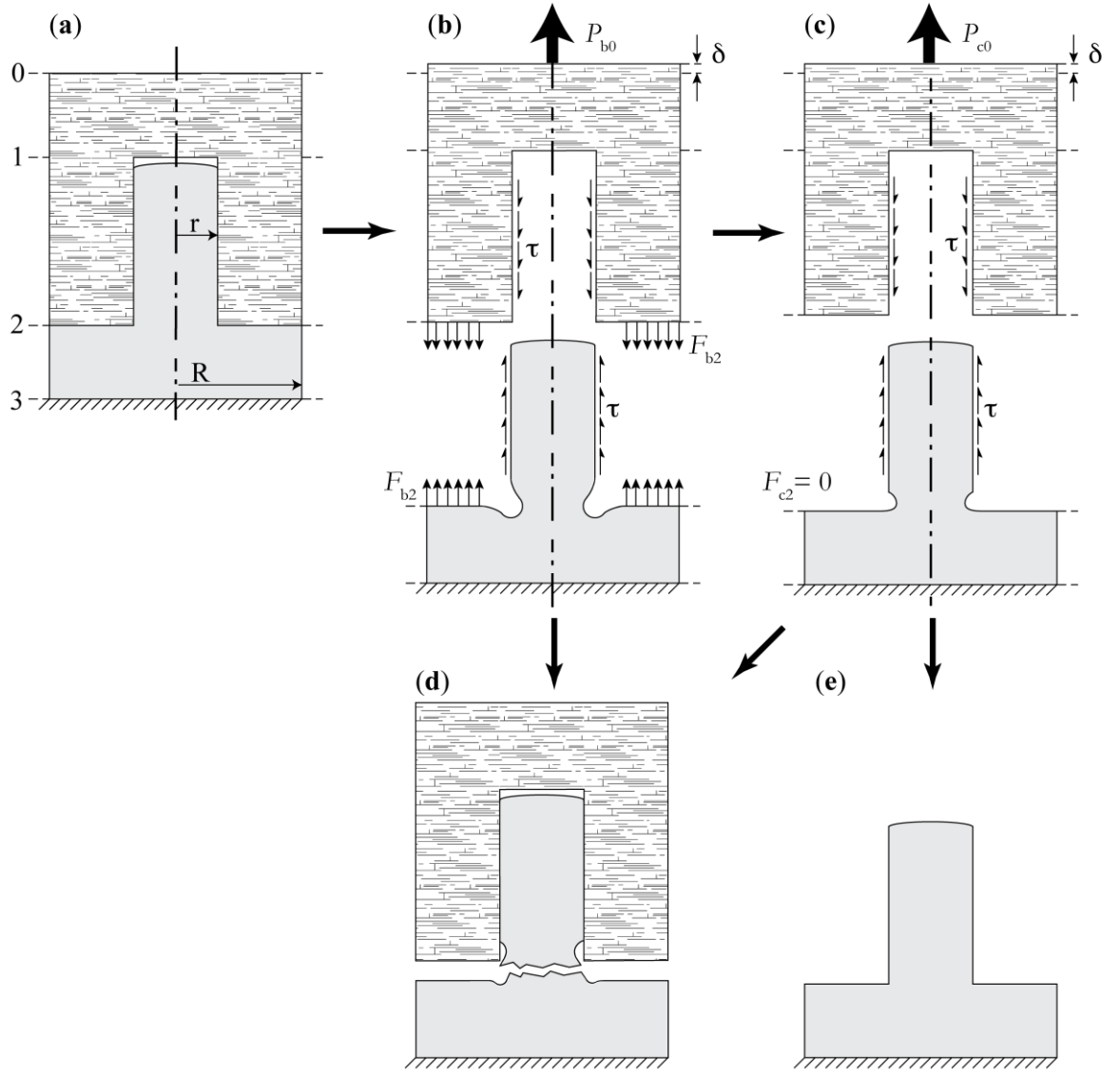


Figure 4.2: Free body diagrams detailing the forces during de-embossing of a polymer post.

The applied force P_{b0} on the stamp is equilibrated by the adhesive force F_{b2} and the shear force τ on the residual layer and post walls respectively. At this point, if the force due to τ on the neck of the post is greater than the polymer yield stress, the post will yield and remain within the stamp **d**. If this does not occur, the stamp and polymer will completely pull away from one another along their faces at z_2 . The polymer post is still within the stamp but the only forces acting against the de-embossing motion are on the sidewalls of the post as in **c**. It is still possible for the post to fail if the shear forces on the sidewalls are great enough. Otherwise, the post will de-emboss with growing ease due to the reducing length of polymer post in contact with the stamp, which τ acts upon, resulting in a formed polymer feature as seen in **e**.

Although the above description of the process is an accurate account of the de-embossing procedure, filling can sometimes occur completely e.g. for embossed trenches to produce a

grating structure. It is also the ideal scenario and the objective of the engineers making these toolsets. Should filling occur completely, an attractive force is seen across the top of the polymer posts and would make the de-embossing more difficult. Because this research is to create an analytical model that describes the process entirely, we shall assume the polymer post fills the stamp completely. Upon de-embossing, when the forces are great enough to cause the polymer post to slip out of the stamp, the force transferred over the post top will reduce to zero and at that moment, would behave as depicted in Figure 4.2 above.

4.2.2 Composite modelling comparison

At nano and micrometre dimensions, the stamp and polymer are similar to a composite material consisting of continuous fibres within a matrix; the stamp features behave as the matrix and the polymer as the fibres, or vice versa depending on the design. Similarly, de-embossing on such small length-scales is analogous to the propagation of a crack transversely through a long fibre composite material under tension. Such calculations have previously been performed for fibre pull-out and long steady-state crack growth in such composites and these are the basis for the calculations used herein to model de-embossing [119, 120]. For ease of explanation, crack propagation herein is referring to mode I fracture and the creation of surfaces between the horizontal surface of the stamp and polymer at z_c .

4.2.3 Assumptions

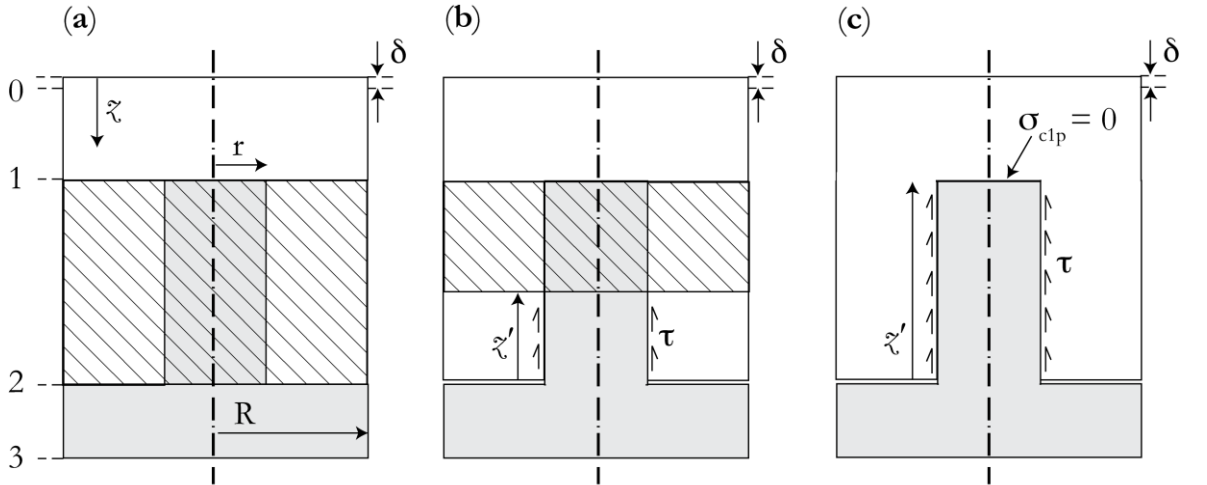


Figure 4.3: (a) Fully bonded state, equal strain at each cross-section; (b) Interfacial critical strain energy release rate overcome but not the side-wall friction; (c) Strain energy release rate and the side-wall friction is overcome enabling de-embossing.

To form an analytical model, the process is divided into the bonded and de-bonded states that occur when de-embossing commences, as shown in Figure 4.3. When bonded (a), the displacement on the stamp results in a uniform strain throughout the model i.e. the stamp and

post have equal strain between z_1 and z_2 , which is depicted by a hatched region. At an increased de-embossing force the polymer begins to de-bond from the stamp. This occurs in a two-part process. Initially **(b)**, the critical interfacial strain energy release rate (G_{ic}) is overcome at z_2 , but the stamp remains adhered due to the friction on the sidewalls of the polymer posts and the adhesion at the top of the polymer post. Finally **(c)**, the stamp can be removed from the polymer when all the attractive forces have been overcome and the de-embossing force only acts against the friction along the polymer sidewalls.

It is assumed that failure will not occur between the substrate and the residual layer interface at z_3 . De-embossing is modelled as a crack propagating at the interface between the residual layer and stamp at z_2 in steady state conditions; in fracture mechanic terms, the crack tip state is independent of the crack length. Initially, the residual layer and stamp are well-bonded. For a steady state crack, the energy needed to create the crack is the difference in system energy before and after crack propagation. Assuming the de-embossing of the stamp from the residual layer can be modelled similarly, this energy method can be employed to calculate the energy states before and after de-embossing in a displacement controlled process.

The model is split up into regions whose strain distributions are calculated separately and are added together to calculate the overall energy. The model is of a single cylindrical post whose unit cell is radius R . It assumes the polymer has solidified, completely filling the mould. Frictional contact is assumed on the vertical sidewalls of the cylinder and attractive surface forces between the top and bottom of the stamp and polymer faces. Adhesion on the sidewalls is accounted for within the sidewall friction; it is acknowledged that this is a simplification, but this is consistent with previous work modelling matrix fracture in composites. The different regions and the layout are shown schematically in Figure 4.3.

To produce a largely analytical model, the following additional assumptions are made:

1. materials are linear elastic, homogeneous and isotropic;
2. a plane strain, axisymmetric model describes the process;
3. the longitudinal (z) stresses are much greater than the other stress components, which are assumed to be negligible.

For an infinitesimal displacement δ , before the creation of the new surfaces at z_2 (which can be thought of in composite material terms as crack propagation), each region experiences an increase in strain energy. Initially in state **a**, region z_{12} behaves as a composite material with equal strains in the two materials. After crack propagation, represented in state **b**, only the region between z_1 and z' behaves as a composite; elsewhere dissimilar strains exist between the polymer and stamp over the slip length z' , extending out from the crack surface. Across

this boundary, it is assumed that there is a constant shear stress τ . For a greater displacement, the slip length increases. De-embossing cannot occur until the slip length is equal to or greater than the length of the polymer post z_{12} . At this point the stress transferred over the top of the post is assumed to be zero and the slip length can be found by

$$z' = \frac{\sigma_0 r_1}{2\tau f}, \quad 4.3$$

where: σ_0 is the stress applied to the top of stamp, r is the post radius and f is the area fraction, which can be written in terms of radii as

$$f = \left(\frac{r}{R}\right)^2, \quad 4.4$$

In addition to the slip length equalling the embedded length of the polymer, another condition must be met for detachment. The adhesive surface energy between the stamp and polymer needs to be overcome; this is quantified as the critical interfacial strain energy release rate G_{IC} . In the model it is assumed that this occurs first to enable slip. This is a reasonable assumption as for practical NIL a low interfacial adhesion must be achieved.

The majority of variables mentioned and to be found in later equations are known, or are easily measured. The τ and G_{IC} values however are dependent on the material types, geometry and surface finish. Such properties are not well known and need to be found through experimentation.

4.2.4 Residual layer stress distribution

After the crack has propagated, the stress distribution in the region z_{23} ; the residual polymer layer below the post feature, changes from a constant stress across the layer into a varying stress, dependent on the depth and radial distance. Initially, a stress function solution satisfying the bi-harmonic equation was utilised. An example of a similar stress state was found [121]. However, this proved too complex and an alternative approach was used, approximating the stress distribution in the residual layer to that of a semi-infinite elastic half-space loaded by a flat punch, as shown in Figure 4.4. Such a distribution was solved by Boussinesq [122]. These equations have been troublesome to solve except for particular geometries. Love [123] created a solution based on partial and complete elliptic integrals that provides the stress value at a given point in a semi-infinite half-space by pressure applied over a circular area. Although these equations are to describe small strains and stresses, they will be used to describe the stresses below the polymer post. They will provide a better

approximation of the larger stresses experienced below the polymer post during de-embossing and will be more realistic than assuming a constant stress state in the region.

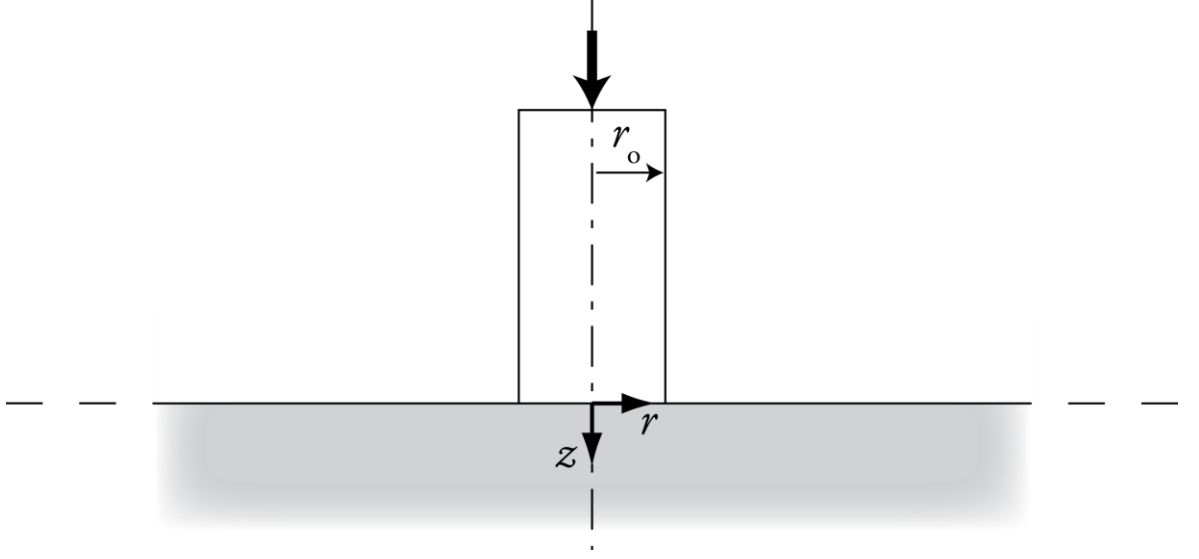


Figure 4.4: Illustration of a cylindrical punch on a semi-infinite half-space under an applied stress. The stress distribution in the residual layer is assumed to be similar.

Using elliptic integrals increases the complexity of the derivation and for the method suggested by Love, calculates the stress at specific co-ordinates, preventing the analytical integration of all the terms in the z and r directions. As these calculations will be used, a unit cell about the specific points is approximated to have the same stress value. A numerical integration of these elements then obtains the cumulative stress value that is used to calculate the strain energy and displacements. This analysis is a compromise between the speed of an analytical method and the ability to calculate the stresses in the material by a numerical method. Because of the use of complete and partial elliptic integrals to find stresses at finite points, the approach does not satisfy the bi-harmonic equation nor is it completely analytical. However, it was felt that this semi-analytical approach was the best strategy to completely model the stress distribution in the entire structure, thereby being able to calculate the strain energies for the different regions.

4.2.5 Matlab script validation

The results for the residual layer stress distribution are obtained using a Matlab script, with a function created by Igor [124] to calculate partial elliptic integrals. To determine the effectiveness of the code, longitudinal stress values need to be verified against those calculated by Love in curvilinear co-ordinates. It was found for the same number of significant figures, the code produced identical values for all variables as calculated by Love, validating the codes efficacy. These results are presented in Appendix D.

To use Love's equations to calculate the stress distribution in the de-embossing model, the script was altered to provide points in an axisymmetric orthogonal co-ordinate system in terms of r and z , instead of from selected k and θ curvilinear co-ordinates, to make the numerical integration simpler. This was achieved by reversing the input and output variables i.e. re-arranging the equations for depth and radius to calculate k and θ values.

The stress variation in the body has a greater dependency on the r -coordinate than the z -coordinate, with the greatest variation in stress occurring below the polymer post edge. To increase the accuracy of the analysis, the points where stress values are calculated are stepped in the r -direction by two logarithmic distributions radiating out from below the post edge so the stress variation is accurately described. Figure 4.5a shows this distribution while Figure 4.5b shows the variation in stress for an applied pressure on a semi-infinite half-space, which will be used to approximate the stress in the residual layer.

The same script is used to calculate the displacement. Only the points directly below the post have their strain values integrated in the z direction, as the free surface should have no displacement. This results in a displacement value for each r -value in the logarithmic scale below the post. A mean of these is used calculated and used in the calculations.

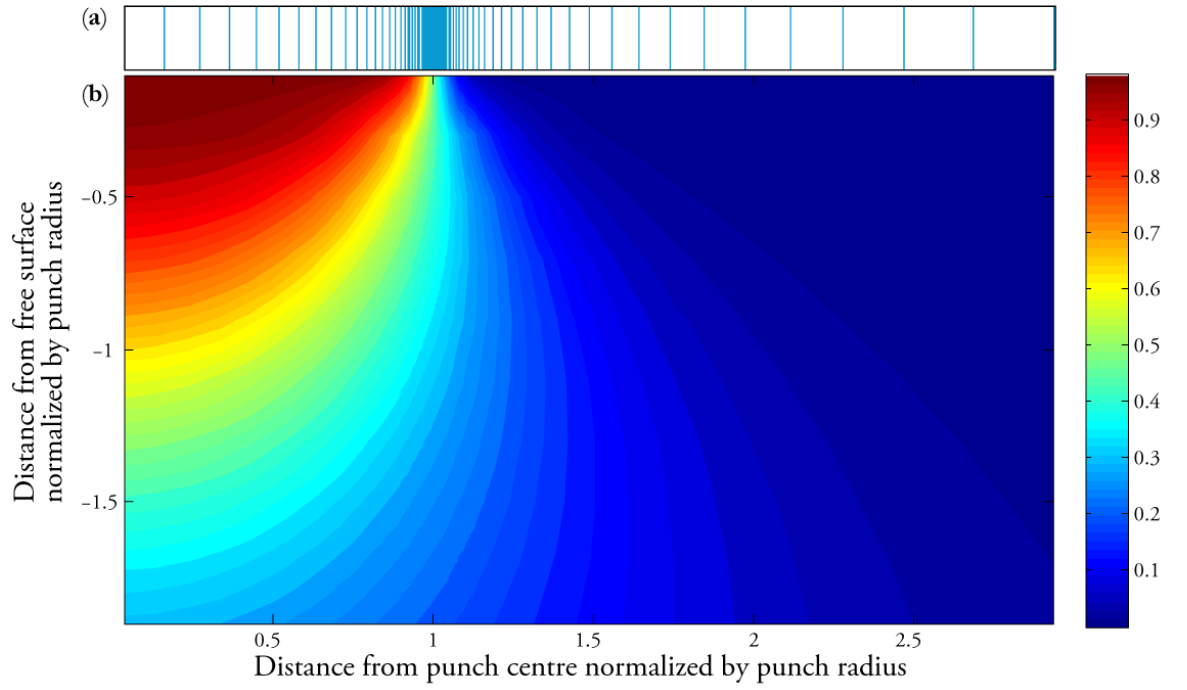


Figure 4.5: a) Two logarithmic distributions emanating out from the punch edge used for the r -values are used calculate the stress in the semi-infinite half-space at different locations; b) Normalized stress distribution σ_z calculated for a semi-infinite half-space that is used to approximate the residual area.

4.2.6 Stamp top stress distribution

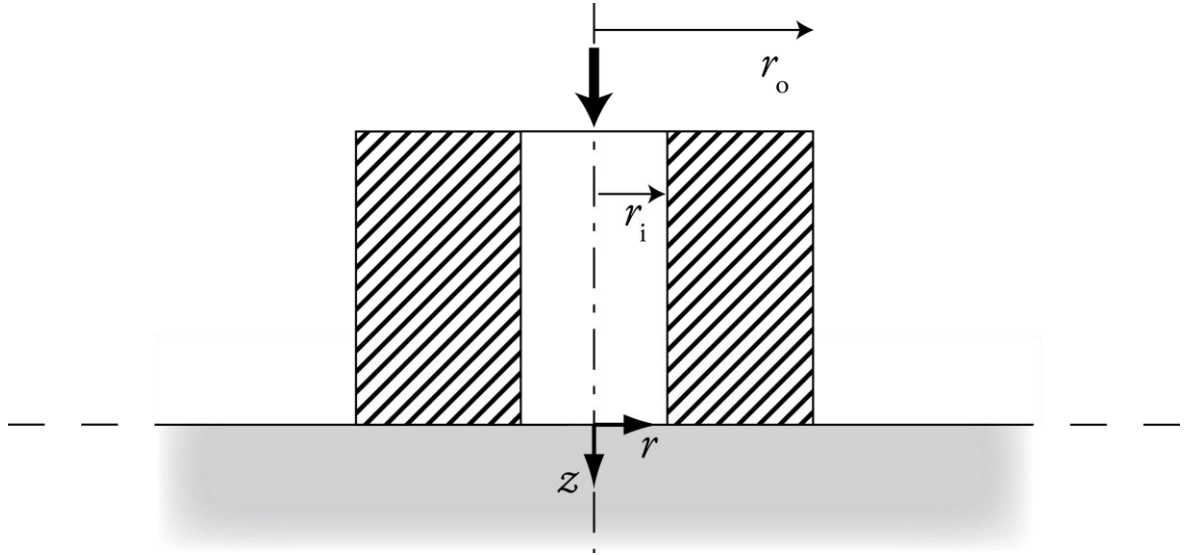


Figure 4.6: Illustration of an axisymmetrical cylinder punch on a semi-infinite half-space under an applied stress. The stress distribution in the stamp top is assumed to be similar.

Upon the slip length z' equalling the length of the polymer post, it is assumed that no stress is transferred over the top of the polymer post. Should G_{ic} also be overcome, the stamp will de-emboss. At this moment the stamp top, the material above the features, takes on a stress distribution also varying in z and r but different to that of the residual layer.

They differ because the stresses transferred to the stamp top by its features are at a radial distance from the axisymmetrical line of the model. Instead, the stamp features behave as a cylindrical punch on a semi-infinite half-space, applying stress between radii r_i and r_o about an axisymmetrical line, as illustrated in

Figure 4.6. To calculate the stress distribution using Love's derivation would involve going back to first principles, as the stress is not applied from the axisymmetrical line. An easier and quicker method that will be used is the superposition principle, which is explained graphically in Figure 4.7. An equivalent stress distribution to the pressure seen by the stamp top is created by starting with an applied pressure across the entire surface. In the model shown in Figure 4.3, the stress value at z_1 , where the stamp features meet the stamp top, is equal to $\sigma_0(1-f)$, a fraction of the stress transferred at z_0 . The stress distribution created by a punch of radius r for the same pressure value is then calculated and subtracted creating a stress distribution for the stamp top. The subtracted stress distribution is calculated in the same manner as for the residual layer using Love's formulae, while the initial state situation has a constant stress value across the whole region.

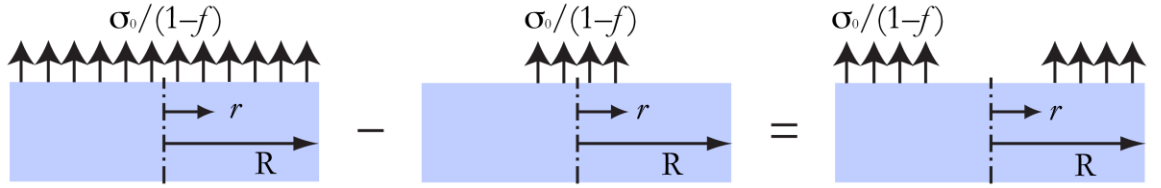


Figure 4.7: Graphic description of the superposition principle, explaining how the stress distribution in the stamp top is calculated.

4.3 ANALYTICAL MODELLING

The model is formulated based on a constant displacement boundary condition. For de-embossing to be successful, two conditions need to be met. Firstly, there must be enough energy available in the system to overcome G_{ic} . Secondly, the complete length of the post must be able to slide relative to the stamp. These two calculations combined with the fixed displacement condition give different initial stress values. Therefore the greater of the two values is used as the defining de-embossing stress. The explicit derivation of the equations for the modelling formulation is presented in Appendix E; in this section only the key equations are shown.

4.3.1 Energy balance equations

With the assumptions used to define the de-embossing stress, the slip length limits the stress that can be applied to the system after the interfaces are created to:

$$\sigma_{0_{sl}} = \frac{2\tau z_{12}f}{r}. \quad 4.5$$

The energy difference before and after de-embossing (state **a** and **c** respectively) is calculated for each region of the model. The total strain energy before interface de-cohesion is given by

$$U_{03_a} = \frac{\sigma_{0_a}^2 A_T}{2} \left(\frac{z_{01}}{E_s} + \frac{z_{12}}{E_c} + \frac{z_{23}}{E_p} \right), \quad 4.6$$

where: U is the strain energy, A_T is the total area of the unit cell, E_s is the Young's modulus of the stamp, E_c is the Young's modulus of the stamp and polymer acting as a composite and E_p is the Young's modulus of the polymer. The strain energy found in the stamp top after de-embossing of the stamp material is described by

$$U_{01_c} = \frac{\pi}{2E_s} \left(\sum_{z_0}^{z_1} \sum_0^R \Delta\sigma_z^2 drdz \right), \quad 4.7$$

where: $\Delta\sigma_z$ is the finite stress per unit area varying in z . The residual layer energy term is

$$U_{23_c} = \frac{\pi}{2E_p} \left(\sum_{z_2}^{z_3} \sum_0^R \Delta\sigma_z^2 drdz \right). \quad 4.8$$

4.7 and 4.8 both use the discretized calculations for estimating the stress after the interface has formed. The polymer post energy is

$$U_{p_b} = \frac{\sigma_0^3 A_p r}{12E_p \tau f^3} \quad 4.9$$

and the stamp features energy is

$$U_{s_b} = \int_0^{z'} \frac{\sigma_s^2 A_s}{2E_s} dz. \quad 4.10$$

Collectively, 4.7 to 4.10 make up the strain energy stored in the system, U_{03c} , upon formation of the interfaces.

The frictional energy term from sliding (V_{sl}) is dependent on the materials' Young's moduli. Upon de-embossing, if the stamp material is stiffer – such as in the majority of TNIL – then

$$V_{sl_p} = \frac{\sigma_0^3 E_s^2 A_p r (1-f)^2}{12E_c^2 E_p \tau f^3}, \quad 4.11$$

whereas if the cured polymer is stiffer – when using a soft stamp as in the majority of UVNIL – the frictional energy term is

$$V_{sl_s} = \frac{\sigma_0^3 E_p^2 A_p r}{12 E_c^2 E_s \tau (1-f)}. \quad 4.12$$

For the given values, the equation used to solve for the initial stress that must be applied to overcome G_{ic} is

$$\sigma_{0_a} \leq \sqrt{\frac{\left(2G_{ic}A_T + U_{03_c} + |V_{sl_p}|\right)}{A_T \left(\frac{z_{01}}{E_s} + \frac{z_{12}}{E_c} + \frac{z_{23}}{E_p}\right)}}. \quad 4.13$$

4.3.2 Constant displacement equations

The calculations used to obtain the stress for constant displacement are derived in a similar method to those of the energy equations: the displacements of each region in the model are added together. Prior to de-embossing in state **a**, the polymer post and stamp features in the region z_{12} are treated as a composite with equal strain at each cross-section. After de-embossing and for a scenario where the stamp is stiffer than the polymer, in either state **b** or **c**, extension in the region between z_1 and z' is solely based on the extension of the softer polymer post. This is because the stiffer stamp is relaxed after forming a free surface across its face at z_2 and physically, only the polymer post transfers the stress from this point to the residual layer. For a stiffer polymer, the opposite is true, with the stress being transferred through the stamp. Within the residual layer and stamp top the extensions are found using the discretized equations for the regions directly below the polymer post and stamp features respectively. The overall equation to calculate the stress is

$$\sigma_{0_a} = \frac{\delta_T}{\left(\frac{z_{01}}{E_s} + \frac{z_{12}}{E_c} + \frac{z_{23}}{E_p}\right)}, \quad 4.14$$

where: δ_T is the total displacement described as

$$\delta_T = \delta_{st} + \delta_p + \delta_{rl}, \quad 4.15$$

where: δ_{st} is the displacement in the stamp top directly above the features, δ_p is the displacement in the polymer post and δ_{rl} is the displacement in the residual layer directly below the post.

With differing conditions and de-embossing sequences, a decision tree is needed within the script. The following section describes the decision making process implemented in the script.

4.3.3 Script procedure

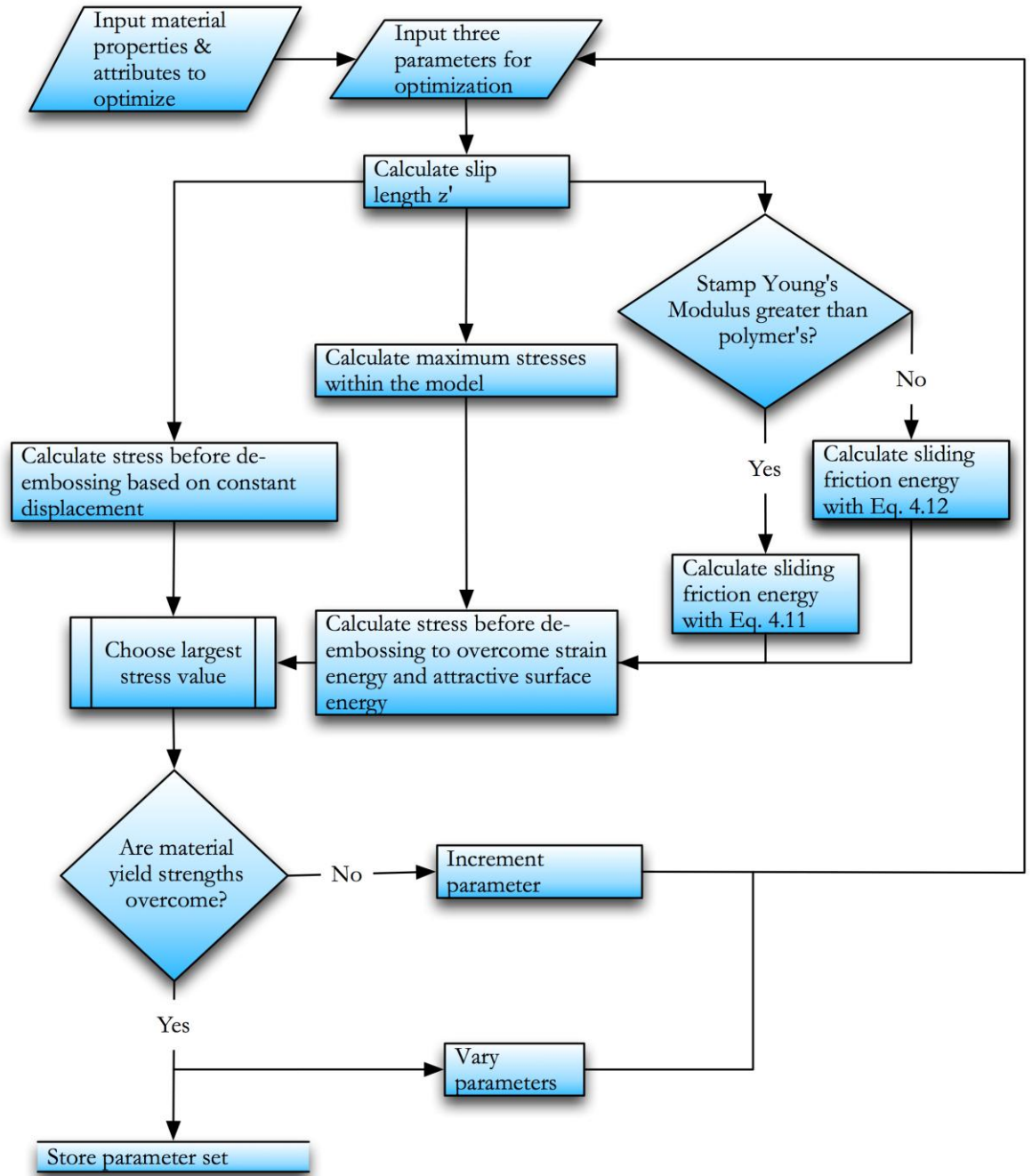


Figure 4.8: De-embossing process tree used in Matlab script.

De-embossing is dynamic by nature. To create equations that describe the problem statically, a decision process is used, switching between equations and limits describing the different conditions. The model can then solve for multiple inputs and calculate which outcome will succeed. Figure 4.8 shows a schematic of the process tree. This is implemented as a Matlab script, which solves for the de-embossing stress applied to the stamp in state **a** (σ_{0a}), as the maximum value of σ_{0c} is fixed by the material and geometry used. The value σ_{0a} has to be

greater than σ_{0b} or σ_{0c} for there to be no loss of energy in the system from the creation of the new surfaces at z_2 , as illustrated in Figure 4.9. The script can be seen in Appendix F.

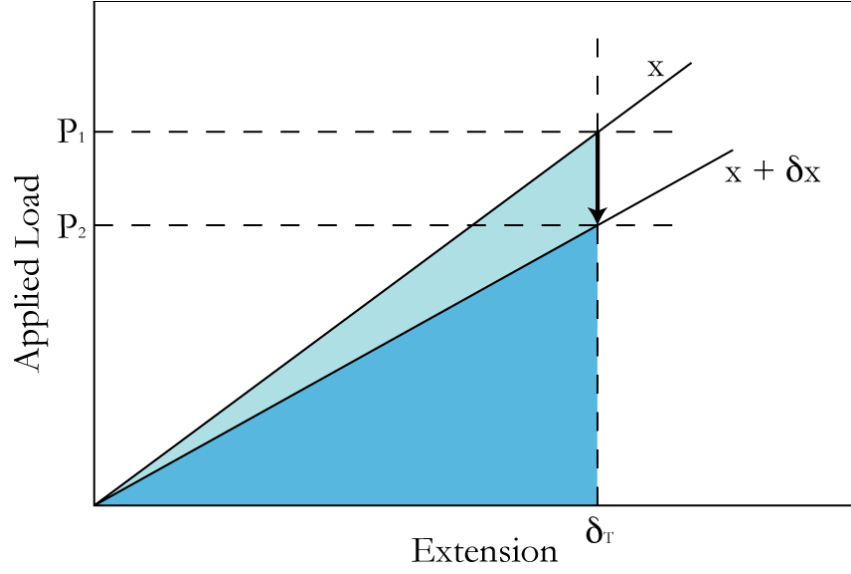


Figure 4.9: Crack extension (x) at constant deflection, results in a decrease in the elastic strain energy/increase in surface energy.

The yield strength failure criterion uses the stresses found at the base of the polymer post and at the top of the stamp features prior to the slip length equalling the post height; state **b** shown in Figure 4.3. In state **c**, the stress transferred across the polymer post top is zero, reducing the de-embossing stress. In state **b** however, stress is transferred across the post top with the stamp features and polymer post behaving as a composite. In this state, a greater stress is created and is found by:

$$\sigma_{0_b} = \frac{2\tau E_c z_{12} f}{E_s r(1-f)}, \quad 4.16$$

which is the equation for slip length in state **b** rearranged and assuming $z'_c \approx z_{12}$.

The maximum stress felt in the polymer and stamp features is during state **b**. For de-embossing to occur, physically the model must pass through state **b**. To account for this, the yield strength failure criterion uses the stresses found at the base of the polymer post and at the top of the stamp features in state **b**; prior to the slip length equalling the post height.

For three chosen variables, two are held while the third is incremented. The script calculates the stresses within the model and then checks to ascertain if either material has yielded. If not, the third element is incremented and the process is repeated until failure occurs. The variable set before failure is seen as the limit for the chosen configuration. The variable combination is stored in a parameter table. The third variable is reset, the second variable is incremented and the procedure is repeated. Once the second and third variables are exhausted, the procedure is

repeated for the variation in the first variable. This enables limit lines for the first variable to be displayed on graphs varying in x and y for the second and third variables respectively.

To enable the model to give useful results, parameter values similar to those used in NIL need to be chosen.

4.3.4 Attribute values

To allow comparison between the process maps, a default set of parameters are used. Of these, three will be varied at any one time for comparison. The majority of these have been chosen based on values regularly found in the field of NIL. The default Young's moduli and yield stress values will be based on Silicon and PMMA for the stamp and polymer respectively as they are widely used. The values for τ and G_{ic} are not as easily characterised. Both are dependent on the material and geometry of the stamp. ASLs may also be used. It has been reported in published articles that G_{ic} values in the range of 0.249-3.64 J/m² have been achieved by experiments investigating the adhesion between stamp and UV curable polymer [115, 117, 118]. The variation is due to different ASLs or materials used. For τ , a value of 0.1 MPa is chosen. Reported values in the composite literature for the maximum interfacial shear stress between the fibres and matrix vary from 26-45 MPa [125-128]. This is the maximum value at the surface and for fibre pullout and tends to have an exponential decline, making the average value somewhat less. The intention in composite research is usually to create a strong bond; making τ as high as the yield shear stress. However, for de-embossing, where the τ should be as low as possible, no experimental results have been found. It is reasonable to expect the imprinting process and the use of ASLs reduce the shear stress by two orders of magnitude, comparable to the observed reduction in G_{ic} . The default attribute values used are:

Table 4.2: Standard material and geometrical values used when constant.

$\tilde{x}_{01} = 1000 \text{ } \mu\text{m},$	$AR = 3,$	$\tau = 0.1 \text{ MPa},$
$\tilde{x}_{12} = 1.2 \text{ } \mu\text{m},$	$f = 0.04,$	$\sigma_{yp} = 67 \text{ MPa},$
$\tilde{x}_{23} = 0.2 \text{ } \mu\text{m},$	$R_E = 1.47059 \times 10^{-2}$	$\sigma_{ys} = 21 \text{ GPa},$
$r = 0.2 \text{ } \mu\text{m},$	$E_p = 2.5 \text{ GPa},$	$G_{ic} = 0.5 \text{ Jm}^{-2}.$
$R = 1 \text{ } \mu\text{m},$	$E_s = 170 \text{ GPa},$	

The aspect ratio (AR) is described as the length of the post (\tilde{x}_{12}) compared to the diameter of the post ($2r$). The Young's moduli ratio R_E compares the polymer to the stamp material. Some

examples will be shown in the following section for a few parameter variations. These will be examined further in the discussion.

4.4 RESULTS

The following process maps illustrate de-embossing contours of a chosen variable, dependent on the parameters selected for the axes variables.

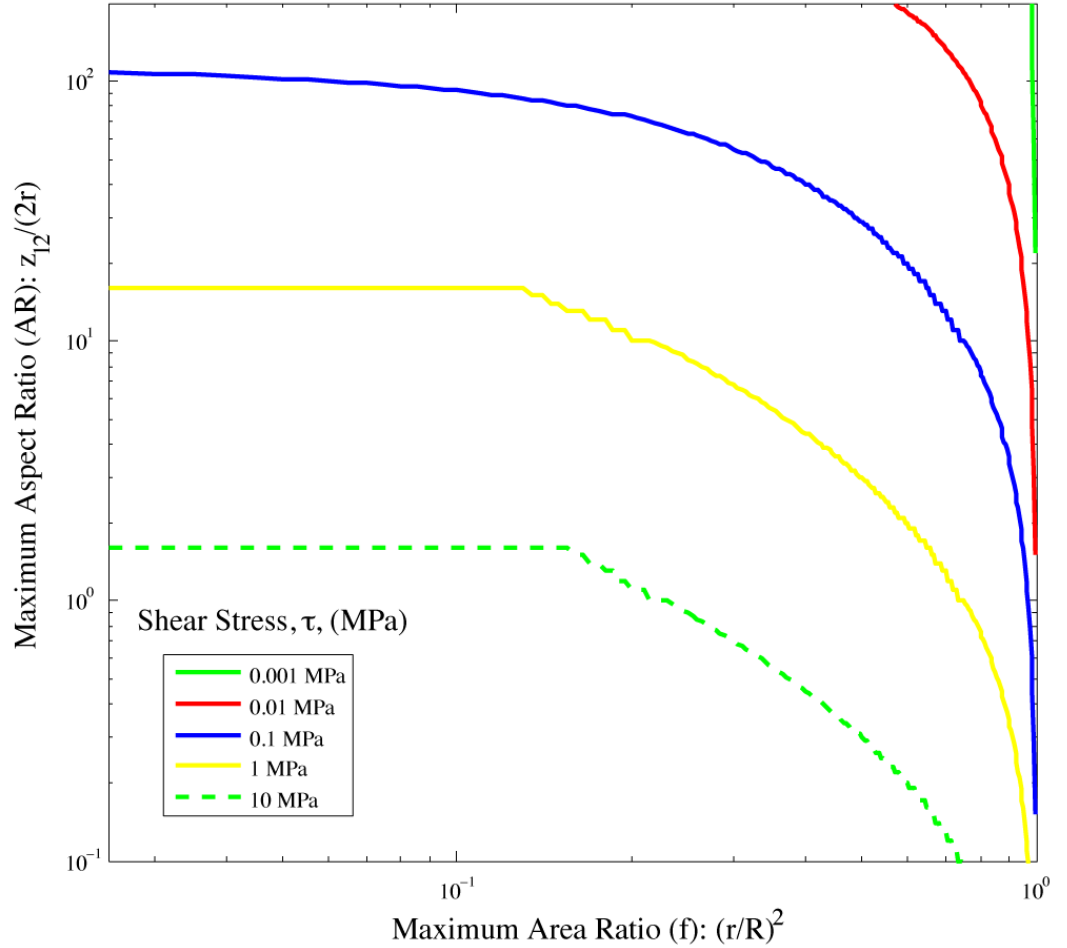


Figure 4.10: De-embossing limits for shear stress (τ) compared to varying aspect ratios (AR) and area fractions (f).

In Figure 4.10 the model is used to compare how achievable aspect ratios and volume fractions depend on the shear stress (τ). As expected, it can be seen that de-embossing becomes more difficult for higher τ values and for greater values of AR and f . With increasing τ , a greater applied stress is needed to overcome the frictional energy. This is also true for increasing AR or f as both increase the post-wall surface area that the shear stress acts upon.

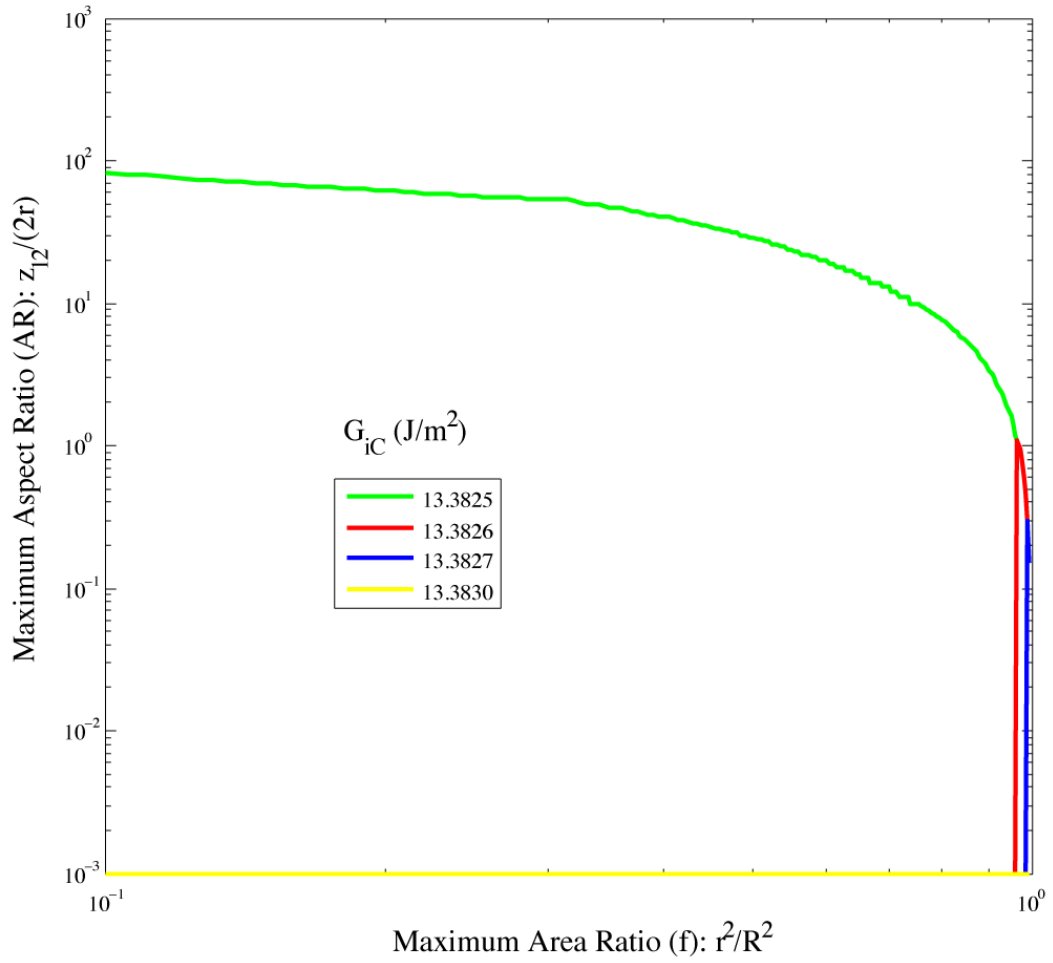


Figure 4.11: De-embossing limits for critical strain energy release rate (G_{ic}) compared to aspect ratio (AR) and area fraction (f).

For the same axes, varying G_{ic} produces the map shown in Figure 4.11. At low values of G_{ic} the model follows the green curve controlled by the bridged-crack strain energy release rate (state **b**), with the post material failing due to the interfacial friction when achieving constant displacement. This is the normal de-embossing process expected for the default attributes chosen and is seen for all f values when G_{ic} is below 13.3825 Jm^{-2} . However, when there is not enough energy to overcome G_{ic} , de-embossing fails. Physically, this is when the polymer comes away from the substrate and is displayed graphically as an extremely low aspect ratio.

Within a narrow band of G_{ic} values, a step change occurs, where the model switches between providing enough energy to overcome the adhesive surface energy between the stamp/polymer boundary and enforcing constant displacement. For greater f values, a larger G_{ic} can be tolerated. However, the effect is minimal, changing the value by $1 \times 10^{-3} \text{ Jm}^{-2}$; lower G_{ic} values were found by using a lower σ_{yp} value than that assigned in Table 4.2.

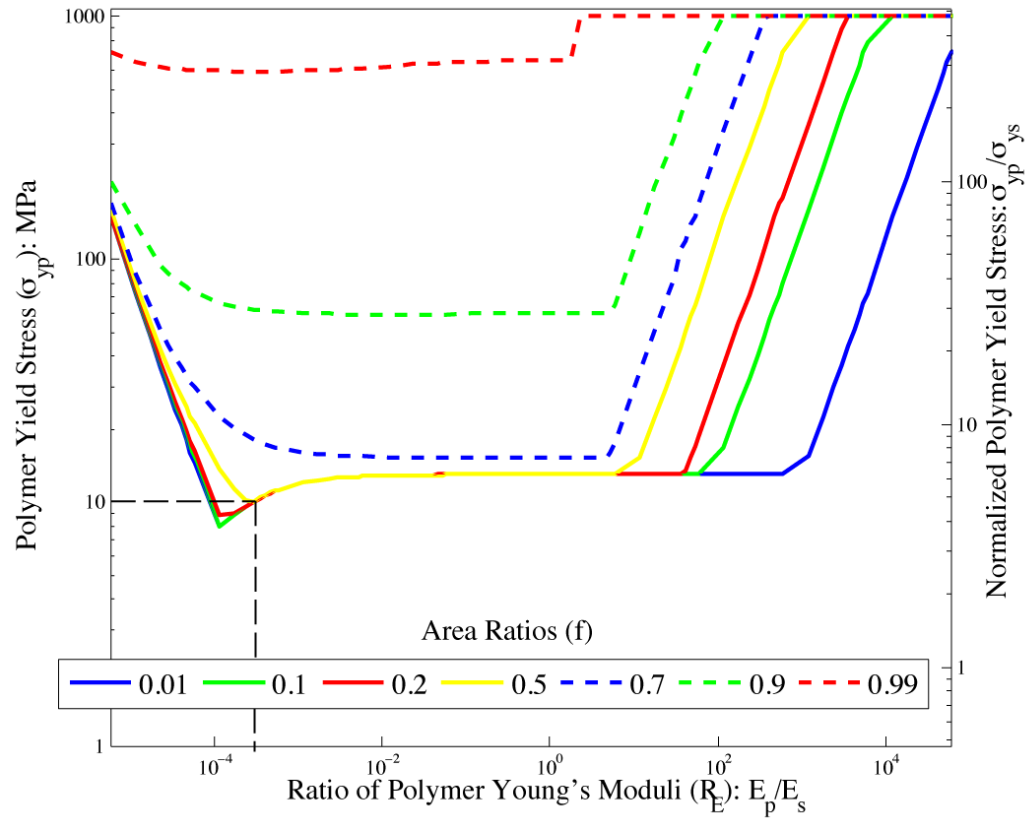


Figure 4.12: De-embossing limits for area fraction (f) as a function of polymer yield strength (σ_{yp}) and stamp/polymer modulus ratio (R_E).

The variation of achievable area fraction (f) with respect to polymer yield stress (σ_{yp}) and Young's moduli ratio (R_E) is shown in Figure 4.12. In this analysis, the Young's Modulus of the stamp was kept constant at a value akin to steel and the Young's Modulus of the polymer was varied. Physically, increasing f results in the polymer post taking up more volume in the unit cell at the cost of the stamp's volume. It also reduces the surface area that G_{ic} acts upon and increases the sidewall surface area that τ acts upon. For a given σ_{yp} the map indicates which f values are achievable. It is noticeable that for a polymer yield stress of 10 MPa, a wide range of area ratios, from 0.01 to 0.5 are achievable if R_E is 2.9×10^{-4} and that minima are seen for f values 0.5 and below. Currently, this R_E value is at the extremes of the potential NIL materials used and in terms of the Young moduli, is similar to imprinting LDPE with a diamond stamp. However, for a fixed post radius of 200 nm and an area ratio between 0.01 and 0.5 as mentioned, an R -value of between 2 μm and 283 nm could be de-embossed respectively. De-embossing becomes significantly more difficult and hence needs a higher yielding polymer for even larger area ratios. In this theoretical analysis, when the polymer becomes stiffer than the stamp, $R_E > 1$ i.e. when the Young's modulus is greater than silicon, de-embossing becomes much harder.

A similar map is obtained when the achievable aspect ratio (AR) is assessed with respect to σ_{yp} and R_E . Figure 4.13 shows when f is a constant 0.04, AR values of up to 20 can be de-embossed with a σ_{yp} of 20 MPa and a R_E between 3.4×10^{-3} and 5.5×10^{-1} . It also clearly shows σ_{yp} minima for aspect ratios of 5 or less; similar trends to those for f . Again, de-embossing is more easily achieved at R_E values below or close to unity for high aspect ratios.

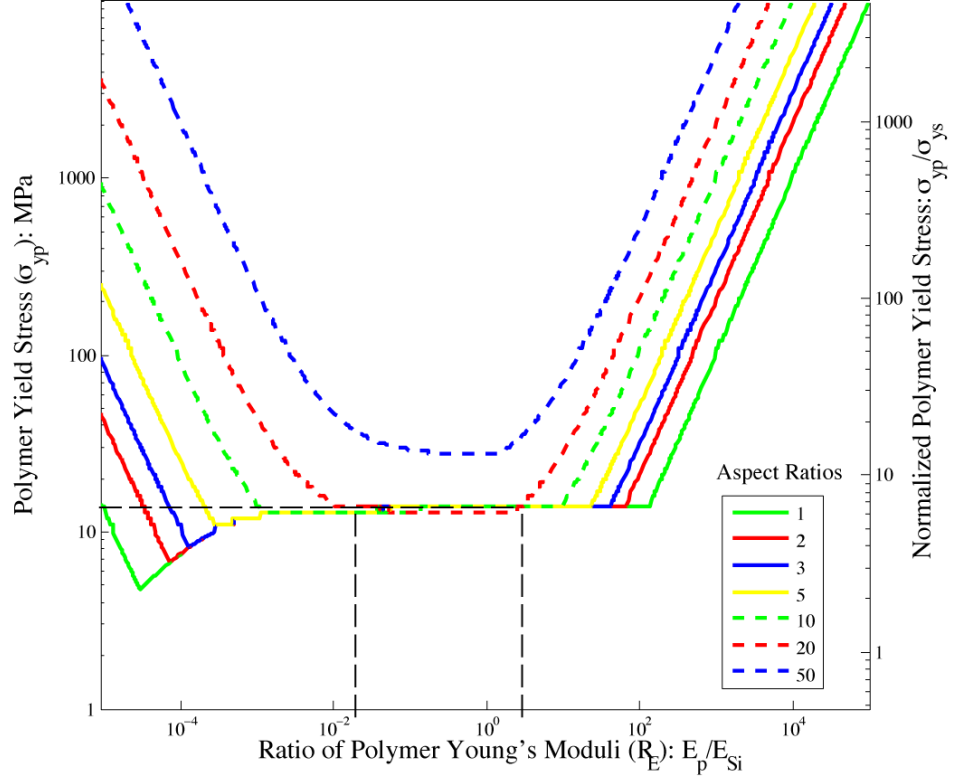


Figure 4.13: De-embossing limits for Aspect ratio, AR , as a function of polymer strength (σ_{yp}), and modulus ratio (R_E).

4.5 DISCUSSION

The graphs clearly show dependencies between variables that are important when designing stamps to produce structures in NIL through de-embossing. An increase in shear stress between the stamp and post sidewalls would reduce the achievable aspect ratios due to a greater post wall surface area for friction to act upon. Similarly, increasing the area ratio has the same effect: increasing the post wall surface area. It is interesting to note that the shear stress needed to achieve aspect ratios of 10, for the example material and geometrical values used, must be less than 10 MPa and that for the value of 0.1 MPa; the predefined value in Table 4.2, an aspect ratio of up to 73 should be achievable. Given that an aspect ratio of 10 is the greatest aspect ratio at micro and nanometre levels to be reported, this suggests either:

1. the sidewall roughness of the stamps used and the surface adhesion along the sidewall causes a shear stress closer to 1 MPa than the initial guess value of 0.1 MPa;
2. another process is occurring that the model does not account for;
3. greater AR values are achievable that have not been tried.

Realistically, the shear stress is not constant along the post. Also, in reality the stamp needs to be ‘peeled’ from the edges to allow air to enter into what would otherwise be a vacuum. The peeling process and the presence of a vacuum at the top of the post, makes it likely that the effective shear stress would indeed be significantly higher than that assumed in the model: the peeling process angling the stamp protrusions causing a horizontal force and the vacuum the top of the polymer post creating a back pressure.

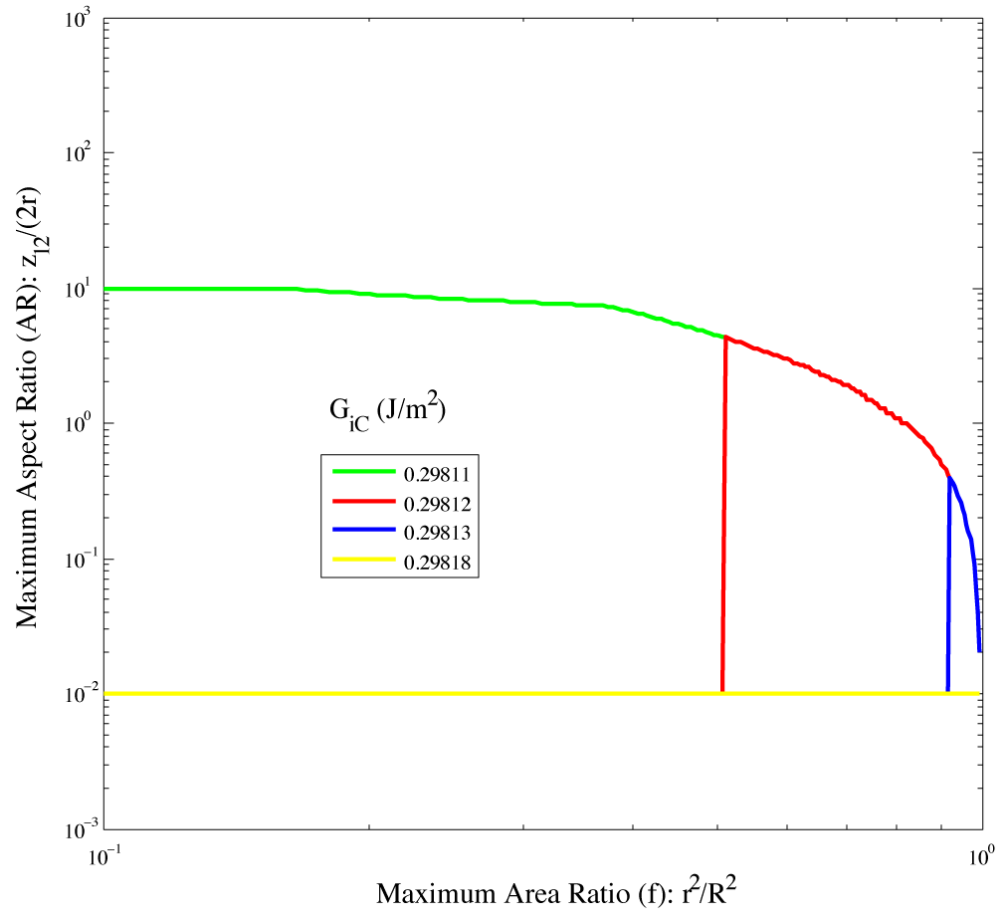


Figure 4.14: De-embossing limits for the strain energy release rate (G_{ic}) compared to the aspect ratio (AR) and area ratio (f), with a polymer yield stress (σ_p) of 10 MPa.

The graph depicting de-embossing for varying critical strain energy release rate values shows an extremely narrow field of only $0.5 \times 10^{-3} \text{ Jm}^{-2}$ where the stuck/release transition occurs for various area ratios. The transition profile is not seen for lower G_{ic} values, such as those found experimentally, in which anti-sticking layers are generally used. When G_{ic} is 0.5 Jm^{-2} or less,

the model predicts that there should be no issues with de-embossing dependant on the strain energy release rate i.e. its effect is not as important as the sliding friction on de-embossing.

With the use of ASLs and other surface treatments low values of adhesion are readily achievable. For the set of values used in Table 4.2, the surface energy becomes less important in the de-embossing process. Should the polymer yield stress be lower than the PMMA value, then the G_{ic} value begins to affect de-embossing. An example is shown in Figure 4.14, in which all the values used are the same as for Figure 4.11, except σ_{yp} is 10 MPa, 57 MPa lower than for PMMA. It can now be seen that the stick/slip transition occurs at G_{ic} of approximately 0.298 Jm^{-2} , values similar to those found experimentally. The area and aspect ratio plots against polymer yield stress and the ratio of Young's moduli are very similar. To achieve high aspect ratios, which would enable a greater variety and/or more efficient devices, having a Young's moduli ratio near unity would be of benefit. The same is seen for high values of area ratio, as would be needed to increase the data storage in hard drives when using discrete track recording (DTR) or bit pattern media (BPM) designs. For area ratios below 0.5 and aspect ratios below 5, the model suggests that the materials with a significantly lower Young's modulus; in the order of 4 to 5 times lower, may be de-embossed with a lower required material yield stress. This behaviour is associated with the effect of the Young's modulus on the strain energy; at low f values, there is a greater volume of stamp than polymer in the slip length region.

4.6 CONCLUSIONS

The model has been used to explore how the various material properties and process variables interact to control the achievable aspect ratios and area fractions for the de-embossing phase of imprint patterning. Simplifying assumptions have been made to describe the process so that a semi-analytical model could be created that describes the trends with key variables. This model is able to determine whether de-embossing can occur for various inputs. The model shows there is a very strong dependence of the achievable aspect ratio on the pattern area ratio and the interfacial shear stress. For the critical strain energy release rate values obtained using fluorinated coatings and current standard polymers, it is unlikely that failure to de-emboss will occur due to adhesion for post radii on the order of 100 nm. However, for lower post diameters and lower polymer yield stresses it becomes increasingly important to minimise the interfacial adhesion value to enable stamp separation. To reduce the yield stress value of the polymer for de-embossing and therefore enable a greater range of materials to be used, the adhesion, as quantified by the interfacial strain energy release rate should be kept to a

minimum. Large area ratios and aspect ratios are more easily achieved by maintaining the polymer/stamp Young's moduli ratio (R_E) in the range 0.003 to 5.

Due to the limitations imposed by simplifying the de-embossing step to enable it to be described mainly by analytical means, the model is able to predict trends as a result of the input parameters but should not be used to estimate the precise values at which de-embossing occurs. More detailed finite element (FE) models, such as those presented in [95, 108-111] are appropriate for the analysis of specific cases. It also does not take into account viscoelastic properties that have been reported in polymers when de-embossing. Nevertheless, the current work provides guidance as to the trends associated with choices of material and process variable and the relative criticality of such choices. Furthermore the modelling provides quantitative insight into the mechanisms behind earlier observations of trends and limits in experimental studies of imprint patterning techniques mentioned in Chapter 2 [129]. This work has been presented and partly published at the 2009 Joint ASCE-ASME-SES Conference of Mechanics and Materials held at Virginia Tech. It has also been submitted to the Journal of Microelectronic Engineering for publication.

Further work that would have been undertaken to improve the model is presented in Section 7.1. Unfortunately no further development into the NIL modelling could be undertaken during the EngD because of a change in research interests of the sponsoring company, which is explained in Part 2 of this thesis.

Part 2

CHAPTER 5: CREASING THIN SHEETS

In January 2009 Polymer Vision purchased Innos. They took on the responsibility for the EngD: the research, the patent, the knowledge of NIL's current processing capabilities and the model of the de-embossing stage. Their main business was the creation of display devices on polymer films; with the objective of providing a 'rollable' display format. An image of one of their devices is shown in Figure 5.1. The initial task was to evaluate whether the EngD research could reveal the patent validity and continue with the previous research achieved during the first Innos-supervised phase of the EngD. This was of some considerable interest to Polymer Vision. However, it was decided that there were greater benefits for the company by directing the research onto another form of material processing knowledge, which had hitherto not received appropriate attention within the company. In the second part of this thesis, the research undertaken was to develop an understanding of creasing and develop design guidelines to reduce or eliminate their effect on the displays.



Figure 5.1: 'Readius' by Polymer Vision, using a display made on a rollable plastic film, enabling the screen size to be larger than the device body.

5.1 POLYMER VISION

Polymer Vision engineers devices with a rollable screen. This is achieved by patterning the electronics that control the display onto a flexible plastic sheet. Over this, a display layer is mounted; the pixels in this layer are controlled by the underlying active matrix of thin film

transistors (TFTs). The entire 'stack' (the collective thickness of the layers), which makes up the display is less than 1 mm thick, enabling the display to be flexible and allowing bending and rolling.

5.1.1 Market potential

With the advancement of mobile phone technologies, telecommunication companies are constantly looking for ways to increase the volume of data sent through their systems. Their current goal is to send high quality visual media to portable devices, thereby maximising the usage of their communication networks and increasing their revenue stream. Currently screens on mobile phones are made on glass or some other rigid substrate. This limits the size of the screen for portable devices, which tend to be small. These devices need to be ergonomically efficient to increase their usability and portability. With the creation of a screen that can be stored in a smaller volume and 'unpacked' to allow for a better visual experience, a display device can be created that is both ergonomic in the way it is used and compact enough to be easily transportable. The type of innovation being offered produces a screen of sufficient size to enhance the visual experience. The market for potential devices is therefore enormous (based on the current mobile phone statistics), with other markets also emerging such as for electronic readers (e-readers). The first generation has recently been launched and are typically devices that store text and still graphics. Currently Polymer Vision is leading rollable display technology and looks to be first to market with RadiusTM.

5.1.2 Device issues

Polymer Vision uses a polyethylene naphthalate (PEN) sheet as the backplane for their displays. The PEN layer is only 25 μm thick, making it susceptible to damage through crinkling with only minimal contact. Crinkles (creases/wrinkles) in the film can cause significant strain, which can damage the stack and damage the electronics, causing pixel and/or line defects in the display. This may even result in the entire screen ceasing to work. The crinkles cause the gold address lines or circuitry to break, which in turn short-circuit the device.

Efforts have been made to reduce the amount of human contact with the device during production. However, the manufacturing process cannot as yet be engineered for full automation.

5.1.3 Research aims

The aim of the research is to study the formation of crinkles in the devices formed during their manufacture. This work looks to provide an understanding into why some crinkles cause

failure while others do not. The outcome is to realise what are the major variables that cause crinkling to be a failure mechanism of the device, so guidelines can be formed to prevent them or considerably reduce their detrimental effect. Understanding why crinkles form will also help to advance future designs, to limit their occurrence and reduce the incidence of defective devices.

The following sections will examine creasing. An understanding of the physical mechanism will be developed, followed by a literature review of the process, which will look at some of the theories and work relating applied strain to crinkling. The experiments and modelling undertaken will be explained and then followed by analyses and results. These will then be discussed and a conclusion from the results will be drawn.

5.2 BACKGROUND RESEARCH

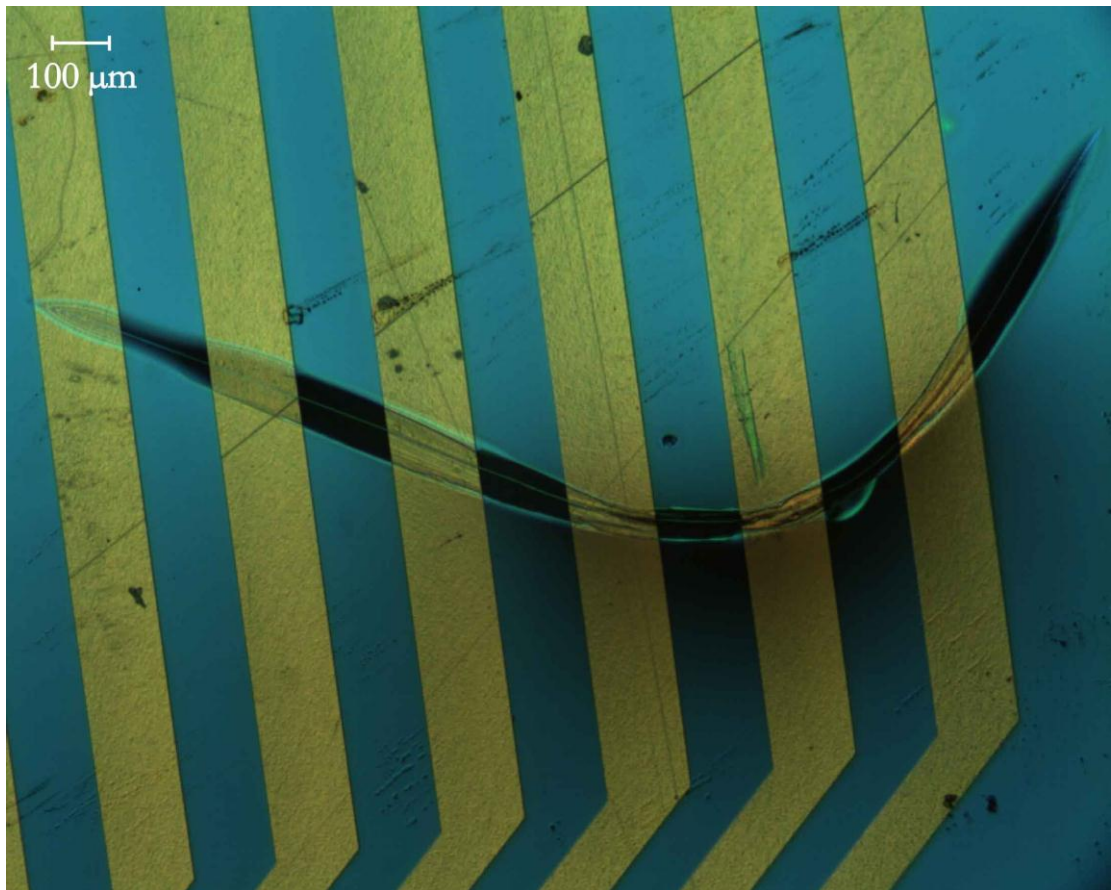


Figure 5.2: Five times magnification of a crease tip in patterned PEN viewed through three filters.

Creasing is the formation of a line or ridge by folding, pressing or crushing. This study will look specifically at the case of the surface being a thin sheet. In such materials, creases are easy to produce. Such an example can be achieved using an A4 sheet of paper. By taking the corner of a flat piece of paper between thumb, index and middle finger and pressing the thumb to travel between the two fingers, one can create a crease. Such a process was used on PEN

material that has been patterned with gold (Au) lines and viewed under a microscope. The tip of the crease formed is shown in Figure 5.2.

The crease can be seen to cut across multiple Au data lines (yellow). Due to the strains on the material, the crease tip formed a dip, whose cross-section looks like a valley, caused by the bending and stretching of the material (this will be discussed later). On closer inspection of the gold lines, it can be seen that such a crease has caused the complete fracture of the patterned Au circuit lines, an example of such a case is shown in Figure 5.3 and Figure 5.4.

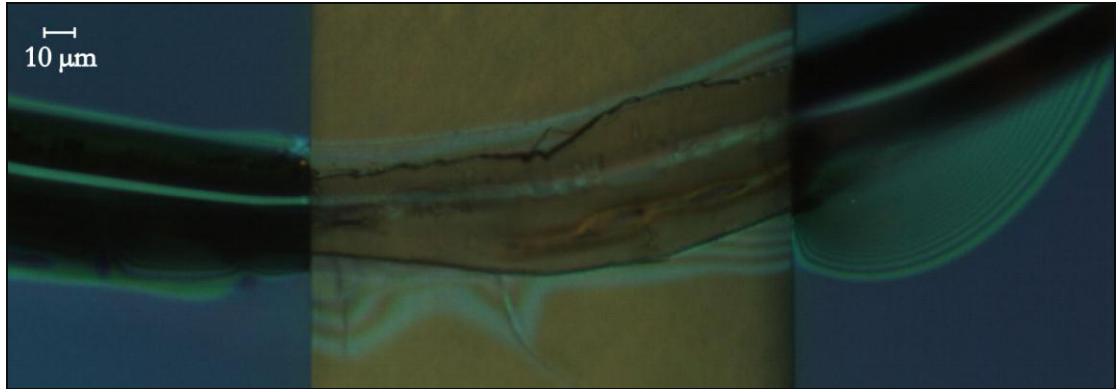


Figure 5.3: Twenty times magnification of the fifth Au line in Figure 5.2. Fibrous edge of the fractured line can be clearly seen, imaged through three filters.

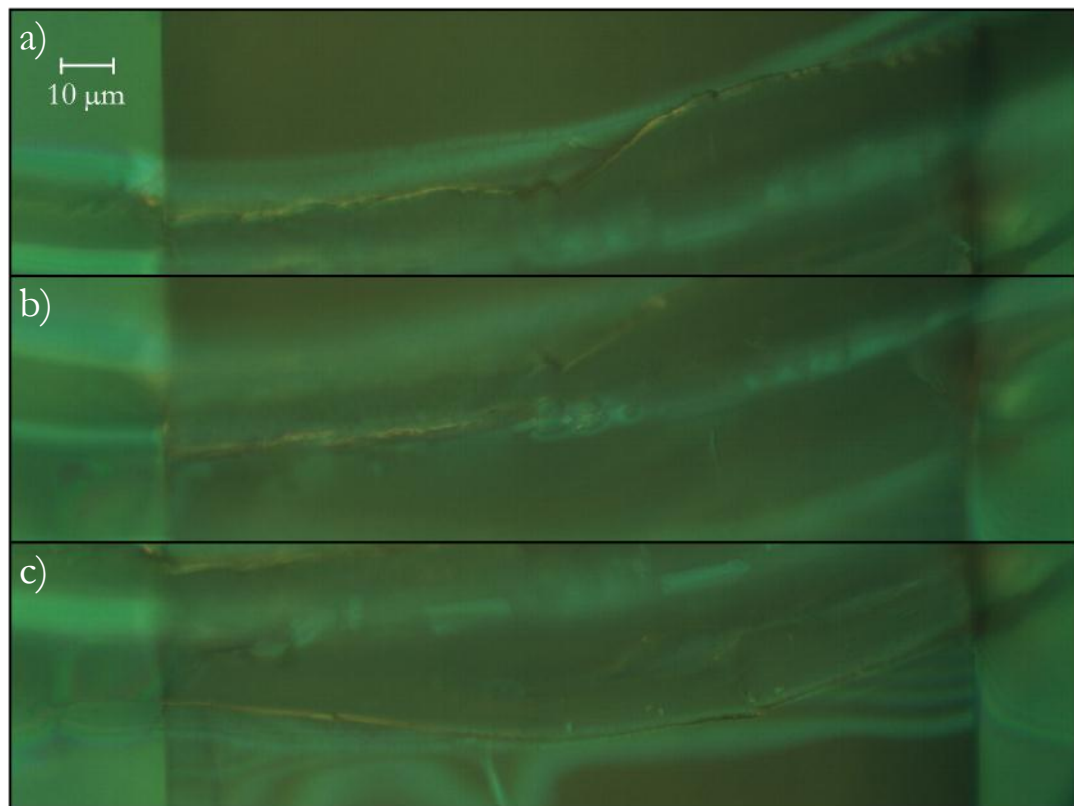


Figure 5.4: Fifty times magnification of the fifth Au line in Figure 5.2; a) Fracture along the top edge in focus; b) Partial fracture along the trough in focus; c) Fracture along the bottom edge in focus.

Both show a magnified image of the fifth Au address line from the left hand side of Figure 5.2. Three fractures have occurred to the circuit line: one either side of the crease and a third in the trough of the valley. This is in agreement with the notion that the fracture will occur at the locations of greatest strain. As the material is initially flat, to form a ‘valley’, large strains must occur at the points of greatest curvature: at the base of the crease and where the crease meets the sheet. The analysis confirmed that a crease is the formation of a ‘puckered’ region in the material, which proves to be destructive for the Polymer Vision device.

5.3 LITERATURE REVIEW

Crumpling, buckling and cracking in a thin sheet occurs as a means for it to achieve its lowest energy state. The analysis of this deformation is not straight forward as it is not only structural but dynamic in nature, needing the mathematics of differential geometry to describe the phenomenon [130]. A brief outline of the underpinning geometrical theory will be given followed by a literature review into the modelling of crease formation. Work on creases will then be reviewed, with the focus directed to the processes, which cause the characteristic crescent shapes to appear in the PEN sheets.

5.3.1 Theorema Egregium

In 1825 Gauss first published his ‘General Investigations of Curved Surfaces’ [131]. Within which, he wrote his ‘remarkable theorem’:

‘If a curved surface is developed upon any other surface whatever, the measure of curvature in each point remains unchanged.’

A result of this theory is that the Gaussian curvature of a surface can be found by measuring lengths and angles on the surface; no further reference is needed to describe how the surface is located in ambient 3D Euclidean space. It is an intrinsic invariant of the surface and therefore never changes under isometric deformations. At a point on a surface, the Gaussian curvature is the product of the principal curvatures of that given point. Developable surfaces are those that have at least one of these two curvatures to be zero. Figure 5.5 shows illustrations of varying Gaussian curvatures.

In three dimensions, the principal curvatures are the maximum and minimum curvatures of the plane curves, which can be found by intersecting surfaces with planes, normal to the tangent plane at that point. The curvature is taken to be positive if the curve turns in the same direction as the surface's chosen normal, otherwise it is negative. Hence for a sphere, in which the principal curvatures both turn in the positive direction at any point on the surface, the Gaussian curvature is positive. Similarly, it is negative for a hyperboloid. For a cylinder, cone

or flat sheet the Gaussian curvature is zero, as at least one of the principal curvatures is zero, making these shapes developable surfaces².

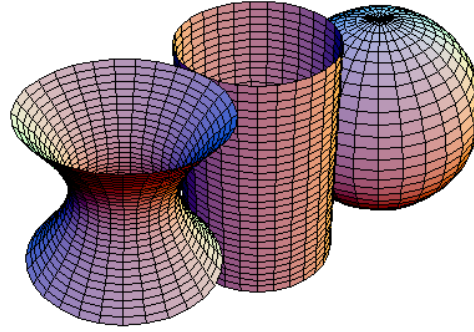


Figure 5.5: A hyperboloid's surface has a negative Gaussian curvature, a cylinder's surface has zero Gaussian curvature and a sphere's surface has a positive Gaussian curvature.

Corollary to Gauss' Theorema Egregium: a surface displaying Gaussian curvature cannot be turned into a surface with a differing Gaussian curvature without crumpling e.g. a flat piece of paper can be turned into a cylinder, as their Gaussian curvatures are the same, but it cannot be turned into a sphere without crumpling. Mathematically, a plane and sphere are not isometric.

5.3.2 Deformation of thin sheets

Deformations that change the Gaussian curvature cannot be isometric. For a thin, isotropic, homogeneous flat sheet there are two primary forms of deformation:

1. stretching in the plane and
2. bending out of the plane.

Both produce strains that are related to the thickness of the sheet. The total energy for the elastic parts is in the order of

$$\text{energy} = b^3 (\text{bending}) + b (\text{stretching}), \quad 5.1$$

where: b is the sheet thickness. This equation was suggested by Rayleigh [132] in 1922 and in effect states that it is energetically favourable to bend rather than stretch a thin sheet.

Deformations can occur by a variety of mechanisms. Bending forces a sheet into a circular arc, such as a cylinder, preserving the middle surface of the sheet, where the straining elements are away from the middle surface. This isometric transformation does not change the Gaussian

² Another way to discover the Gaussian curvature is to cast a shadow with a triangle onto the shape in question (creating a geodesic triangle on the surface). On a sphere, the sum of the internal angles of the cast shadow's triangle will exceed π , making it a positive Gaussian curvature. When the sum of the angles is less than π , it will have a negative Gaussian curvature, whilst if the sum of the angles is exactly π , the Gaussian curvature is zero.

curvature; it remains invariant. Buckling is the instability that arises in compliant structures under compressive loading. Euler presented his solution for buckling [133], suggesting that for long slender members, the geometric properties and therefore their stiffness, which resists axial torsion and deformation through bending, are functions of only their length. Buckling does not necessarily change the Gaussian curvature as it may just cause bending. However, excessive buckling, when the object is unable to bend any further to accommodate deformation, may change it non-isometrically. This has the potential to cause creasing, which is the formation of a ridge in a flat sheet by folding, pressing or crushing. Crumpling is the act of crushing, causing an item such as a sheet to become creased and wrinkled by the processes explained above.

When physical constraints are applied that are not isometric, such as pinning the sheet whilst applying a pressure e.g. holding a piece of paper between the fingers and pressing firmly with the thumb, deformations are created that change the Gaussian curvature, also causing the elastic sheet to stretch. As this is energetically unfavourable, the sheet instead crumples; accommodating the energy of deformation by bending in one direction almost universally. However, the constraint of crumpling: confining the sheet into a smaller volume, means the sheet must deform by stretching in small regions, giving rise to peaks and ridges, where deformation is highly localised [134]. It is these peaks that can be seen to occur in the thin PEN material that Polymer Vision use in the production of their devices.

5.3.3 Energy focusing

The sharp structure of ridges and creases formed when crumpling a thin sheet is a form of energy focusing [135]. The first quantitative research on a crumpled structure came from Euler [136], whose analysis of buckling produced the first critical values in considering bending and compression of struts. However, it gave no information on stress focusing. The formal basis for understanding strongly deformed membranes came from Föppl and von Karman (FvK) in their equations [137], which have a variation structure so the stationary solutions minimize an ‘energy’ functional. The nonlinear coupling of the FvK equations are able to describe the buckling out of plane of an elastic plate and often lead to buckling events, which are localised and give rise to the gathering of energy in a small region. Witten and Li [138] demonstrated a scaling law for the asymptotic limit in thin sheets, showing that energy is concentrated principally in lines joining adjacent vertex points of maximal curvature. Kergosien [139] studied the formation of creases and created simulation software that described the onset of creases, avoiding the analysis of the tip by creating an algorithm to choose between two types of applicable surfaces. However, it was Ben Amar and Pomeau [140]

who first studied individual vertices in detail, to create elasticity equations to describe parts of the developable cone that is formed. They showed that by solving the FvK equations to find the minimum elastic energy of a bent plate, the solution is not always a smooth surface but can be a developable surface, up to a small flexural part. This they called a developable cone, which is a surface that satisfies Gauss' 'Theorema Egregium' in almost all situations except at the tip of the cone. Here, what should be zero Gaussian curvature for a developable surface, strictly speaking, takes on 'finite values'. A region of high curvature exists, whose size is dependent on the thickness of the sheet. The stress focusing at this singularity causes – in most practical applications – the yield limit of the elastic material to be exceeded, causing plasticity or fracture in materials, creating a permanent scar.

5.3.4 Developable cones

A developable cone (d-cone) is a special form of a developable surface. This can be created from a plane without changing distances. It has a zero Gaussian curvature everywhere, except at the tip [141]. Its shape is isometric to the plane almost everywhere, enabling it to be made by bending a flat sheet with the stretching only occurring at the tip. Figure 5.6 and Figure 5.7 show a d-cone created in paper from above and below. However, this is not sufficient to specify a d-cone uniquely as further boundary conditions are needed to enforce the constraint of bending deformation only occurring away from the tip [142].

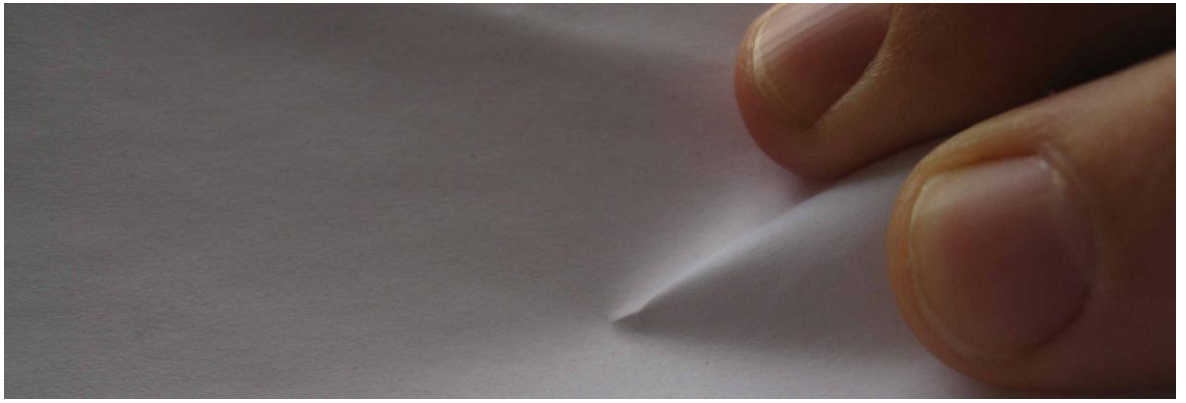


Figure 5.6: D-cone from above, pinching paper between thumb and two fingers.



Figure 5.7: D-cone from below, pinching paper between thumb and two fingers.

First researched by Amar and Pomeau [140], a great deal of interest has ensued in characterising and describing d-cones mathematically. The first published work to follow was by Cerda and Mahadevan [142], who produced an analytical solution for the universal shape of a d-cone, which enabled characterisation of the singularity far from the tip. They verified the solution experimentally and went further to produce a scaling relation for the size of the region where the Gaussian curvature is not zero (the crescent singularity). Further research by them highlighted that the initial stages of crumpling, in which a large amount of deformation occurs, is dominated solely by bending strain energy. They analysed a d-cone formed by pushing a sheet transversely through a cylindrical frame, shown in Figure 5.8. The image sequence shows the fine point on a compass arm being pushed down into a cup. The sheet finds it ‘energetically favourable’ to bend instead of stretch causing a segment of the circular sheet to ‘pop’ up and, excluding the small localised region near the point of the compass (the crescent singularity), enables the sheet to accommodate the displacement of the centre and the deformation of the sheet mainly through bending. This keeps the sheet isometric and without changing the Gaussian curvature (again, apart from at the crescent singularity). When pushed above a critical load, Cerda and Mahadevan found the sheet to be dynamically unstable [143]. Such a form was studied experimentally and numerically, providing geometric data for the formation of d-cones [134].

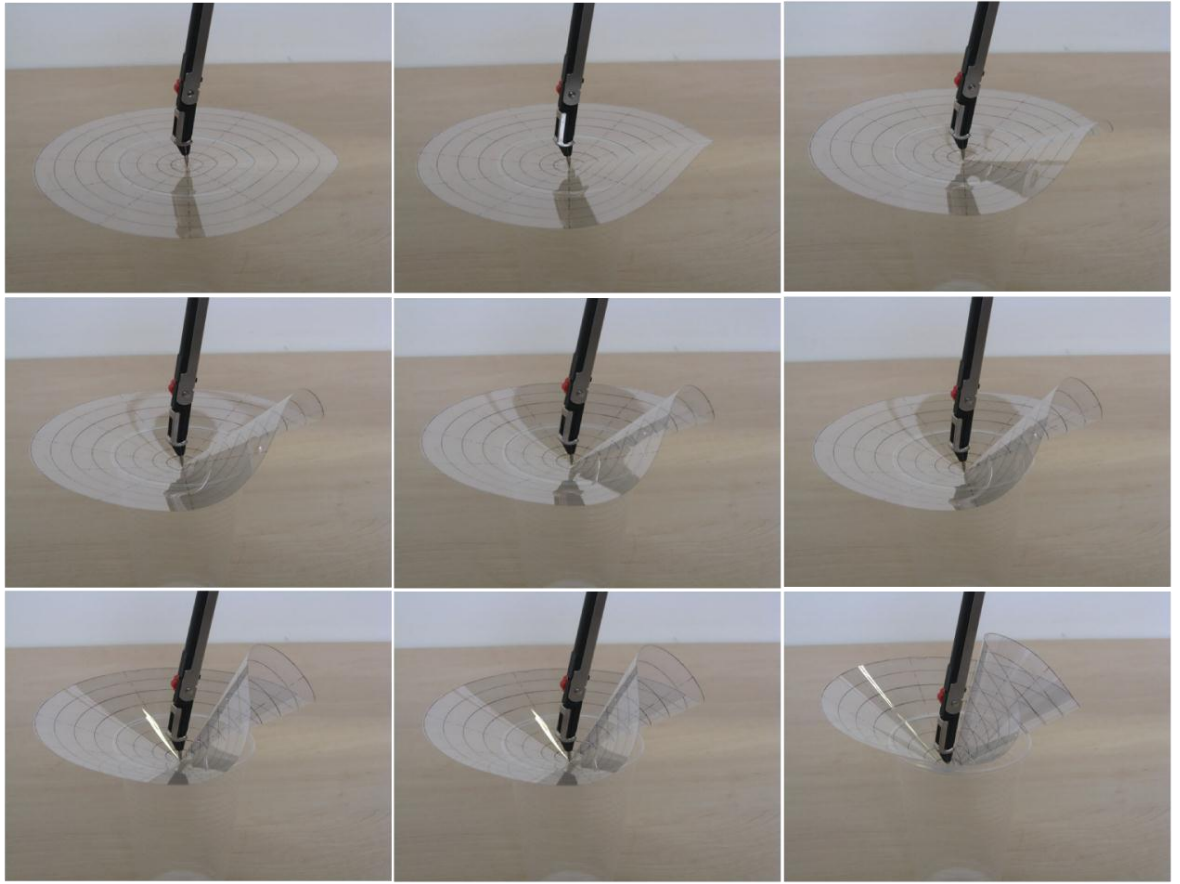


Figure 5.8: Static sequence showing the formation of a developable cone.

Chaïeb and Melo have also studied the formation of a d-cone experimentally [141, 144]. Their set-up provided force feedback for the onset of a developable cone. A profilometer was also used to measure the cone shape. They found for real sheets that the aperture angle of the d-cone depends on the frame, that the crescent curvature has two regimes: a parabolic form for small deformations with a singularity size in the order of the frame radius and a hyperbolic form at high deformations, whose singularity is confined to a small region about the tip. From this they were able to calculate the energy to form the scar: the *singularity energy*, but did not study the crescent singularity formation in any detail.

A differing approach has been taken by Farmer and Calladine [145] to study the geometrical features of a d-cone. In their model, they replaced the crease with an idealised ‘sharp’ crease. Instead of becoming diffuse near the periphery, their prescribed crease had two radial lines. The deformed shape created then consists of two cones to enable easier analysis of a d-cone. Using the model they found geometric relationships using Gauss’ theorems on in-extensional deformation for large rotations, which fit well with geometric relations found experimentally.

Liang and Witten [146] published work looking at d-cones in a similar geometric configuration to Cerda and Mahadevan. They found through testing and geometrical measurements that they agreed with the scaling force of the core region. However, they were unable to justify the

arguments leading to their prediction. They discovered that a d-cone produced without an applied force at the core demonstrates a different scaling behaviour, while the mean curvature of a d-cone obeys an unanticipated constraint, vanishing at the container edge for a wide range of shapes.

Other work has been published on localised geometrical defects and their effects on crumpling, buckling and ridges. These works have used the d-cone research to look at other affects. Balankin *et al.* [147] looked at the roughness of crumpling thin sheets into balls, Das *et al.* [148] studied the formation of singularities in cylindrical elastic shells, Guven and Muller [149] presented a framework to describe the patterns of a folded sheet of paper, while DiDonna [150] looked at the buckling transition of ridges in thin sheets.

5.4 D-CONE FINITE ELEMENT ANALYSIS

The literature research showed that the damage caused to the Polymer Vision's devices was through the formation of crescent singularities. It was noted that little numerical modelling has been done on the strains and displacements of d-cones and none that the author is aware of with commercial software packages that Polymer Vision could use. Such modelling work would provide Polymer Vision with the tools to understand what displacements and effects may be applied before a critical strain is reached that causes the device to fail.

The following sections detail the development of a finite element model, to analyse the formation of a developable cone and to predict the strains and displacements produced. For validation, the model was compared with the experimental work published by Cerda and Mahadevan for differing element formations. The chosen element theory and modelling decisions were then applied to a specific geometry relevant to a Polymer Vision's device configuration in Chapter 6. As this model had different boundary conditions, further validation was sought against physical experiments, where strains and displacements have been measured using digital image correlation (DIC) software. Results for both validation steps are presented and discussed.

5.4.1 Numerical software

There are two types of coding widely available within FE software: implicit and explicit coding. Implicit coding is dependent on the calculation of displacement at incremental time steps and requires the time derivatives, which are unknown and need to be calculated. The method is therefore computationally costly but to their advantage, usually unconditionally stable. It is best used to obtain a solution for structures that only have low natural frequencies excited via transient loads [151]. ANSYS finite element (FE) analysis software using implicit

coding and has been used to model and simulate a vast array of engineering applications including fluid mechanics, electromagnetic and solid mechanics problems.

For large deformation problems and high strains, such as the formation of a d-cone, an implicit code is unable to compute the strains and displacements, terminating the analysis early because the deflections are too large. To model such large deformations, an explicit code solver is needed. In explicit code, the displacements at a later timestep are independent of the acceleration. Instead, the method uses historical information consisting of displacements and time derivatives of displacement. Explicit coding is conditionally stable and uses a critical time-step that must not be exceeded. It is computationally less costly than implicit techniques and is most effectively used for model high deformation problems that see wave propagation through structures due to high velocities. In these scenarios, the higher frequency modes must be taken into account [151]. In collaboration with the Livermore Software Technology Corporation (LSTC), LS-DYNA software can be combined with ANSYS and enables ANSYS written code to be translated for an explicit analysis and solved. For a greater control in the post-processing step, explicit modelling can also be edited in LSTC's LS-PREPOST software and implemented directly into the LS-DYNA solver by commands in MS-DOS.

To model the d-cone, similar to that considered by Cerda and Mahadevan, code for an explicit solving procedure was written for ANSYS (with an LS-DYNA licence) in a '.mac' file extension. When executed in ANSYS, the script produced an LS-DYNA solver file; a file with a '.k' extension. The 'run' was then terminated, allowing the '.k' file to be edited manually in a text-editor or in LS-PREPOST, to adjust the set-up and enable collection of displacement and contact pressure information. The newly edited '.k' file was solved using LS-DYNA called from MS-DOS and upon completion, processed in LS-PREPOST software.

5.4.2 Cylindrical rim d-cone

A d-cone created from a sheet pushed into a circular rim by a pointer was modelled using the LS-DYNA solver, with the geometry and constraints put forward by Cerda and Mahadevan. The analysis consisted of a circular sheet's centre being displaced distance d to 0.9 of the rim's radius r , down and through the rim, using a pointer. The opening angle of the d-cone for various depths was measured and compared to values in Figure 3 (a) from [134], to deduce the commercial software's capabilities in modelling the phenomenon.

The rim was constrained in all degrees of freedom; the pointer was constrained to move only in the z -direction, while the sheet had no constraints applied. The sheet was kept in place by contact with the rim on its underside and with the pointer above. Such a model is equivalent

to a pen pushing a sheet into a cup as in Figure 5.8. The code for producing the initial model in ANSYS is shown in Appendix G, the important variables used are listed in Table 5.1.

Table 5.1: Attribute values used for the creation of the ANSYS model.

Attribute	Short form	Value	Attribute	Short form	Value
PEN density	ρ_{pen}	1360 kgm ⁻³	Rim contact inner radius	r_2	30 mm
PEN Young's modulus	E_{pen}	6.3501 GPa	Rim contact outer radius	r_3	40 mm
PEN Poisson's ratio	ν_{pen}	0.435	Mass scaling	mk	-1×10^{-7}
Sheet radius	R	50 mm	Velocity	vel	280 ms ⁻¹
Sheet thickness	b	100 μm	Time	$tval$	0.1 s
Rim radius	r	30 mm	Hourglass coefficient	hg	0.05

5.4.3 ANSYS options

Compared to the PEN material, the rim and pointer are rigid with stiff material properties. Therefore, 'solid elements' were chosen in ANSYS to model these objects. For the FE to work, material properties are needed for all elements. For the rim and pointer, steel properties were used but with a Poisson's ratio of 0, which helps ANSYS to solve quicker. This is an acceptable step to take in FE modelling as all the significant deformation occurs in the PEN.

An element that can cope with high deformations in a thin sheet was needed. As the in-plane and bending strains in the process of crinkling are more important than the through-thickness strain, shell elements were chosen, which only consider the strains and displacements at the surfaces and mid-plane, making them more efficient for modelling thin materials.

The sheet was comprised of explicit thin structural shell elements, named shell163 in ANSYS, as these shells are specifically suited for use in the LS-DYNA solver [152]. It is a 4-node element with bending and membrane capabilities, permitting in-plane and normal loads. At each node the element has 12 degrees of freedom: translations, velocities and accelerations in the x, y and z directions and rotations about these co-ordinates. The material properties of PEN are used for the sheet [153]. The material properties should have little affect on the opening angle based on the analytical equations derived in [134], but are needed for solving in LS-DYNA.

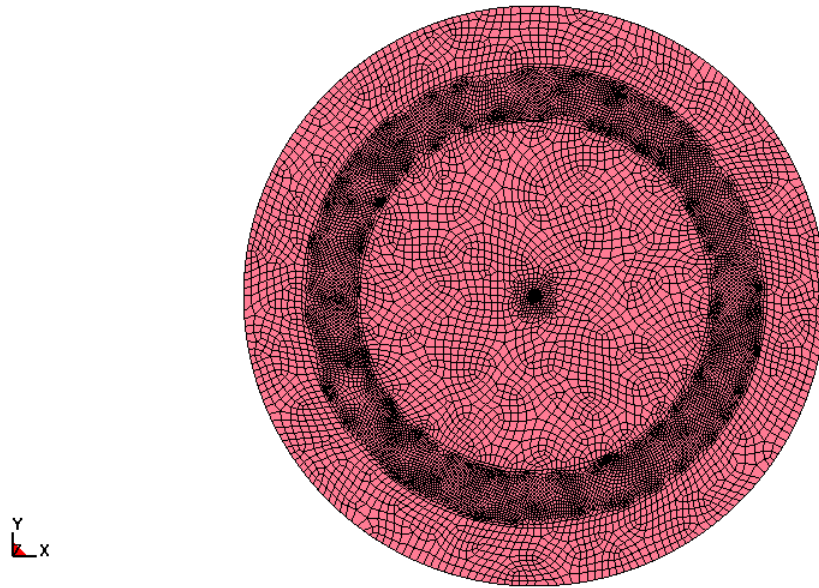


Figure 5.9: Free mesh of sheet employed in ANSYS with mesh refinement in contact regions.

To enable a d-cone to appear, instability needs to be introduced into the sheet. This was achieved using a random mesh pattern, which provided imperfections that cause stress focusing. This was achieved using the free mesh option with quadratic elements in ANSYS, as displayed in Figure 5.9. Varying the divisions of the radial lines used to create the sheet geometry controls the initial size of the sheet mesh. Twelve radial lines arranged as three concentric circles create the sheet: the sheet edge circle and two circles that form the ‘rim contact’ region. Mesh refinement was used in this contact region and at the centre of the sheet where contact occurs with the rim and pointer respectively, to increase modelling accuracy.

Automatic surface to surface (ASTS) contact was employed in the analysis as it allowed contact information to be gathered during the analysis [154]. A frictional coefficient (μ) can be added but Cerda and Mahadevan’s analysis assumed a frictionless contact so μ was omitted. To reduce the central processing unit (CPU) time, mass scaling, which is the addition of nonphysical mass to a structure, was implemented in the solving sequence. This increased the time-step used in the analysis by adjusting elements whose calculated values were smaller than the pre-defined value. This was chosen so that fewer than 100 elements were altered by manually checking these elements using the ANSYS command EDTP. Mass-scaling adds a small amount of mass to the part and slightly alters the centre of gravity. However, by keeping these variations below 10 %, substantial gains in solving times were achieved that outweigh the error introduced [154]. A negative sign informs the software to specify the mass scaling to the smallest 100 elements.

The pointer introduces the displacement to the sheet. A velocity was applied to the pointer for a period of time so that by the end of the analysis, the pointer had displaced by a depth d . To

increase the speed of the analysis, higher velocities were used for shorter time spans. Care has been taken not to use excessive velocities, as these can cause shockwaves and problems in the analysis. In addition, with the analysis in the millimetre length scale, a more convenient set of units was chosen. Instead of using metre, kilogram and/or second (MKS) units, an mMKS system was used, where a millimetre was the length unit, which further helps to reduce the analysis solving time. This altered the Young's modulus in the model by 1×10^{-3} , the density by 1×10^{-9} , the length by 1×10^3 and the velocity by 1×10^3 .

5.4.4 LS-DYNA options

The '.k' LS-DYNA file created from solving in ANSYS LS-DYNA was manually edited in LS-PREPOST. The amendments to the LS-DYNA cards are shown in Table 5.2.

Table 5.2: New values used for LS-DYNA control cards for model set-up.

Card	Variable	Value	Card	Variable	Value
*Contact_Surface_to _Surface	<i>MPR</i>	1	*Control_Accuracy	<i>INN</i>	2
*Contact_Surface_to _Surface	<i>SPR</i>	1	*Control_Bulk_Viscosity	<i>TYPE</i>	-1

Having *MPR* and *SPR* take the value of 1 included the master and slave interface force information from contact in the NCFORC database card. This information was then stored in an interface force file, named 'inter', and used to monitor node contact. This was achieved by writing 's=inter' after the command to invoke the LS-DYNA solver through batch processing, which can be seen in the script file in Appendix H. Changing *INN* to 2 made the results insensitive to the node numbering order in the elements, which may have otherwise caused inaccurate values and high deformations. Assigning *TYPE* the value -1 initiated global bulk viscosity coefficients, which inhibited the shock discontinuities into rapidly varying but continuous transition regions and prevents the internal energy from being computed in the shell elements, which is important when higher velocities are experienced in a dynamic analysis [155]. Discussed below, other LS-DYNA cards were altered that enabled the use of different solving elements.

5.4.5 Solving elements

There are many shell element formations that can be used in LS-DYNA that have different benefits and qualities, depending on the type of analysis being undertaken. The following six element solver set-ups were compared to understand which type was best suited to modelling

the developable cone phenomenon, based on speed, robustness and comparison to the analytical opening angle. These were:

1. Belytschko-Lin-Tsay (BT) element
2. BT element with Belytschko-Wong-Chaing warping stiffness added (BTW)
3. BTW element with full projection added (BTWP)
4. Belytschko-Wong-Chaing element (BWC)
5. Fully integrated shell element (FIS)
6. FIS element with hourglass mode type 8 initiated (FISH).

Two other element theories were considered: selective reduced integration of Hughes-Liu shell elements and the same again using a co-rotational system. However, these fully integrated elements were computationally inefficient and were unable to perform the analysis within an acceptable time frame. The Hughes-Liu element theory was the first shell to be implemented by LS-DYNA, the selective reduced integration rule results in four in-plane points being used, which would increase the operations count by up to three or fourfold, as an extra calculation loop is included to update the stress and force contributions [156].

Each solving element was used in the same geometrical and loading configuration, so they could be compared with the analytical calculations for the variation in a d-cone opening angle. The values to be edited in the LS-DYNA cards are shown in Table 5.3. Subsequently the mesh was used for the configuration relevant to Polymer Vision. The control shell ‘Additional variables’ used were chosen from the recommendations in the LS-DYNA theory manual [156-158].

Table 5.3: LS-DYNA card alterations to implement various shell theories.

Card	Element	Variable	Value	Additional variable
*Control_Shell	BT	Theory	2	
*Control_Shell	BTW	Theory	2	BWC to 1
*Control_Shell	BTWP	Theory	2	BWC to 1, PROJ to 1
*Control_Shell	BWC	Theory	10	
*Control_Shell	FIS	Theory	16	
*Control_Shell	FISH	Theory	16	*Hourglass: IHQ to 8

The default shell element in LS-DYNA for explicit problems is the BT shell [157]. These are documented to be the fastest type available in the solver. There are additions that can be made to the BT element solver and other element solvers that may capture the analysis with more

detail or a higher accuracy, but come with the cost of longer solving times. BT is based on a perfectly flat geometry without considering warping. Incorrect results may occur through twisting, as the nodal points of the elements used in discretization are not coplanar [157]. BTW uses the BT element and includes shell warping stiffness from Belytschko-Wong-Chiang shells, calculated using the drill projection; a 7-mode projection matrix with three rigid body rotation modes and four nodal drill rotation modes, while BTWP uses full projection instead of drill projection. The benefit of drill projection is that it is very efficient, hardly increasing processing times. However, a loss of invariance to rigid body motion can occur when elements are highly warped making the element inaccurate, even though they are more flexible by the 1-point quadrature shell element [155]. It is recommended not to use the drill projection in impact analysis as elements with little or no warping in the reference configuration can become highly warped in the deformed configuration. Belytschko and Leviathan reported that the cost increase of drill projection is 7 % in LS-DYNA, while full projection is closer to 50 % [155]. BWC uses a similar shell to BT but with an improved transverse shear treatment, necessary for the shell to pass the patch test³ [159].

The 5th and 6th elements in the list are all fully integrated. FIS is similar to BT but with co-rotational stress updates. It uses strain interpolation, helping to alleviate rigid ‘locking’ of the mesh and enhance in-plane bending behaviour. By updating the local element coordinate system that rotates with the material, it accounts for rigid body motion, while automatically satisfying frame invariance of the constitutive equations [158]. FISH is the same element as FIS, but with full projection warping stiffness included, producing results with greater accuracy but a time penalty of up to 25 % on FIS [160].

³ The patch test provides an indication of the quality of an element used. It uses a partial differential equation in a scenario where the exact solution is known. To pass the patch test, the finite element solution must produce the same values as the exact solution.

5.4.6 Opening angle measurement method

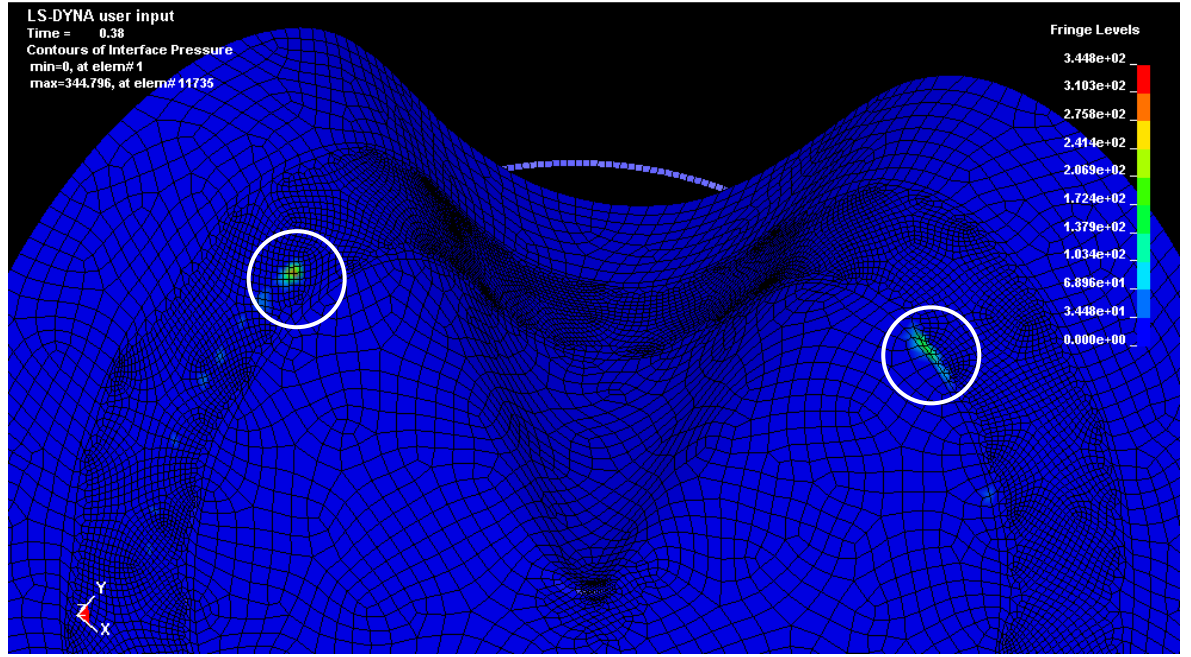


Figure 5.10: Interface pressures show sheet contact with rim providing d-cone location and size.

Interface force files for each analysis of the six elements have been used to monitor the opening angle of the d-cone. The regions of higher contact pressure on the rim that match up to the d-cone of the sheet provide knowledge of where the d-cone contacts the rim, as shown in Figure 5.10. This distance can then be measured using the ‘Measure’ option in LS-PREPOST, as depicted in Figure 5.11. The chord length is related to the opening angle of the d-cone through the re-arrangement of the cosine rule, as an isosceles triangle, which can be produced with the centre of the circular rim. The measurement was performed on the rim rather than the sheet as it was rigid and all distances are known. The opening angle is given by

$$A = \cos^{-1} \left[\frac{(b^2 + c^2 - a^2)}{(2bc)} \right], \quad 5.2$$

where: A is the opening angle opposite the measured chord a , in radians, b and c are the two sides of equal length. The error associated with this measurement was of the order of the rim division value, which has been segmented into 360 elements, making it ± 0.44 mm. Each interface force file held up to 100 increment steps. The opening angle was calculated for every increment for each of the element theories analysed.

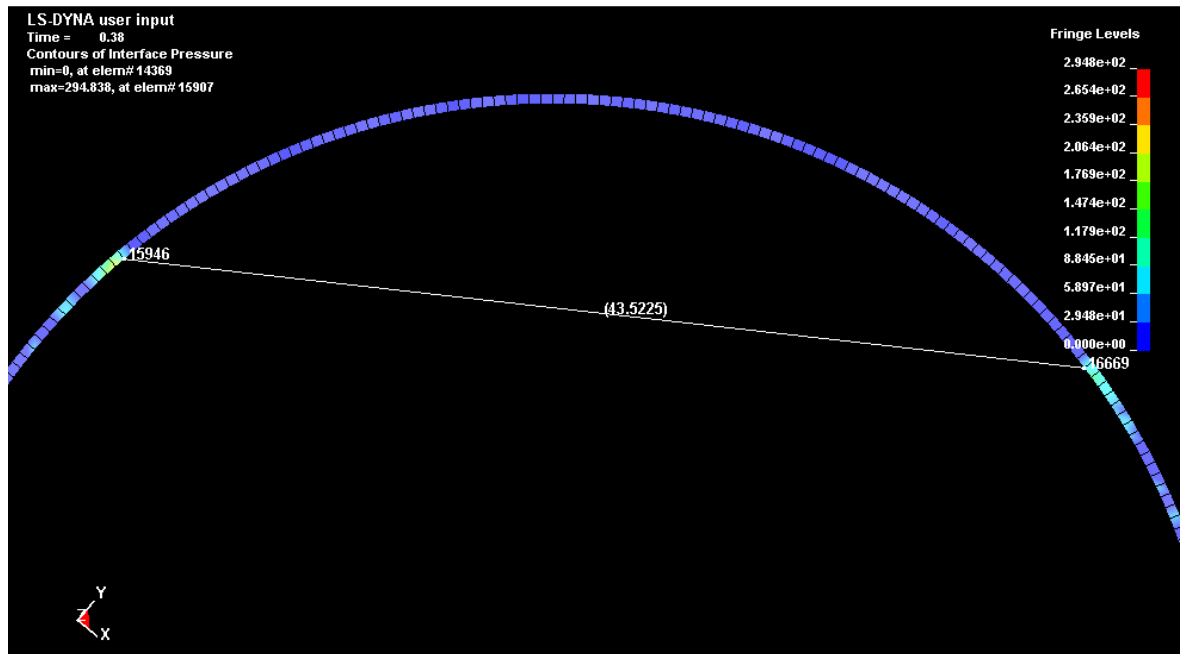


Figure 5.11: Chord measured on the rim at contact points with d-cone.

5.5 D-CONE RESULTS

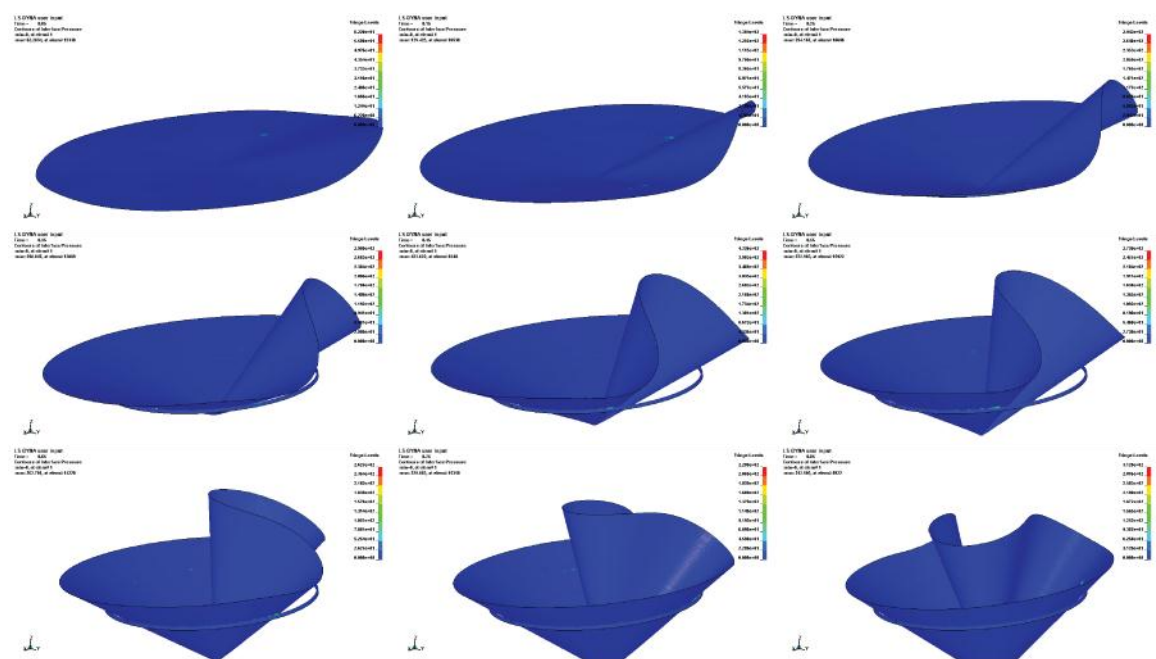


Figure 5.12: D-cone forming for various central displacements, from left to right.

The 6 element formations were viewed in LS-PREPOST. Figure 5.12 shows the development of a cone using BT elements at a z -displacement of $0.05R$ and at increments of 0.1 until $0.85R$, where R was the rim radius. The shape formation of the d-cone was as expected. It can also be seen that the d-cone begins to travel across to the opposing side. The rotation of the mesh on the rim was unexpected and was not reported in Cerda and Mahadevan's work. It is believed to be due to the dynamic nature of the FE modelling, using large velocities and small

time-step values to enable the model to solve in an adequate time. Cerda and Mahadevan predict the d-cone touches the opposing side at $0.97R$ [134]. Each element tested formed a similar developable cone structure.

The six element theories chosen are plotted for speed of analysis in Figure 5.13. All were computed using a Linux 2.6.9 operating system, using dual-processor 64 bit AMD Opteron chips in single precision mode⁴. The BWC and FIS elements failed to complete. It is assumed this is because the elements were unable to model the large deformations imposed by the analysis. To aid comparison of the element performances however, linear extrapolations have been calculated to predict how long they would have taken to complete. The graph highlights that the two fully integrated cases took more CPU time for the analysis.

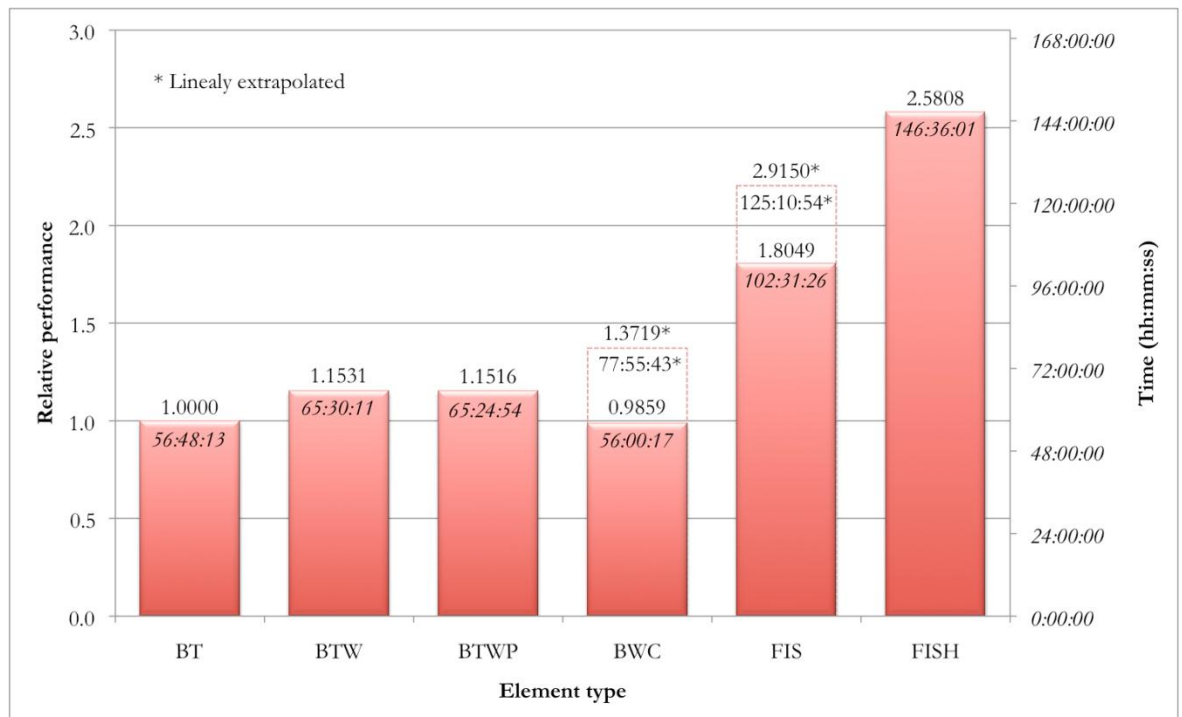


Figure 5.13: Comparison of solving times in LS-DYNA for different element theories used.

The opening angles for each simulation were compared to the analytical opening angle found by Cerda and Mahadevan for various z -displacement values. Cerda and Mahadevan were contacted for the original data to produce their results. However, they were unable to provide the raw data to re-produce their graph. Figure 5.14 shows a copy of the graph published detailing the opening angle as a function of vertical displacement. Only the first and last values can be accurately read from their results as an unknown unit was used on the y-axis. However,

⁴ Single precision mode enables the software to run using only a single processor, such was the licence available at the time of research.

these are the minimum and maximum opening angle values and occur at the beginning and at the end of the application of \tilde{x} -displacement, so a straight line was drawn between them on the graph for ease of comparison. Figure 5.15 displays the opening angles for the 6 element theories. All show a dynamic response, which reduces in amplitude with displacement (this is explained in Section 5.6). For each FEA set, a linear trend line has been added to give an indication of the variation in opening angle, although the response reported by Cerda and Mahadevan was not linear. It can be seen that FIS provides the most similar gradient. However, it has a larger opening angle offset. BTWP and BWC have some of the closest values to those obtained by Cerda and Mahadevan's analytical values, but do not have a similar trend of increasing opening angle.

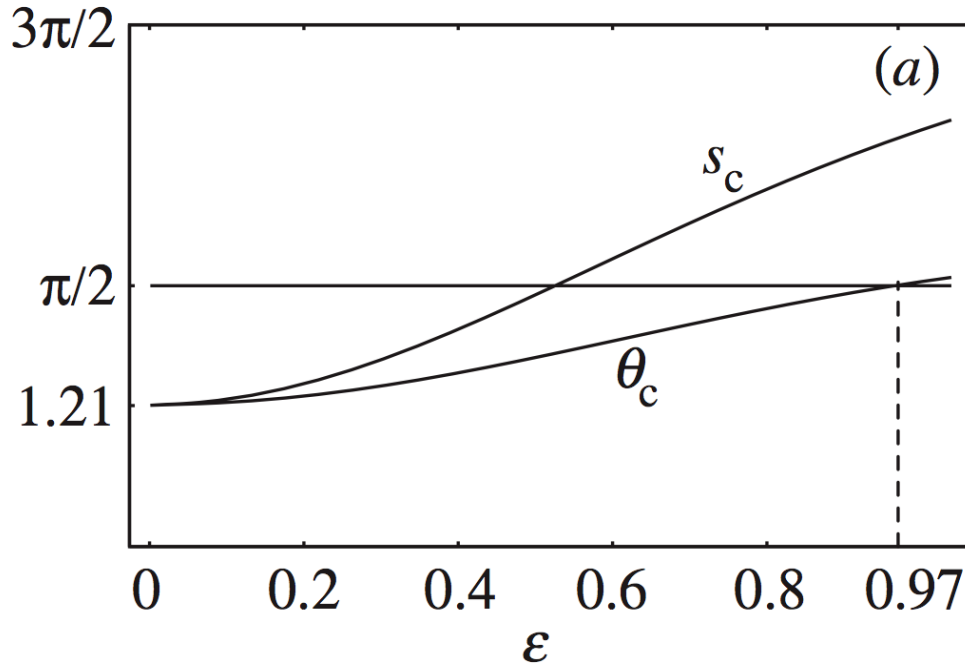


Figure 5.14: Mahadevan and Cerda's published S-curve of numerical values of the contact arc length (s_c) and its projection (θ_c) as a function of the vertical displacement ϵ [134].

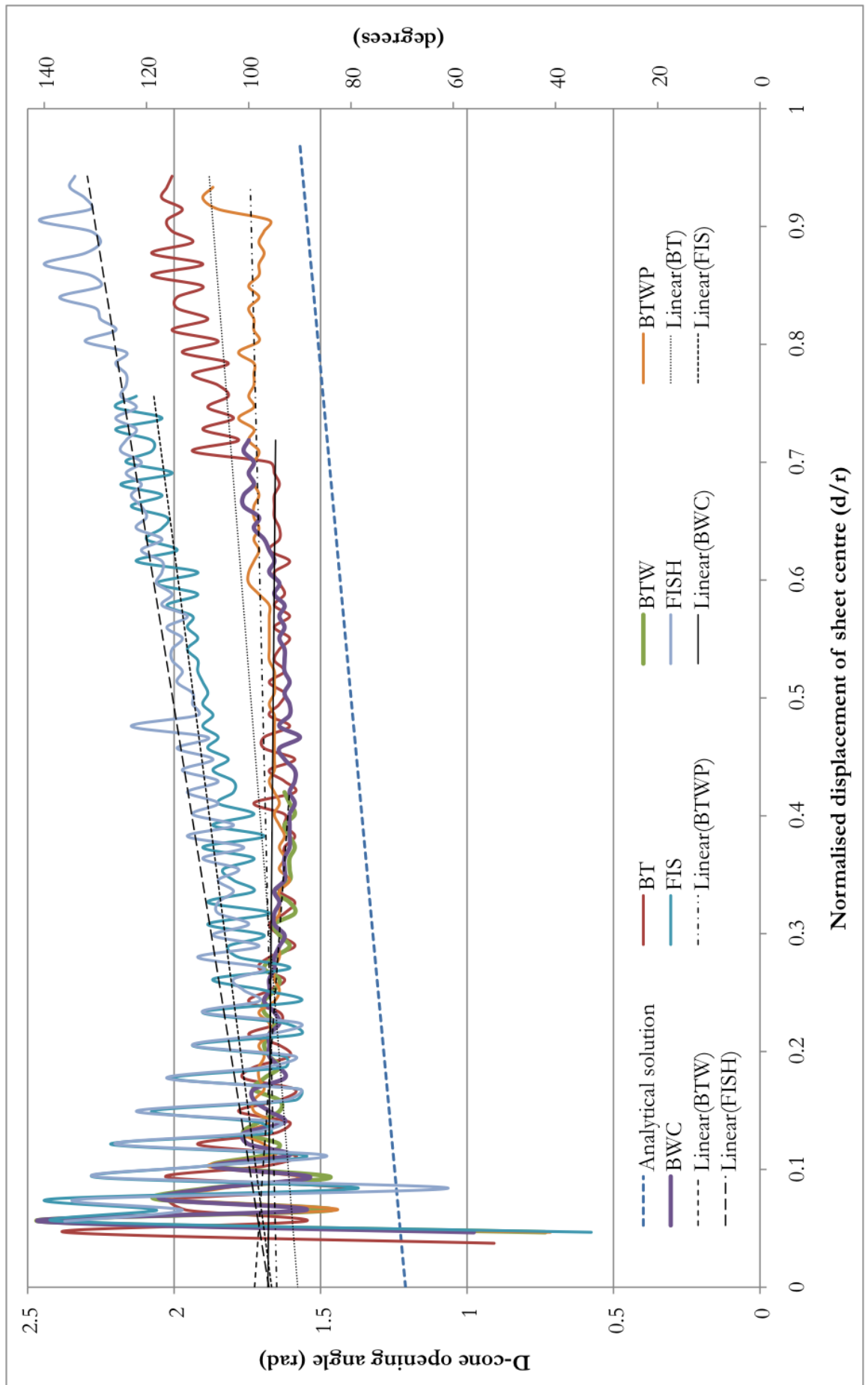


Figure 5.15: Element theory comparison for the creation of a developable cone.

5.6 D-CONE ELEMENT DISCUSSION

The results predict a dynamic, oscillating response for all the elements tested. Although these results are not ideal, they were expected due to the use of high velocities in the model and the resultant high frequencies, which were created by the pointer contacting the sheet. Because of the high deformation of the sheet, implicit elements, which would have avoided the dynamic response, were not considered. One option that would avoid or reduce the dynamic response in the model would be to reduce the speed of the pointer. However, the time-step used between each computation was -1×10^{-7} s, which is based on the formula

$$\Delta t_e = \frac{L_s}{c}, \quad 5.3$$

where: Δt_e is the time-step, L_s is the characteristic length and c is the speed of sound within the material. As the speed of sound was set by the PEN material constants, the only way to increase the time-step⁵ would be to increase the element size. Larger element sizes perform poorly and were observed to crash due to the high deformation in the sheet, while small elements resulted in a smaller time-step. Mass scaling has been used to increase the time-step as explained in Section 5.4.3 to speed up the analysis. It was decided, in light of the complications discovered, the current configuration would be used, even though a dynamic response was produced, as the analysis should be thorough but not too intensive on computer resources. A linear trend-line was therefore included to help display the general variation of the opening cone angle.

5.6.1 Element choice

The original analysis by Cerda and Mahadevan showed a variation of opening angle more similar to a faint s-curve than a linear response. However, without valid data, the curve data cannot be compared directly. Choosing the element theory based on the trend-line angle does not guarantee the closest fit. The element choice was therefore made with greater weighting on the element robustness and solving time, which can be accurately compared. Based on the information collected from the research, the Belytschko-Lin-Tsay (BT) element will be used for the remainder of the work.

⁵ The negative sign specifies that density is added to the 100 smallest elements. The absolute value is being referred to when increasing or decreasing the size of the time-step.

CHAPTER 6: DEVELOPABLE CONE FORMATION

The aim of the research is to understand how picking up a thin sheet manually, using two fingers and a thumb in a ‘pincer’ motion can cause damage, as observed in Polymer Vision’s displays, during manufacturing. Modelling the way in which two fingers and a thumb create a d-cone in a sheet introduces an array of variables such as the width between the fingers, their diameters and the dimensions of the sheet's geometry being affected. A specific configuration was chosen that would allow many of these variables to be tested. The Polymer Vision display is made such that the screen is bonded to the centre of a PEN sheet, creating a region of greater thickness, stiffening the structure. The critical areas are therefore the regions surrounding the screen on the thinner PEN material, which experience larger strains. An experiment that analyses the effects seen in these critical areas was devised. A rectangular sheet was used, with one fixed edge and a three-point bending mechanism applied to the opposite side, as illustrated in Figure 6.1. In addition to the physical experiment, a Finite Element (FE) model was created to aid in the validation of the experimental setup, with the aim of establishing a design methodology based on FE modelling.

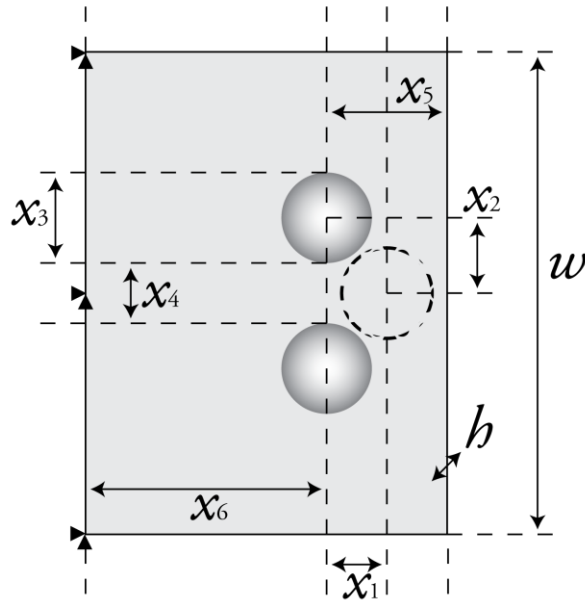


Figure 6.1: Variables for the three-point bending set-up, consisting of a thin sheet clamped on one side.

The potential test variables are illustrated in Figure 6.1. The values used are listed in Table 6.1. The fixed edge acts in a similar manner to the thickened region and stiffens the sheet. This edge is clamped in the experiments. The three-point bending arrangement mimics the manner in which fingers are used to pick up the sheet, causing bending, and how this causes stiffening. The experiment consists of two hemispherical loading prongs being lowered from above, normal to the sheet, simulating the fingers. Below is a single hemispherical support at the

same height as the clamped edge, which mimics the thumb. It is offset behind the two upper hemispheres as a thumb is in relation to the fingers when picking up a sheet. This particular configuration is used so that the resulting d-cone formed in the sheet can be seen from above enabling measurements to be taken.

In an experimental set-up, all the variables listed in Figure 6.1 can be varied, with the prongs being interchangeable with other prongs of other diameters. It was decided that the most important parameters for initial testing were the sheet thickness b and the offset between the fixed edge to the centres of the closest hemispheres x_6 . The other variables were to remain constant, based on the anthropometrics of the hands and the device configuration.

Table 6.1: Variables used for d-cone analysis on a clamped sheet.

Variable	Value	Variable	Value
x_1	10 mm	x_5	20 mm
x_2	17.5 mm	x_6	20, 30, 40, 50 mm
x_3	20 mm	b	25, 50, 125 μm
x_4	15 mm	w	100 mm

The three thickness variables were predetermined by the PEN sheet thicknesses that Polymer Vision were able to supply, while x_6 was chosen because it allowed the analysis to determine how the stiffening along the display affected the outer regions.

6.1 PHYSICAL EXPERIMENTAL COMPARISON

The work needs to capture the strain and displacement data at the position where a d-cone will form. Using a resistance strain gauge was considered but rejected, as its thickness would stiffen the thin PEN sheets, thereby invalidating the measurement, whilst the solvent might have also affected the properties of the PEN. Digital image correlation (DIC) was chosen as the optimum technique available to measure the strains and the three dimensional movement of the sheet.

A test rig using a jig and an Instron ePULS tensile testing machine was used, as shown in Figure 6.2. The jig clamped one end of a PEN sheet, while the other side rested on a hemispherical plunger attached directly to the testing machine cross-head. This enabled an adapted three-point bend test; with the two offset plungers applying force from above. Appendix I shows the design drawings for the creation of the jig, which can be altered to test for the different variables in Table 6.1.

The Instron testing machine with Bluehill software was used to apply a fixed displacement to the prongs. From the sheet surface, they displaced downwards by up to 10 mm. During this process, DIC was used to capture sheet movement and distortion. A light source was needed to increase the camera aperture and provide a greater depth of field. This needed to be placed as far away as possible to make the light more diffuse and to reduce glare. Another anti-glare measure was to paint the arms of the prongs black. The hemispherical ends of the prongs were not painted. This is because a smooth surface enables a better comparison between tests; a painted surface increases the frictional contact and might have an inconsistent stick/slip relationship with the PEN patterned sheet, which would have hindered any comparison and affected the d-cone formation.

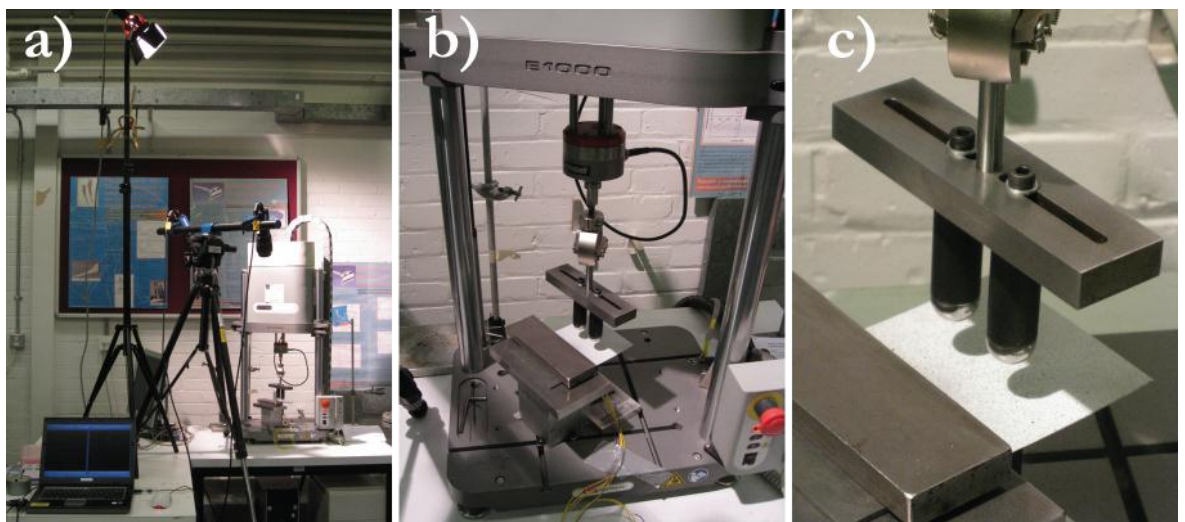


Figure 6.2: (a) Test set-up (b) Instron set-up (c) Jig used for physical d-cone experiment.

6.1.1 Digital image correlation set-up

DIC uses numerical algorithms to track the speckle pattern movement. Using one camera, 2D information regarding displacements and strains can be achieved. With two cameras, a 3D representation of deformation and strain can be recorded. The cameras needed to be placed equidistant from a sample at an angle to one another, as depicted in Figure 6.3. Ideally, an angle of 30° should be created with the sample, between the lines of sight of both cameras. Once the cameras have been set-up, they need calibrating to pre-defined standard patterns. This enables the pattern recognition software to calculate the displacements and strains in the sample. The pattern needs to be random, otherwise it is likely for a lot of deformation that the software will mistakenly identify one region as another, causing the technique to fail.

For the experiment, a 3D High Resolution Correlation System, comprising of cameras, connectors, lighting and computer hardware with Vic3D software from Correlated Solutions, supplied by Limess, was obtained from the Engineering and Physical Sciences Research

Council (EPSRC) ‘Engineering Instrument Pool’, which could track speckles larger than 2 – 3 pixels of the camera’s charge coupled device (CCD). The software allowed the user to choose the size of the ‘subset’: the area of the elements being tracked and the ‘step-size’: the spacing between analysed points. In DIC software systems, reducing the subset size leads to greater precision, whereas increasing the subset size improves the accuracy and ability of the program to provide solutions. The subset size needs to be large enough so that a sufficiently distinctive pattern is contained within each area used for correlation. Reducing the step-size increases the overlap between subsets, which increases solution accuracy, however it also extends the analysis time, which varies inversely with the square of the step-size e.g. an analysis using a step-size of 1 pixel takes 25 times longer than a step-size of 5 pixels.

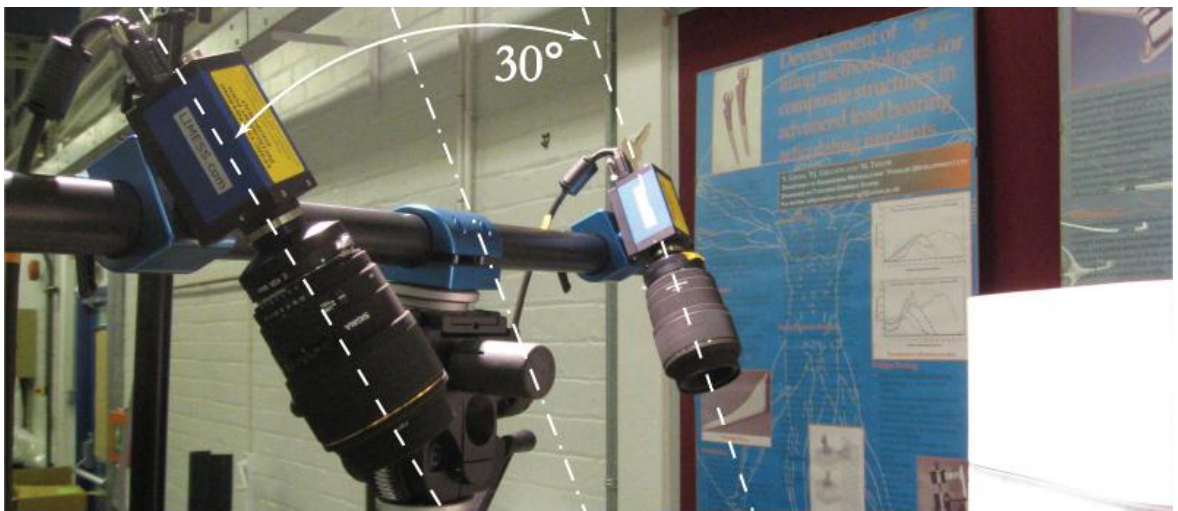


Figure 6.3: DIC camera set-up, with cameras equidistant to the sample and at angles of about 30°.

The capabilities of the Limes system have been compared to an alternative system available in the School of Engineering Sciences and also with strain gauge results on tensile test specimens [3]. Based on these findings and because a small subset is needed to identify the values at the crescent singularity more accurately, a subset of 16×16 pixels with step-size of 4 pixels (an overlap of 25 %) was chosen for processing the d-cone test data.

6.1.2 DIC error measurement

To provide an indication of the DIC system’s accuracy for measuring strain in the speckled PEN material, four constant displacement tensile tests were performed on 10×150 mm strips, using the Limes system to analyse the strain and displacement. The software recorded test data from a small region in the middle of the specimens. The Instron testing machine had the capability of measuring the displacement. However, the testing machine displacement output does not take into consideration the compliance of the system, which prevents a direct measurement comparison. From the four DIC tests, the mean strain and standard deviation

values were calculated. It was seen that the standard deviation value increased with strain. At a mean strain of 10 %, the standard deviation was 0.5 %. However, in the adapted 3-point bend tests, the key areas of interest were in lower strain values of up to 2 %, this is explained later in Section 6.3. Within this strain, the largest error measured was 0.12 %, which will be used as the error associated with the DIC measurements.

6.1.3 DIC speckle pattern

The PEN films being tested are transparent and so need a random speckle pattern to be applied. This was achieved using spray paint. Such a coat adds a considerable thickness to the thin films, which alters their physical properties, especially if two paint tones are used, which would produce a greater contrast but a thicker layer. Instead, a single layer of white paint was used to produce an inconsistent layer of dots of varying sizes. Using a single colour caused less stiffening, as complete coverage was not needed. However, the paint still had a stiffening effect, particularly on the 25 μm thick films.

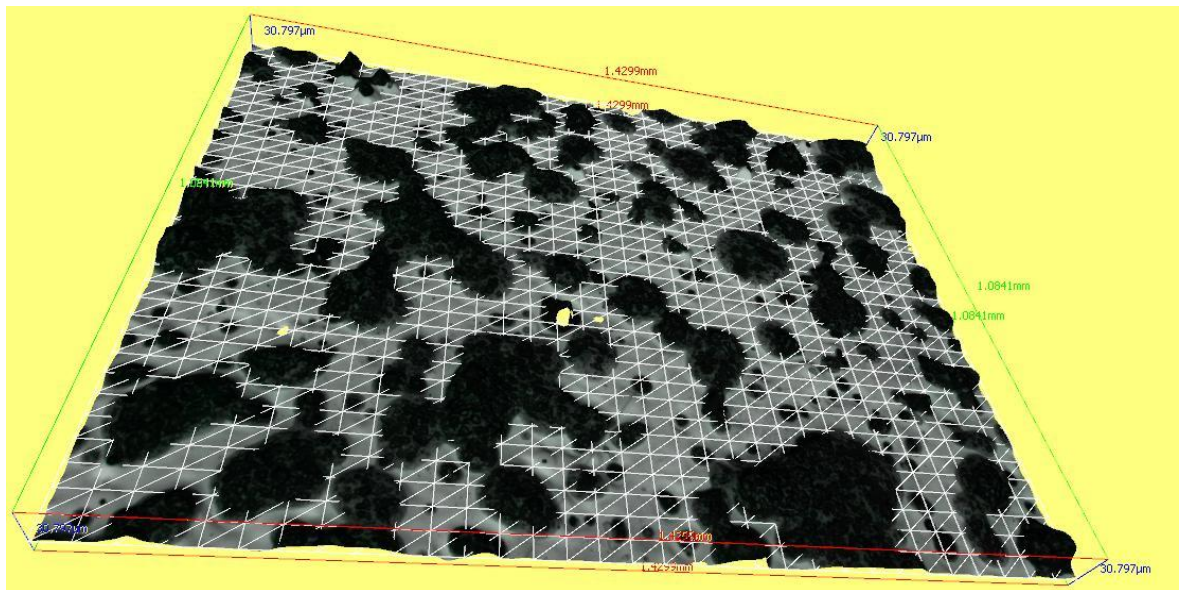


Figure 6.4: Alicona™ image analysis of paint speckles on PEN sheet.

An Alicona™ Infinite Focus surface profileometer was used to gain an estimate of the thickness added by spray painting, by measuring the heights of paint speckles. A high power, white LED coaxial light is used to illuminate a sample. Via a beam splitter, the toolset can measure the surface of a material by interferometry. Figure 6.4 shows the profile of such a test segment. The software was able to record the surface profile of 1.5 mm² regions. A significant error was introduced in the height measurement of the paint speckles due to the wavy surface of the underlying PEN material. The software minimised this by creating a reference plane as a base datum for measuring heights. This is graphically illustrated as a grid

of white triangles. Using two randomly chosen areas, the overall mean height of the areas was $4.20\text{ }\mu\text{m}$, with a standard deviation of $4.81\text{ }\mu\text{m}$ ⁶.

6.1.4 Experimental set-up

The DIC software was set to take photographs every 0.25 s. The Bluehill software was programmed so that the displacement caused by the plungers was 1 mm every second until a total of 10 mm was achieved. This enabled a photograph to be taken for every 0.25 mm of displacement, producing a total of 80 photographs by the two cameras for each test specimen. Increasing the frequency of image capture in the DIC software further would have greatly increased the analysis time. It would have also required additional memory storage: 18 experiments in total were undertaken, which in total produced 1,440 '.tiff' images.

In setting up a test, the plungers were positioned so that they touched the surface of the sheet with as little pressure as possible, making this the base datum for subsequent displacement measurements. At the time of the experiment the tensile testing machine software did not offer a triggering system that could connect to the DIC software. Instead the researcher had to start the Bluehill and Vic3D software manually at the same time.

6.1.5 Digital image correlation analysis

One analysis was undertaken for each configuration of the variables b and x_6 . For an x_6 of 20 mm, three samples were tested for each sheet thickness, so the DIC measurements could be ratified for their consistency. In processing the information, various strain values, including the Von Mises strain (ϵ_{VM}), and out of plane displacements were calculated.

In post-analysis, the software was unfortunately unable to map and follow the speckle patterns automatically. This requires the user to instruct the programme manually to follow triangulated speckles for every pair of images for the analyses. Thereafter the software is able to process the data and produce displacement and strain information.

Trying to gather the strain information for the entire sheet proved ineffective due to regular data drop-out, large sheet displacements and long solution times. The Vic3D software processed the data more quickly and with greater accuracy for smaller regions. In such a scenario, the user needs to choose the smallest area about the crescent singularity terminus

⁶ Having a standard deviation greater than the mean highlights the variation in the sample. This is because the measurement of height is taken from a reference plane as a base datum. This causes certain regions to be lower than the plane, as can be seen in the image, with some black speckles appearing below the white triangle mesh. With the software referring to the reference plane, negative distances are also measured, causing a larger standard deviation.

that enables the terminus to be seen throughout the experiment, as this region has the highest strain and can be easily compared to the finite element (FE) model.

Data sampling from the DIC images relied on the judgement of the researcher in determining the most effective points for data collection. It is understood that the greatest strain occurs at the apex. However, in nearly all the tests, the apex was characterised by a glare line. This concealed the speckles in the region, which prevented the software from gathering accurate strain and displacement data for the crescent terminus and the immediately adjacent areas once glare began to occur. It is up to the user's discretion in these circumstances to manually choose the location of the terminus, which needs to be as close to the apex as possible. There is the additional complexity in choosing a location: it needs to have enough sampling points to offer conclusive results, while being close to the maximum strain value associated with the crescent singularity. Consequently some locations nearer the apex cannot be chosen. Such a choice can have a severe effect on the strain variation presented for the terminus, as the strain near the apex varies greatly over a very small area, making a significant difference to the strain values collected.

6.2 FINITE ELEMENT ANALYSIS

To validate the results produced by the experimental setup, a new '.mac' script was written for use in ANSYS LS-DYNA – the explicit-code FE computer modelling software – that is shown in Appendix G. The code uses Belytschko-Lin-Tsay element theory as referred to in Section 5.6.1. As in Section 5.4.4, the '.mac' file produces an LS-DYNA '.k' file for editing in LS-PREPOST so that greater control over the analysis could be achieved to aid solving. As in Table 5.2, the same alterations have been made for INN and TYPE to 2 and -1 respectively. The variations to MPR and SPR were not needed, as contact forces were not collected. All the analyses were again undertaken on the Iridis computing cluster at the University of Southampton, using the Linux 2.6.9 operating system and 64-bit AMD Opteron dual-processors with single precision, as discussed in section 5.5. A minimum of 2 GB of RAM was initially utilised for the analyses.

6.2.1 Three point bend simulation

This simulation assumed that the edge furthest away from the hemispheres was fixed in space and had all degrees of freedom (DOF) constrained. The single hemisphere below the sheet was also stationary with all DOF constrained. The two hemispheres above the sheet in the simulation moved only in the z -direction, starting at the initial sheet surface, to be displaced 10 mm in the downward dimension (z -axis) during the analysis. The formation of the d-cone is

shown graphically in Figure 6.5. The hemispheres are displayed as transparent meshes to enable the d-cone to be clearly seen. Measurements were collected from the upper surface of the shell element – the surface in contact with the two hemispheres – as it is the speckle pattern surface from which the DIC values were calculated with, as discussed in Section 6.1.

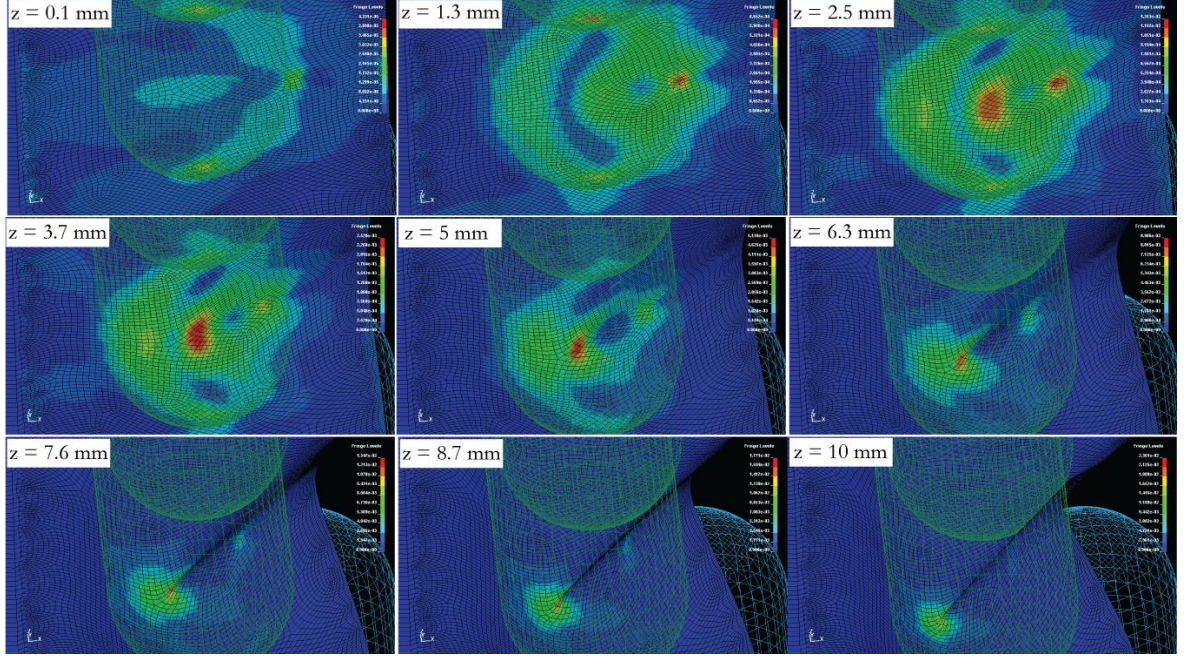


Figure 6.5: D-cone formation in a sheet with one fixed edge produced by a three-point bend analysis.

Data was gathered for the element with the greatest y strain (ϵ_y) at the end of the simulations (Section 6.3.1 explains why ϵ_y is used). For the same element, the x -displacement information is also stored. LS-DYNA can output information for any element constituting the sheet. In the formation of a d-cone, the crescent singularity initially formed in a different position from its ultimate location at the point of greatest strain. Both the DIC and FE software is able to output data for each individual element or location, but cannot automatically output the maximum values for each time-step. As a consequence, the results gathered from the FE analysis were for the element where the crescent singularity was located at the end of the experiment. From here on, this location will be referred to as the *terminus* and it will enable a direct comparison with the DIC data, described below in Section 6.1.5.

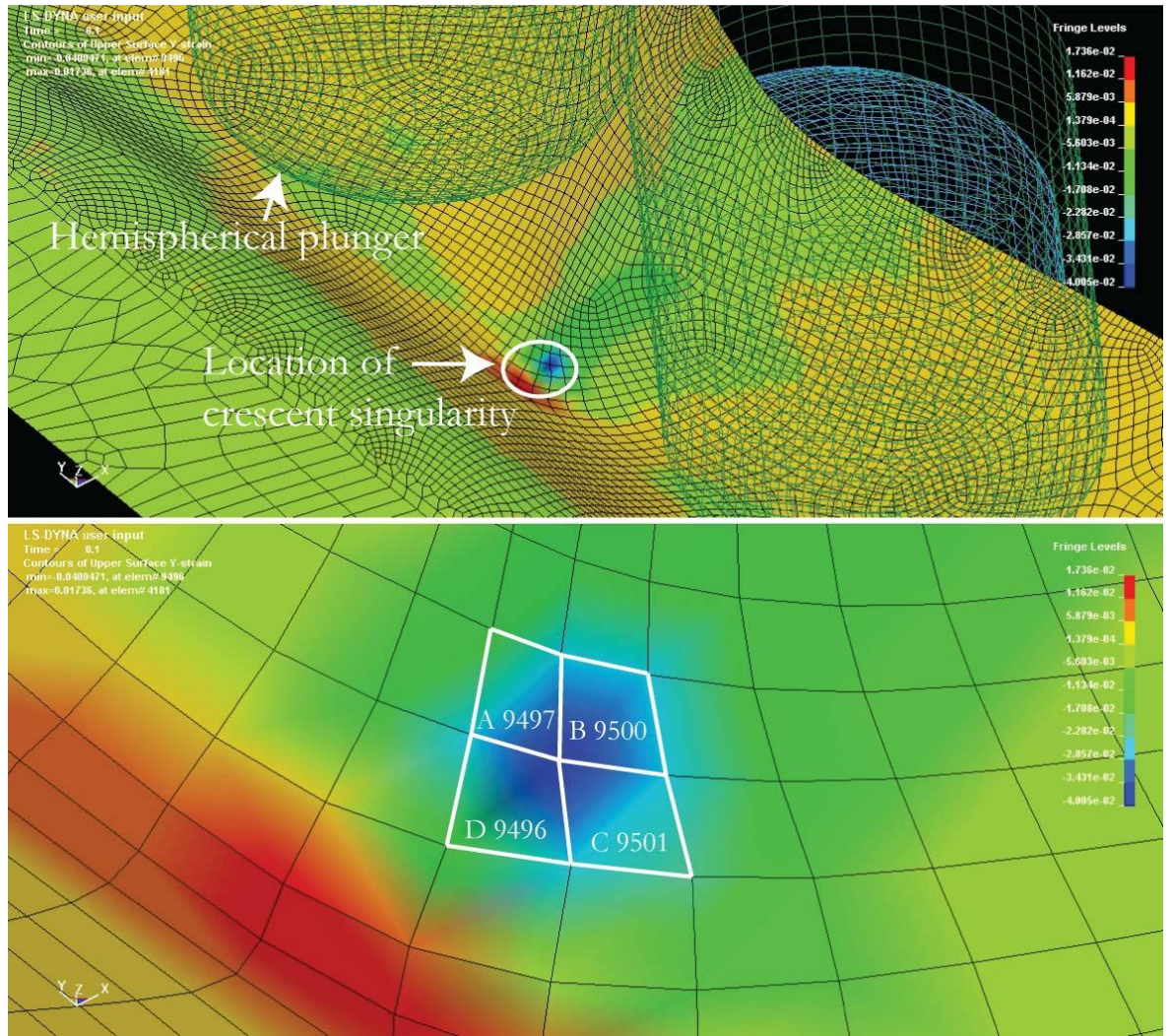


Figure 6.6: Choosing elements with the greatest ε_y at $z = 10$ mm, for $h = 125$ μm and $x_0 = 20$ mm.

The LS-PREPOST graphical user interface (GUI) shows the elements at greatest strain as darker shades of red as in Figure 6.6, this helps with choosing the elements that need to be compared. For the twelve analyses conducted, the elements in the final time-step were chosen with the greatest ε_y . These were examined in more detail so that the element with the largest final strain could be chosen, as shown in Figure 6.7. In this analysis element 9496 had the largest final ε_y strain. Data for the chosen element can then be exported and compared to the DIC data.

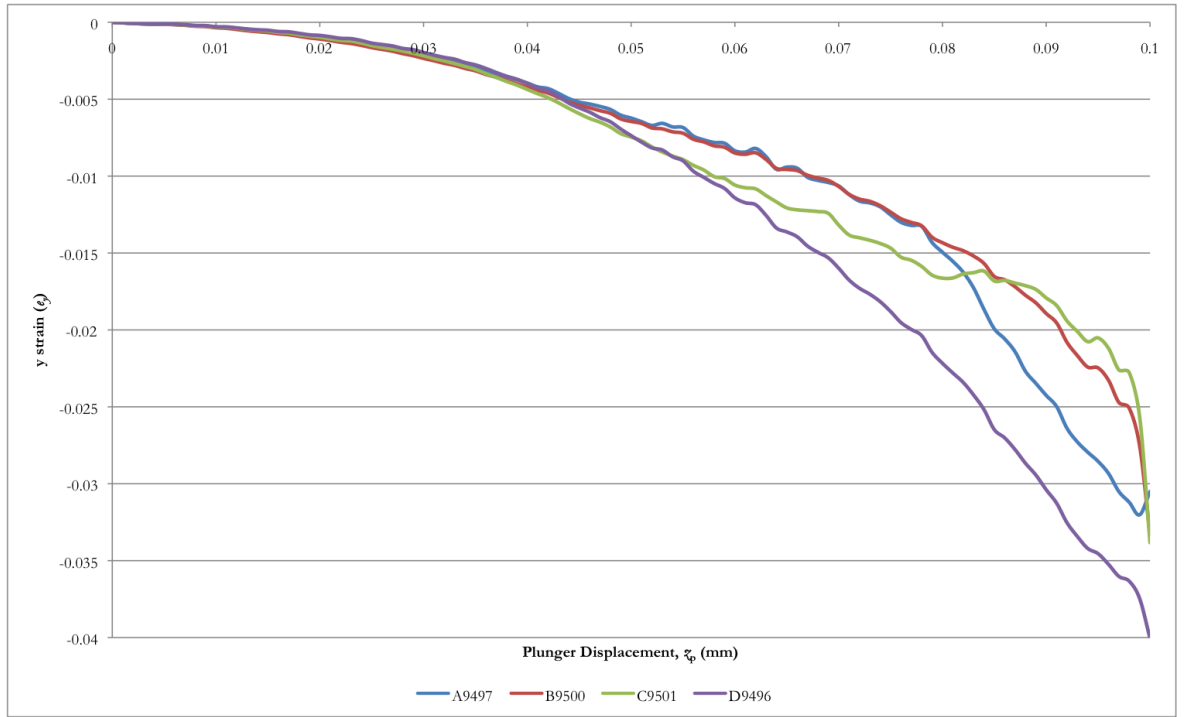


Figure 6.7: Graph indicating the ϵ_y strain of the elements about the point of the terminus.

6.2.2 FE veracity

In Section 5.6, Belytschko-Lin-Tsay elements were recommended for use, based on their speed and capability. They work by using one point quadrature in the plane of the element, which calculates values explicitly but can result in hourglassing [157]. By making a comparison of the ‘hourglass’ energy with the ‘internal’ energy of the model the validity of the model solutions can be checked.

Hourglassing occurs in explicit elements with one-point integration. Although these elements are robust for large deformations and save processor time, they are prone to ‘zero-energy’ modes. These are usually oscillatory, having larger frequencies than those of the overall structural response; the result produces mathematical states that are not physically feasible. They typically have no stiffness and demonstrate a zigzag appearance to a mesh as depicted in Figure 6.8. Hourglassing is an artefact that must be avoided as it can invalidate the results and therefore needs to be minimised. As a general guideline, the hour-glassing energy should not exceed 10 % of the internal energy [161]. For each FE model, internal energy and hourglass energy data was collected. In models that showed excessive hourglassing, re-runs were re-submitted to obtain valid results by making the following alterations:

1. smaller shell elements in the sheet and on the hemisphere tips;
2. smaller sub-step times of 3×10^{-8} s;

3. the *Control_Accuracy card variable OSU is set to 1, enabling second order stress updates to occur; which are needed if elements are subjected to large rotations;
4. increased loading velocity of 200 ms^{-1} and a shorter time-span of 0.05 s: displacement remains 10 mm after analysis.

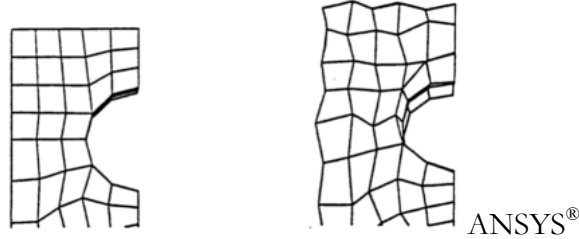


Figure 6.8: The effect of hourglassing on an explicit dynamic analysis [161].

The first three alterations cause an increase in processor time. This was balanced out by increasing the speed at which the hemispheres travelled, which reduced the overall time of the analysis. Even with these additional modifications the resulting solution times for the analyses were in the region of 60 hours. RAM memory needed to be increased to a minimum of 4 GB due to the greater number of elements in the model, while the greater velocity of the loading points might also have led to an initial dynamic response as previously seen in

Figure 5.15.

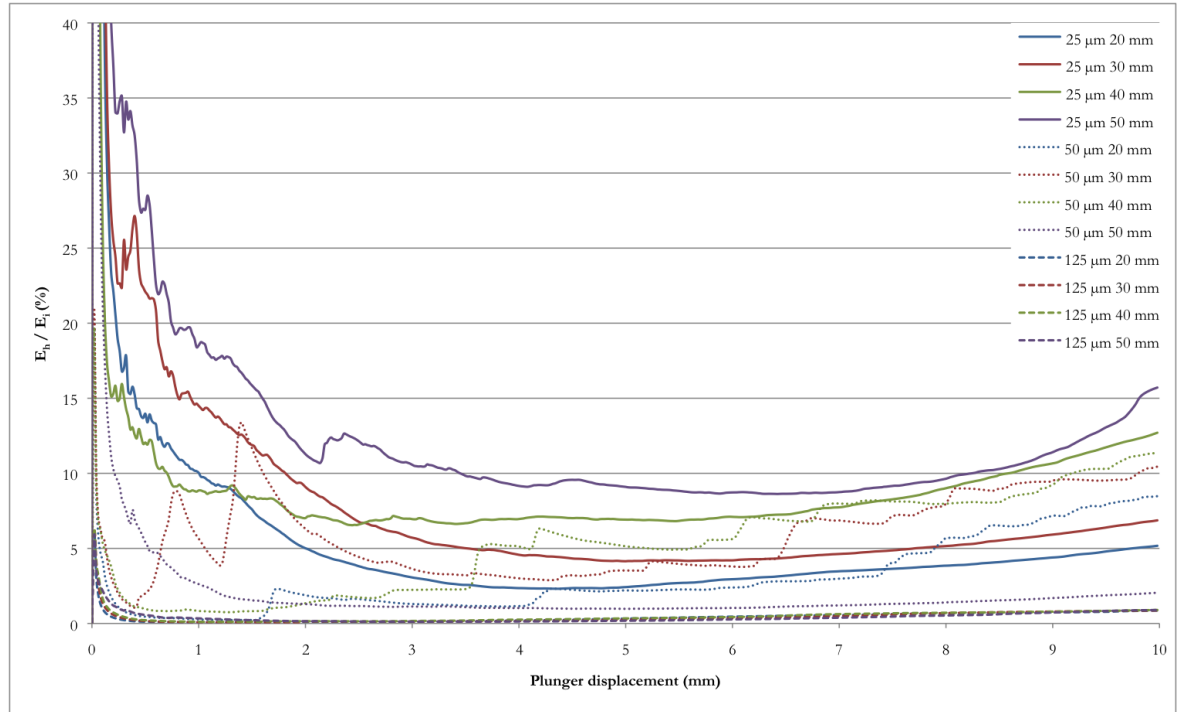


Figure 6.9: Hourglassing energy as a percentage of internal energy for all FE models.

The hourglass energy (E_h) data for each analysis was compared in Figure 6.9 as a percentage of the internal energy (E_i). The resultant values all seemed to be above 10 % at the start of the

analysis. This was due more to the E_i being a very small value at the beginning of the analysis rather than the E_h value being large, as minimal energy had been transferred into the sheet. Hourglassing seemed to be more of a problem for the analyses of thinner sheets. For 125 μm thick sheets the E_h values were under 1 % of the E_i after 0.5 s and remained so for the entire analyses suggesting these models are accurate, while smaller values of b all had greater values, most notably for the 25 μm sheets for the first 2 s. All FE analyses showed E_h values below 10 % of E_i between 4 and 8.5 s.

6.3 EXPERIMENTAL RESULTS AND DISCUSSION

The first comparison made was for the direct strains in the x and y directions and the xy shear strain against plunger displacement (\tilde{x}_p) for an b of 125 μm and an x_0 of 20 mm. It was seen in the DIC experiments with PEN sheets of 25 and 50 μm thickness that d-cones had already begun to form with only a 1 % strain at their apex and with 2 % strain for 125 μm sheets. As the d-cone produces a crescent singularity at its point due to the sheet needing to bend and stretch, it causes the PEN device to deform, which in Polymer Vision's devices would cause the address lines in the circuitry to fail. The results will therefore display the data up to a strain of 2 % as any more than this is superfluous. For every experimental configuration, videos of colour contour maps, showing the variation in Von Mises strain (ϵ_{VM}) on the surface of the specimens are shown on the DVD located in Appendix J. In some cases d-cones did not form, whilst a large number suffered from data 'fallout', resulting in fewer data samples in the strain measurements and consequentially discontinuities in the contour maps.

Due to the quantity of data, each set of results will be discussed individually. The FE results are displayed as thick continuous or thick dashed lines for strain and displacement results respectively. To help with the comparison, the DIC strain measurements are displayed as a paler colour to the corresponding FE values. In addition, diamond markers show where the Vic3D algorithm produced strain and displacement results. Conclusions are then presented collectively.

6.3.1 DIC and FE direct and shear strain values

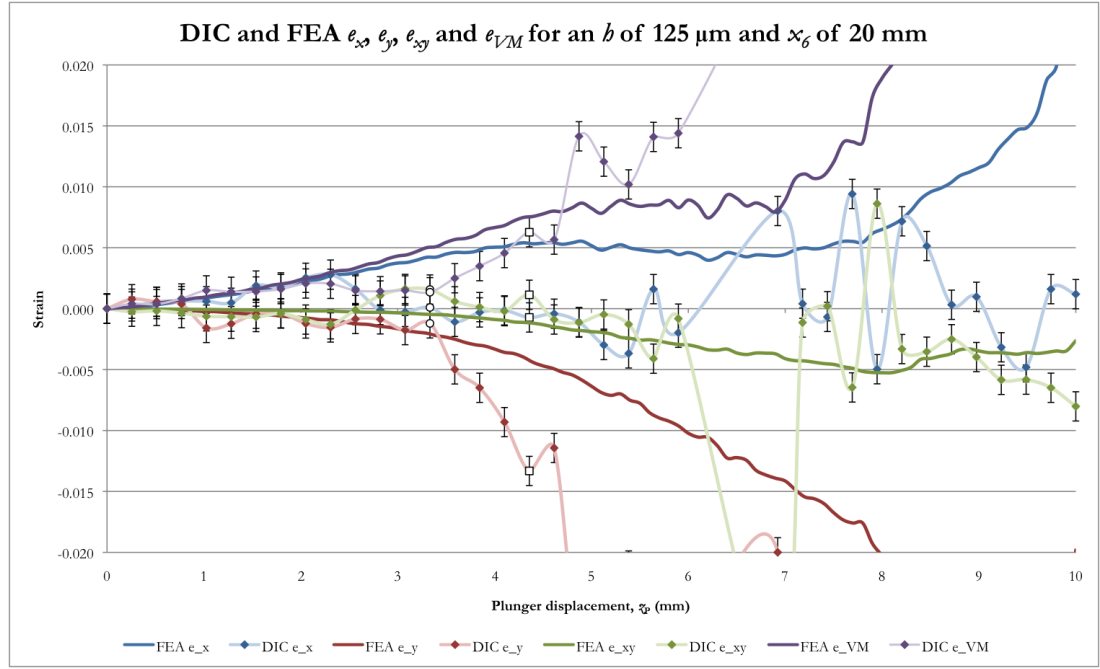


Figure 6.10: Variation in ϵ_x , ϵ_y , ϵ_{xy} and ϵ_{VM} , for an h of 125 μm and an x_6 of 20 mm.

Figure 6.10 shows the variation with strains for the terminus with respect to plunger displacement. It is clear that even with the error bars taken into consideration, there is a discrepancy between the DIC and FE values at displacements larger than 2 mm. The DIC strain values do not allude to the fact that the sheet initially bulged upwards in an unexpected, ‘pinched’ profile. At displacements just less than 3 mm, the DIC ϵ_x and ϵ_{xy} values vary unexpectedly, which ties in with the sheet ‘snapping’ into a form that goes on to produce a d-cone. A black circle marker on the graph indicates the first visual signs that a d-cone shape is forming⁷. Even with the unexpected ‘pinching’ and fluctuation in the DIC results, there are distinct similarities between the measurement methods for the first 3 mm of z_p displacement. Afterwards, the values reported by the two techniques for ϵ_x vary considerably, although ϵ_{xy} and ϵ_y demonstrate some similarities in trends between the experiment and the model predictions.

The DIC ϵ_x varies sign throughout the analysis, which is unexpected along the axis perpendicular to the clamped edge, while it has little in common to the FE ϵ_x values. One possible explanation is revealed by a snapshot of the FE analysis at a z of 5 mm, shown in

⁷ Deciding on the visual signs that determine when a d-cone forms depends on the observer's visual acuity. Experience can be quickly attained in recognising the manifestation of this shape. A tell-tale sign is the bunching of speckles along lines that lead to an apex. These can be seen in the videos and is a distinguishing characteristic of a d-cone.

only that it is similar to the FE values. Most useful are the ϵ_x and ϵ_y data sets. Easier to depict in the FE analysis, the ϵ_y absolute value initially shows a gentle increase with plunger displacement. The point of greatest rate increase occurs around 4 mm. After this point, an almost linear variation with δ_p is seen. In the ϵ_x values, a point of inflection occurs at 4 mm. The DIC data does not show this behaviour in the ϵ_x values because of the glare. However, something similar is seen in the ϵ_y values even with glare present, this could be because the software finds it easier to calculate strain information as a result of the greater displacement. A gradient change in ϵ_y is seen in the same region as the three-dimensional formation of the d-cone is observed.

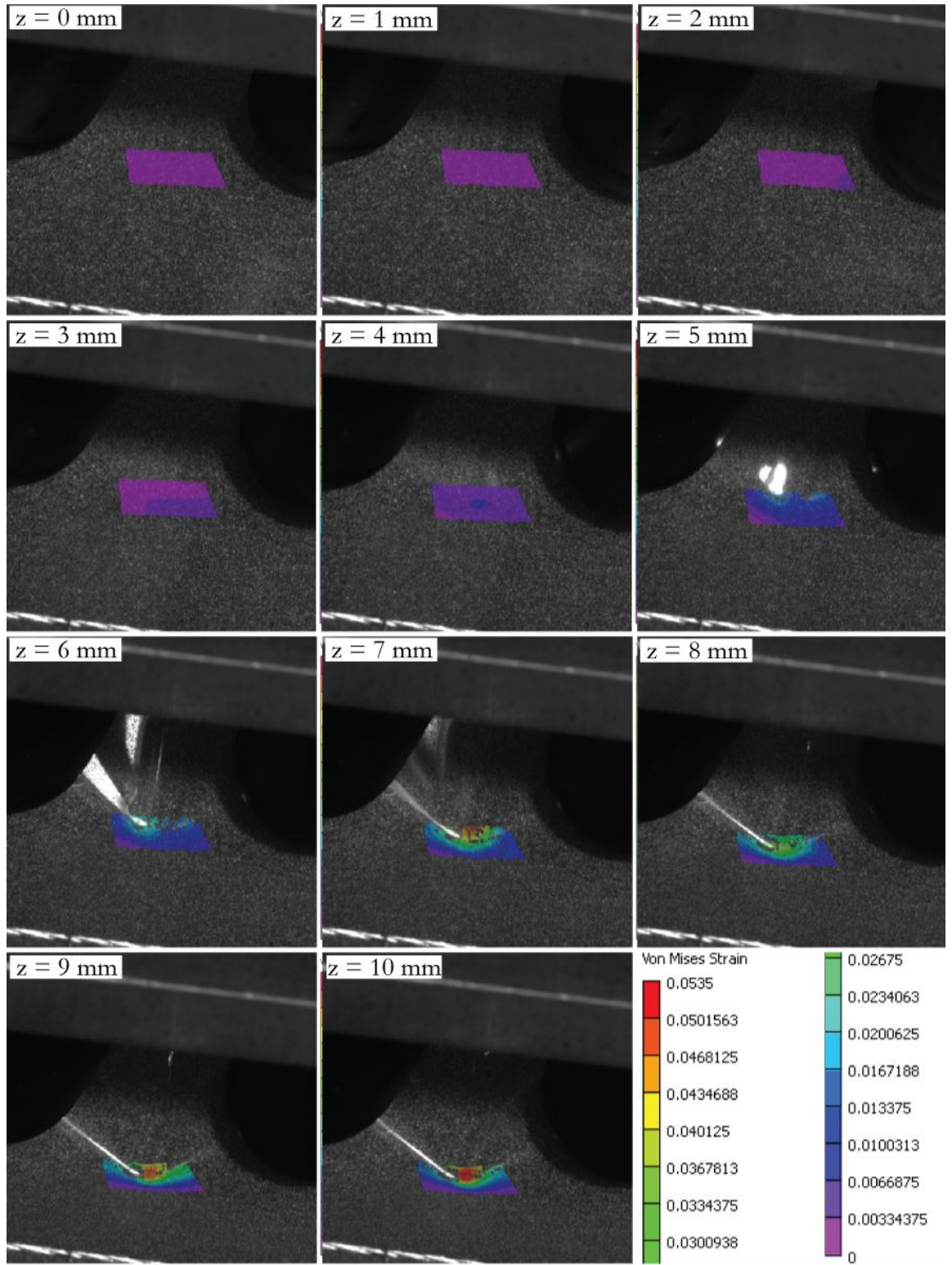


Figure 6.12: DIC interval photos of a d-cone formation for a PEN sheet with an h of $125\ \mu\text{m}$ and an x_0 of $20\ \text{mm}$.

Another set of variables that act as indicators in the d-cone formation and inform us about the capability of the DIC technique is the displacement of the terminus.

6.3.2 DIC and FEA sheet displacement

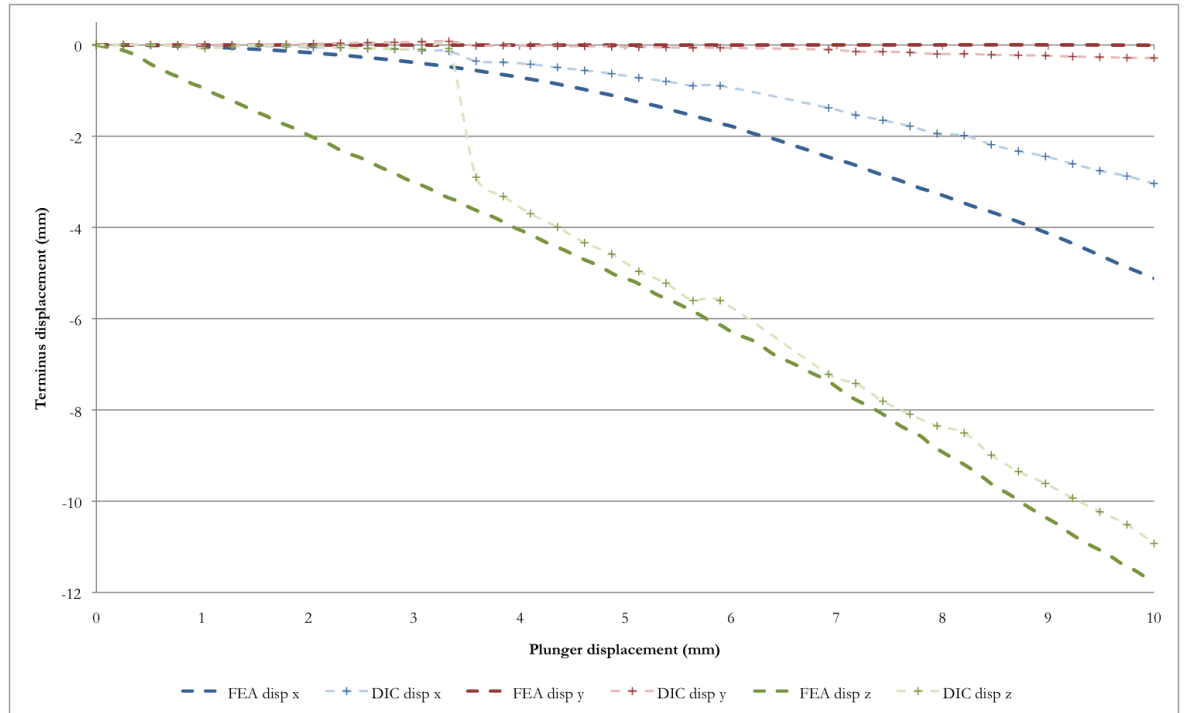


Figure 6.13 DIC and FE x , y and z displacement for an h of 125 μm and x_0 of 20 mm.

The displacement of the terminus for the FE model and DIC test is represented in Figure 6.13. Vic3D presented no displacement error values. It is safe to assume there is a minimum error of $\pm 4.81 \mu\text{m}$, as indicated in Section 6.1.3, which is too small to be shown on these graphs. Although the data highlights the movement of the terminus, it does not identify the deformation of a d-cone.

The data from the FE model and DIC test compare well. The ‘pinched’ form taken by the PEN sheet in the DIC test is followed by its ‘snapping’ into the expected shape; this is indicated by the gradient change after 3 mm in the z displacement. Thereafter, the values follow the FE results consistently, and they displace downward at a similar rate, although they do demonstrate an offset. A similar trend is seen in the terminus movement perpendicular to the clamped edge along the x -axis, with the movement predicted by the FE model being greater than that reported by the DIC values. Lastly, the y -axis results are most encouraging: the FE model assumes negligible movement along this axis and the DIC results are very similar, showing only a little movement when the ‘snap’ action occurs and then a small deviation to one side toward the end of the test.

6.3.3 Data representation

Together, the strain and displacement information from the DIC tests provided strong evidence that the technique works; it followed the crescent singularity and even showed an

indication of the strains on the sheet. Because of the wealth of information provided by the test, the remaining results have been grouped, firstly comparing data with identical b and then x_6 values. Only the ε_x and ε_y results will be shown as it was felt that z-axis data was the most important with regards to displacement, while the ε_y value is the most straightforward to compare between the FE and DIC techniques and may provide an insight into the applied displacement at which a d-cone forms.

6.3.4 Mesh dependency

For the FE analyses, repeat models were run with a different sheet element density for x_6 values of 30 mm, to check the mesh dependency and validate the results. The aim was to compare the strains and displacements of the terminus to prove that the mesh shape had not affected the results. The finer mesh analyses each took over 160 hours to complete, with the finer mesh analysis for an b of 25 μm failing to complete in the allotted time on the Iridis system; it terminated after solving for up to a plunger displacement of 6.5 mm. All the standard models were made up of 27,273 elements, while the 25 μm finer mesh model used 192,292 elements and the 50 and 125 μm models 133,528 elements. The increase in elements was mainly within the sheet that modelled the PEN material, while the rest were used to increase the number of elements used on the tips of the hemispherical prongs.

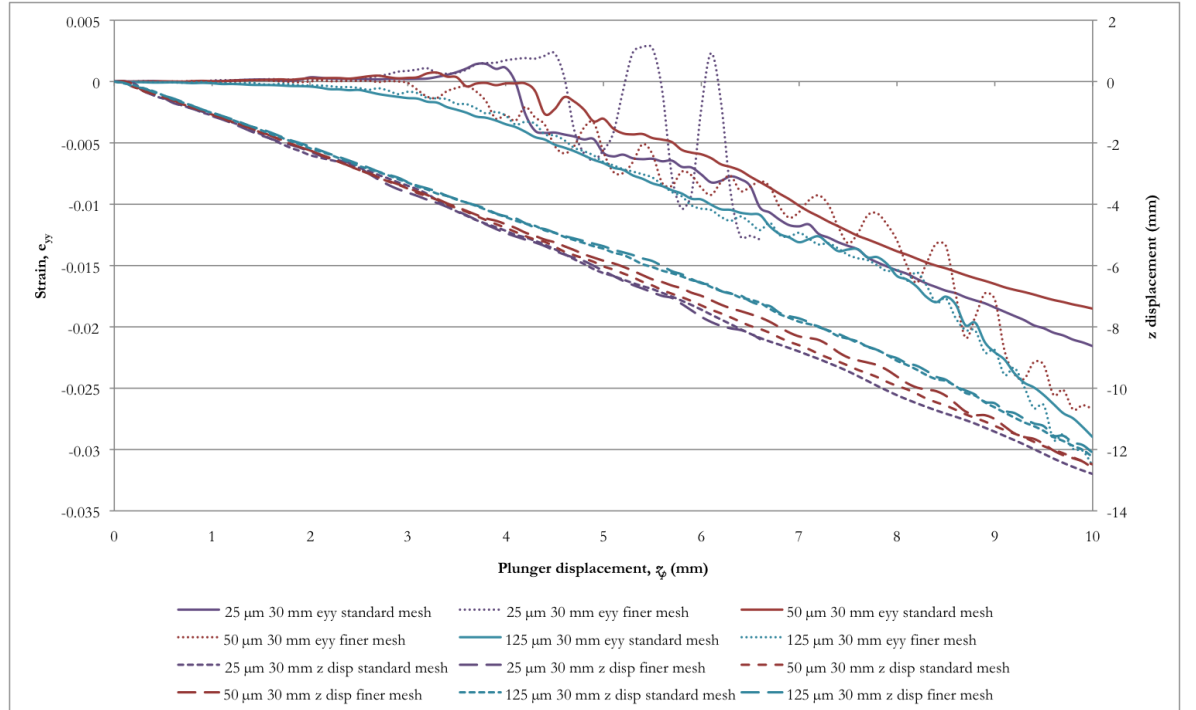


Figure 6.14: Mesh dependency comparison for varying thicknesses and an x_6 of 30 mm.

As can be seen in Figure 6.14, which shows the results of the comparison, similar trends were reported in the ε_y and ε_x data for the standard and finer mesh models. For the 25 μm , both ε_y

data sets followed the same projection, with the finer mesh reporting a larger amplitude in the varying strain before the early termination. By watching the film of the computer simulation, it is easy to see that the terminus has failed to follow the crescent singularity, which moves back and forth in the y-plane. Increasing the sheet thickness sees a better comparison between the different meshes. The 50 μm finer mesh again showed a fluctuating ε_y at the terminus because of movement from the crescent singularity, while the 125 μm models compared very well with similar results. The z displacements of the termini showed a better agreement between the mesh densities, with the 50 μm models having the largest difference in values. These results highlight the problem of following the crescent singularity but confirm the models independence from the mesh shapes.

6.3.5 PEN sheets 25 μm thick

For an x_6 of 20 mm, no credible DIC ε_y values could be gathered from any of the three repeat tests, making a consistency analysis for the DIC technique unavailable. Good sampling rates were initially seen for the remaining three DIC data sets in Figure 6.15 for the ε_y variation with z_p . The onset of glare at 5 and 4.5 mm for an x_6 value of 40 and 50 mm respectively caused these sampling rates to diminish.

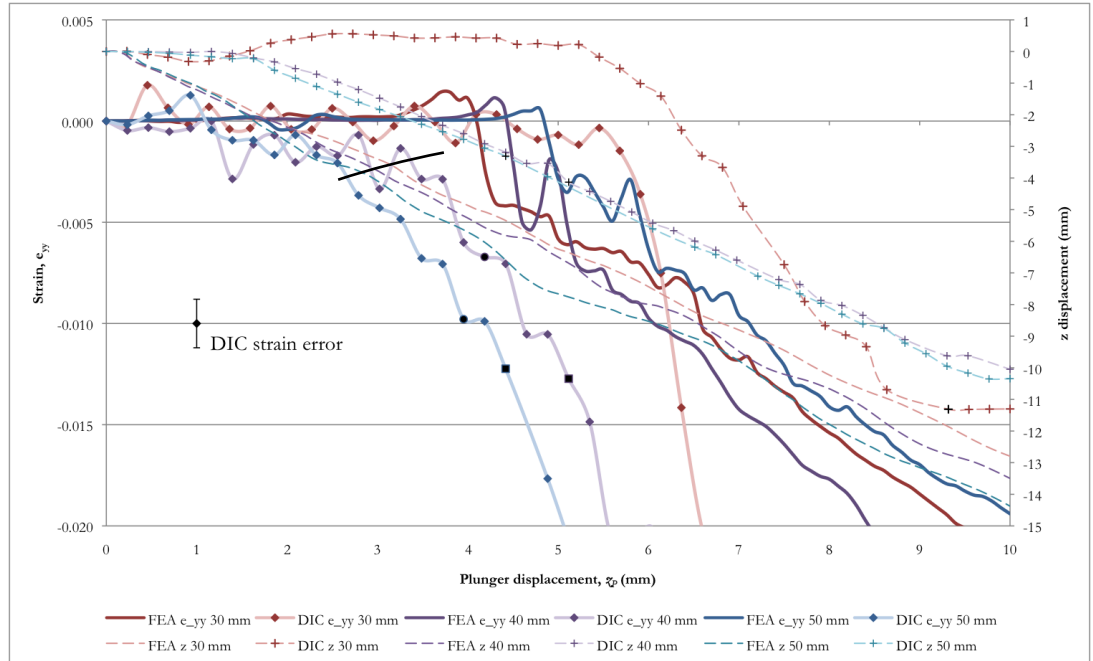


Figure 6.15: DIC and FE ε_y and z displacement information for 25 μm sheets.

The DIC data showed an exponential increase in negative ε_y for each data set, which occurred at a smaller z_p value for increasing x_6 values. The graph lines each suggested a possible ‘shoulder’, created by a gradient increase. This shoulder occurred before the visual verification of a d-cone and thus could be the moment when the d-cone formed. The shoulders in the

varying x_6 results seem to occur around a value of 0.003 strain and are highlighted by a black line.

The 30 mm test showed a 'pinched' formation, as shown in Figure 6.16, up until a plunger displacement of 9 mm, when it 'snapped' into the d-cone, unfortunately making these results incomparable to the FE d-cone model.

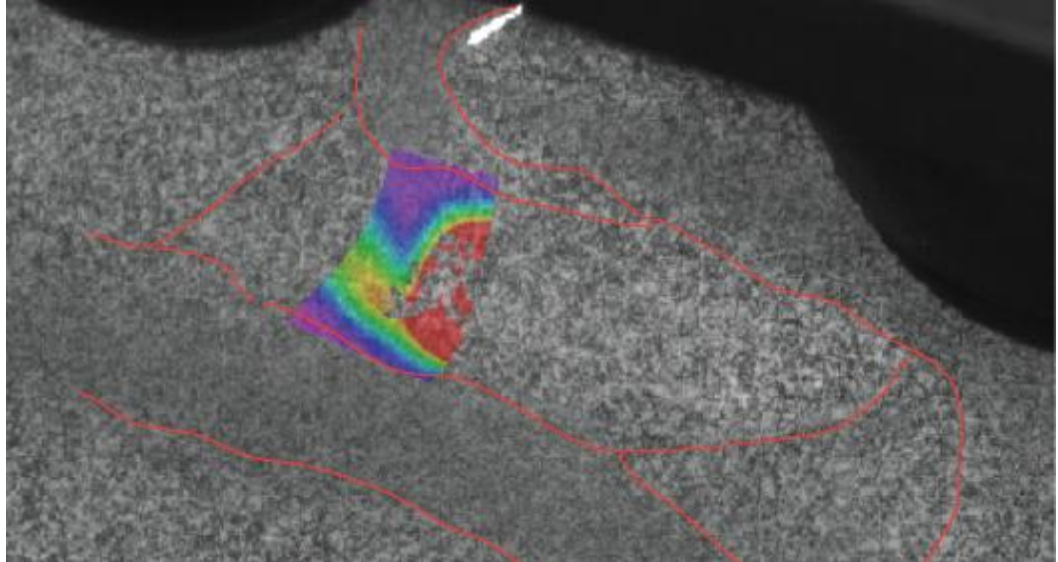


Figure 6.16: Distorted ridge formation for $x_6 = 25 \mu\text{m}$ and $h = 30 \text{ mm}$ sheet at $z_p = 7 \text{ mm}$, highlighted in red. Sheet 'snaps' to ideal d-cone shape afterwards, initiating from the line of glare at top of image.

The FE modelling showed similar qualities to the DIC results, with a change in ϵ_y at the termini during the formation of the d-cones. The gradients were not as steep as the DIC results, and occurred at a deeper plunger displacement, while the gradual increase in negative ϵ_y initially was not seen in the FE results, which may be a fault of the data capture method, as explained below. Of the FE data sets, the 50 mm analysis is likely to be the least accurate as it suffered the most hourglassing of the FE analyses. However, the results are most encouraging, with similarities being seen between the DIC experiments and FE predictions. The FE models would be more realistic if the crescent singularities were tracked through the entire analyses instead of only in the element at the terminus.

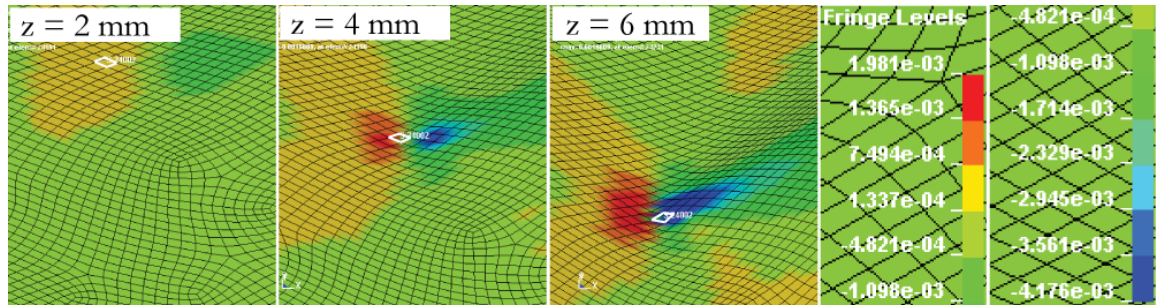


Figure 6.17: FE ε_y snapshots for x_6 of 30 mm, showing the crescent singularity moving towards the terminus.

The FE results do not show the true account of the ε_y variation for the crescent singularity. Snapshots from the FE model (with the hemispherical plungers hidden) for an x_6 of 30 mm are shown in Figure 6.17. The graph in Figure 6.15 displays the termini information, which in the analyses are not following the crescent singularity until after 4 s. Initially and at 2 mm, the termini in the FE analyses are observed to be at the side of the clamped edge of the crescent singularity location, indicating a small positive strain (yellow colours). At 4 mm, the crescent singularity moves towards the terminus, causing it to pass through a region of pronounced positive strain (red colours). By 6 mm displacement, the termini and crescent singularities of all three analyses are coincident, reporting negative ε_y values (observable as the blue colours).

The z displacement data for the DIC measurements at x_6 of 20 mm clearly displays characteristics that indicate an alternative sheet deformation mode, which has been referred to previously as ‘pinched’. The remaining two DIC analyses both demonstrate a lag period until 2 mm displacement before the termini begin to displace. Afterwards, both move at almost identical rates. The displacement gradients for the DIC results were very similar to the FE termini displacement gradients. A difference in their results is due to the FE analyses predicting displacement of the termini immediately. Both DIC and FE results indicate greater z displacement values for larger x_6 values.

6.3.6 PEN sheets 50 μm thick

There are similarities discernable between the 50 μm values shown in Figure 6.18 as for the 25 μm results. The DIC and FE ε_y predictions both indicate shoulders due to the change in gradients. However, the 50 μm DIC results seemed to occur at greater ε_y values: around -0.004, while the results differed as a greater ε_y was reported for a decreasing x_6 value, which was a reversal of the trend seen in the 25 μm data.

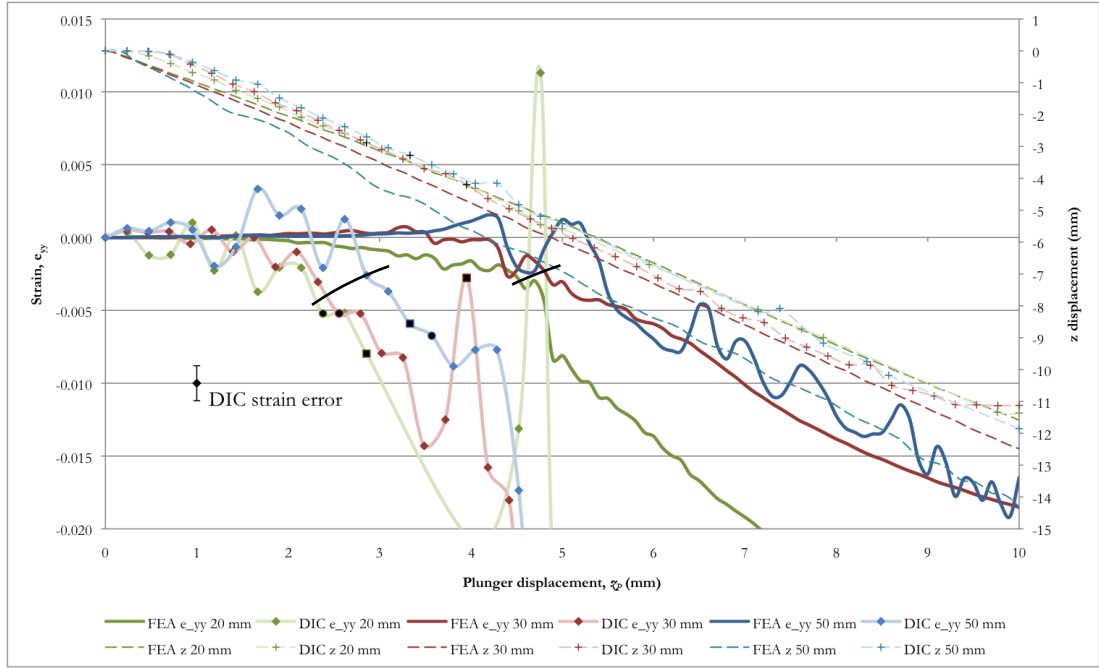


Figure 6.18: DIC and FE ε_y and z displacement information for 50 μm sheets.

The FE 50 μm results showed a similar lag in ε_y variation with z_p , just as in the 25 μm findings. For the FE results with an x_6 of 20 and 30 mm, similar characteristics to the experimental DIC values were displayed: first a shallow gradient was observed followed by a steeper gradient in the ε_y/z_p variation. The relationship between ε_y and x_6 that was seen for the DIC results was mirrored in the FE model, with an x_6 of 20 mm resulting in the greatest strain.

The DIC z displacement data suggests that glare has a limited effect on the displacement data. All the DIC displacements showed a lag between plunger movement and terminus. However, they all followed a similar linear relationship between z displacement of the termini and z_p , while a similar gradient was also seen in the FE values. Likewise as in the 25 μm data, the displacement of the terminus in the z direction occurred straight away and created an offset between the measured DIC and modelled FE values. The FE results suggest a greater amount of movement occurs for greater values of x_6 , however this cannot be deduced from the DIC findings.

6.3.7 PEN sheets 125 μm thick

The last set of results for a constant sheet thickness compared ε_y for an b of 125 μm , shown graphically in Figure 6.19. Beginning with the DIC ε_y data, a shoulder was again seen when the size of ε_y increased in [negative] value at a greater rate with z_p . This gradient change is highlighted by a solid black line and was seen to occur before the visual signs of the d-cone's formation, but at a similar range of ε_y values as reported for the 25 and 50 μm sheets.

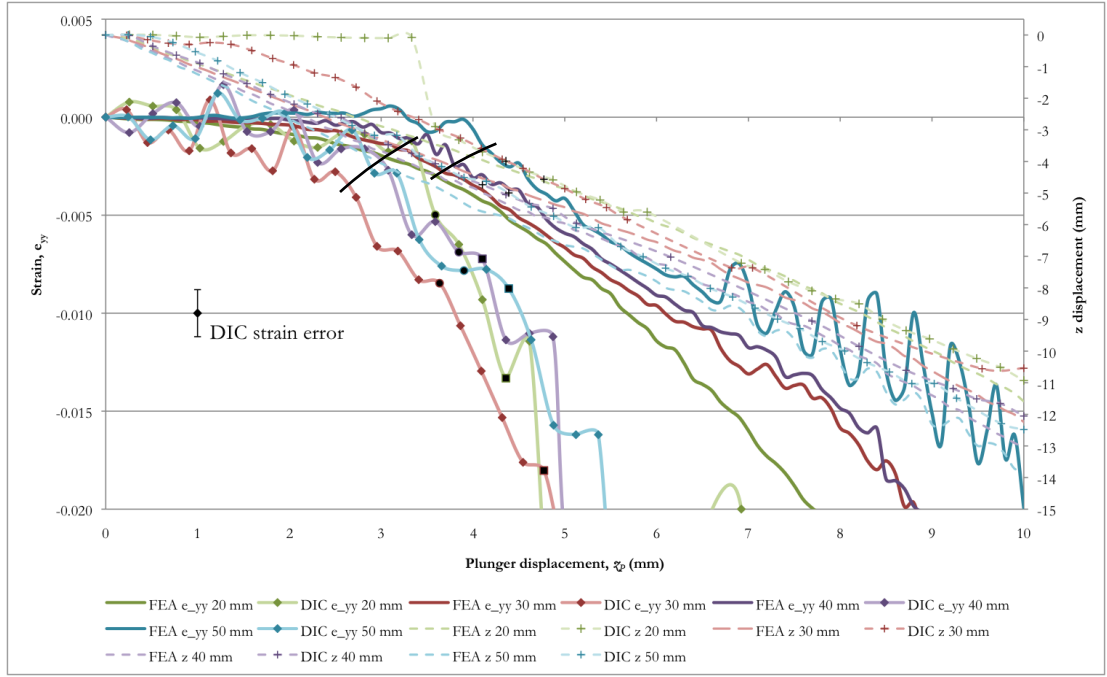


Figure 6.19: DIC and FE ε_y and z displacement information for 125 μ m PEN sheets.

The FE ε_y results are encouraging for an x_6 of 20, 30 and to some extent 40 mm, which showed behaviour similar to the DIC results: displaying a shoulder where the gradients changed. However, as seen in the 50 μ m results, the FE values demonstrated a more gradual initial slope in ε_y values, less pronounced shoulders occurring at a higher plunger displacement; at around 4 mm here, while the ε_y values thereafter were at a lesser gradient. The FE data for an x_6 of 50 mm reports an initial positive strain, later turning negative. It then showed fluctuations while decreasing in value. This effect was due to the termini not following the crescent singularity and therefore inaccurate data was reported from the adjacent areas; this was described in Section 6.3.5.

The DIC z displacement data again reported similar findings as in the 25 and 50 μ m results. The displacement data appeared to be largely unaffected by glare, while values for an x_6 of 20 and 30 mm showed ‘pinched’ formations to begin with that afterwards took on the expected d-cone form. Again, the DIC data demonstrated a slight delay in reporting termini z displacement with z_p . However, their gradients were much more similar to their FE counterparts than in the previous results.

6.3.8 Constant thickness discussion

It is clear from the results presented herein that there was evidence that linked the ε_y to the onset of a d-cone, most notably the demonstration of a shoulder in the values that marked the variation of ε_y with z_p and that this occurred between 0.1 and 0.4 % strain. It was less clear what effect the x_6 value had on the onset of a d-cone as it varied for each sheet thickness

tested. It may be too subtle for it to be seen in these results or possibly other factors, such as material defects, set-up errors or calibration issues may have interfered with the relationship. Although the z displacement data showed whether a ‘pinched’ formation would occur, it gave no insight into when a d-cone would form. The height positions of the termini when the d-cone was observed varied and depended on the thickness but not demonstrably in a fashion that could suggest any correlation. The FE results suggested that the explicit code was able to model a d-cone formation in an elastic model. However, it underestimated the magnitude of the strain and showed movement of the crescent singularity about the region of the terminus that was not visible to the observer. Alternatively, this underestimation of strain and lag time may be linked to the stiffening effect the spray paint may have had on the PEN sheets.

The following section will report on the results for the variation of ε_y and z with z_p for fixed x_6 values, to see if any relationships between varying the thickness are discernible.

6.3.9 20 mm between fixed edge and prongs

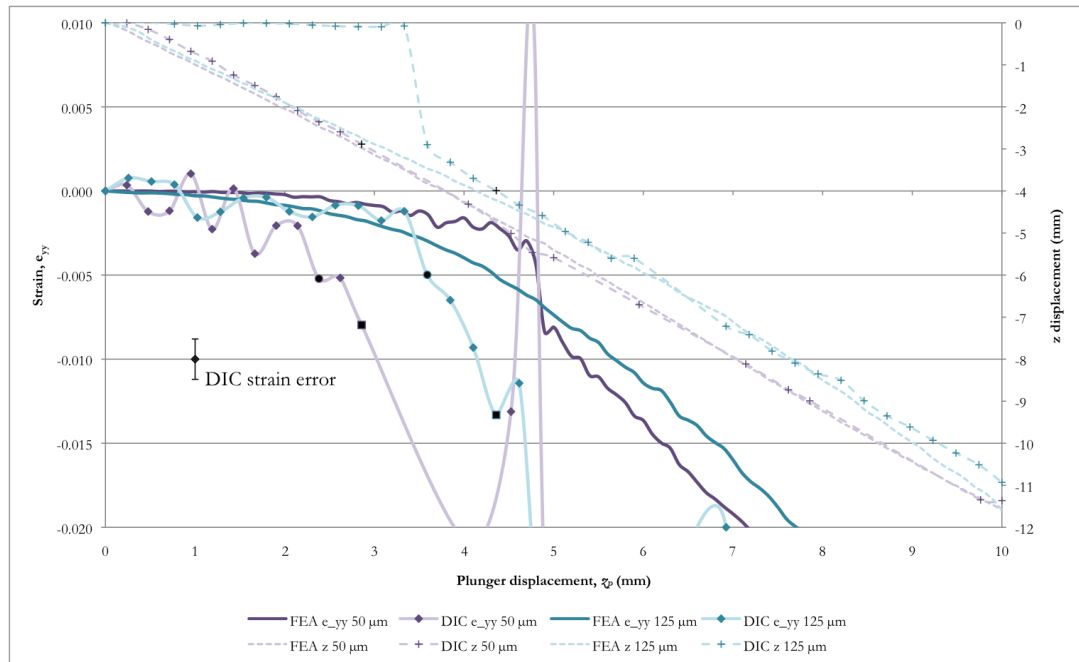


Figure 6.20: DIC and FE ε_y and z displacement information for x_6 of 20 mm.

No data could be gathered from the three repeated experiments for an h of 25 μm . The remaining two DIC data sets provided one set of results from the three repeat tests, which are displayed in Figure 6.20. They showed good sampling rates until glare was reported; represented on the graphs as a square black marker. The DIC results showed a higher strains at the termini in comparison to the FE value, which had lower strain values for a given plunger displacement, as reported for the constant thickness comparisons. The 50 μm FE data

appeared to be unreliable due to the software not correctly following the crescent singularity, as previously demonstrated.

Ignoring the initially ‘pinched’ profile for the 125 μm DIC results, there was a good match between the FE and DIC termini displacement data. Both thicknesses showed a constant change in z with z_p after 3.5 s. An offset between the values was seen, with the thinner sheet reporting greater movement.

6.3.10 30 mm between fixed edge and prongs

Data was available for all the b variations for an x_0 of 30 mm, shown in Figure 6.21. A ‘pinched’ profile was seen for the 25 μm DIC values until 9 mm plunger displacement, which had severely affected the z displacement and ε_y data. The remaining two thicknesses showed similar values for ε_y , with the thicker 125 μm data displaying a greater strain. Both provided good sampling rates that demonstrated shoulders from changes in their respective ε_y gradients.

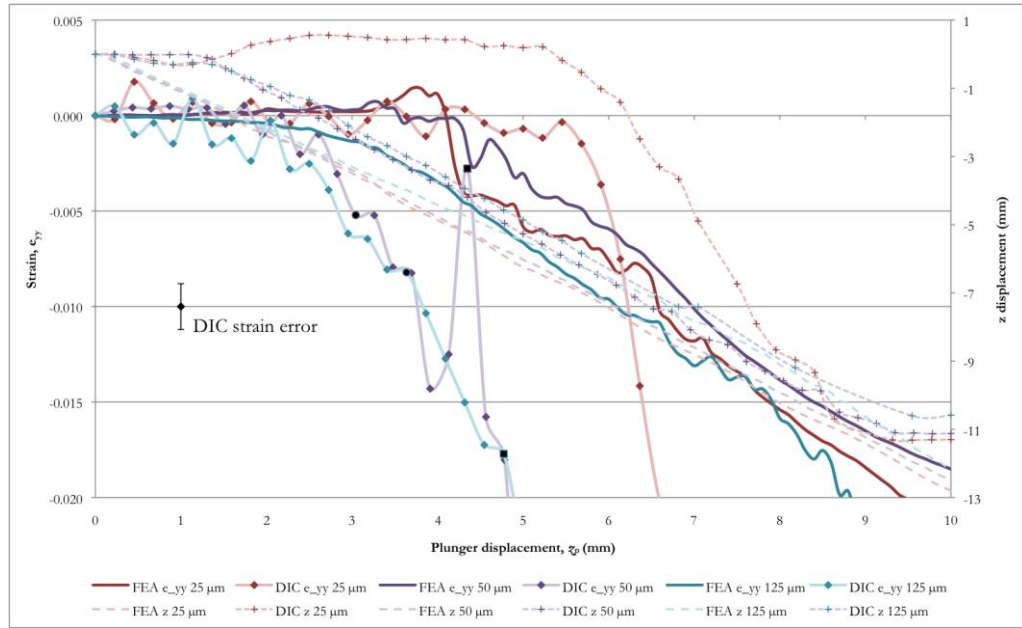


Figure 6.21: DIC and FE ε_y and z displacement information for x_0 for 30 mm.

As previously observed, the FE data displayed smaller ε_y values. Fluctuations in the 25 μm values suggest that the terminus did not track the crescent singularity throughout. The same can be said for the 50 μm data. The 125 μm values reported the largest ε_y values and a steady curve until 6.5 mm of z_p .

The z displacement data showed a similar pattern as in the 20 mm results in Section 6.3.9. The DIC results for 25 μm showed a pinching effect in the sheet, as confirmed in the video of the analysis. Both the 50 and 125 μm results reported similar z displacement values for the DIC and FE results, with an increase in z displacement of the termini with z_p , seen in both the DIC

and FE values. The DIC results showed a delay with \tilde{z}_p and then demonstrated a similar gradient to the FE results.

6.3.11 40 mm between fixed edge and prongs

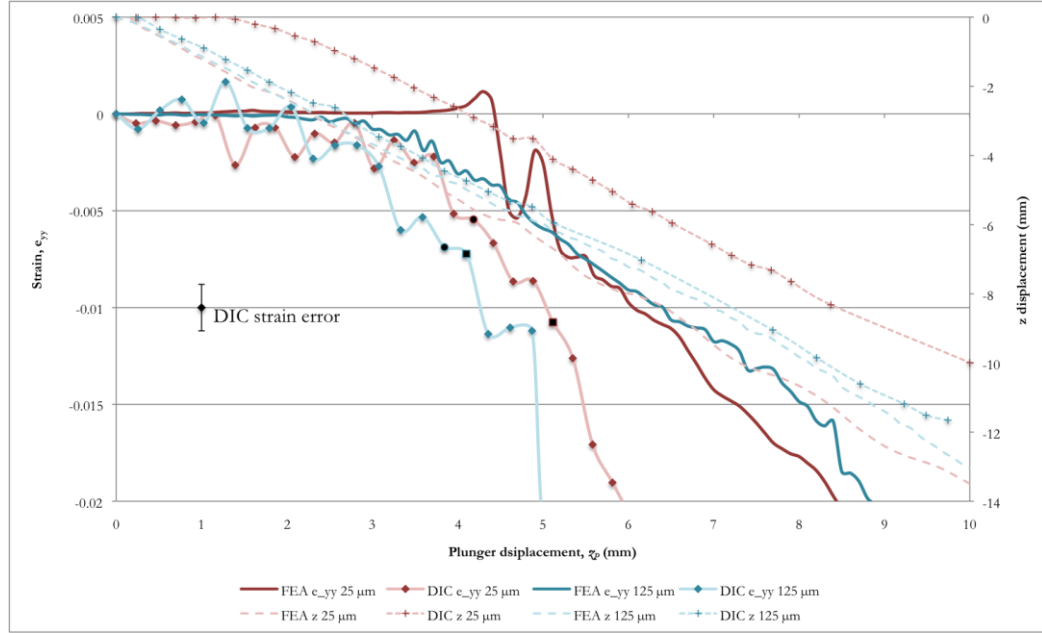


Figure 6.22: DIC and FE ε_y and z displacement information for x_0 of 40 mm.

The FE results added little to the comparison with the 25 μm , the terminus not following the crescent singularity. The 125 μm experimental data showed a shoulder due to the change in ε_y with \tilde{z}_p but again, these had smaller absolute values than predicted by the DIC model.

A good match between the 125 μm \tilde{z} displacement experimental data and FE predictions was seen, with both displaying termini movement from the offset. This was not seen for an b of 25 μm , which showed the DIC data having a delay in movement. The DIC values suggested an increase in the \tilde{z} displacement with thickness, the FE results contradicted this, suggesting the opposite correlation. It is curious that a delay was observed for an b of 125 μm when the offset was 30 mm as in section 6.3.10, but not for 40 mm, suggesting some discrepancy in the results.

6.3.12 50 mm between fixed edge and prongs

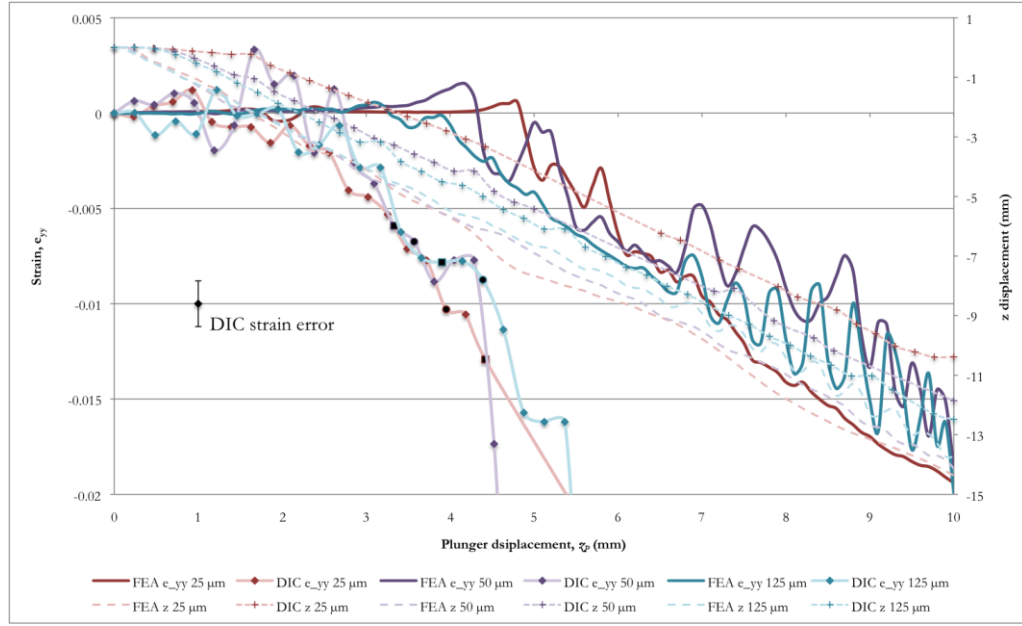


Figure 6.23: DIC and FE ε_y and z displacement information for x_6 of 50 mm.

All the DIC and FE results for an x_6 of 50 mm were successfully recorded and are represented in Figure 6.23. All the DIC ε_y results for the various h values seemed to behave in a similar fashion: almost all within limits of the error associated with the strain values. This data suggested that at higher x_6 values, the thickness had less influence on the ε_y induced at the termini. Such a suggestion was generally supported by the FE data, which showed a good deal of fluctuation by to not following the crescent singularity. However, such a claim was not supported by the previous results, as an increase in ‘bunching’ of the ε_y values was not seen in the graphs for an increasing x_6 .

The z displacement showed similar gradients for both DIC and FE results. However, the DIC and FE results completely contradicted one another: the DIC results suggested an increase in thickness caused an increase in termini displacement, while the FE data presumed the reciprocal correlation. All of the DIC results displayed a delay before movement occurred, which was most noticeable for an h of 25 μm .

6.3.13 Constant offset discussion

The results for a constant offset were compared to assess the effect of the thickness on strain and displacement at the termini, which should be the most important variable in the formation of a d-cone. Unfortunately the results have not been able to prove this, with discontinuities, a lack of sufficient data and variation between the results for differing offset values. Neither the DIC or FE results verified the relationship between the thickness and y -

strain. Theoretically, the thicker 125 μm sheets suffer greater strains on the surfaces as they have a larger distance to their neutral axis; bending produces a greater component of strain. The four graphs did not suggest a coherent relationship between the ε_z displacement with ε_p and b . the first two x_6 values of 20 and 30 mm suggested that both the FE predictions and experimental DIC measurements correspond well: greater ε_z displacement occurred from the thinner sheets. However, these two graphs had the least results to compare. The graphs for an x_6 of 40 and 50 mm suggested that the FE and DIC results contradict one another, while both have a full complement of results. The DIC results suggested a greater ε_z displacement of the termini for the thicker sheets, the FE results reporting the reciprocal correlation. Here, it is likely the FE results are the least accurate, as seen in the fluctuation of the strain values during their analyses.

6.4 CONCLUSIONS

The research successfully produced the first comparison between numerical and experimental analysis of the d-cone phenomenon in flexible polymer sheets, as used for Polymer Vision's displays. Of the two types of analyses undertaken, the consistency of the FE data and the amount of data fallout from the DIC experiments suggests the FE models are more believable. Restrictions of both techniques will be discussed in Section 7.1.

The experiments undertaken showed a change in strain once the d-cone forms, which causes a crescent singularity and that this occurs between 0.1 and 0.4 % strain, depending on the sheet thickness and plunger offset. The results show that there is an effect on the strain introduced by varying x_6 and at all thicknesses. Such information could be used for design guidelines to prevent failure from crescent singularity formation. However, the exact relationship could not be determined. The lack of continuity in results between the sheet thickness and strain was surprising, since the thickness has such a significant effect on the bending energies.

Although there is no absolute criterion for crescent singularity formation derived from the results, the grouping of all the strain data for varying thicknesses for the largest offset value of 50 mm may suggest that at larger x_6 values, the thickness has much less of an effect. It is more likely to be experimental error that has caused these results to behave this way. However, should this effect be proven true, it could help the manufacturing process to prevent d-cone formation, regardless of sheet thickness. Further experimentation is required with better data capture techniques.

The ε_z displacement of the sheet provides no information to suggest the formation of a d-cone. The ε_z value, at which they form, in relation to the sheet's initial position, changed

depending on the sheet thickness and offset, but no correlation could be seen to suggest a trend. The \tilde{x} displacement data does enable the researcher to realise when a ‘pinched’ form is occurring.

The effect of sheet thickness on the \tilde{x} displacement of the termini is not understood. At the short x_0 lengths measured, the DIC and FE results agree. At the longer lengths, they contradict one another. The origins of this contradiction are unclear. Refinement of the experimental and FE modelling are clearly required.

The experiments outlined in this chapter are not precisely analogous to picking up a sheet with fingers. When manually undertaken, one does not have displacement or load control and so a direct comparison is not possible. The experiments do however enable the variables related to picking up a sheet manually to be compared and repeated, to understand their effect. The design of the experiment and its set-up has been successful in isolating and comparing the effects of single variables and can be used to analyse a wealth of other variables and their combinations.

CHAPTER 7: OVERALL CONCLUSIONS AND FUTURE WORK

The research described in this thesis has investigated the capabilities of Nanoimprint Lithography (NIL). The processing technique was chosen as the sponsoring company, Innos, owned an EVG aligner bonder and wanted to increase their capabilities with the toolset, so a thorough knowledge on the technique was deemed essential, to see if Innos could add market value to the process. The study was published showing the current trends and capabilities of the process. It highlighted that:

1. feature sizes of smaller than 50 nm have yet to be proven on large imprint areas, such as wafers larger than 100mm diameter;
2. the largest aspect ratios to be produced at nanometre resolution were 11;
3. few relief heights have been made greater than the initial resist thickness used;
4. tolerances of less than a tenth of the imprint feature size have been reported.

This research into NIL revealed the lack of modelling of the process, with no guidelines or knowledge of what was physically achievable. It was felt that a model detailing what patterns are achievable by the technique would bring commercial benefit to Innos. The research concentrated on the physical process of de-embossing by creating a semi-analytical model based on elastic fracture mechanics. It provided predictions of the achievable limits for de-embossing as a function of key geometrical variables and material properties. Process ‘maps’ were created showing de-embossing limits. They showed a strong dependence of the achievable aspect ratio on the pattern area ratio and the interfacial shear stress. For typical polymer yield stresses the critical interfacial strain energy release rate has little affect on de-embossing. Large area ratios and high aspect ratios can be achieved by keeping the ratio of polymer and stamp Young’s moduli between 0.001 and 1. The model provides key insights into the physical origins of previously observed limits on the achievable aspect ratios and area ratios achieved by imprint patterning. The research has been presented at conferences and has been published in conference proceedings, with a detailed article to be published in a journal.

During the research the sponsoring company became Polymer Vision. It was felt that there were other areas of research that would provide a greater benefit, which were also characterising materials used for microelectronics. The research looked into the effect of crinkling, which was felt to be a process causing defects during the manufacturing process by Polymer Vision. Explicit finite element (FE) computer models in LS-DYNA were compared to the analytical research on crinkling, to find the best variables to model the effect. It was

found that the Belytschko-Lin-Tsay shell element offered the best capabilities, offering similar results to analytical calculations on developable cone structures whilst solving the quickest.

An experimental set-up was conceived that would enable the research to independently vary attributes to understand their effect. Using an adapted three-point bend test, PEN sheets were analysed using digital image correlation (DIC) whilst being displaced. The same set-up was modelled using finite element analysis to validate the experimental results. The DIC results showed a variation in strain with plunger displacement before the visual appearance of a developable cone and that it occurred between 0.1 and 0.4 % *in-plane* strain. The FE data showed a similar trend to the DIC results, showing a change in strain once a d-cone began to form. Improvements and suggestions were then made advising how to make the DIC and FE models more accurate. To the author's knowledge, this is the first study to produce comparisons between numerical and experimental analysis of the d-cone phenomenon in flexible polymer sheets and the first study in developable cones using DIC techniques. The results are to be published in an article.

7.1 FUTURE WORK

The research undertaken covered a variety of topics important to the polymeric electronic industry. However, improvements and additions can be made to the work described in this thesis. This section provides recommendations for furthering the work presented here.

The study into the process capabilities of NIL is a useful tool for the industry to use as a gauge on progress, helping to track the technique's advancement whilst making available the current capabilities to the public. One of the recurring issues faced was the sparsity of the data available in the open literature. If NIL is to achieve widespread application it is vital that its process capabilities are quantitatively defined so that the process can be used where it can be shown to offer an advantage. This work should be regarded as an initial step to defining NIL's process capabilities with regular updates being made to the 'maps'.

The de-embossing model is the first step to producing an analytical model that will help the industry with a tool that improves stamp design and configuration. The model in its current configuration has the potential to show further relationships between other variable combinations not presented in this thesis. However, the current model is not perfect, using discretized equations and being limited to a unit cell of a cylindrical post. Future versions could use the theory presented by Filon [121] to keep the model completely analytical as referred to in Section 4.2.3. Other opportunities are available to improve its capabilities, such as using a varying shear stress along the length of the polymer post, which is a more realistic scenario than assuming a constant value, or by making the model solve for viscoelastic

scenarios, again a more realistic assumption. The current model was never critiqued against FE or experimental analysis and was only compared to generalised knowledge gathered from published literature on NIL. The model needs to be validated by FE modelling of the same unit cell and chosen variables. Also, NIL experiments need to be undertaken whose parameters can be varied and specifically chosen to match those varied in the semi-analytical model to enable a comparison and evaluation of its capabilities.

It has been difficult to provide definitive information from the DIC and FE results. The main causes for this were the errors introduced through the experiment from the various parameters and the limitations of the experimental set-up. These caused inaccuracies and have prevented results from being gathered. The lack of data that could be gathered from the crescent singularity in the DIC experiments and the lack of dependable FE models due to the hourglassing also hindered the results. This in turn has affected the ability to draw conclusions from the results, as one of the goals of the research was to find correlations between the variables and the strains produced. However, the experiments have provided the author with the knowledge of what can be done to make them more successful in future and the following sections discuss improvements that should be made to the experimental and FE analysis techniques.

7.1.1 DIC data capture improvement

Using a sampling frequency of 4 images per mm of the plunger movement has proven to be too low. It does not capture the moment a ‘pinched’ form ‘snaps’ into a d-cone, which might prove useful in understanding the phenomenon. It also does not provide enough data points, which would help the Vic3D software to solve with better accuracy; whether by overcoming data fall out or by following the termini better, but would also help the researcher to understand what is happening graphically in better detail, especially when the strain variation with plunger displacement changes, which is extremely important with regard to the onset of a crescent singularity. Increasing the sampling frequency increases the reliability of the results by reducing the movement between each image. Future experiments should use a minimum sampling frequency of 10 images per mm of plunger displacement.

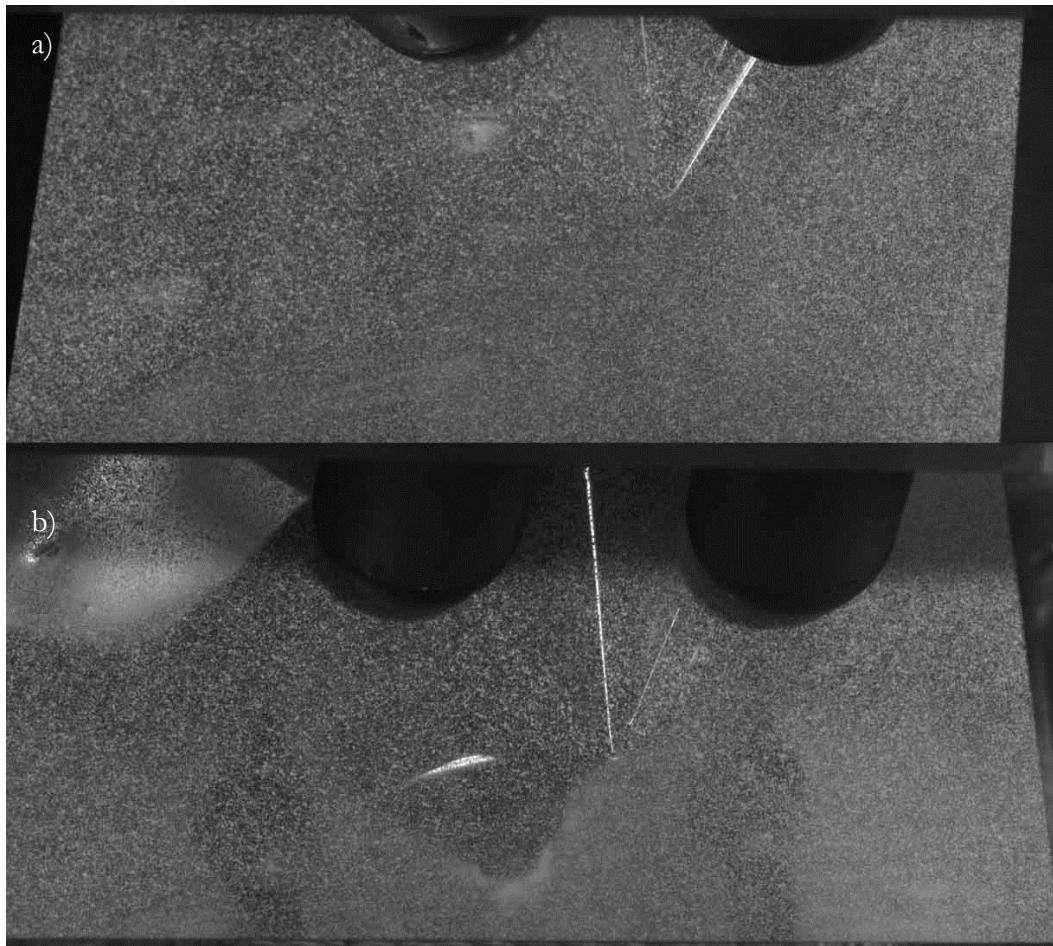


Figure 7.1: DIC image through a) right camera; b) left camera, displaying hazy regions and glare.

The DIC data collected is unfortunately not as consistent or as credible as expected. Due to data fall out, there were fewer results than image sets. The main causes of data fallout were not understood until after the experiment, and emerged during the processing of the results. These were glare, reflections and visual loss of the tracked region. Glare and reflections from the sheet surface significantly affected the quality of the images. During testing, the system provides the user with visual footage through the right hand camera, an example is shown in Figure 7.1 a). Glare can be seen in this image, which prevents the camera from capturing the location of the speckles in and around the target area, but because of the configuration used, the left hand camera images showed a general haze over the majority of the speckled area, shown in Figure 7.1 b). This was due to the ‘direct’ lighting used⁸ and the characteristic transparency of the sheet brought about by spray-painting only one colour. The effects of the glare and haziness intensified at larger plunger displacements, which makes speckle recognition in the Vic3D software extremely difficult, causing a resulting loss in data.

⁸ A gauze had been added to diffuse the light but with little success.

Other effects that prevented data capture were related to the termini not being picked up by the cameras. Too much displacement of the sheet makes it impossible to follow the terminus, preventing the software from generating the strain data. This was seen for an x_6 of 20 mm, as the cameras, which remain static throughout, could not see the termini end locations as they moved out of view. For large distortions, the sheets developed steep slopes facing away from the camera from the fixed edge up to the crescent singularity, causing the contrast between the speckles and sheet to reduce. This tended to happen to a greater extent for shorter values of x_6 . The outcome produced regions of low contrast; which appeared grey in the images and not defining a clear speckle pattern, preventing the software from mapping the movement and gathering strain information. The effect can be seen at the bottom of Figure 7.2.

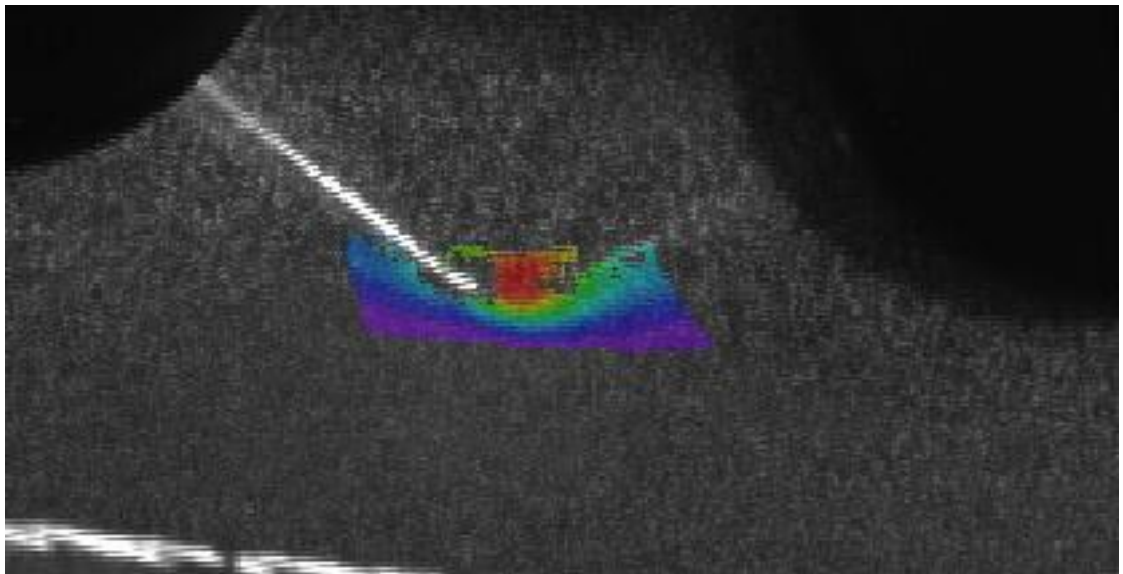


Figure 7.2: DIC correlated strain data. Data loss can be seen due to glare and regions of low contrast.

The visual effects that have caused the data fallout in the analyses could be severely reduced. Instead of spray-painting the sheets to create a speckled pattern, microcontact printing could be used. This would create a complete film of a random pattern, with a resolution as small as $10\text{ }\mu\text{m}$, sufficient for the Vic3D software and only $1\text{ }\mu\text{m}$ thick instead, reducing the stiffening effect caused by adding another layer. A completely patterned surface would reduce the effect of local strain variations that are created by the uneven speckle pattern currently used. It would also reduce or possibly prevent glare occurring, as the matt paint would reflect less than the glossy transparent PEN material, improving data capture. More ambient lighting instead of a spotlight would enable a larger aperture to be used that would keep the sheet in focus while being displaced, reducing the potential for glare. Finally, the jig could be slightly altered so it may be used to the side of a tensile test machine: currently the plungers are in line with the machine. This would allow the placement of the cameras to be almost directly above the sheet, which would enable a continuous line of sight with the crescent singularity.

7.1.2 FE data discussion

Using models made up of more elements and/or with fully integrated elements, as discussed in Section 5.6, would produce more detailed and accurate results. These options would reduce or eliminate hourglassing respectively, making the models behave in a more realistic manner, such as by using fully integrated shell (FIS) elements suggested in Section 5.5. The drawback of such modelling would be much longer solving times. However, facilities are available for such modelling, such as Iridis 3 at the University of Southampton, especially if a multi-processor LS-DYNA license is made available, which could reduce the solving times. More in-depth knowledge of the FE software and experience in using advanced aspects of the knowledge base; the effects and variables within LS-DYNA, would be useful to aid modelling and would benefit this research.

Both the DIC and FE results are for the terminus. However, as reported, the DIC and FE analyses did not always follow the location of the crescent singularity throughout the analyses. Future DIC data analysis and FE modelling should look to track the location of the crescent singularity more precisely. This could be achieved through a programming script, such as those previously created in MATLAB shown in Appendix F, which would find the element with the greatest strain at each timestep and follow its progression, regardless of the element. This would provide data that is directly comparable, which describes more comprehensively the progression of the crescent singularity: the actual strains at that location, which may in turn reveal a correlation between the crescent singularity displacement with the variables tested.

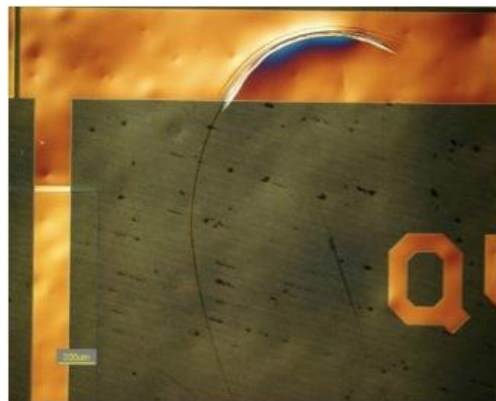


Figure 7.3: Fracture possibly caused by crescent singularity movement, Polymer Vision 2008.

Finally, mapping the movement of the d-cone in relation to the sheet may also answer another phenomenon seen by Polymer Vision. Figure 7.3 shows a tear in one of their sheets. Together with the knowledge of when the strain at the crescent singularity is about to cause failure, mapping its movement may also explain the arc lines of fracture as the ‘drawing’ effect of the crescent singularity occurs.

REFERENCES

1. The Nobel Foundation©. *The Nobel Prize in Chemistry 2000*. Nobel Web AB; 2009. Available from: http://nobelprize.org/nobel_prizes/chemistry/laureates/2000/index.html. (accessed 11th September 2009);
2. Hecker K. *Organic and Printed Electronics*. Organic Electronics Association. 2009.
3. Tsutsui T, Fujita K. The Shift from "Hard" to "Soft" Electronics. *Advanced Materials*. 2002; 14(13-14):949-52.
4. Chou SY, Krauss PR, Renstrom PJ. Imprint of sub-25 nm vias and trenches in polymers. *Applied Physics Letters*. 1995; 67(21):3114-16.
5. Colburn M, Johnson S, Stewart M, Damle S, Bailey T, Choi B, Wedlake M, Michaelson T, Sreenivasan SV, Ekerdt J. Step and flash imprint lithography: a new approach to high-resolution patterning. In: Vladimirovsky Y, editor. *Emerging Lithographic Technologies III*; Santa Clara, CA, USA. 1999. p.379-89.
6. Hirai Y, Konishi T, Kikuta H, Kawata H. Multi-layered resist process in nanoimprint lithography for high aspect ratio pattern. *Microelectronic Engineering*. 2006; 83(4-9):869-72.
7. Nakamatsu K, Tone K, Matsui S. Nanoimprint and lift-off process using poly(vinyl alcohol). *Japanese Journal of Applied Physics, Part 1*. 2005; 44(11):8186-8.
8. Pfeiffer K, Reuther F, Fink M, Gruetzner G, Carlberg P, Maximov I, Montelius L, Seekamp J, Zankovych S, Sotomayor-Torres CM, Schulz H, Scheer H-C. A comparison of thermally and photochemically cross-linked polymers for nanoimprinting. *Microelectronic Engineering*. 2003; 67-68(1):266-73.
9. Hiroshima H, Komuro M, Kasahara N, Kurashima Y, Taniguchi J. Elimination of pattern defects of nanoimprint under atmospheric conditions. *Japanese Journal of Applied Physics, Part 1*. 2003; 42(6 B):3849-53.
10. Johnson SC, Bailey TC, Dickey MD, Smith BJ, Kim EK, Jamieson AT, Stacey NA, Ekerdt JG, Willson CG, Mancini DP, Dauksher WJ, Nordquist KJ, Resnick DJ. Advances in step and flash imprint lithography. In: Engelstad RL, editor. *Emerging Lithographic Technologies VII*; Santa Clara, CA, USA. SPIE-Int. Soc. Opt. Eng; 2003. p.197-202.
11. Austin MD, Ge H, Wu W, Li M, Yu Z, Wasserman D, Lyon SA, Chou SY. Fabrication of 5 nm linewidth and 14 nm pitch features by nanoimprint lithography. *Applied Physics Letters*. 2004; 84:5299.
12. Beck M, Graczyk M, Maximov I, Sarwe EL, Ling TGI, Keil M, Montelius L. Improving stamps for 10 nm level wafer scale nanoimprint lithography. *Microelectronic Engineering*. 2002; 61(62):441-8.
13. Finder C, Beck M, Seekamp J, Pfeiffer K, Carlberg P, Maximov I, Reuther F, Sarwe EL, Zankovich S, Ahopelto J. Fluorescence microscopy for quality control in nanoimprint lithography. *Microelectronic Engineering*. 2003; 67:623-8.
14. Park S, Schiff H, Padeste C, Schnyder B, Kotz Ru, Gobrecht J. Anti-adhesive layers on nickel stamps for nanoimprint lithography. *Microelectronic Engineering*. 2004; 73-74:196-201.
15. Resnick DJ, Sreenivasan SV, Willson CG. Step & flash imprint lithography. *Materials Today*. 2005; 8(2):34-42.
16. Islam R, Wieder B, Lindner P, Glinsner T, Schaefer C. One micron precision optically aligned method for hot-embossing and nanoimprinting. In: *Proceedings of IEEE Sensors 2002*; Orlando, FL, USA. IEEE; 2002. p.931-5.
17. Choi J, Nordquist K, Cherala A, Casoose L, Gehoski K, Dauksher WJ, Sreenivasan SV, Resnick DJ. Distortion and overlay performance of UV step and repeat imprint lithography. *Microelectronic Engineering*. 2005; 78:633-40.

18. Li M, Chen L, Zhang W, Chou SY. Pattern transfer fidelity of nanoimprint lithography on six-inch wafers. *Nanotechnology*. 2003; 14(1):33-6.
19. Scheer HC, Wissen M, Bogdanski N. Issues in nanoimprint processes: the imprint pressure. In: *Microprocesses and Nanotechnology Conference Digest of Papers 2004 International*; 26-29 October; Hotel Hankyu Expo park, Osaka, Japan. Tokyo, Japan: Japan Society of Applied Physics; 2004. p.52-3.
20. Cross GLW, O'Connell BS, Pethica JB, Schulz H, Scheer HC. Instrumented indentation testing for local characterisation of polymer properties after nanoimprint. *Microelectronic Engineering*. 2005; 78-79:618-24.
21. Rowland HD, Sun AC, Schunk PR, King WP. Impact of polymer film thickness and cavity size on polymer flow during embossing: toward process design rules for nanoimprint lithography. *Journal of Micromechanics and Microengineering*. 2005; 15(12):2414-25.
22. Bonnecaze RT, Reddy S. Simulation of fluid flow in the step and flash imprint lithography process. *Microelectronic Engineering*. 2005; 82(1):60-70.
23. Rowland HD, Sun AC, Schunk PR, King WP. Impact of polymer film thickness and cavity size on polymer flow during embossing: toward process design rules for nanoimprint lithography. *Journal of Micromechanics and Microengineering*. 2005; 15(12):2414-25.
24. Scheer HC, Bogdanski N, Wissen M. Issues in nanoimprint processes: the imprint pressure. *Japanese Journal of Applied Physics*. 2005; 44(7B):5609-16.
25. Chou SY, Krauss PR, Renstrom PJ. Nanoimprint lithography. *Journal of Vacuum Science & Technology B*. 1996; 14(6):4129-33.
26. Lin C-H, Chen R, Su C-C, Chang F-Y. Ultrasonics for nanoimprint lithography. In: *5th IEEE Conference on Nanotechnology*; 15 July; Nagoya, Japan. IEEE, Piscataway, NJ 08855-1331, United States; 2005. p.647-50.
27. Tan H, Kong L, Li M, Steere C, Koecher L. Current status of Nanonex nanoimprint solutions. In: Mackay RS, editor. *Emerging Lithographic Technologies VIII*; 20th May; Bellingham, WA, USA. SPIE; 2004. p.213-21.
28. Bender M, Otto M, Hadam B, Spangenberg B, Kurz H. Multiple imprinting in UV-based nanoimprint lithography: related material issues. *Microelectronic Engineering*. 2002; 61:407-13.
29. Chou SY, Krauss PR, Zhang W, Guo L, Zhuang L. Sub-10 nm imprint lithography and applications. *Journal of Vacuum Science & Technology B*. 1997; 15(6):2897-904.
30. Jaszewski RW, Schiff H, Gobrecht J, Smith P. Hot embossing in polymers as a direct way to pattern resist. *Microelectronic Engineering*. 1998; 41-42:575-8.
31. Colburn M, Byung Jin C, Sreenivasan SV, Bonnecaze RT, Willson CG. Ramifications of lubrication theory on imprint lithography. *Microelectronic Engineering*. 2004; 75(3):321-9.
32. Roy E, Kanamori Y, Belotti M, Chen Y. Enhanced UV imprint ability with a tri-layer stamp configuration. *Microelectronic Engineering*. 2005; 78:689-94.
33. Bender M, Plachetka U, Ran J, Fuchs A, Vratzov B, Kurz H, Glinsner T, Lindner F. High resolution lithography with PDMS molds. *Journal of Vacuum Science and Technology B*. 2004; 22(6):3229-32.
34. Pfeiffer K, Fink M, Ahrens G, Gruetzner G, Reuther F, Seekamp J, Zankovych S, Sotomayor Torres CM, Maximov I, Beck M. Polymer stamps for nanoimprinting. *Microelectronic Engineering*. 2002; 61:393-8.
35. Cheng X, Li D, Guo LJ. A hybrid mask–mould lithography scheme and its application in nanoscale organic thin film transistors. *Nanotechnology*. 2006; 17(4):927-32.
36. Gourgon C, Perret C, Tallal J, Lazzarino F, Landis S, Joubert O, Pelzer R. Uniformity across 200 mm silicon wafers printed by nanoimprint lithography. *Journal of Physics D Applied Physics*. 2005; 38(1):70-3.

37. Sim Y-s, Kim K-d, Jeong J-h, Sohn H, Lee E-s, Lee S-c. Wafer deformation in ultraviolet-nanoimprint lithography using an element-wise patterned stamp. *Microelectronic Engineering*. 2005; 82(1):28-34.
38. Obducat. *Products*. Malmö 2006. Available from: <http://www.obducat.com/Default.aspx?ID=32>. (accessed 11 December 2011);
39. Vratzov B, Fuchs A, Lemme M, Henschel W, Kurz H. Large scale ultraviolet-based nanoimprint lithography. *Journal of Vacuum Science & Technology B*. 2003; 21:2760.
40. Abdo AY, Zheng L, Wei A, Mikkelsen A, Nellis G, Engelstad RL, Lovell EG. Simulating fabrication and imprinting distortions in step-and-flash imprint lithography templates. *Microelectronic Engineering*. 2004; 73:161-6.
41. Sim Y, Kim K, Jeong J, Sohn H, Lee E, Lee S. Wafer deformation in ultraviolet-nanoimprint lithography using an element-wise patterned stamp. *Microelectronic Engineering*. 2005; 82(1):28-34.
42. Lazzarino F, Gourgon C, Schiavone P, Perret C. Mold deformation in nanoimprint lithography. *Journal of Vacuum Science & Technology B*. 2004; 22:3318.
43. Schulz H, Wissen M, Bogdanski N, Scheer HC, Mattes K, Friedrich C. Impact of molecular weight of polymers and shear rate effects for nanoimprint lithography. *Microelectronic Engineering*. 2006; 83(2):259-80.
44. Wang JJ, Chen L, Tai S, Deng X, Sciortino PF, Deng J, Liu F. Wafer-based nanostructure manufacturing for integrated nano optic devices. *Journal of Lightwave Technology*. 2005; 23(2):474-85.
45. Kim WS, Yoon KB, Bae BS. Nanopatterning of photonic crystals with a photocurable silica–titania organic–inorganic hybrid material by a UV-based nanoimprint technique. *Journal of Materials Chemistry*. 2005; 15:4535-9.
46. Colburn M, Suez I, Choi BJ, Meissl M, Bailey T, Screenivasan SV, Ekerdt JG, Willson CG. Characterization and modeling of volumetric and mechanical properties for step and flash imprint lithography photopolymers. *Journal of Vacuum Science and Technology B*. 2001; 19(6):2685-9.
47. Lecarpentier G. Nanoimprinting Stepper with Hot Embossing and UV-NIL Capability [Presentation]. Presented at: *LITHO2006*; Marseille. 2006. http://www.lithoconf.com/Full%20contributions/Lecarpentier_LITHO2006.pdf (accessed 19 December 2011).
48. Hiroshima H, Komuro M, Kurashima Y, Sang Hoon K, Muneishi T. Step-and-repeat photo-nanoimprint system using active orientation head. *Japanese Journal of Applied Physics, Part 1*. 2004; 43(6B):4012-16.
49. Zhao Y, Cui T. Fabrication of high-aspect-ratio polymer-based electrostatic comb drives using the hot embossing technique. *Journal of Micromechanics and Microengineering*. 2003; 13(3):430-5.
50. Dumond JJ, Low HY, Rodriguez I. Isolated, sealed nanofluidic channels formed by combinatorial-mould nanoimprint lithography. *Nanotechnology*. 2006; 17(8):1975-80.
51. Schulz H, Wissen M, Bogdanski N, Scheer HC, Mattes K, Friedrich C. Choice of the molecular weight of an imprint polymer for hot embossing lithography. *Microelectronic Engineering*. 2005; 78:625-32.
52. Bogdanski N, Wissen M, Ziegler A, Scheer HC. Temperature-reduced nanoimprint lithography for thin and uniform residual layers. *Microelectronic Engineering*. 2005; 78:598-604.
53. Konishi T, Kanakugi T, Toyota H, Kawata H, Hirai Y. Nanoimprint lithography for high aspect ratio patterns. In: *International Microprocesses and Nanotechnology Conference*; 26-29 October; Osaka, Japan. 2004. p.126-7.
54. Wu W, Jung GY, Olynick DL, Straznicki J, Li Z, Li X, Ohlberg DAA, Chen Y, Wang SY, Liddle JA, Tong WM, Williams RS. One-kilobit cross-bar molecular memory circuits at 30-nm half-pitch fabricated by nanoimprint lithography. *Applied Physics A: Materials Science & Processing*. 2005; V80(6):1173-8.

55. Bai P, Auth C, Balakrishnan S, Bost M, Brain R, Chikarmane V, Heussner R, Hussein M, Hwang J, Ingerly D, James R, Jeong J, Kenyon C, Lee E, Lee SH, Lindert N, Liu M, Ma Z, Marieb T, Murthy A, Nagisetty R, Natarajan S, Neiryneck J, Ott A, Parker C, Sebastian J, Shaheed R, Sivakumar S, Steigerwald J, Tyagi S, Weber C, Woolery B, Yeoh A, Zhang K, Bohr M. A 65nm logic technology featuring 35nm gate lengths, enhanced channel strain, 8 Cu interconnect layers, low-k ILD and 0.57 m2 SRAM cell. In: *IEEE International Electron Devices Meeting*; San Francisco, CA, United states. IEEE; 2004. p.657-60.
56. IBM Research. *IBM Research Demonstrates Path for Extending Current Chip-Making Technique*. IBM; 2006. Available from: <http://www-03.ibm.com/press/us/en/pressrelease/19260.wss>. (accessed 5 December 2011);
57. Austin MD, Zhang W, Ge H, Wasserman D, Lyon SA, Chou SY. 6 nm half-pitch lines and 0.04 μm 2 static random access memory patterns by nanoimprint lithography. *Nanotechnology*. 2005; 16(8):1058-61.
58. Esch MB, Kapur S, Irizarry G, Genova V. Influence of master fabrication techniques on the characteristics of embossed microfluidic channels. *Lab Chip*. 2003; 3(2):121-7.
59. Maile BE, Henschel W, Kurz H, Rienks B, Polman R, Kaars P. Sub-10 nm Linewidth and Overlay Performance Achieved with a Fine-Tuned EBPG-5000 TFE Electron Beam Lithography System. *Japanese Journal of Applied Physics*. 2000; 1(39):6836.
60. Hiroshima H, Kurashima Y, Komuro M. Line Width Reproducibility of Photo-Nanoimprints. *Japanese Journal of Applied Physics*. 2005; 44(7B):5622.
61. Sematech. *Accelerating the Next Technology Revolution - 2005 Annual Report* 2005.
62. Trybula W, Wright RL, Adusumilli KM, Goodall RK. An Analysis: Traditional Semiconductor Lithography Versus Emerging Technology (Nano Imprint). In: *Proceedings of the Winter Simulation Conference*; 4-7 December; Orlando, FL, USA. ACM; 2005. p.2218-22.
63. Sreenivasan SV, Willson CG, Schumaker NE, Resnick DJ. Low-cost nanostructure patterning using step and flash imprint lithography. In: Peckerar MC, Michael T. Postek J, editors. *Nanostructure Science, Metrology, and Technology*; 5 September; Gaithersburg, MD, USA. SPIE; 2001. p.187-94.
64. Stetten Fv. FlowMap - Microfluidic Roadmap for the Life Sciences. In: *Microfluidic Symposium*; Hannover Fair, Germany. Licom; 2004.
65. Hara Y. *Hitachi GST Unveils Perpendicular HDDs*. CMP Media; 2006. Available from: <http://www.eetimes.com/electronics-products/other/4084258/Hitachi-GST-unveils-perpendicular-HDDs>. (accessed 5 December 2011);
66. LaPedus M. *Nanoimprint Litho Makes its Mark at SPIE*. CMP Media; 2005. Available from: <http://www.eetimes.com/electronics-news/4068479/Nano-imprint-litho-tool-shipped-to-Toshiba>. (accessed 5 December 2011);
67. Kitade Y, Komoriya H, Maruyama T. Patterned media fabricated by lithography and argon-ion milling. *IEEE Transactions on Magnetics*. 2004; 40(4):2516-8.
68. Albrecht M, Rettner CT, Best ME, Terris BD. Magnetic coercivity patterns for magnetic recording on patterned media. *Applied Physics Letters*. 2003; 83(21):4363-5.
69. Wachenschwanz D, Jiang W, Roddick E, Homola A, Dorsey P, Harper B, Treves D, Bajorek C. Design of a manufacturable discrete track recording medium. *IEEE Transactions on Magnetics*. 2005; 41(2):670-5.
70. Moritz J, Buda L, Dieny B, Nozie`res JP, van de Veerdonk RJM, Crawford TM, Weller D. Writing and reading bits on pre-patterned media. *Applied Physics Letters*. 2004; 84(9):1519-21.
71. Hattori K, Ito K, Soeno Y, Takai M, Matsuzaki M. Fabrication of discrete track perpendicular media for high recording density. *IEEE Transactions on Magnetics*. 2004; 40(4):2510-5.
72. Hand A. *EUV Lithography Makes Important Advances*. 2006. Available from: <http://www.reed->

- electronics.com/semiconductor/article/CA6375403?pubdate=10%2F1%2F06.
(accessed 1 October 2006);
73. Rudmann H, Rossi M. Design and fabrication technologies for ultraviolet replicated micro-optics. *Optical Engineering*. 2004; 43(11):2575-82.
 74. Ahn SW, Lee KD, Kim DH, Lee SS. Polymeric wavelength filter based on a Bragg grating using nanoimprint technique. *IEEE Photonics Technology Letters*. 2005; 17(10):2122-4.
 75. Seekamp J, Zankovych S, Helfer AH, Maury P, Torres CMS, Böttger G, Liguda C, Eich M, Heidari B, Montelius L. Nanoimprinted passive optical devices. *Nanotechnology*. 2002; 13(5):581-6.
 76. Ahn SW, Lee KD, Kim JS, Kim SH, Lee SH, Park JD, Yoon PW. Fabrication of subwavelength aluminum wire grating using nanoimprint lithography and reactive ion etching. *Microelectronic Engineering*. 2005; 78:314-8.
 77. Belotti M, Torres J, Roy E, Pèpin A, Chen Y, Gerace D, Andreani LC, Galli M. Replication of photonic crystals by soft ultraviolet-nanoimprint lithography. *Journal of Applied Physics*. 2006; 99(2):24309-1-4.
 78. Cardinale GF, Skinner JL, Talin AA, Brocato RW, Palmer DW, Mancini DP, Dauksher WJ, Gehoski K, Le N, Nordquist KJ. Fabrication of a surface acoustic wave-based correlator using step-and-flash imprint lithography. *Journal of Vacuum Science & Technology B*. 2004; 22(6):3265-70.
 79. Chu P, Zhan T, Hong FC, Liao L, Hon MH. Fabrication of large-scaled organic light emitting devices on the flexible substrates using low-pressure imprinting lithography. *IEEE Transactions on Electron Devices*. 2005; 52(8):1722-6.
 80. Leising G, Stadlober B, Haas U, Haase A, Palfinger C, Gold H, Jakopic G. Nanoimprinted devices for integrated organic electronics. *Microelectronic Engineering*. 2006; 83(4-9):831-8.
 81. Zhang W, Chou SY. Fabrication of 60-nm transistors on 4-in. wafer using nanoimprint at all lithography levels. *Applied Physics Letters*. 2003; 83(8):1632-4.
 82. Luo G, Maximov I, Adolph D, Graczyk M, Carlberg P, Ghatnekar-Nilsson S, Hessman D, Zhu T, Liu Z, Xu HQ. Nanoimprint lithography for the fabrication of interdigitated cantilever arrays. *Nanotechnology*. 2006; 17(8):1906-10.
 83. Pépin A, Youinou P, Studer V, Lebib A, Chen Y. Nanoimprint lithography for the fabrication of DNA electrophoresis chips. *Microelectronic Engineering*. 2002; 61:927-32.
 84. Mills CA, Martinez E, Bessueille F, Villanueva G, Bausells J, Samitier J, Errachid A. Production of structures for microfluidics using polymer imprint techniques. *Microelectronic Engineering*. 2005; 78:695-700.
 85. Lee N, Kim Y, Kang S, Hong J. Fabrication of metallic nano-stamper and replication of nano-patterned substrate for patterned media. *Nanotechnology*. 2004; 15(8):901-6.
 86. Yong C, Gun-Young J, Ohlberg DAA, Xuema L, Stewart DR, Jeppesen JO, Nielsen KA, Stoddart JF, Williams RS. Nanoscale molecular-switch crossbar circuits. *Nanotechnology*. 2003; 14(4):462-8.
 87. Sakurai M. A single-domain 26 nm-pitch pattern for the XY quantum dot media template. In: *IEEE Conference on Nanotechnology*; 12-14 August; San Francisco, CA, USA. IEEE-NANO; 2003.
 88. Miles J. University of Manchester. Personal Communication. 11 October 2006.
 89. Guo LJ. Recent progress in nanoimprint technology and its applications. *Journal of Physics D: Applied Physics*. 2004; 37(7):123-41.
 90. Cheng X, Li D, Guo LJ. A hybrid mask-mould lithography scheme and its application in nanoscale organic thin film transistors. *Nanotechnology*. 2006; 17(4):927-32.
 91. Obducat. *Mass Production Breakthrough for Obducat's NIL Technology*. Malmö 2006. Available from:
<http://obducat.net.dynamicweb.dk/Default.aspx?ID=428&M=News&PID=383&NewsID=23>. (accessed 30 June 2006);

92. NanoOpto. *Products*. 2006. Available from: <http://www.nanoopto.com/products/index.html>. (accessed 18 September 2006);
93. Balla T, Spearing SM, Monk A. An assessment of the process capabilities of nanoimprint lithography. *Journal of Physics D: Applied Physics*. 2008; 41(17):174001 (10 pp.).
94. Balla T, Reader A, van Aerle N, inventors; *Fabricaiton of Planar Electronic Circuit Devices*. WO 2008/133515 A3 (Patent). 2008.
95. Worgull M, Hetu JF, Kabanemi KK, Hecke M. Modeling and optimization of the hot embossing process for micro- and nanocomponent fabrication. *Microsystem Technologies*. 2006; 12(10-11):947-52.
96. Heyderman LJ, Schiff H, David C, Gobrecht J, Schweizer T. Flow behaviour of thin polymer films used for hot embossing lithography. *Microelectronic Engineering*. 2000; 54(3-4):229-45.
97. Scheer HC, Schulz H. A contribution to the flow behaviour of thin polymer films during hot embossing lithography. *Microelectronic Engineering*. 2001; 56(3-4):311-32.
98. Hiroshima H. Quick cavity filling in UV nanoimprint using pentafluoropropane. *Japanese Journal of Applied Physics*. 2008; 47(6):5151-5.
99. Leveder T, Landis S, Davoust L, Chaix N. Flow property measurements for nanoimprint simulation. *Microelectronic Engineering*. 2007; 84(5-8):928-31.
100. O'Connell B, Cross GLW, Pethica JB, Oliver W. Nanorheology of squeezed polymer films. In: *Conference on Nanotechnology*; 12-14 August; San Francisco, CA, USA. IEEE-NANO; 2003. p.793-6.
101. Cross G, Langford R, O'Connell B, Pethica J. The mechanics of nanoimprint forming. In: *Fundamentals of Nanoindentation and Nanotribology III*; 29 November - 3 December; Boston, MA, USA. Materials Research Society; 2005. p.R1.6.1.
102. Cross GLW. The production of nanostructures by mechanical forming. *Journal of Physics D: Applied Physics*. 2006; (20):R363.
103. Lei KF, Li WJ, Yam Y. Effects of contact-stress on hot-embossed PMMA microchannel wall profile. *Microsystem Technologies*. 2005; 11(4-5):353-7.
104. Jeong JH, Choi YS, Shin YJ, Lee JJ, Park KT, Lee ES, Lee SR. Flow behavior at the embossing stage of nanoimprint lithography. *Fibers and Polymers*. 2002; 3(3):113-9.
105. Mendels D-A. Multi-scale modelling of nano-imprint lithography. In: *International Society for Optical Engineering*; San Jose, CA, United States. SPIE; 2006. p.615113.
106. Yu Z, Gao H, Chou SY. RIMS (real-time imprint monitoring by scattering of light) study of pressure, temperature and resist effects on nanoimprint lithography. *Nanotechnology*. 2007; 18(6):065304.
107. Jung GY, Li Z, Wu W, Ganapathiappan S, Li X, Olynick DL, Wang SY, Tong WM, Williams RS. Improved pattern transfer in nanoimprint lithography at 30 nm half-pitch by substrate-surface functionalization. *Langmuir*. 2005; 21(14):6127-30.
108. Worgull M, Hecke M. New aspects of simulation in hot embossing. *Microsystem Technologies*. 2004; 10(5):432-7.
109. Worgull M, Hecke M, Schomburg WK. Large-scale hot embossing. *Microsystem Technologies*. 2005; 12(1-2 SPEC ISS):110-5.
110. Yuhua G, Gang L, Yin X, Yangchao T. Study of the demolding process - implications for thermal stress, adhesion and friction control. *Journal of Micromechanics and Microengineering*. 2007; 17(1):9-19.
111. Song Z. *Study of Demolding Process in Thermal Imprint Lithography via Numerical Simulation and Experimental Approaches*. Baton Rouge: Louisiana State Univeristy; 2007.
112. Maboudian R, Carraro C. Surface engineering for reliable operation of MEMS devices. *Journal of Adhesion Science and Technology*. 2003; 17(4):583-91.
113. Maboudian R, Ashurst W, Carraro C. Tribological challenges in micromechanical systems. *Tribology letters*. 2002; 12(2):95-100.

114. Ashurst W, Yau C, Carraro C, Maboudian R, Dugger M. Dichlorodimethylsilane as an anti-stiction monolayer for MEMS: a comparison to the octadecyltrichlorosilane self-assembled monolayer. *Journal of Microelectromechanical Systems*. 2001; 10(1):41-9.
115. Jang E-J, Park Y-B, Lee H-J, Choi D-G, Jeong J-H, Lee E-S, Hyun S. Effect of surface treatments on interfacial adhesion energy between UV-curable resist and glass wafer. *International Journal of Adhesion and Adhesives*. 2009; 29(6):662-9.
116. Tallal J, Gordon M, Berton K, Charley AL, Peyrade D. AFM characterization of anti-sticking layers used in nanoimprint. *Microelectronic Engineering*. 2006; 83(4-9):851-4.
117. Taniguchi J, Kawasaki T, Tokano Y, Kogo Y, Miyamoto L, Komuro M, Hiroshima H, Sakai N, Tada K. Measurement of adhesive force between mold and photocurable resin in imprint technology. In: *International Microprocesses and Nanotechnology Conference*; Shimane, Japan. Japan Soc. Appl. Phys; 2001. p.4194-7.
118. Houle FA, Rettner CT, Miller DC, Sooriyakumaran R. Antiadhesion considerations for UV nanoimprint lithography. *Applied Physics Letters*. 2007; 90(21):213103.
119. Aveston J, Kelly A, Cooper GA. Single and multiple fracture (Single and multiple fractures in brittle matrix fibrous composites, discussing fracture energetics, stress-strain curves and hysteresis effects). In: *The Properties of Fibre Composites*; 4 November; Teddington, Middx, England; United Kingdom. IPC Science and Technology Press Ltd; 1971. p.24-6.
120. Zok FW, Spearing SM. Matrix crack spacing in brittle matrix composites. *Acta Metallurgica et Materialia*. 1992; 40(8):2033-43.
121. Filon LNG. On the Elastic Equilibrium of Circular Cylinders under Certain Practical Systems of Load. *Philosophical Transactions of the Royal Society of London Series A*. 1902; 198:147-233.
122. Boussinesq J. *Application des potentiels: à l'étude de l'équilibre et du mouvement des solides élastiques*. Paris: Gauthier-Villars; 1885.
123. Love AEH. The Stress Produced in a Semi-Infinite Solid by Pressure on Part of the Boundary. *Philosophical Transactions of the Royal Society of London Series A*. 1929; 228:377-420.
124. Igor M. Elliptic Integrals of three types and Jacobian Elliptic Functions. Matlab Central. 2005. Available from: <http://www.mathworks.com/matlabcentral/fileexchange/8805>. (accessed 23 April 2009)
125. Bennett JA, Young RJ. The effect of fibre-matrix adhesion upon crack bridging in fibre reinforced composites. *Composites Part A: Applied Science and Manufacturing*. 1998; 29(9-10):1071-81.
126. Chohan V, Galiotis C. Interfacial measurements and fracture characteristics of 2D microcomposites using remote laser Raman microscopy. *Composites Part A: Applied Science and Manufacturing*. 1996; 27(9):881-8.
127. Galiotis C, Chohan V, Paipetis A, Vlattas C. Interfacial measurements and fracture characteristics of single and multi-fiber composites by remote laser Raman microscopy. In: Spragg CJ, Drzal LT, editors. *The Symposium on Fiber, matrix, and interface properties*; 14 November; Phoenix, AZ, USA. ASTM; 1996. p.19-33.
128. Piggott MR, Xiong Y, editors. Direct observation of debonding in fiber pull-out specimens 1996; Phoenix, AZ, USA: ASTM.
129. Balla T, Spearing SM. Optimisation of Micro and Nano-Imprinting. In: *Joint ASCE-ASME-SES Conference on Mechanics and Materials*; 24-27 June; Virginia Tech. ASCE-ASME-SES; 2009.
130. Marder M, Deegan RD, Sharon E. Crumpling, buckling, and cracking: Elasticity of thin sheets. *Physics Today*. 2007; 60(2):33-8.
131. Gauss C. *General investigations of curved surfaces of 1827 and 1825*: The Princeton University Library; 1902.
132. Rayleigh JWS. *The Theory of Sound*. 2nd ed. London: Macmillan; 1842.

133. Richards R. Introduction. *Principles of Solid Mechanics*: CRC Press; 2001.
134. Cerda E, Mahadevan L. Confined developable elastic surfaces: cylinders, cones and the Elastica. *Proceedings of the Royal Society A-Mathematical Physical and Engineering Sciences*. 2005 Mar; 461(2055):671-700.
135. Witten TA. Stress focusing in elastic sheets. *Reviews of Modern Physics*. 2007 Apr-Jun; 79(2):643-75.
136. Timoshenko S, Lessells J. *Applied Elasticity*: Westinghouse Technical Night School Press; 1925.
137. Pomeau Y. Buckling of thin plates in the weakly and strongly nonlinear regimes. *Philosophical Magazine Part B*. 1998; 78(2):235-42.
138. Witten TA, Li H. Asymptotic Shape of a Fullerene Ball. *Europhysics Letters*. 1993; 23(1):51-5.
139. Kergosien YL, Gotoda H, Kunii TL. Bending and Creasing of Virtual Paper. *Computer Graphics and Applications*. 1994 Jan; 14(1):40-8.
140. Amar MB, Pomeau Y. Crumpled paper. *Proceedings of the Royal Society of London, Series A*. 1997; 453(1997):729-55.
141. Chaieb S, Melo F. Crescent singularities and stress focusing in a buckled thin sheet: Mechanics of developable cones. *Physical Review E*. 1999 Nov; 60(5):6091-103.
142. Cerda E, Mahadevan L. Conical surfaces and crescent singularities in crumpled sheets. *Physical Review Letters*. 1998 Mar; 80(11):2358-61.
143. Cerda E, Chaieb S, Melo F, Mahadevan L. Conical dislocations in crumpling. *Nature*. 1999 Sep; 401(6748):46-9.
144. Chaieb S, Melo F. From creases to conical deflections in a buckled thin sheet: stress focusing vs singularities in strong deformations of a thin elastic sheet. *Journal of the Mechanics and Physics of Solids*. 2000 Mar; 48(3):565-79.
145. Farmer SM, Calladine CR. Geometry of "developable cones". *International Journal of Mechanical Sciences*. 2005 Apr-May; 47(4-5):509-20.
146. Liang T, Witten TA. Crescent singularities in crumpled sheets. *Physical Review E*. 2005 Jan; 71(1).
147. Balankin AS, Huerta OS, Cortes Montes De Oca R, Ochoa DS, Martinez Trinidad J, Mendoza MA. Intrinsically anomalous roughness of randomly crumpled thin sheets. *Physical Review E*. 2006; 74(6).
148. Das M, Vaziri A, Kudrolli A, Mahadevan L. Curvature condensation and bifurcation in an elastic shell. *Physical Review Letters*. 2007 Jan; 98(1).
149. Guven J, Muller MM. How paper folds: bending with local constraints. *Journal of Physics A-Mathematical and Theoretical*. 2008 Feb; 41(5).
150. DiDonna BA. Scaling of the buckling transition of ridges in thin sheets. *Physical Review E*. 2008 Jul; 66(1).
151. Edeko E. *Simulation of Birdstrike on Stiffened Composite Panels* [MSc]: Cranfield University; 2007.
152. ANSYS® Academic Research. Chapter 4. Element Library. *Release 110 Documentation for ANSYS*. Canonsburg 2007.
153. Teijin DuPont Films. *TEONEX® Q83*, Center RDPSD.
154. ANSYS® Academic Research. Commands reference. *Release 110 Documentation for ANSYS*. Canonsburg 2007.
155. Livermore Software Technology Corporation. Section 8: *Control_Shell. *LS-DYNA® Keyword User's Manual*. Version 971/Release 4 ed 2009. p. 627.
156. Livermore Software Technology Corporation. Section 10.6. Fully Integrated Hughes-Liu Shells. *LS-DYNA® Theory Manual* 2006. p. 10.2.
157. Livermore Software Technology Corporation. Section 7. Belytschko-Lin-Tsay Shell. *LS-DYNA® Theory Manual* 2006. p. 7.1.
158. Livermore Software Technology Corporation. Section 9. Type 16: Fully Integrated Shell. *LS-DYNA® Theory Manual* 2006. p. 9.1.

159. Livermore Software Technology Corporation. Section 7.6. Belytschko-Wong-Chiang Improvements. *LS-DYNA® Theory Manual* 2006. p. 7.9.
160. Livermore Software Technology Corporation. Section 16: *Hourglass. *LS-DYNA® Keyword User's Manual*. Version 971/Release 4 ed 2009. p. 850.
161. ANSYS® Academic Research. Chapter 9. Hourglassing. *Release 110 Documentation for ANSYS*. Canonsburg 2007.
162. Lichtenberger R. LIMESS Messtechnik und Software GmbH. Personal Communication. 19 August 2010.

APPENDIX A: PUBLICATIONS

1. Balla T, Spearing SM and Monk A. *An assessment of the process capabilities of nanoimprint lithography*. Journal of Physics D: Applied Physics, 2008. **41**(17): p. 174001 (10 pp.).
2. Balla T and Spearing SM, editors. Optimisation of Micro and Nano-Imprinting. *Joint ASCE-ASME-SES Conference on Mechanics and Materials*; 2009 24-27 June; Virginia Tech.

UNDER REVIEW

1. Balla T and Spearing SM. *Optimization of Micro and Nanoimprint De-Embossing by Elastic Fracture Modelling*. Journal of Microelectronic Engineering, 2012.

APPENDIX B: COMPANY QUESTIONNAIRE

1. Do you sell your products worldwide?
2. Who is your biggest buyer?
3. How big are the devices?
4. What are the smallest dimensions on your devices?
5. What are important process drivers/inputs in the creation of your products? (i.e. materials, time, cost) and why?
6. Is pattern size important in your design? Whether in the fabrication process or the final device?
7. How many masks do you use to make your device?
8. What fabrication steps do you use to make your device?
9. What fabrication specifications are needed for your products (i.e. class 100 environment, no use of Au)?
10. From starting a set of wafers, how quickly do you expect your products to be fabricated?
11. When you produce/design your devices, what process alterations would make your product better or otherwise would be beneficial?
12. What tolerances are acceptable?
13. What materials do you use?
14. Would you prefer to make your device from other materials and why?
15. Is complete creation of device in one process path important to you
16. What part of the fabrication process would you like to see improved to benefit your product?
17. Do you use nanoimprint lithography? Why?
18. Could you suggest anybody else that I should speak to?

APPENDIX C: PATENT

(12) INTERNATIONAL APPLICATION PUBLISHED UNDER THE PATENT COOPERATION TREATY (PCT)

(19) World Intellectual Property Organization
International Bureau



(43) International Publication Date
6 November 2008 (06.11.2008)

PCT

(10) International Publication Number
WO 2008/133515 A3

- (51) International Patent Classification:
H01L 51/10 (2006.01) *H01L 51/52* (2006.01)
- (21) International Application Number:
PCT/NL2008/050255
- (22) International Filing Date: 25 April 2008 (25.04.2008)
- (25) Filing Language: English
- (26) Publication Language: English
- (30) Priority Data:
0708032.8 25 April 2007 (25.04.2007) GB
- (71) Applicant (for all designated States except US): **POLYMER VISION LIMITED** [NL/NL]; High Tech Campus 48, NL-5656 AE Eindhoven (NL).
- (72) Inventors; and
- (75) Inventors/Applicants (for US only): **READER, Alec** [GB/GB]; c/o Innos Limited, Second Avenue, Millbrook Industrial Estate, Southampton SO15 0DJ (GB). **VAN AERLE, Nicolaas Aldegonda Jan Maria** [NL/NL]; Stiffelio 13, NL-5629 NL Eindhoven (NL). **BALLA, Tobias**; c/o Material Research Group, 3025 Eustice Building, University of Southampton, Southampton SO17 1BJ (GB).
- (74) Agent: **HATZMANN, M., J.**; Vereenigde, Johan de Wittlaan 7, NL-2517 JR Den Haag (NL).
- (81) Designated States (unless otherwise indicated, for every kind of national protection available): AE, AG, AL, AM, AO, AT, AU, AZ, BA, BB, BG, BH, BR, BW, BY, BZ, CA, CH, CN, CO, CR, CU, CZ, DE, DK, DM, DO, DZ, EC, EE, EG, ES, FI, GB, GD, GE, GH, GM, GT, HN, HR, HU, ID, IL, IN, IS, JP, KE, KG, KM, KN, KP, KR, KZ, LA, LC, LK, LR, LS, LT, LU, LY, MA, MD, ME, MG, MK, MN, MW, MX, MY, MZ, NA, NG, NI, NO, NZ, OM, PG, PH, PL, PT, RO, RS, RU, SC, SD, SE, SG, SK, SL, SM, SV, SY, TJ, TM, TN, TR, TT, TZ, UA, UG, US, UZ, VC, VN, ZA, ZM, ZW.
- (84) Designated States (unless otherwise indicated, for every kind of regional protection available): ARIPO (BW, GH, GM, KE, LS, MW, MZ, NA, SD, SL, SZ, TZ, UG, ZM, ZW), Eurasian (AM, AZ, BY, KG, KZ, MD, RU, TJ, TM), European (AT, BE, BG, CH, CY, CZ, DE, DK, EE, ES, FI, FR, GB, GR, HR, HU, IE, IS, IT, LT, LU, LV, MC, MT, NL, NO, PL, PT, RO, SE, SI, SK, TR), OAPI (BF, BJ, CF, CG, CI, CM, GA, GN, GQ, GW, ML, MR, NE, SN, TD, TG).
- Published:
— with international search report

[Continued on next page]

(54) Title: FABRICATION OF PLANAR ELECTRONIC CIRCUIT DEVICES

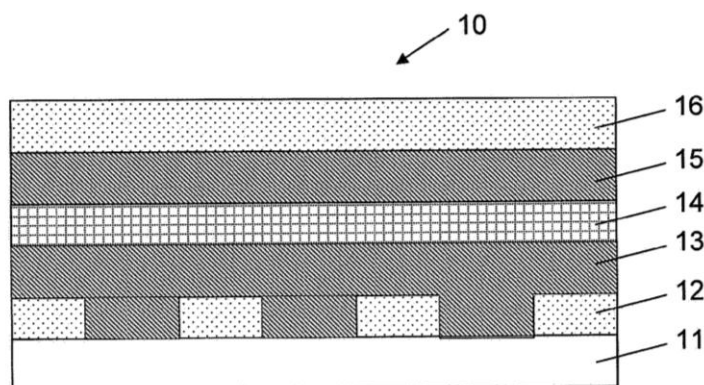


Fig 1

(57) Abstract: A method is provided of fabricating a multilayer planar electronic circuit device on a substrate comprising the steps providing a patterned layer of a first conducting material, depositing a layer of a first insulating material and providing a patterned layer of a second conducting material. The method enables the fabrication of complex electronic circuit devices by depositing core material layers and forming the required conducting structures using an imprinting technique. High tolerances are possible at fast processing speed, while keeping processing material costs low.

WO 2008/133515 A3

APPENDIX D: LOVE'S RESULTS COMPARISON

Table a: Dimensionless variables and stresses calculated by Love.

414

A. E. H. LOVE ON STRESS PRODUCED IN A SEMI-INFINITE

TABLE I.

ϕ .	$k = \sin 5^\circ$.		$k = \sin 15^\circ$.		$k = \sin 30^\circ$.		$k = \sin 50^\circ$.	
	ρ/a .	z/a .	ρ/a .	z/a .	ρ/a .	z/a .	ρ/a .	z/a .
0	0.840	0	0.589	0	0.323	0	0.132	0
10	0.842	0.028	0.593	0.072	0.338	0.117	0.136	0.152
20	0.849	0.055	0.607	0.143	0.354	0.235	0.146	0.311
30	0.860	0.081	0.631	0.213	0.382	0.357	0.164	0.483
40	0.875	0.105	0.665	0.277	0.424	0.483	0.195	0.676
50	0.894	0.127	0.710	0.346	0.484	0.615	0.244	0.901
60	0.916	0.145	0.766	0.406	0.566	0.752	0.323	1.17
70	0.942	0.160	0.833	0.460	0.675	0.892	0.452	1.51
80	0.970	0.170	0.911	0.504	0.819	1.03	0.663	1.91
90	1	0.175	1	0.536	1	1.15	1	2.28
100	1.03	0.175	1.10	0.553	1.22	1.26	1.51	2.88
110	1.06	0.169	1.20	0.552	1.48	1.32	2.21	3.33
120	1.09	0.158	1.31	0.530	1.77	1.33	3.10	3.63
130	1.12	0.142	1.41	0.487	2.07	1.27	4.10	3.70
140	1.14	0.120	1.50	0.422	2.36	1.14	5.14	3.47
150	1.16	0.094	1.58	0.337	2.62	0.934	6.10	2.94
160	1.18	0.065	1.65	0.235	2.82	0.664	6.87	2.14
170	1.19	0.033	1.69	0.121	2.96	0.345	7.37	1.12
180	1.19	0	1.70	0	3	0	7.55	0

TABLE II.

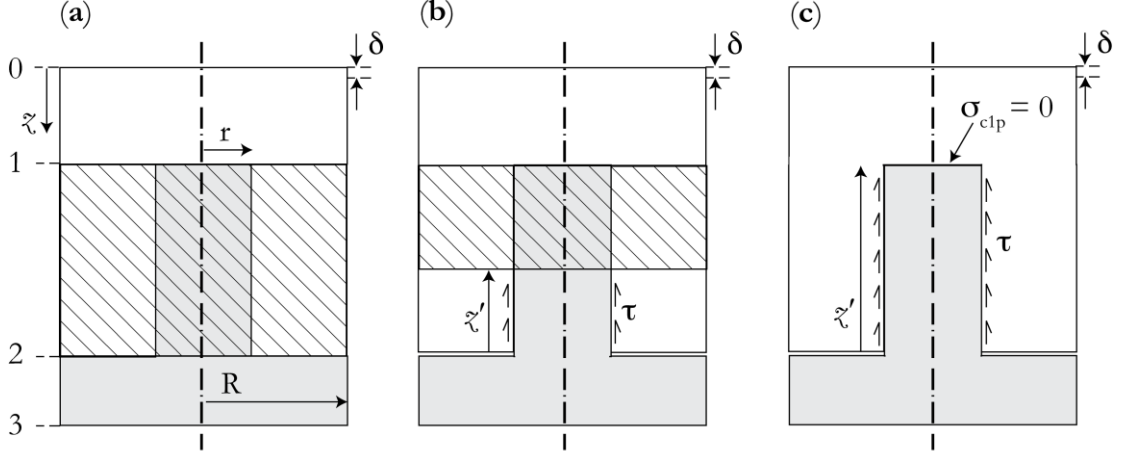
ϕ .	$k = \sin 5^\circ$.		$k = \sin 15^\circ$.		$k = \sin 30^\circ$.		$k = \sin 50^\circ$.	
	$\widehat{\rho\rho}/p$.	\widehat{zz}/p .	$\widehat{\rho\rho}/p$.	\widehat{zz}/p .	$\widehat{\rho\rho}/p$.	\widehat{zz}/p .	$\widehat{\rho\rho}/p$.	\widehat{zz}/p .
0	0.75	1	0.75	1	0.75	1	0.75	1
10	0.634	0.999	0.615	0.998	0.589	0.998	0.560	0.996
20	0.525	0.990	0.490	0.987	0.440	0.982	0.387	0.972
30	0.430	0.968	0.382	0.959	0.313	0.941	0.243	0.912
40	0.355	0.927	0.298	0.909	0.213	0.872	0.135	0.812
50	0.300	0.866	0.235	0.836	0.144	0.777	0.064	0.679
60	0.266	0.786	0.197	0.743	0.102	0.661	0.025	0.529
70	0.249	0.690	0.178	0.636	0.080	0.538	0.009	0.382
80	0.245	0.583	0.172	0.523	0.073	0.416	0.006	0.256
90	0.247	0.472	0.173	0.411	0.073	0.307	0.007	0.160
100	0.249	0.363	0.176	0.307	0.075	0.215	0.012	0.095
110	0.245	0.264	0.174	0.217	0.075	0.143	0.015	0.054
120	0.229	0.178	0.165	0.142	0.072	0.088	0.014	0.030
130	0.199	0.109	0.146	0.085	0.065	0.050	0.012	0.015
140	0.151	0.058	0.116	0.044	0.053	0.025	0.011	0.007
150	0.088	0.025	0.077	0.019	0.037	0.010	0.008	0.003
160	0.009	0.008	0.029	0.006	0.018	0.003	0.004	0.001
170	0.080	0.001	0.027	0.001	0.004	0.000	0.000	0.000
180	0.176	0	0.087	0	0.028	0	0.004	0

Table b: Dimensionless variables and stresses calculated by Matlab.

	k = sin 5°		k = sin 15°		k = sin 30°		k = sin 50°	
Φ (°)	ρ/a	z/a	ρ/a	z/a	ρ/a	z/a	ρ/a	z/a
0	0.8397	0	0.5888	0	0.3333	0	0.1325	0
10	0.8419	0.0279	0.5934	0.0717	0.3384	0.1166	0.1356	0.1524
20	0.8485	0.0551	0.6075	0.1429	0.3542	0.235	0.1455	0.311
30	0.8595	0.0811	0.6313	0.2129	0.382	0.3568	0.164	0.4827
40	0.8746	0.1052	0.6652	0.2809	0.424	0.4833	0.1946	0.6758
50	0.8937	0.1267	0.7098	0.3459	0.4838	0.6152	0.2437	0.9013
60	0.9163	0.1451	0.7656	0.4061	0.5657	0.7522	0.3228	1.1729
70	0.9419	0.1596	0.8327	0.4595	0.6754	0.8918	0.452	1.5057
80	0.9701	0.1697	0.9112	0.5038	0.8186	1.0289	0.663	1.9113
90	1	0.175	1	0.5359	1	1.1547	1	2.3835
100	1.0308	0.175	1.0975	0.5529	1.2216	1.2569	1.5083	2.8828
110	1.0617	0.1694	1.2009	0.5518	1.4805	1.3203	2.2126	3.3316
120	1.0914	0.1583	1.3062	0.5304	1.7676	1.3295	3.0974	3.6329
130	1.119	0.1418	1.4089	0.4873	2.0671	1.2718	4.1036	3.6987
140	1.1433	0.1203	1.5033	0.4224	2.3584	1.1398	5.1392	3.4732
150	1.1635	0.0944	1.5841	0.3372	2.618	0.9342	6.0968	2.9426
160	1.1785	0.065	1.6461	0.2352	2.8231	0.6636	6.871	2.1369
170	1.1878	0.0331	1.6851	0.1208	2.9547	0.3447	7.3742	1.1239
180	1.191	0	1.6984	0	3	0	7.5486	0

	k = sin 5°		k = sin 15°		k = sin 30°		k = sin 50°	
Φ (°)	$\sigma(r)/P$	$\sigma(z)/P$	$\sigma(r)/P$	$\sigma(z)/P$	$\sigma(r)/P$	$\sigma(z)/P$	$\sigma(r)/P$	$\sigma(z)/P$
0	0.75	1	0.75	1	0.75	1	0.75	1
10	0.6337	0.9987	0.6153	0.9984	0.5889	0.9976	0.5603	0.9963
20	0.5249	0.99	0.4899	0.9872	0.4399	0.9815	0.3868	0.972
30	0.4304	0.9675	0.3818	0.9588	0.3129	0.9414	0.2425	0.9122
40	0.3546	0.9268	0.2962	0.9085	0.214	0.8725	0.1346	0.8124
50	0.2998	0.866	0.235	0.8356	0.1446	0.7767	0.0639	0.6793
60	0.2655	0.7859	0.1969	0.743	0.102	0.6615	0.025	0.529
70	0.2488	0.6898	0.1778	0.6364	0.0805	0.5378	0.009	0.3819
80	0.2446	0.583	0.1721	0.5233	0.0731	0.4167	0.0061	0.2558
90	0.2469	0.4719	0.1734	0.4113	0.073	0.3073	0.0085	0.1603
100	0.249	0.3634	0.1756	0.3073	0.075	0.2151	0.0116	0.0953
110	0.2448	0.2636	0.1739	0.2164	0.0754	0.1423	0.0135	0.0543
120	0.2292	0.1777	0.1646	0.1418	0.0723	0.0881	0.0138	0.0297
130	0.1986	0.1088	0.1456	0.0846	0.0648	0.05	0.0128	0.0153
140	0.1513	0.0583	0.1162	0.0444	0.0529	0.0251	0.0107	0.0072
150	0.0876	0.0255	0.0768	0.019	0.0372	0.0104	0.0078	0.0028
160	0.0094	0.0077	0.0286	0.0057	0.018	0.0031	0.0042	0.0008
170	-0.0801	0.001	-0.0266	0.0007	-0.0038	0.0004	0.0001	0.0001
180	-0.1763	0	-0.0867	0	-0.0278	0	-0.0044	0

APPENDIX E: STRAIN ENERGY DERIVATION



Polymer (p) post stress derivation:

$$(\sigma_p + d\sigma_p)\pi r^2 = \sigma_p\pi r^2 - 2\pi r\tau dz,$$

$$d\sigma_p = \frac{2\tau}{r} dz,$$

$$\sigma_p = \frac{2\tau z}{r} + A,$$

$$z = 0, \quad \sigma_p = \sigma_{p_2} = \frac{\sigma_0}{f},$$

$$\sigma_p = \frac{\sigma_0}{f} - \frac{2\tau z}{r}.$$

After the interfaces are created, the stress is limited by the slip length. Maximum stress in state **c**:

$$z = z' = z_{12}, \quad \sigma_p = \sigma_{p_{1c}} = 0, \quad \sigma_0 = \sigma_{0_{sl}},$$

$$\sigma_{0_{sl}} = \frac{2\tau z_{12}f}{r}, \text{ which is Equation 4.5.}$$

This equation can also be rearranged to calculate the ‘slip length’ (z') for a given stress:

$$\sigma_{0_{sl}} = \sigma_0;$$

$$z' = \frac{\sigma_0 r}{2\tau f}.$$

Stress in the polymer post can then be written in terms of slip length by substituting in for τ .

$$\sigma_p = \frac{\sigma_0}{f} \left(1 - \frac{z}{z'} \right).$$

Total strain energy before de-cohesion:

$$U_{03_a} = U_{01_a} + U_{12_a} + U_{23_a}.$$

The polymer post and stamp (s) behave as a composite (c) in state **a**:

$$\frac{\sigma_0}{E_c} = \frac{\sigma_{p_1}}{E_p} = \frac{\sigma_{s_1}}{E_s},$$

$$U_{03_a} = \frac{\sigma_{0_a}^2 A_T}{2} \left(\frac{z_{01}}{E_s} + \frac{z_{12}}{E_c} + \frac{z_{23}}{E_p} \right), \text{ which is Equation 4.6.}$$

Strain energy in polymer base:

$$U_{01_c} = \frac{\pi}{2E_s} \left(\sum_{z_0}^{z_1} \sum_0^R \Delta \sigma_z^2 dr dz \right), \text{ which is Equation 4.7.}$$

As described in Section 4.2.4, discrete values for the stress are integrated together.

Strain energy in stamp top:

$$U_{23_c} = \frac{\pi}{2E_p} \left(\sum_{z_2}^{z_3} \sum_0^R \Delta \sigma_z^2 dr dz \right), \text{ which is Equation 4.8.}$$

As described in Section 4.2.5, discrete values for the stress are integrated together.

Polymer post energy after de-embossing:

$$U_{p_b} = \int_0^{z'} \frac{\sigma_p^2 A_p}{2E_p} dz.$$

Substitute in the equation for the stress in a polymer post:

$$U_{p_b} = \frac{\sigma_0^2 A_p}{2E_p f^2} \int_0^{z'} \left(1 - \frac{z}{z'} \right)^2 dz,$$

$$U_{p_b} = \frac{\sigma_0^2 A_p}{2E_p f^2} \left[z - \frac{z^2}{z'} + \frac{z^3}{3z'^2} \right]_0^{z'},$$

$$U_{p_b} = \frac{\sigma_0^2 A_p z'}{6E_p f^2},$$

$$U_{p_b} = \frac{\sigma_0^3 A_p r}{12E_p \tau f^3}, \text{ which is Equation 4.9.}$$

Stamp features energy after de-embossing:

$$U_{s_b} = \int_0^{z'} \frac{\sigma_s^2 A_s}{2E_s} dz,$$

$$\sigma_s = \frac{2\tau rz}{(R^2 - r^2)} + A,$$

$$z = 0, \quad \sigma_s = 0,$$

$$\sigma_s = \frac{2\tau rz}{(R^2 - r^2)}.$$

Substitute into the rearranged equation for z' :

$$\sigma_s = \frac{\sigma_0 r^2 z}{(R^2 - r^2) f z'},$$

$$\sigma_s = \frac{\sigma_0}{(1-f)} \frac{z}{z'}.$$

$$U_{s_b} = \frac{\sigma_0^2 A_s}{2E_s (1-f)^2} \int_0^{z'} \frac{z^2}{z'^2} dz,$$

$$U_{s_b} = \frac{\sigma_0^2 A_s}{2E_s (1-f)^2} \left[\frac{z^3}{3z'^2} \right]_0^{z'},$$

$$U_{s_b} = \frac{\sigma_0^2 A_s z'}{6E_s (1-f)^2},$$

$$U_{s_b} = \frac{\sigma_0^3 A_s r}{12E_s \tau (1-f)^2 f}, \text{ which is Equation 4.10.}$$

Frictional energy term due to sliding contact with stiffer stamp material:

$$E_s > E_p,$$

Sliding friction due to post extension relative to stamp:

$$V_{sl_p} = 2\pi\tau r \int_0^{z'} \Delta V dz, \quad \Delta V = |\delta_s - \delta_p|$$

$$\delta_s = e_s dz,$$

$$\delta_p = e_p dz,$$

$$|\delta_s - \delta_p| = \left| \frac{\sigma_s}{E_s} - \frac{\sigma_p}{E_p} \right| dz,$$

$$|\delta_s - \delta_p| = -\frac{\sigma_0}{E_p f} + \frac{2\tau z}{E_p r} + \frac{2\tau r z}{E_s(R^2 - r^2)} dz,$$

$$|\delta_s - \delta_p| = \frac{\tau z^2}{E_p r} + \frac{\tau r z^2}{E_s(R^2 - r^2)} - \frac{\sigma_0 z}{E_p f} + A,$$

$$|\delta_s - \delta_p| = 0, \quad z = z',$$

$$A = \frac{\sigma_0 z'}{E_p f} - \frac{\tau z'^2}{E_p r} - \frac{\tau r z'^2}{E_s(R^2 - r^2)},$$

$$|\delta_s - \delta_p| = \frac{\tau}{E_p r} (z^2 - z'^2) + \frac{\tau r}{E_s(R^2 - r^2)} (z^2 - z'^2) - \frac{\sigma_0}{E_p f} (z - z'),$$

$$V_{sl_p} = 2\pi\tau r \int_0^{z'} |\delta_s - \delta_p| dz,$$

$$V_{sl_p} = 2\pi\tau r \left[\frac{\tau z^3}{3E_p r} - \frac{\tau z'^2 z}{E_p r} + \frac{\tau z^3 r}{3E_s(R^2 - r^2)} - \frac{\tau z'^2 z r}{E_s(R^2 - r^2)} + \frac{\sigma_0 z' z}{E_p f} - \frac{\sigma_0 z^2}{2E_p f} \right]_0^{z'},$$

$$V_{sl_p} = 2\pi\tau r \left[-\frac{2\tau z'^3}{3E_p r} - \frac{2\tau z'^3 r}{3E_s(R^2 - r^2)} + \frac{\sigma_0 z'^2}{2E_p f} \right],$$

Substitute in for z' :

$$\sigma_p = \frac{\sigma_0}{f} - \frac{2\tau z}{r},$$

$$z = z', \quad \sigma_p = \sigma_{p_1},$$

$$\sigma_{p_1} = \frac{\sigma_0}{f} - \frac{2\tau z'}{r}.$$

Within the region at the top of the post the strains are all equal, behaving as a composite. For this region:

$$\sigma_0 A_T = \sigma_{p_1} A_p + \sigma_{s_1} A_s \text{ and } \frac{\sigma_0}{E_c} = \frac{\sigma_{p_1}}{E_p} = \frac{\sigma_{s_1}}{E_s}.$$

Substituting for σ_{s_1} :

$$\sigma_0 A_T = \sigma_{p_1} A_p + \sigma_0 A_s \frac{E_s}{E_c},$$

$$\sigma_{p_1} = \sigma_0 \left(\frac{A_T}{A_p} - \frac{A_s E_s}{A_p E_c} \right),$$

$$\sigma_{p_1} = \frac{\sigma_0}{f} \left(1 - \frac{E_s(1-f)}{E_c} \right),$$

$$\frac{\sigma_0}{f} \left(1 - \frac{E_s(1-f)}{E_c} \right) = \frac{\sigma_0}{f} - \frac{2\tau z'}{r},$$

$$\frac{2\tau z'}{r} = \frac{\sigma_0 E_s(1-f)}{E_c f},$$

$$z' = \frac{\sigma_0 E_s r(1-f)}{2E_c \tau f}.$$

Substituting into our equation for the slip friction energy:

$$V_{sl_p} = 2\pi\tau r \left[-\frac{2\tau}{3E_p r} \frac{\sigma_0^3 E_s^3 r^3 (1-f)^3}{8E_c^3 \tau^3 f^3} - \frac{2\tau r}{3E_s(R^2 - r^2)} \frac{\sigma_0^3 E_s^3 r^3 (1-f)^3}{8E_c^3 \tau^3 f^3} + \frac{\sigma_0}{2E_p f} \frac{\sigma_0^2 E_s^2 r^2 (1-f)^2}{8E_c^2 \tau^2 f^2} \right]$$

$$V_{sl_p} = 2\pi\tau r \left[-\frac{\sigma_0^3 E_s^3 r^3 (1-f)^3}{12E_c^3 E_p \tau^2 f^2} - \frac{\sigma_0^3 E_s^2 r^4 (1-f)^3}{12E_c^3 \tau^2 (R^2 - r^2) f^3} - \frac{\sigma_0^3 E_s^2 r^2 (1-f)^2}{8E_c^2 E_p \tau^2 f^3} \right],$$

$$V_{sl_p} = \frac{\pi\sigma_0^3 E_s^3 r^3 (1-f)^2}{6E_c^2 \tau f^3} \left[-\frac{E_s(1-f)}{E_c E_p} - \frac{r^2(1-f)}{E_c(R^2 - r^2)} + \frac{3}{2E_p} \right],$$

$$\frac{r^2}{R^2 - r^2} = \frac{f}{1-f},$$

$$V_{sl_p} = \frac{\sigma_0^3 E_s^2 A_p r(1-f)^2}{12E_c^2 \tau f^3} \left[\frac{3}{E_p} - \frac{2E_s(1-f)}{E_c E_p} + \frac{2f}{E_c} \right],$$

$$V_{sl_p} = \frac{\sigma_0^3 E_s^2 A_p r(1-f)^2}{12E_c^3 E_p \tau f^3} [3E_c - 2E_s(1-f) - 2E_p f],$$

$$E_c = E_p f + E_s(1 - f),$$

$$V_{sl_p} = \frac{\sigma_0^3 E_s^2 A_p r (1 - f)^2}{12 E_c^2 E_p \tau f^3}, \text{ as in Equation 4.11.}$$

This is the same equation as derived by Aveston, Cooper & Kelly [119] except theirs is per unit area, hence an extra f is here and is half the size as we are only interested about one side of the crack.

The frictional energy term due to sliding contact with stiffer polymer material provides a different value. This is because it is now the polymer post that does not yield as:

$$E_p > E_s,$$

which means a new energy term for the sliding friction is need. The sliding friction due to the stamp extension relative to the post:

$$V_{sl_s} = 2\pi\tau r \int_0^{z'} \Delta V dz, \quad \Delta V = |\delta_s - \delta_p|,$$

$$|\delta_s - \delta_p| = \left| \frac{\sigma_s}{E_s} - \frac{\sigma_p}{E_p} \right| dz.$$

Stress variation in the stamp:

$$\sigma_s = -\frac{2\tau z r}{(R^2 - r^2)} + A,$$

z' increasing from stamp top to polymer (changed datum):

$$z = 0, \quad \sigma_s = \frac{\sigma_0}{(1 - f)},$$

$$\sigma_s = -\frac{2\tau z r}{(R^2 - r^2)} + \frac{\sigma_0}{(1 - f)},$$

Stress variation in post:

$$\sigma_p = \frac{2\tau z}{r} + A,$$

$$z = 0, \quad \sigma_p = 0,$$

$$\sigma_p = \frac{2\tau z}{r}.$$

Putting these into the equation for sliding friction for the stamp:

$$|\delta_s - \delta_p| = \left| -\frac{2\tau rz}{E_s(R^2 - r^2)} + \frac{\sigma_0}{E_s(1-f)} - \frac{2\tau z}{E_p r} \right| dz,$$

$$|\delta_s - \delta_p| = -\frac{\tau rz^2}{E_s(R^2 - r^2)} + \frac{\sigma_0 z}{E_s(1-f)} - \frac{\tau z^2}{E_p r} + A,$$

$$|\delta_s - \delta_p| = 0, \quad z = z',$$

$$|\delta_s - \delta_p| = \frac{\sigma_0}{E_s(1-f)}(z - z') - \frac{\tau r}{E_s(R^2 - r^2)}(z^2 - z'^2) - \frac{\tau}{E_p r}(z^2 - z'^2),$$

$$V_{sl_s} = 2\pi\tau r \left[\frac{\sigma_0}{E_s(1-f)} \left(\frac{z^2}{2} - z'z \right) + \frac{\tau r}{E_s(R^2 - r^2)} \left(z'^2 z - \frac{z^3}{3} \right) + \frac{\tau}{E_p r} \left(z'^2 z - \frac{z^3}{3} \right) \right]_0^{z'},$$

$$V_{sl_s} = 2\pi\tau r \left[-\frac{\sigma_0 z'^2}{2E_s(1-f)} + \frac{2\tau z'^3 r}{3E_s(R^2 - r^2)} + \frac{2\tau z'^3}{3E_p r} \right].$$

Calculating \mathcal{Z}' for V_{sl_s} :

$$\sigma_p = \frac{2\tau z}{r},$$

$$z = z', \quad \sigma_p = \sigma_{p_1},$$

$$\frac{\sigma_0}{E_c} = \frac{\sigma_{p_1}}{E_p} = \frac{\sigma_{s_1}}{E_s},$$

$$\sigma_{p_1} = \frac{\sigma_0 E_p}{E_c},$$

$$z' = \frac{\sigma_0 E_p r}{2\tau E_c}.$$

Substituting \mathcal{Z}' in the sliding friction for the stamp energy term:

$$V_{sl_s} = 2\pi\tau r \left[-\frac{\sigma_0^3 E_p^2 r^2}{8E_c^2 E_s \tau (1-f)} + \frac{\sigma_0^3 E_p^3 r^4}{12E_c^3 E_s \tau^2 (R^2 - r^2)} + \frac{\sigma_0^3 E_p^2 r^2}{12E_c^3 \tau^2} \right],$$

$$V_{sl_s} = \frac{\sigma_0^3 E_p^2 A_p r}{4E_c^2 \tau} \left[-\frac{1}{E_s(1-f)} + \frac{2E_p f}{3E_c E_s(1-f)} + \frac{2}{3E_c} \right],$$

$$V_{sl_s} = \frac{\sigma_0^3 E_p^2 A_p r}{12E_c^3 E_s \tau (1-f)} \left[-3E_c + 2E_p f + 2E_s(1-f) \right].$$

We know that:

$$\frac{E_s^2(1-f)^2}{E_p f^3} : \frac{E_p^2}{E_s(1-f)}. \text{ With this substitution into the equation we are left with:}$$

$$V_{sl_s} = \frac{\sigma_0^3 E_p^2 A_p r}{12 E_c^2 E_s \tau (1-f)}, \text{ as in Equation 4.12.}$$

The strain energy release rate (G_{IC}) is given by:

$$G_{IC} \leq U_{03_a} - U_{03_c} - |V_{sl}|.$$

Rearranging this term and substituting U_{03_a} creates an equation that can be used to calculate the de-embossing stress needed to be applied. For a stiffer stamp:

$$\sigma_{0_a} \leq \sqrt{\frac{(2G_{IC}A_T + U_{03_c} + |V_{sl_p}|)}{A_T \left(\frac{z_{01}}{E_s} + \frac{z_{12}}{E_c} + \frac{z_{23}}{E_p} \right)}}, \text{ as in Equation 4.13.}$$

The overall stress imposed on the top of the stamp to cause de-embossing for constant displacement conditions:

$$\sigma_{0_a} = \frac{\delta_T}{\left(\frac{z_{01}}{E_s} + \frac{z_{12}}{E_c} + \frac{z_{23}}{E_p} \right)}, \text{ as in Equation 4.14.}$$

The total displacement (δ_T) in state **b** or **c** is the sum of the displacements for each region of the model:

$$\delta_T = \delta_{st} + \delta_p + \delta_{rl},$$

where δ_{st} is the displacement of the stamp top and in **c** is found by:

$$\delta_{st} = \frac{z_{01}}{E_s} \left(\frac{1}{n} \sum_{i=1}^n \left(\sum_{z_0}^{z_1} \Delta \sigma_z^2 drdz \right)_i \right),$$

where n is the sampling value in the r -direction. This equation calculates the displacement for a given r , adds up these values (n in total) and then finds the mean. A similar equation is used for the displacement in the residual layer (δ_{rl}) in **b** and **c**:

$$\delta_{rl} = \frac{z_{23}}{E_p} \left(\frac{1}{n} \sum_{i=1}^n \left(\sum_{z_2}^{z_3} \Delta \sigma_z^2 drdz \right)_i \right),$$

while the displacement in the polymer post (δ_p) is found by:

$$\delta_p = \frac{2\tau z_{12}}{E_p r}.$$

Should the polymer be stiffer than the stamp, the displacement between z_1 and z_2 is due to the stamp and is found by:

$$\delta_s = -\frac{2\tau z_{12}r}{E_s(R^2 - r^2)} + \frac{\sigma_0}{E_s(1-f)}.$$

APPENDIX F: MATLAB CODE

SHEAR STRESS CALCULATION

```
% De-embossing graphs for varying shear stress plotted on varying aspect
% and area ratios
% T Balla
% February 2009
%%%%%%%%%%%%%%%%%%%%%%%%%%%%%%%%%%%%%%%%%%%%%%%%%%%%%%%%%%%%%%%%%%%%%%%%
% Creates graph of Shear stresses versus area ratios for various different%
% materials (of differing Young's Modulus and Yield Strength). The graph %
% shows this information for different Aspect Ratios (6). %
%%%%%%%%%%%%%%%%%%%%%%%%%%%%%%%%%%%%%%%%%%%%%%%%%%%%%%%%%%%%%%%%%%%%%%%%

%% Clear memory, format and set up file paths
clear all
format short eng

%% Loop to vary values in search of G
Gln = [0.01 1 0.5 3 5 10];
f_step = 0.005; % Increment value
f_min = 0.005;
f_max = 0.995;
f_v = f_min:f_step:f_max; % Range
Asp_step = 0.1;
Asp_min = 0.1;
Asp_max = 200;
Asp = 0.01:0.01:1;
Asps2 = 1.1:0.1:10;
Asps3 = 11:1:200;
Asp(1,101:190) = Asps2(1,:);
Asp(1,191:380) = Asps3(1,:);

%% Increment values
nn1 = (f_max-f_min)/f_step + 1; % Area ratio
G1 = 1; % Result taking

%% Set initial values
z01 = 1000e-6; % Depth of stamp before features
z23 = 200e-9; % Depth of residual layer below post

%% Material set
% Young's Modulus, Yield strength; row order
nameEs = ['Silicon']; % In Matlab, these need to be curly brackets
Es1 = [170e9;21e9]; % Silicon, Nickel, Silica Glass, Steel (Tensile)
nameEp = ['PMMA']; % In Matlab, these need to be curly brackets
Ep1 = [2.5e9;67.0e6]; % PMMA, SU8, PS, PC; row order
r = 200e-9; % Post radius
T1 = [1e2 1e3 1e4 1e5 1e6 1e7]; % Assumed shear stress on posts
t_v = size(T1,2); % Max aspect ratio

% Young's Modulus and Yield Strength
Es = Es1(1,1);
YEs = Es1(2,1);
Ep = Ep1(1,1);
YEp = Ep1(2,1);

tic % Begin timing
Results = 0;
csize = 0;
for g = 1:t_v %size(Gln,2)
    Gic = Gln(3); % Critical strain energy release rate
    T = T1(g); % Aspect ratio
    for i=1:nn1
        GiV_broke = 0;
        f = f_v(i); % Area ratio
        for h = 1:int16(size(Asp,2))
```

```

        if GiV_broke == 0
            AsR = Asp(h);
            z12 = AsR.*2.*r;    % Post height
            R = r./(sqrt(f));    % Area radius
            At = pi.*R.^2;    % Total area
            Ap = pi.*r.^2;    % Post area
            As = pi.*(R.^2-r.^2);    % Non-post area
            n = Es.*As./(Ep.*Ap);    % Ratio value
            Ec = f.*Ep + (1-f).*Es;    % Composite modulus
            s0b = (2.*T.*z12.*f)./r;    % Post-crack stress
            s0bi = 2*T*z12*Ec*f/(Es*r*(1-f));    % Stress to overcome post
            % Calculate stress and energy values
            [s0at deltt GiV GiV_broke GiM fail sval s0a1 s0a2 Url2 ...
             Up2 Us2 Ust2 Vsl] = dispcomp(f,z12,r,R,At,Ap,As,Ep,...
             Es,Ec,s0b,s0bi,z01,z23,T,GiC,YEp,YEs);
%% Stressmap data
        if GiV_broke > 0
            [csize, rsize] = size(Results);
            Rval = csize+G1;
        else
            [csize, rsize] = size(Results);
            Rval = csize+G1;
        end
        Results(Rval,1) = T;    %#ok<AGROW>
        Results(Rval,2) = f;    %#ok<AGROW>
        Results(Rval,3) = AsR;    %#ok<AGROW>
        Results(Rval,4) = s0at;    %#ok<AGROW>
        Results(Rval,5) = sval;    %#ok<AGROW>
        Results(Rval,6) = s0b;    %#ok<AGROW>
        Results(Rval,7) = fail;    %#ok<AGROW>
        Results(Rval,8) = GiV_broke;    %#ok<AGROW>
        Results(Rval,9) = GiC;    %#ok<AGROW>
    end
end
end
end

% Grab values before failure
V1 = [1,1,1,1];
Results1 = inf(size(f_v,2),size(T1,2)+1);
Results1(:,1) = f_v;
for i = 1:size(Results,1)
    if Results(i,8) > 0 && (Results(i,2) == Results(i-1,2))
        fval = int16(Results(i-1,2)/f_step);
        if Results(i,1) == 1e2
            Results1(fval,2) = Results(i-1,3);
        elseif Results(i,1) == 1e3
            Results1(fval,3) = Results(i-1,3);
        elseif Results(i,1) == 1e4
            Results1(fval,4) = Results(i-1,3);
        elseif Results(i,1) == 1e5
            Results1(fval,5) = Results(i-1,3);
        elseif Results(i,1) == 1e6
            Results1(fval,6) = Results(i-1,3);
        elseif Results(i,1) == 1e7
            Results1(fval,7) = Results(i-1,3);
        elseif Results(i,1) == 1e8
            Results1(fval,8) = Results(i-1,3);
        end
    elseif Results(i,8) > 0
        fval = int16(Results(i,2)/f_step);
        if Results(i,1) == 1e2
            Results1(fval,2) = Results(i,3);
        elseif Results(i,1) == 1e3
            Results1(fval,3) = Results(i,3);
        elseif Results(i,1) == 1e4
            Results1(fval,4) = Results(i,3);
        elseif Results(i,1) == 1e5
            Results1(fval,5) = Results(i,3);
        elseif Results(i,1) == 1e6
            Results1(fval,6) = Results(i,3);
        end
    end
end

```

```

        Results1(fval,6) = Results(i,3);
    elseif Results(i,1) == 1e7
        Results1(fval,7) = Results(i,3);
    elseif Results(i,1) == 1e8
        Results1(fval,8) = Results(i,3);
    end
end
end
    %% Write info to text file
    savinfo2 = ['save arap_t.txt', ' Results1' , ' -ascii -tabs'];
    eval(savinfo2)
toc        % End timing
timed = toc;
save('timed.txt', 'timed', '-ascii')

```

EQUATIONS 4.13 AND 4.14 SCRIPT

```

% Gvalues function. Finds values for Results table
function [s0at deltt GiV GiV_broke GiM fail sval s0a1 s0a2 Url2 Up2 Us2...
    Ust2 Vsl] =...
dispcomp(f,z12,r,R,At,Ap,As,Ep,Es,Ec,s0b,s0bi,z01,z23,T,Gic,YEp,YEs)

% Base and Stamp-Top Energy and Displacement Values
sf2b = s0b./f; % Stress at base of post
sf2bi = s0bi/f; %
[Url2, deltrlb] = base(sf2b,r,R,Ep,z23); % Solves for
% strain energy and displacements in the residual layer
sml = s0b./(1-f); % Stress at stamp and feature interface
sml_i = s0bi/(1-f);
[Ust2, delts] = stamp(sml,r,R,Es,z01); % Solves for
% strain energy and displacements in the stamp top

% Initial post displacement (when top of post has composite stress)
% Was incorrect with a 1/f. Changed on 5/5/09
deltp = z12^2*T/(Ep*r);

% Total displacement post crack
deltt = deltrlb + deltp + delts;
% Stress to de-embossing pre-crack
s0a1 = deltt/(z01/Es + z12/Ec + z23/Es);

% Energy in post for complete de-embossing
Up2 = (s0b^3*Ap*r/(12*Ep*T*f^3));

% Energy in stamp features for complete de-embossing
Us2 = (s0b^3*As*r/(12*Es*T*(1-f)^2*f));

if Es >= Ep
    % Energy to overcome sliding friction for complete de-embossing P.ff of
    % calcs
    Vsl = (s0b^3*Es^2*Ap*r*(1-f)^2)/(12*Ec^2*Ep*T*f^3);
    %Vsl = (s0b^3*r*Ap*(2-(Es*As/(Ep*Ap)))/(12*T*Es*f^2*(1-f)));
else
    Vsl = (s0b^3*Ep^2*Ap*r)/(12*Ec^2*Es*T*(1-f));
    %Vsl = s0b^3*Ap*r*(1/((1-f)*Es) - 2/(Ep*f))/(12*T*f^2);
end

%% GiM term for full de-embossing energy equations
% Total energy after crack propagation
U2 = abs(Up2) + abs(Us2) + abs(Url2) + abs(Ust2);

% Calculate stress to equal displacement in U2
s0a2 = sqrt((2*((Gic*At) + U2 + abs(Vsl)))/(At*(z12/Ec + z23/Ep + z01/Es)));

if s0a1 > s0a2
    s0a = s0a1;
    sval = 1;
else

```



```

        s0a = s0a2;
        sval = 2;
    end
    s0at = s0a;
    GiM = (s0at^2*At*(z12/Ec + z23/Ep + z01/Es)/2 - U2 - abs(Vs1)) / (At);

    if (sf2b > YEp) %#ok<BDSCI>
        GiV_broke = GiM;
        GiV = 0;
        fail = 1;
    elseif (sm1 > YEs) %#ok<BDSCI>
        GiV_broke = GiM;
        GiV = 0;
        fail = 2;
    elseif (s0a > YEs)
        GiV_broke = GiM;
        GiV = 0;
        fail = 3;
    elseif (s0a > YEp)
        GiV_broke = GiM;
        GiV = 0;
        fail = 4;
    elseif (sf2bi > YEp)
        GiV_broke = GiM;
        GiV = 0;
        fail = 5;
    elseif (sm1i > YEs)
        GiV_broke = GiM;
        GiV = 0;
        fail = 6;
    else
        GiV_broke = 0;
        GiV = GiM;
        fail = 1111;
    end
end

```

RESIDUAL LAYER SCRIPT

```
% base
% T Balla
% June 2007
%%%%%%%%%%%%%%%%%%%%%%%%%%%%%%%%%%%%%%%%%%%%%%%%%%%%%%%%%%%%%%%%%%%%%%%%
% File to solve stress distribution, displacement and energy      %
% values in a semi-infinite half space, to use as an approximation %
% for material below the post, using elliptic integrals, assuming %
% constant displacement conditions. Calculates energy values for   %
% finite elements using a 'for' loop for various z values. element %
% sizes can be altered. Assumes stress value is constant in each   %
% element then adds all energy values together                     %
%%%%%%%%%%%%%%%%%%%%%%%%%%%%%%%%%%%%%%%%%%%%%%%%%%%%%%%%%%%%%%%%%%%%%%%%

function [Url2, deltrlb] = base(sf2b, r, R, Ep, z23)

%% Values needed for calculations
n1 = 100; % Sampling value in r direction
n2 = 10; % Sampling value in z direction
n3 = n1/2;
Pr = -sf2b;
ym = Ep;
da = 0.1; % lamda, Lamé's elastic constant
mu = 0.1; % mu, Lamé's elastic constant
zr = z23; % Depth value of residual layer
ab = R;
a = r;

%% Matrices to store values
ezzmatrix = zeros(n1,n2); % Create matrix to write to
zmatrix = zeros(n2,1);
szzmat = zeros(n1,n2); % ''

%% Loop to solve for various depths (z values)
for qq1 = 1:n2 % Loop to calculate pp = pp(z)
    zrld = zr./n2; % Sample sizes in z direction
    z = qq1.*zrld - 0.5.*zrld; % z value, depth
    zmatrix(qq1) = z; % write z value to matrix

%% normal distribution log lines in r direction
    i1 = 1:n3; % Sampling steps up to post radius
    rd1 = (a)/1000;
    yrd1 = exp(log(1000)/(n3)); % Sampling distance equation
    elements1 = (yrd1).^i1; % Sampling points
    pe1a = (rd1*elements1)'; % Distance from centre line
    pe1 = a-pe1a;
    pe1 = flipud(pe1);

    i2 = 1:n3; % Sampling steps from post radius
    rd2 = (ab-a)/1000;
    yrd2 = exp(log(1000)/(n3)); % Sampling distance equation
    elements2 = (yrd2).^i2; % Sampling points
    pe2a = (rd2*elements2)'; % Distance from centre line
    pe2 = pe2a ;%- pe2a(1);
    pe2 = pe2 + a;
    doh = (pe2(1) - pe1(n3))*0.8;
    pe1 = pe1 + doh;
    p = cat(1,pe1, pe2); % Sampling points together
    qq2 = 1:(n1-1);
    pe = (p(qq2)+ p(qq2+1))/2;
    pe(n1) = ab;
    pe(1,2) = 0;
    pe(2:n1,2) = pe(1:(n1-1),1);
    r1 = sqrt((p - a).^2 ...
        + z.^2); % r1, distance of point P from M1
    r2 = sqrt((p + a).^2 ...
        + z.^2); % r2, distance of point P from M2
```

```

k = r1./r2; % k, r1 r2 ratio. Also the modulus
% of the elliptic integrals
the = acos((p - a)./r1); % Angle theta, of the angle P-M1-x
v = asin(2*a.* ...
    sin(pi - the)./r2); % v, elliptic argument. K > v > 0

%% Elliptic Integrals, complete and incomplete
kb = sqrt(1 - (k).^2); % Elliptic integral parameter
mC = kb.^2; % Complete elliptic integral modulus
[Kb,Eb] = ellipke(mC); % Complete elliptic integral
mI = k.^2; % Incomplete elliptic integral modulus
[F,E] = elliptic12(the,mI); % Incomplete elliptic integral

%% Differential equations
DVz = -Pr.*2*(Kb.*E - (Kb-Eb).*F - Kb.*k.*sin(the));
D2Vz = Pr.*(2*Kb./r2 - (r2./p.^2 + (p.^2 + a.^2 + z.^2).* ...
    (p.^2 - a.^2 - z.^2)./(r1.^2.*r2.*p.^2)).*Eb);

%% Stress formulas
zz = (DVz - z.*D2Vz)./(2*pi);
szzmat(:,qq1) = zz;

%% Find zz strain energy for element
rint1 = pe(:,2); %ok<NBRAK> % Integral limits
rint2 = pe(:,1); %ok<NBRAK>
vol = pi.*zrld.*(rint2.^2 ... % Volume of element
    - rint1.^2);
ezzmatrix(:,qq1) = (0.5.* ...
    (zz.^2).*vol)./ym; % Strain energy
end

%% Calculate delta and energy values
ezzt = sum(ezzmatrix'); % Sums energy values in each column
Url2bb = abs(sum(ezzt')); % Sums column energy values together
Url2 = Url2bb; %ok<AGROW>

%% delta for mean of first n3 values (post width)
deltb1 = szzmat(1:n3,:).*zrld./ym;
deltb = sum(deltb1');
deltrlb = mean(deltb(1:n3));

```

APPENDIX G: ANSYS FE CODE

CIRCULAR RIM MODEL

```
!Code written by Tobias Balla
!Creates a d-cone in ANSYS LS-DYNA similar to that modelled by Cerda
!and Mahadevan. Solves for dcone and outputs internal energy, hour
!glass energy, nodal positions and forces.

FINISH
/CLEAR
/PLOPTS,LOGO,0    ! Get rid of logo for text
/REPLOT
KEYW,PR_SET,1      !GUI filtering: structural
KEYW,PR_STRUC,1
KEYW,LSDYNA,1

/FILNAME, dcone, 1
/PREP7
CSYS,0
!!!!!!!!!!!!!!!!!!!!!!!!!!!!!!!!!!!!!!!!!!!!!!!!!!!!!!!!!!!!!!!!!!!!!!
!Create parameters
!!!!!!!!!!!!!!!!!!!!!!!!!!!!!!!!!!!!!!!!!!!!!!!!!!!!!!!!!!!!!!!!!!!!!!

*SET,NSTEPS,500    !Time steps to capture in .his file

!Material properties
*SET,E,6.3501e6      !PEN Young's Modulus
*SET,nu,0.435        !PEN Poisson's ratio
*SET,dnst,1360e-9    !PEN density
*SET,MRC,0.3         !Mooney-Rivlin constants

*SET,E1,200e6        !Steel Young's Modulus
*SET,nul,0           !Steel Poisson's ratio
*SET,dnst1,7900e-9   !Steel density

!Sheet dimensions
*SET,R,50            !Outer radius
*SET,thick,100e-3    !Sheet thickness

!Rim dimensions
*SET,OFFSET,50e-3    !Offset distance between top of torus and surface
*SET,minrad,0.5      !Torus minor radius
*SET,majrad,30       !Torus inner radius
*SET,tdepth,1        !torus depth

!Point info
*SET,pntdisp,50e-3   !Offset
*SET,pntrad,1        !Radius
*SET,pntheight,0.1

!Mesh dimensions
*SET,contactinner,majrad    !Inner mesh radius
*SET,contactouter,majrad+10
```

```

*SET,MRannl,6          !Inner annulus radius
*SET,MAinner,6         !Inner mesh azimuthal
*SET,Rimazi,30
*SET,Rimside,2
*SET,Rimtop,1

*SET,M6,4
*SET,M10,6
*SET,M15,8
*SET,M30,90
*SET,Pcurve,2
*SET,Pazi,2
*SET,Prad,2
*SET,Pline,1
*SET,cna,48            !Contact region mesh size - azimuthal
*SET,cnr,6             !Contact region mesh size - radial
*SET,AZIOUT,24         !
*SET,RADOUT,8          !
*SET,rimmesh,6         !Per quarter, the amount of segments for the
mesh

*SET,MASSK,-1e-7
!Positive: all elements adjusted to achieve time step
!Negative: only for those smaller

!Velocity and time values
*SET,vel,280           !Displacement on sheet, cannot be more than
0.97*majrad
*SET,tval,0.1

!!!!!!!!!!!!!!!!!!!!!!!!!!!!!!!!!!!!!!!!!!!!!!!!!!!!!!!!!!!!!!!!!!!!!!!!!!!!
!Elements used
!!!!!!!!!!!!!!!!!!!!!!!!!!!!!!!!!!!!!!!!!!!!!!!!!!!!!!!!!!!!!!!!!!!!!!!!!!!!
ET,1,SHELL163          !Explicit Thin Structural Shell
KEYOPT,1,1,2           !Default Belytschko-Tsay
R,1                    !Assign real constants
RMODIF,1,1,0.833,3,thick,thick,thick,thick,    !Integration points and
thickness
! SHRF (Shear factor)=5/6 (Default)
! NIP(No. int. pnts): 2 for elastic, 3-5 for plastic behaviour

ET,2,SOLID164          !Solid elements for edge
KEYOPT,2,1,1           !Default
KEYOPT,2,5,0           !Default
ET,3,SOLID164          !Solid elements for pointer
KEYOPT,3,1,1           !Default
KEYOPT,3,5,0           !Default

!!!!!!!!!!!!!!!!!!!!!!!!!!!!!!!!!!!!!!!!!!!!!!!!!!!!!!!!!!!!!!!!!!!!!!!!!!!!
!Materials properties
!!!!!!!!!!!!!!!!!!!!!!!!!!!!!!!!!!!!!!!!!!!!!!!!!!!!!!!!!!!!!!!!!!!!!!!!!!!!
MP,DENS,1,dnst         !Material 1: Linear -Sheet
MP,EX,1,E
MP,NUXY,1,nu
EDSHELL,20,-1,1,2,1,1

EDMP,RIGI,2,7,7        !Material 2: All movement constrained (Support)

```

```

MP,DENS,2,dnst1
MP,EX,2,E1
MP,NUXY,2,nul

EDMP,RIGI,3,4,7  !Material 3: Pushing material (Pen)
MP,DENS,3,dnst1
MP,EX,3,E1
MP,NUXY,3,nul

!!!!!!!!!!!!!!!!!!!!!!!!!!!!!!!!!!!!!!!!!!!!!!!!!!!!!!!!!!!!!!!!!!!!!!
!Creating geometries
!!!!!!!!!!!!!!!!!!!!!!!!!!!!!!!!!!!!!!!!!!!!!!!!!!!!!!!!!!!!!!!!!!!!!!

!Sheet Geometry
!!!!!!!!!!!!!!!!!!!!!!!!!!!!!!!!!!!!!!!!!!!!!!!!!!!!!!!!!!!!!!!!!!!!!!
k,1,0,0,0
circle,1,contact inner
circle,1,contact outer
circle,1,R
AL,1,2,3,4
AL,1,2,3,4,5,6,7,8
AL,5,6,7,8,9,10,11,12
ASEL,S,,1,3
CM,SHEET,AREA
ALLSEL      !Select all
ASEL,S,,2
CM,SHEETCONTACT,AREA  !Create rim contact area component
ALLSEL

!Rim geometry
!!!!!!!!!!!!!!!!!!!!!!!!!!!!!!!!!!!!!!!!!!!!!!!!!!!!!!!!!!!!!!!!!!!!!!
!Keypoint (KP) for centre of node rim
K,14,0,0,-(OFFSET),

!KPs to make cylinder with sq top
K,15,MAJRAD,0,-(OFFSET),
K,16,MAJRAD+MINRAD,0,-(OFFSET),
K,17,MAJRAD,0,-(OFFSET+tdepth)
K,18,MAJRAD+MINRAD,0,-(OFFSET+tdepth)

!KPs to make rim to drag around
K,19,0,-MAJRAD,-(OFFSET)
K,20,-MAJRAD,0,-OFFSET
K,21,0,MAJRAD,-OFFSET

!Lines for cylinder
LSTR,15,16 !13
LSTR,15,17 !14
LSTR,16,18 !15

!Lines to drag along
LARC,15,19,14,MAJRAD !16
LARC,19,20,14,MAJRAD !17
LARC,20,21,14,MAJRAD !18
LARC,21,15,14,MAJRAD !19

!Lines to drag around

```

```

ADRAG,13,14,15,,,,,16,17,18,19
ASEL,S,,,4,15
CM,RIM,AREA !Rim area component
allsel

!!!!!!!!!!!!!!!!!!!!!!!!!!!!!!!!!!!!!!!!!!!!!!!!!!!!!!!!!!!!!!!!!!!!!!
!Create point to displace sheet
!!!!!!!!!!!!!!!!!!!!!!!!!!!!!!!!!!!!!!!!!!!!!!!!!!!!!!!!!!!!!!!!!!!!!!

!Code to produce area to sweep
!!!!!!!!!!!!!!!!!!!!!!!!!!!!!!!!!!!!!!!!!!!!!!!!!!!!!!!!!!!!!!!!!!!!!!
!KPs FOR POINT SIDE PROFILE
K,38,0,0,PNTDISP
K,39,0,0,(PNTDISP+PNTRAD)
K,40,0,PNTRAD,PNTDISP+PNTRAD
K,41,0,PNTRAD,PNTDISP+PNTHEIGHT+PNTRAD
K,42,0,0,PNTDISP+PNTHEIGHT+PNTRAD

!Create lines
LARC,38,40,39,PNTRAD !L48
LSTR,40,41 !L49

AROTAT,48,49,,,,,38,42,360,3
ASEL,S,,,16,21
CM,POINT,AREA !Point area component
ALLSEL

!!!!!!!!!!!!!!!!!!!!!!!!!!!!!!!!!!!!!!!!!!!!!!!!!!!!!!!!!!!!!!!!!!!!!!
!Sheet segmentation & meshing
!!!!!!!!!!!!!!!!!!!!!!!!!!!!!!!!!!!!!!!!!!!!!!!!!!!!!!!!!!!!!!!!!!!!!!
LSEL,S,,,1,12
LESIZE,ALL,, ,60, ,1, , ,1, !Line divisions, affects mesh density
ALLSEL
TYPE,1 !Element type - Shell
REAL,1 !Constant set
MSHAPE,0,2D !Quad elements
MSHKEY,0 !Free meshing
Mat,1 !PEN material
SMRT,10 !Automatid meshing, 1-fine 10-coarse (coarse of
LESIZE=60)
CMSEL,S,SHEET,AREA
AMESH,ALL
ALLSEL

!!!!!!!!!!!!!!!!!!!!!!!!!!!!!!!!!!!!!!!!!!!!!!!!!!!!!!!!!!!!!!!!!!!!!!
!Refine sheet about point and rim to stop hourglassing
!!!!!!!!!!!!!!!!!!!!!!!!!!!!!!!!!!!!!!!!!!!!!!!!!!!!!!!!!!!!!!!!!!!!!!
!Sheet touching point
NSEL,S,LOC,X,-pntrad*5,pntrad*5
NSEL,R,LOC,Y,-pntrad*5,pntrad*5
NSEL,R,LOC,Z,0
ESLN,S,1
EREFINE,ALL,,,1,,CLEAN !Clean's up mesh

NSEL,S,LOC,X,-pntrad*1.5,pntrad*1.5
NSEL,R,LOC,Y,-pntrad*1.5,pntrad*1.5
NSEL,R,LOC,Z,0

```

```

ESLN,S,1
EREFINE,ALL,,,2,,SMOOTH      !Smooth's up mesh
epplot

```

```

!Sheet touching rim
ASEL,S,,,2
ESLA,S
EREFINE,ALL,,,2,,clean
ALLSEL
ASEL,S,,,2
ESLA,S
CM,SHEETCONTACTRIM,ELEM

```

```

!!!!!!!!!!!!!!!!!!!!!!!!!!!!!!!!!!!!!!!!!!!!!!!!!!!!!!!!!!!!!!!!!!!!!!!!!!!!
!Element and node sheet components
!!!!!!!!!!!!!!!!!!!!!!!!!!!!!!!!!!!!!!!!!!!!!!!!!!!!!!!!!!!!!!!!!!!!!!!!!!!!
CMSEL,S,SHEET,AREA
ESLA,S
CM,sheetelem,elem
NSLE,S,1
CM,sheetnode,node
allsel
CMSEL,S,sheetcontact,area
esla,s
CM,sheetcontactelem,elem
NSLA,s,1
CM,sheetcontactnode,node
allsel

```

```

!!!!!!!!!!!!!!!!!!!!!!!!!!!!!!!!!!!!!!!!!!!!!!!!!!!!!!!!!!!!!!!!!!!!!!!!!!!!
!Rim segmentation & meshing
!!!!!!!!!!!!!!!!!!!!!!!!!!!!!!!!!!!!!!!!!!!!!!!!!!!!!!!!!!!!!!!!!!!!!!!!!!!!
TYPE,2
MAT,2
MSHAPE,0,2D!Triangles =1
MSHKEY,1      !Free meshing =0

```

```

LSEL,S,,,38
LSEL,A,,,36
LSEL,A,,,43
LSEL,A,,,45
LSEL,A,,,22
LSEL,A,,,24
LSEL,A,,,29
LSEL,A,,,31
LESIZE,ALL, , ,90, ,1, , ,1,
allsel

```

```

LSEL,S,,,23
LSEL,A,,,30
LSEL,A,,,37
LSEL,A,,,13
LSEL,A,,,44
LESIZE,ALL, , ,1, ,1, , ,1,
ALLSEL
CMSEL,S,rim,area

```



```

AMESH,ALL
CMSEL,S,RIM,AREA
ESLA,S
CM,rimelem,elem
ALLSEL

!!!!!!!!!!!!!!!!!!!!!!!!!!!!!!!!!!!!!!!!!!!!!!!!!!!!!!!!!!!!!!!!!!!!!!
!Point segmentation & Meshing
!!!!!!!!!!!!!!!!!!!!!!!!!!!!!!!!!!!!!!!!!!!!!!!!!!!!!!!!!!!!!!!!!!!!!!
CMSEL,S,POINT,AREA

TYPE,3      !Solid 164 element type
Mat,3       !Constrained material except in z-direction
MSHAPE,0,2D !Triangle elements
MSHKEY,2    !Mesh type (2 try mapped, if not, free)
SMRT,4
AMESH,ALL
ALLSEL

!!!!!!!!!!!!!!!!!!!!!!!!!!!!!!!!!!!!!!!!!!!!!!!!!!!!!!!!!!!!!!!!!!!!!!
!Node component names
!!!!!!!!!!!!!!!!!!!!!!!!!!!!!!!!!!!!!!!!!!!!!!!!!!!!!!!!!!!!!!!!!!!!!!
!Rim surface nodes
ASEL,S,,,5
ASEL,A,,,8
ASEL,A,,,11
ASEL,A,,,14
CM,RIMTOP,AREA
ALLSEL

CMSEL,S,RIMTOP,AREA
ESLA,S,1
CM,RIMCONTACTSELEM,ELEM
NSLA,S,1
CM,RIMCONTACTSNODE,NODE
ALLSEL

CMSEL,S,SHEETCONTACTRIM,ELEM
NSLE,S,1
CMSEL,A,RIMCONTACTSNODE,NODE
CM,CONTACTNODES,NODE
ALLSEL

CMSEL,S,SHEETCONTACTRIM,ELEM
CMSEL,A,RIMCONTACTSELEM,ELEM
CM,CONTACTELEMS,ELEM
ALLSEL

!Point nodes
NSEL,S,LOC,Z,PNTDISP+PNTHEIGHT+PNTRAD
NSEL,R,LOC,Y,PNTRAD
NSEL,R,LOC,X,0
CM,POINTNODES,NODE
ALLSEL

!!!!!!!!!!!!!!!!!!!!!!!!!!!!!!!!!!!!!!!!!!!!!!!!!!!!!!!!!!!!!!!!!!!!!!

```

```

!Contact elements
!!!!!!!!!!!!!!!!!!!!!!!!!!!!!!!!!!!!!!!!!!!!!!!!!!!!!!!!!!!!!!!!!!!!!!!!!!!!
EDPART,CREATE
EDCGEN,ASTS,      1,      2,0,0,0,0,0, , , , ,0,10000000,0,0
EDCGEN,ASTS,      3,      1,0,0,0,0,0, , , , ,0,10000000,0,0

EDCONTACT,0.6,0,2,0,1,1,1,4,0
EDSP,OFF,' ',' ',1,

!!!!!!!!!!!!!!!!!!!!!!!!!!!!!!!!!!!!!!!!!!!!!!!!!!!!!!!!!!!!!!!!!!!!!!!!!!!!
!Solving steps !!!!!!!!!!!!!!!!!!!!!!!!!!!!!!!!!!!!!!!!!!!!!!!!!!!!!!!!!!!!!
!!!!!!!!!!!!!!!!!!!!!!!!!!!!!!!!!!!!!!!!!!!!!!!!!!!!!!!!!!!!!!!!!!!!!!!!!!!!
/SOL

!!!!!!!!!!!!!!!!!!!!!!!!!!!!!!!!!!!!!!!!!!!!!!!!!!!!!!!!!!!!!!!!!!!!!!!!!!!!

!Hourglass control
!!!!!!!!!!!!!!!!!!!!!!!!!!!!!!!!!!!!!!!!!!!!!!!!!!!!!!!!!!!!!!!!!!!!!!!!!!!!
EDHGLS,0.15      !Standard LS-DYNA viscous form
!EDMP,HGLS,1,3    !Otherwise, Flanagan-Belytschko VISCOUS form with
                  !exact volume integration of solid elements

!!!!!!!!!!!!!!!!!!!!!!!!!!!!!!!!!!!!!!!!!!!!!!!!!!!!!!!!!!!!!!!!!!!!!!!!!!!!
!Model loads
!!!!!!!!!!!!!!!!!!!!!!!!!!!!!!!!!!!!!!!!!!!!!!!!!!!!!!!!!!!!!!!!!!!!!!!!!!!!
*dim,TIMINGS,array,2,1,!dimension the array parameter time
*dim,VELZ,array,2,1,    !dimension the array parameter zdisp

TIMINGS(1)=0,tval
VELZ(1)=-vel,-vel! z displacement
TIME,tval

EDCTS,MASSK,0.9, !Mass scaling

EDLOAD,ADD,VZ,0,POINTNODES,TIMINGS(1),VELZ(1), 0 !Apply loads

EDENERGY,1,1,1,1 !Switch on all energy options

SAVE,dcone,db

!!!!!!!!!!!!!!!!!!!!!!!!!!!!!!!!!!!!!!!!!!!!!!!!!!!!!!!!!!!!!!!!!!!!!!!!!!!!
!Output files for Post26
!!!!!!!!!!!!!!!!!!!!!!!!!!!!!!!!!!!!!!!!!!!!!!!!!!!!!!!!!!!!!!!!!!!!!!!!!!!!
EDHTIME,NSTEPS    !Specify the number of time steps
                  ! for time-history results.
EDHIST,CONTACTELEMS    !Specify the name of the element component.
EDHIST,CONTACTNODES    !Specify the name of the nodal component.

EDOUT,GLSTAT
EDOUT,MATSUM
EDOUT,NODOUT
EDOUT,NCFORC
!EDOPT,ADD,,BOTH !Adds LS-PREPOST solutions

!!!!!!!!!!!!!!!!!!!!!!!!!!!!!!!!!!!!!!!!!!!!!!!!!!!!!!!!!!!!!!!!!!!!!!!!!!!!
SOLVE
!!!!!!!!!!!!!!!!!!!!!!!!!!!!!!!!!!!!!!!!!!!!!!!!!!!!!!!!!!!!!!!!!!!!!!!!!!!!

```

```
FINISH
SAVE,dcone,db
/EOF !File finished
```

```
!!!!!!!!!!!!!!!!!!!!!!!!!!!!!!!!!!!!!!!!!!!!!!!!!!!!!!!!!!!!!!!!!!!!!!
!Useful post-processing commands, copy and paste
!!!!!!!!!!!!!!!!!!!!!!!!!!!!!!!!!!!!!!!!!!!!!!!!!!!!!!!!!!!!!!!!!!!!!!
```

```
!View final displaced shape, true scale
/post1
/DSCALE,1,1.0
SET, LAST
PLNSOL, U, SUM, 0, 1.0
```

THREE-POINT BEND MODEL

```
FINISH
/CLEAR
/PLOPTS,LOGO,0    ! Get rid of logo for text
/REPLOT
KEYW,PR_SET,1      !GUI filtering: structural
KEYW,PR_STRUC,1
KEYW, LSDYNA,1
/FILNAME, datest, 1
/PREP7
CSYS,0

!!!!!!!!!!!!!!!!!!!!!!!!!!!!!!!!!!!!!!!!!!!!!!!!!!!!!!!!!!!!!!!!!!!!!!!!!!!!
!Create parameters
!!!!!!!!!!!!!!!!!!!!!!!!!!!!!!!!!!!!!!!!!!!!!!!!!!!!!!!!!!!!!!!!!!!!!!!!!!!!

!Material properties
*SET,Epen,6.3501e6      !PEN Young's Modulus
*SET,nupen,0.435        !PEN Poisson's ratio
*SET,dnstpen,1360e-9     !PEN density
*SET,MRC,0.3            !Mooney-Rivlin constants
*SET,Este,200e6         !Steel Young's Modulus
*SET,nuste,0 !0.3       !Steel Poisson's ratio
*SET,dnstste,7900e-9    !Steel density
!Sheet dimensions
*SET,length,60          !Length: 80-50 70-40 60-30
*SET,length1,100
*SET,thick,125e-3!Sheet thickness
*SET,width,100          !Width
*SET,width1,100
*SET,clamp,10           !Clamp depth
!Sheet specific points
*SET,x1,10              !Point offset
*SET,x2,10              !Overhang length
*SET,x5,15              !Distance between supports
!Point info
*SET,offset,62.5e-3     !Offset
*SET,prad,10            !Radius
*SET,plength,40
*SET,x6,width/2-x5/2-2*prad !Distance to sheet edge, depends on x5 &
r
!Force, displacement and time values
*SET,disp,0
*SET,vel,100           !Displacement on sheet, cannot be more than
0.97*majrad
*SET,tval,0.1
*SET,NSTEPS,500        !.HIS POST26 TIMESTEPS
*SET,MASSK,-3.9e-8     !Negative: only applied to elements of a
smaller time step size
!Positive: all elements

!!!!!!!!!!!!!!!!!!!!!!!!!!!!!!!!!!!!!!!!!!!!!!!!!!!!!!!!!!!!!!!!!!!!!!!!!!!!
!Elements used
```

```

!!!!!!!!!!!!!!!!!!!!!!!!!!!!!!!!!!!!!!!!!!!!!!!!!!!!!!!!!!!!!!!!!!!!!!!!!!!!

ET,1,SHELL163          !Explicit Thin Structural Shell
KEYOPT,1,1,2           !Default Belytschko-Tsay
R,1                    !Real constants including integration points and
thickness
RMODIF,1,1,0.833,3,thick,thick,thick,thick,
! SHRF (Shear factor)=5/6
! NIP(No. int. points)=2 for elastic behaviour, 3-5 for plastic
behaviour
ET,2,SOLID164          !Solid elements for edge
KEYOPT,2,1,1           !Default
KEYOPT,2,5,0           !Default
ET,3,SOLID164          !Solid elements for pointer
KEYOPT,3,1,1           !Default
KEYOPT,3,5,0           !Default

!!!!!!!!!!!!!!!!!!!!!!!!!!!!!!!!!!!!!!!!!!!!!!!!!!!!!!!!!!!!!!!!!!!!!!!!!!!!
!Materials properties
!!!!!!!!!!!!!!!!!!!!!!!!!!!!!!!!!!!!!!!!!!!!!!!!!!!!!!!!!!!!!!!!!!!!!!!!!!!!

MP,DENS,1,dnstpen      !Material 1: Linear -Sheet
MP,EX,1,Epen
MP,NUXY,1,nupen
EDMP,HGLS,1,0,0.1,1.5,0.06,
EDHGLS,0.1,
EDSHELL,20,-1,1,2,1,1
EDMP,RIGI,2,7,7       !Material 2: All movement constrained (Support
prong)
MP,DENS,2,dnstste
MP,EX,2,Este
MP,NUXY,2,nuste
EDMP,RIGI,3,4,7       !Material 3: Pushing material (Pushing prongs)
MP,DENS,3,dnstste
MP,EX,3,Este
MP,NUXY,3,nuste

!!!!!!!!!!!!!!!!!!!!!!!!!!!!!!!!!!!!!!!!!!!!!!!!!!!!!!!!!!!!!!!!!!!!!!!!!!!!
!Creating geometries

!!!!!!!!!!!!!!!!!!!!!!!!!!!!!!!!!!!!!!!!!!!!!!!!!!!!!!!!!!!!!!!!!!!!!!!!!!!!
!Sheet Geometry
!!!!!!!!!!!!!!!!!!!!!!!!!!!!!!!!!!!!!!!!!!!!!!!!!!!!!!!!!!!!!!!!!!!!!!!!!!!!

k,1,0,0,0
k,2,length,0,0
k,3,length,width,0
k,4,0,width,0
k,5,clamp,0,0
k,6,clamp,width,0
A,1,5,6,4
A,5,6,3,2
ASEL,S,,,1,2
CM,SHEET,AREA
ALLSEL

!!!!!!!!!!!!!!!!!!!!!!!!!!!!!!!!!!!!!!!!!!!!!!!!!!!!!!!!!!!!!!!!!!!!!!!!!!!!

```

```

!Create prongs
!!!!!!!!!!!!!!!!!!!!!!!!!!!!!!!!!!!!!!!!!!!!!!!!!!!!!!!!!!!!!!!!!!!!!!!!!!!!

!Keypoint for centre of support prong
K,7,length-x2,width/2,-(offset)
!KPs to make the prong
K,8,length-x2,width/2,-(offset+prad)
K,9,length-x2,width/2,-(offset+prad+plength)
K,10,length-x2,width/2+prad,-(offset+prad+plength)
K,11,length-x2,width/2+prad,-(offset+prad)
!Lines for prong
LSTR,10,11 !
LARC,11,7,8,prad !
AROTAT,8,9,,,,,7,9,360,3
!Component creation
ASEL,S,,,3
ASEL,A,,,5
ASEL,A,,,7
CM,SUPPORTSIDES,AREA
ALLSEL
ASEL,S,,,4
ASEL,A,,,6
ASEL,A,,,8
CM,SUPPORTTOP,AREA
ALLSEL
CMSEL,S,SUPPORTTOP,AREA
CMSEL,A,SUPPORTSIDES,AREA
CM,SUPPORT,AREA
!Keypoint for centre of prong 1
K,16,length-x2-x1,x6+prad,(offset)
!KPs to make the prong
K,17,length-x2-x1,x6+prad,(offset+prad)
K,18,length-x2-x1,x6+prad,(offset+prad+plength)
K,19,length-x2-x1,x6,(offset+prad+plength)
K,20,length-x2-x1,x6,(offset+prad)
LSTR,19,20 !L17
LARC,20,16,17,prad !L18
AROTAT,20,21,,,,,16,18,360,3
!Keypoint for centre of prong 2
K,25,length-x2-x1,width-x6-prad,(offset)
!KPs to make the prong
K,26,length-x2-x1,width-x6-prad,(offset+prad)
K,27,length-x2-x1,width-x6-prad,(offset+prad+plength)
K,28,length-x2-x1,width-x6,(offset+prad+plength)
K,29,length-x2-x1,width-x6,(offset+prad)
LSTR,28,29 !L29
LARC,29,25,26,prad !L30
AROTAT,32,33,,,,,25,27,360,3
!Area to connect prongs: single entity
LSTR,21,32
LSTR,23,30
AL,40,44,28,45
!Component creation
ASEL,S,,,10
ASEL,A,,,12
ASEL,A,,,14
ASEL,A,,,16

```

```

ASEL,A,,,18
ASEL,A,,,20
CM,PRONGTOPS,AREA
ALLSEL
ASEL,S,,,9
ASEL,A,,,11
ASEL,A,,,13
ASEL,A,,,15
ASEL,A,,,17
ASEL,A,,,19
CM,PRONGSIDES,AREA
ALLSEL
CMSEL,S,PRONGSIDES,AREA
CMSEL,A,PRONGTOPS,AREA
ASEL,A,,,21
CM,PRONGS,AREA

!!!!!!!!!!!!!!!!!!!!!!!!!!!!!!!!!!!!!!!!!!!!!!!!!!!!!!!!!!!!!!!!!!!!!!!!!!!!
!Sheet segmentation & meshing
!!!!!!!!!!!!!!!!!!!!!!!!!!!!!!!!!!!!!!!!!!!!!!!!!!!!!!!!!!!!!!!!!!!!!!!!!!!!

LSEL,S,,,2
LSEL,A,,,4
LSEL,A,,,6
LESIZE,ALL,,,WIDTH1,,1,,1
ALLSEL
LSEL,S,,,5
LSEL,A,,,7
LESIZE,ALL,,, (LENGTH1) ,,1,,1
ALLSEL
LSEL,S,,,1
LSEL,A,,,3
LESIZE,ALL,,,CLAMP/5,,1,,1
TYPE,1                      !Element type - Shell
REAL,1
MSHAPE,0,2D                 !Triangle elements is 1
MSHKEY,0                     !Free meshing
Mat,1                        !PEN material
SMRT,10
CMSEL,S,SHEET,AREA
AMESH,ALL
NSEL,S,LOC,X,clamp,length
NSEL,R,LOC,Y,0,100
NSEL,R,LOC,Z,0
ESLN,S,1
EREFINE,ALL,,,1,,CLEAN
ALLSEL
CMSEL,S,SHEET,AREA
CM,SHEETELEM,ELEM
NSLA,S,1
CM,SHEETNODE,NODE
ALLSEL

!!!!!!!!!!!!!!!!!!!!!!!!!!!!!!!!!!!!!!!!!!!!!!!!!!!!!!!!!!!!!!!!!!!!!!!!!!!!
!Support segmentation & meshing
!!!!!!!!!!!!!!!!!!!!!!!!!!!!!!!!!!!!!!!!!!!!!!!!!!!!!!!!!!!!!!!!!!!!!!!!!!!!

```

```

LSEL,S,,,15
LSEL,A,,,17
LSEL,A,,,19
LESIZE,ALL,,,12,,1,,,1
ALLSEL
TYPE,2
MAT,2
SMRT,3
MSHAPE,0,2D
MSHKEY,0
CMSEL,S,SUPPORT,AREA
AMESH,ALL
!Point nodes
NSEL,S,LOC,Z,-(offset),-(prad/2)
ESLN,S,1
EREFINE,ALL,,,2,,clean
ALLSEL
CMSEL,S,SUPPORTTOP,AREA
ESLA,S
CM,SUPPORTTOPELEM,ELEM
NSLA,S,1
CM,SUPPORTTOPNODES,NODE
ALLSEL

!!!!!!!!!!!!!!!!!!!!!!!!!!!!!!!!!!!!!!!!!!!!!!!!!!!!!!!!!!!!!!!!!!!!!!!!!!!!
!Prong segmentation & Meshing
!!!!!!!!!!!!!!!!!!!!!!!!!!!!!!!!!!!!!!!!!!!!!!!!!!!!!!!!!!!!!!!!!!!!!!!!!!!!

LSEL,S,,,27
LSEL,A,,,29
LSEL,A,,,31
LSEL,A,,,39
LSEL,A,,,41
LSEL,A,,,43
LESIZE,ALL,,,12,,1,,,1
ALLSEL
TYPE,3          !Solid 164 element type
Mat,3          !Constrained material except in z-direction
MSHAPE,0,2D !Quadrilateral elements
MSHKEY,0      !Mapped mesh
CMSEL,S,PRONGS,AREA
SMRT,3
AMESH,ALL
!Point nodes
NSEL,S,LOC,Z,(offset),(prad/2)
ESLN,S,1
EREFINE,ALL,,,2,,clean
ALLSEL
CMSEL,S,PRONGS,AREA
ESLA,S
CM,PRONGSELEM,ELEM
ALLSEL

!!!!!!!!!!!!!!!!!!!!!!!!!!!!!!!!!!!!!!!!!!!!!!!!!!!!!!!!!!!!!!!!!!!!!!!!!!!!
!Node component names
!!!!!!!!!!!!!!!!!!!!!!!!!!!!!!!!!!!!!!!!!!!!!!!!!!!!!!!!!!!!!!!!!!!!!!!!!!!!

```



```

!Sheet
CMSEL,S,SHEET,AREA
NSLA,S,1
CM, SHEETNODES,NODE
ALLSEL
!Prong nodes
KSEL,S,,,19
NSLK,S
CM,PRONGNODE,NODE
ALLSEL
!DL,4,1,ALL,0
!Constrain edge
!LSEL,S,,,4
!NSLL,S,1
!CM,FIXEDEDGE,NODE
DA,1,ALL,0
ALLSEL

!!!!!!!!!!!!!!!!!!!!!!!!!!!!!!!!!!!!!!!!!!!!!!!!!!!!!!!!!!!!!!!!!!!!!!!!!!!!
!Contact elements
!!!!!!!!!!!!!!!!!!!!!!!!!!!!!!!!!!!!!!!!!!!!!!!!!!!!!!!!!!!!!!!!!!!!!!!!!!!!

!LS-DYNA contact set-up between sheet and rim
EDCGEN,AG,,,0,0,0,0,0, , , , ,0,10000000,0,0
!Hourglass control
EDHGLS,0.05
EDCONTACT,0.5,0,2,0,1,1,1,4,0
EDSP,OFF,' ',' ',1,

!!!!!!!!!!!!!!!!!!!!!!!!!!!!!!!!!!!!!!!!!!!!!!!!!!!!!!!!!!!!!!!!!!!!!!!!!!!!
!Solving Steps
!!!!!!!!!!!!!!!!!!!!!!!!!!!!!!!!!!!!!!!!!!!!!!!!!!!!!!!!!!!!!!!!!!!!!!!!!!!!
/SOL

!!!!!!!!!!!!!!!!!!!!!!!!!!!!!!!!!!!!!!!!!!!!!!!!!!!!!!!!!!!!!!!!!!!!!!!!!!!!
!Model loads
!!!!!!!!!!!!!!!!!!!!!!!!!!!!!!!!!!!!!!!!!!!!!!!!!!!!!!!!!!!!!!!!!!!!!!!!!!!!

*dim,DISPS,array,2,1
*dim,TIMINGS,array,2,1,      !dimension the array parameter time
*dim,VELZ,array,2,1,      !dimension the array parameter zdisp
DISPS(1)=DISP,DISP
TIMINGS(1)=0,tval
VELZ(1)=-vel,-vel! z displacement
TIME,tval
!Mass scaling
EDCTS,-MASSK,0.9,
!Application of loads
EDLOAD,ADD,VZ,0,PRONGNODE,TIMINGS(1),VELZ(1), 0
EDENERGY,1,1,1,1 !Switch on all energy options
SAVE,datest,db

!!!!!!!!!!!!!!!!!!!!!!!!!!!!!!!!!!!!!!!!!!!!!!!!!!!!!!!!!!!!!!!!!!!!!!!!!!!!
!Output files for Post26
!!!!!!!!!!!!!!!!!!!!!!!!!!!!!!!!!!!!!!!!!!!!!!!!!!!!!!!!!!!!!!!!!!!!!!!!!!!!

EDHTIME,NSTEPS !Specify the number of time steps

```

```

! for time-history results.
NSEL,S,LOC,X,clamp+5,length-x1-x2
NSEL,R,LOC,Y,40,60
NSEL,R,LOC,Z,0
CM,POINTNODE,NODE
ESLN,S,1
CM,POINTELEM,ELEM
ALLSEL
EDHIST,POINTELEM      !Specify the name of the element component.
EDHIST,POINTNODE      !Specify the name of the nodal component.
EDOUT,GLSTAT
EDOUT,MATSUM
EDOPT,ADD,,LSDYNA

!!!!!!!!!!!!!!!!!!!!!!!!!!!!!!!!!!!!!!!!!!!!!!!!!!!!!!!!!!!!!!!!!!!!!!!!!!!!

/eof
SOLVE
FINISH
SAVE,datest,db

```


APPENDIX H: IRIDIS SUBMISSION SCRIPT

```
#!/bin/bash

# Run 4 subjobs simultaneously on a single node, in separate directories

# set default resource requirements for job
# - these can be overridden on the qsub command line (this is for a 80 hour job)
#PBS -l nodes=1:ppn=4
#PBS -l walltime=150:00:00

# set names of job directories

job_dir1=/scratch9/tobes/cone10
job_dir2=/scratch9/tobes/cone16

# Run 2 subjobs
# use separate input & output files in each subdirectory

cd $job_dir1
/local/ansys_inc/V11SP1/v110/ansys/bin/lsdyna110 pr=aa_r_dy i=dcone.k s=inter &

cd $job_dir2
/local/ansys_inc/V11SP1/v110/ansys/bin/lsdyna110 pr=aa_r_dy i=dcone.k s=inter &

# (the "&" at the end of the line runs the commands in the background,
# and moves to the next executable line without waiting for completion)

# wait for all subjobs to complete (otherwise the script thinks it's finished!)
wait
```


APPENDIX I: JIG DESIGN DRAWINGS

4 sets of 3-point bend pieces are needed to be made. All will have the ball bearing located and adhered to a depression on the spigots. The 4th set I think will be the hardest, with 2 mm ball bearings needing to be located and adhered onto smaller spigots.


UNLES OTHERWISE SPECIFIED: DIMENSIONS ARE IN MILLIMETERS		FINISH:		DEBUR AND BREAK SHARP EDGES	
SURFACE FINISH:		TOLERANCES:			
		LINEAR:			
		ANGULAR:			
DRAWN	NAME	SIGNATURE	DATE		
CHECKED					
APPROVED					
WPG					
G/A					
				MATERIAL: Steel	

DO NOT SCALE DRAWING		REVISION 2	

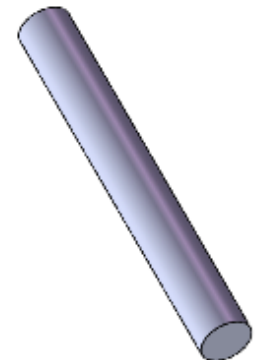
TITLE:	
3 point bend rig	

DWG NO.		A4	

1		2		3		4		5		6	
A		B		C		D					

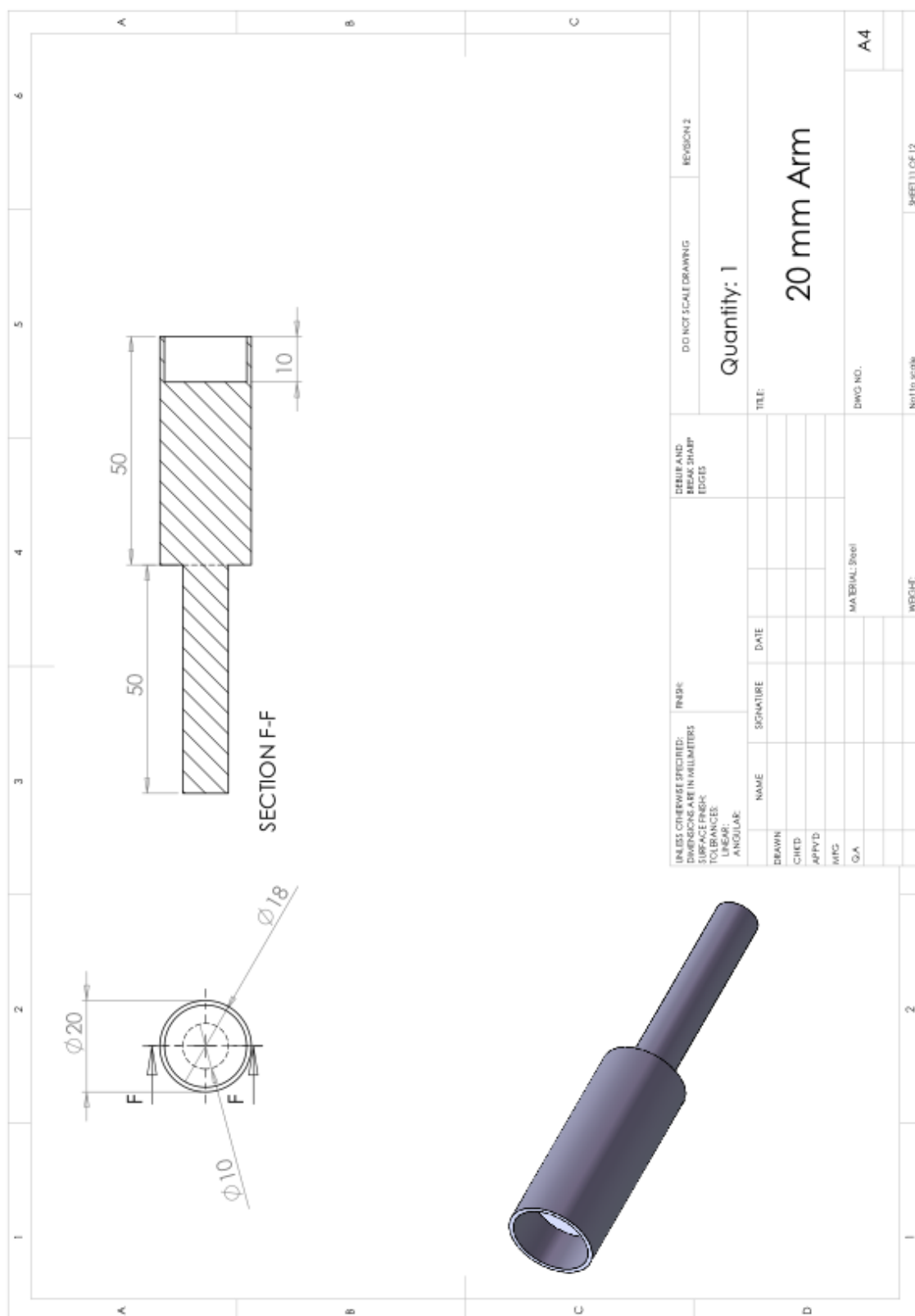


80



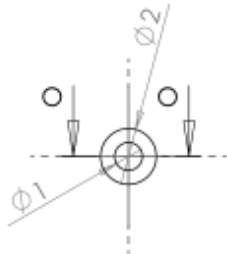
Spigot to be adhered to 3 point bend rig with araldite.


UNLESS OTHERWISE SPECIFIED: DIMENSIONS ARE IN MILLIMETERS SURFACE FINISH TO STANDARDS TOLERANCES: LINEAR ANGULAR				INSIDE DATE		DEBurr AND BREAK SHARP EDGES		DO NOT SCALE DRAWING		REVISION 2	
								Quantity: 1			
DRAWN CHECKED APPROVED MFG Q.A.				NAME SIGNATURE DATE		TITLE: <h2 style="text-align: center;">Base Spigot</h2>		DWG NO. A4		Not to scale SHEET 3 OF 12	




1		2		3		4		5		6	
A		B		C		A		B		C	
<p>Wire to be fixed into 2 mm hole using Araldite.</p>											
UNLESS OTHERWISE SPECIFIED: DIMENSIONS ARE IN MILLIMETERS SURFACE FINISH TO STANDARDS TOLERANCES: LINEAR ANGULAR						INSIDE		DEBUR AND BREAK SHARP EDGES		DO NOT SCALE DRAWING	
REVISION 1						Quantity: 1					
TITLE:						Small sphere arm					
DRAWN						NAME		SIGNATURE		DATE	
CHECKED											
APPROVED											
MFG											
Q.A.											
MATERIAL: Steel						DWG NO.		A4			
WBSHC						Not to scale		SHEET 9 OF 12			

1		2		3		4		5		6	
A		B		C		D		E		F	



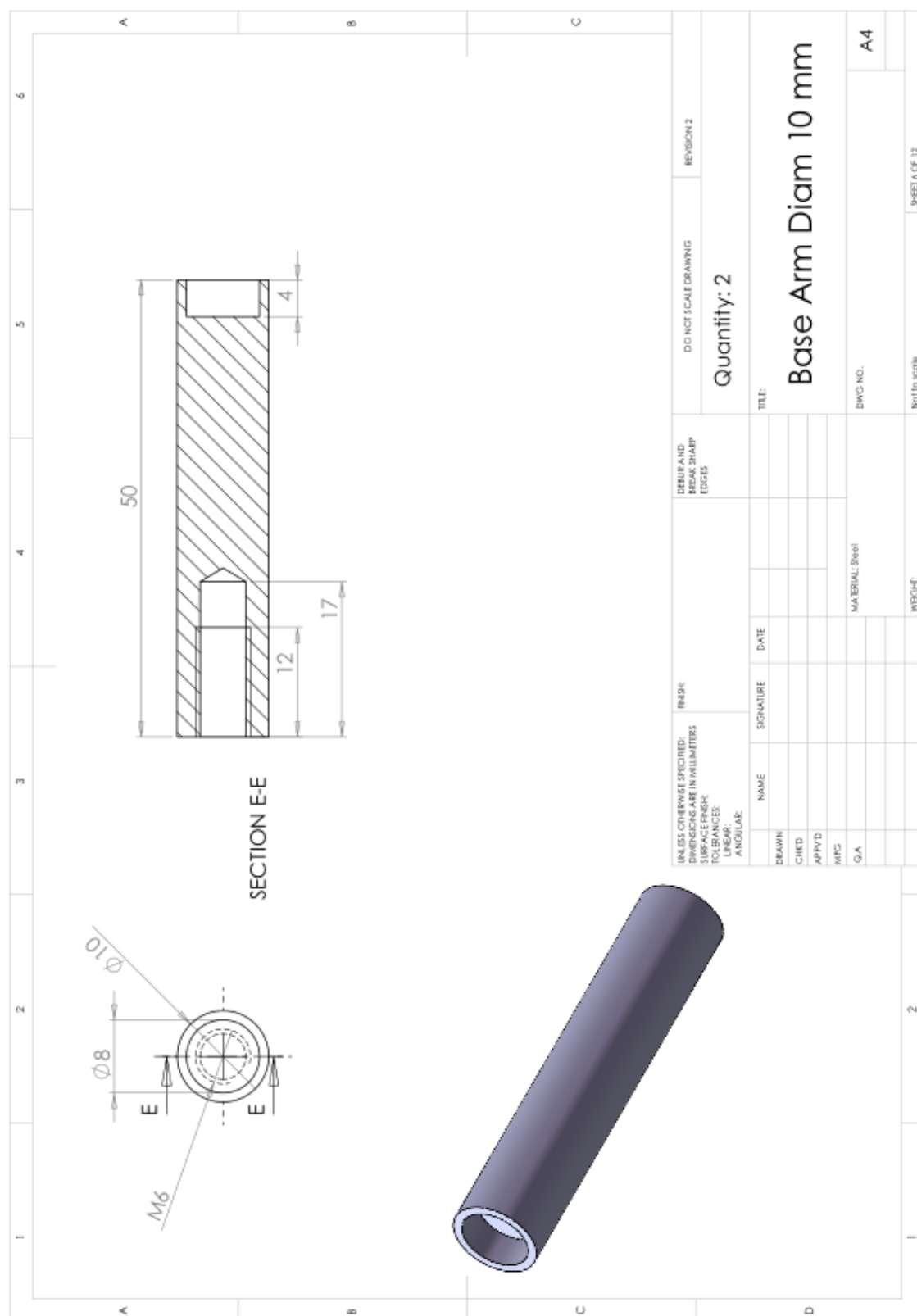


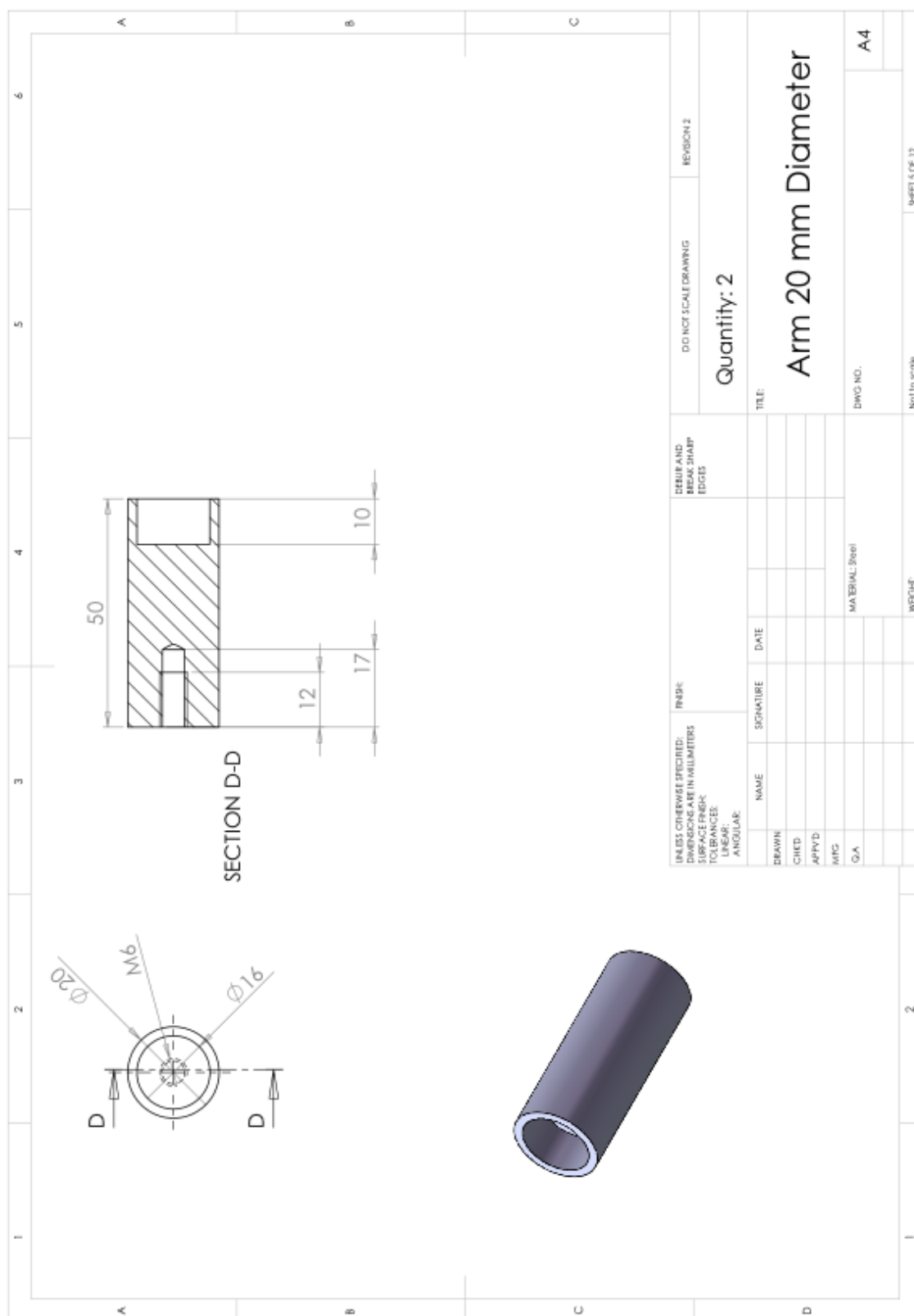


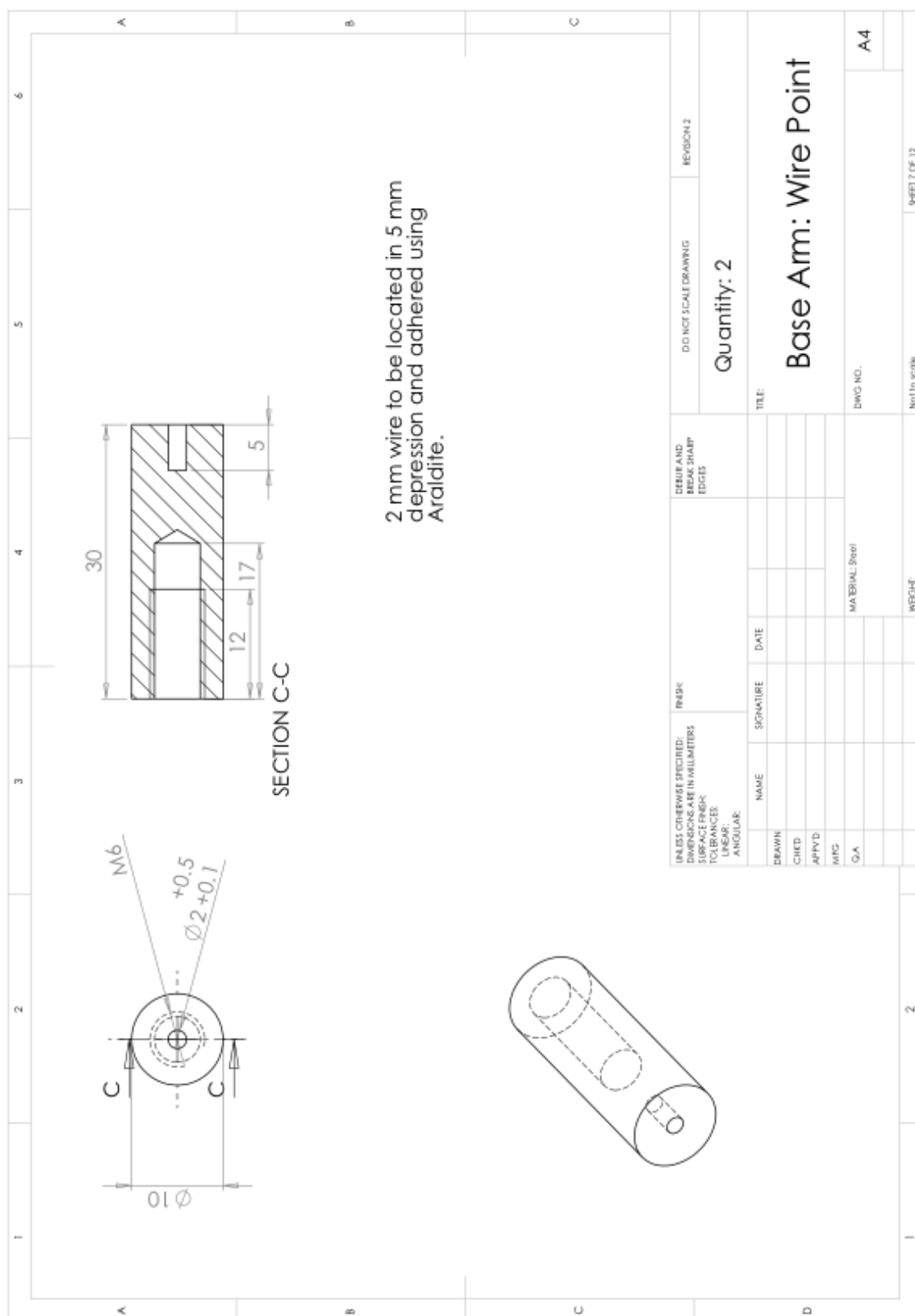
SECTION O-O

1 mm depression to locate ball bearing. Araldite to be used to adhere into place.

UNLESS OTHERWISE SPECIFIED: DIMENSIONS ARE IN MILLIMETERS TOLERANCES: FRACTIONS DECIMALS ANGULAR				FINISH:		DEBurr AND BREAK SHARP EDGES		DO NOT SCALE DRAWING		REVISION 2	
								Quantity: 3			
								TITLE:		Wire	
								DWG NO.		A4	
								MATERIAL: Steel		Not to scale	
								WBSHC		SHEET 8 OF 12	







APPENDIX J: DVD MATERIAL
